Thermal and Visual Operational Characteristics of Multi-Microchannel Evaporators using Refrigerants

THÈSE N^{O} 5594 (2012)

PRÉSENTÉE LE 14 DECEMBRE 2012
À LA FACULTÉ DES SCIENCES ET TECHNIQUES DE L'INGÉNIEUR
LABORATOIRE DE TRANSFERT DE CHALEUR ET DE MASSE
PROGRAMME DOCTORAL EN ENERGIE

ÉCOLE POLYTECHNIQUE FÉDÉRALE DE LAUSANNE

POUR L'OBTENTION DU GRADE DE DOCTEUR ÈS SCIENCES

PAR

Sylwia SZCZUKIEWICZ

acceptée sur proposition du jury:

Dr F. Maréchal, président du jury
Prof. J. R. Thome, Dr N. Borhani, directeurs de thèse
Dr M. Farhat, rapporteur
Prof. M. E. Poniewski, rapporteur
Dr R. Revellin, rapporteur

ÉCOLE POLYTECHNIQUE
FÉDÉRALE DE LAUSANNE

Suisse
2012

"Bogaty znajdzie bogatszego od siebie, sławnego zaćmi cudza większa sława,
potężnego potężniejszy pokona..."
– *Quo Vadis*, Henryk Sienkiewicz

I dedicate this thesis to my beloved parents, Janina and Alfred.

Acknowledgements

The current research project has been carried out at the Heat and Mass Transfer Laboratory, École Politechnique Fédérale de Lausanne (LTCM, EPFL), under the supervision of Prof. John R. Thome and Dr. Navid Borhani, to whom I am greatly thankful for their invaluable guidance throughout my Ph.D. studies and careful reading of this manuscript. This work would not be possible without their confidence and support.

The study was funded by the Nano-Tera RTD project CMOSAIC (ref. 123618) financed by the Swiss Confederation and scientifically evaluated by SNSF, which are gratefully acknowledged. I would like to thank the Microelectronic Systems Laboratory (LSM, EPFL) for manufacturing the test sections, for bonding the Advanced Thermal Packaging group (IBM Zürich) and the ATSE-Workshop ATME for the work done on the experimental facility. Especially, I would like to appreciate the precious advices I have received from Laurent Chevalley. I wish to further thank Honeywell Inc. (Samuel Yana Motta) for providing the R1234ze(E) test fluid.

It is my pleasure to thank my committee members: Prof. Mieczysław E. Poniewski, Dr. François Maréchal, Dr. Mohamed Farhat, and Dr. Rémi Revellin for their time in evaluating my thesis, together with their constructive remarks and suggestions that helped me to improve this manuscript.

I wish to acknowledge my colleagues of the LTCM lab; it has been a pleasure to work with you all. In particular, I thank to Dr. Eugene van Rooyen, who was always available for research consultations. Special thanks to my friend Sepideh Khodaparast for long hours of constructive discussions and her presence from the beginning until the end of my Ph.D. studies. I am greatly thankful to my friends: Bogdan A. Nichita, Gustavo Rabello dos Anjos, Nicolas Lamaison, Mirco Magnini, Jackson B. Marcinichen, Giulia Tagliabue, Arturo González Gil, and Ewa Dachowski for all the international dinners we had. Many thanks to Duan Wu and Marco Milan, with whom I shared the time of writing this thesis. I would also like to thank to Cécile Taverney and Nathalie Matthey-de-l'Endroit for their encouragement in completing this work. Finally, I wish to express my gratitude to Iwona Olkisz and Elyes Cheikh for helping me to discover all those beautiful places, not only in Switzerland.

Last but not least, many thanks to my family and my dear parents, Janina and Alfred to whom this thesis is dedicated, for their endurance and understanding in any time of my life...

Abstract

Two-phase flow operational stability of refrigerants R245fa, R236fa, and R1234ze(E) in $100 \times 100\,\mu\text{m}^2$ multi-microchannels for cooling of future high-performance 3D stacked architectures with interlayer cooling has been addressed in the current experimental investigation. Without any inlet restrictions in the micro-evaporator, significant flow instabilities, back flow, and flow maldistribution led to high-amplitude and high-frequency temperature and pressure oscillations. Such undesired phenomena were inhibited by placing rectangular restrictions (micro-orifices) at the inlet of each channel, thus ensuring a wide range of stable two-phase flow operating conditions. The effects of different orifice expansion ratios and fluids on the performance of the evaporator were studied by using suitably designed modular test sections.

Simultaneous high-speed video and infra-red camera visualizations of the two-phase flow and heat transfer dynamics across the micro-evaporator area allowed the various different operating regimes to be identified and then represented by the two-phase flow operational maps. Two-phase flow flashed by the micro-orifices was identified as the optimal operating condition, while dissipating high heat fluxes and keeping the junction chip temperature below a typical CPU operating condition. In the present study, a novel in-situ *pixel by pixel* technique was developed to calibrate the raw infra-red images, thus converting them into two-dimensional temperature fields of 10'000 pixels over the test section surface. A comprehensive analysis of those temperature maps supported by the flow visualization videos confirmed that the two-phase flow patterns appearing in the channel and the transitions between them have a remarkable influence on the heat transfer coefficients, which were determined taking into account 3D heat spreading. The inlet and the outlet restriction pressure losses were quantified in order to accurately simulate the hydraulic performance of microchannel evaporators and provide more reliable heat transfer data.

The heat transfer coefficients were determined with a very fine resolution that enabled the trends in the heat transfer coefficients along the channel length in the neighborhood of the flow transition from coalescing bubble to the annular flow to be studied in detail. It was shown that the heat transfer coefficient does not change sharply at the transition zone, but rather has a smooth change in trend. The characteristic U-shape of the heat transfer coefficient trend was observed, where the descending branch of the curve corresponds to the coalescing elongated bubble flow regime, while ascending one represents the increasing heat transfer coefficient in the annular flow regime. A good agreement of the experimental heat transfer coefficients and one existing flow pattern-based prediction method was found and a new vapor quality buffer is proposed as an update of this model.

Keywords: Multi-microchannels, Silicon evaporator, Two-phase flow cooling, Refrigerants, Flow visualization, Infra-red thermometry, Flow stabilities, Inlet restrictions / micro-orifices, Operational map, Pressure drop, Heat transfer coefficient.

Version abrégée

La présente étude expérimentale concerne la stabilité des écoulements biphasiques des réfrigérants R245fa, R236fa et R1234ze(E) dans des micro-canaux multiples de dimensions $100 \,\mathrm{x}\, 100\,\mu\mathrm{m}^2$ pour le refroidissement "inter-couche" des futurs processeurs 3D de hautes performances. Si aucune restriction n'est placée à l'entrée des micro-canaux composant les micro-évaporateurs, des instabilités ainsi que des inversions de sens et des mauvaises distributions de l'écoulement peuvent mener à des oscillations à haute fréquence et de grande amplitude des champs de pression et température. De tels phénoménes ont été inhibés en plaçant des restrictions rectangulaires (micro-orifices) à l'entrée de chaque canal. Ceci permet d'assurer un écoulement biphasique stable pour une large gamme de conditions expérimentales. Les performances des micro-évaporateurs sont étudiées en fonction du rapport d'expansion dans les orifices et du type de fluide.

La visualisation simultanée par caméra rapide et par caméra infrarouge permet l'identification de différents régimes d'opération et conduit à la création de carte opératoire d'écoulements biphasiques. Les conditions opératoires optimales ont été obtenues pour un écoulement biphasique créé par "flashing" (chute soudaine de pression) au niveau des micro-orifices. Ces conditions ont permis d'évacuer de larges flux de chaleur en conservant la température du pseudo-processeur en dessous de température typique d'opération de CPU. Dans la présente étude, une nouvelle technique in-situ, pixel par pixel, a été développée pour calibrer les images infrarouges, permettant ainsi d'obtenir un champ de température de 10'000 pixels sur la section d'essai. L'analyse de ces champs de température supportée par la visualisation des écoulements confirme que le type d'écoulement a une grande influence sur les coefficients de transfert thermique (déterminés en prenant en compte la conduction en 3 dimensions dans l'évaporateur). Les pertes de charge à l'entrée et à la sortie des canaux ont été quantifiées de façon à décrire précisément les performances hydrauliques des micro-évaporateurs et de fournir des données de transferts thermiques fiables.

Les coefficients de transfert thermiques ont donc été obtenues avec une grande résolution ce qui permet de décrire au mieux la transition entre le régime de bulles coalescentes et le régime annulaire. Il est montré que le coefficient de transfert thermique ne change pas de façon abrupte lors de la transition mais plutôt de façon continue. La forme en U caractéristique a été observée, la partie descendante correspondant au régime de bulles coalescentes, tandis que la partie ascendante représente le régime annulaire. Une bonne comparaison entre les données obtenues expérimentalement et une méthode de prédiction basée sur une carte d'écoulement a été obtenue. Enfin, un nouvel effet du titre en vapeur a été ajouté à cette méthode de prédiction pour améliorer sa précision.

Mots clés: Multi-micro-canaux, Évaporateur en silicone, Refroidissement diphasique, Réfrigérant, Visualisation d'écoulement, Thermométrie infrarouge, Dtabilités, Micro-orifices, Carte opératoire, Perte de charge, Coefficient de transfert thermique.

Contents

Acknowledgements **vii**

Abstract **ix**

Version abrégée **xi**

List of Figures **xvii**

List of Tables **xxvii**

Nomenclature **xxix**

1 Introduction and research motivation **1**

2 State-of-the-art review on microscale two-phase flows and heat transfer **5**

2.1 Channel size 5

2.2 Two-phase pressure drop 8

2.3 Infra-red camera measurements applied to microchannels 11

2.4 Flow boiling heat transfer 15

2.5 Axial conduction effects on heat transfer data 20

2.6 Two-phase flow visualization 22

2.7 Summary and problem statement 27

3 Experimental set-up **29**

3.1 Flow boiling test facility 29

3.2 Micro-evaporators 34

4 Experiments, operating conditions, and data reduction 41

4.1 Experiments 41

4.1.1 Single-phase flow tests 42

4.1.2 Two-phase flow tests 46

4.2 Fluids 48

4.3 Operating conditions 48

4.4 Data reduction procedure 50

4.4.1 Channel mass flux 50

4.4.2 Pressures 50

4.4.3 Base and wall heat fluxes 58

4.4.4 Base and footprint temperatures 59

4.4.5 Fluid temperature and inlet subcooling 60

4.4.6 Vapor quality 61

4.4.7 Heat transfer coefficient 62

4.5 Heat conduction schemes 62

5 Two-phase flow and temperature visualizations 67

5.1 Two-phase flow operational maps 67

5.2 Two-phase flow operating regimes 81

5.3 Temperature visualization 87

5.4 Conclusions 98

6 Pressure drop 99

6.1 Adiabatic results 99

6.1.1 Total pressure drop 99

6.1.2 Inlet restriction pressure loss 101

6.2 Diabatic results 104

6.2.1 Total pressure drop . . . 104

6.2.2 Outlet restriction pressure loss . . . 109

6.2.3 Channel pressure drop . . . 117

6.3 Fluid temperature . . . 121

6.4 Conclusions . . . 125

7 Two-phase flow heat transfer 127

7.1 Transitions for stable flows . . . 127

7.2 Comparison between 1D and 3D heat conduction schemes . . . 130

7.3 Heat transfer coefficient trend with 3D heat spreading . . . 134

7.4 Wall heat transfer coefficients . . . 136

7.4.1 Effect of channel mass flux . . . 136

7.4.2 Effect of wall heat flux . . . 138

7.4.3 Effect of fluid properties . . . 139

7.4.4 Effects of orifice expansion ratio . . . 140

7.5 Comparison with prediction methods . . . 141

7.6 Conclusions . . . 148

8 Concluding remarks and recommendations for further investigations 151

8.1 Final remarks . . . 151

8.2 Future recommendations . . . 153

A Error propagation 155

A.1 Fluid properties . . . 155

A.1.1 Single-phase flow . . . 155

A.1.2 Two-phase flow . . . 155

A.2 Derived parameters . . . 156

A.2.1 Expansion ratio . . . 156

A.2.2 Aspect ratio . . . 156

A.2.3 Channel mass flux . . . 156
A.2.4 Base heat flux . . . 156
A.2.5 Pressures . . . 157
A.2.6 Frictional channel pressure drop . . . 158
A.2.7 Vapor quality . . . 158
A.2.8 Silicon thermal conductivity . . . 158
A.2.9 Footprint temperature . . . 158
A.2.10 Heat transfer coefficient . . . 159
A.2.11 Multi-dimensional heat conduction . . . 159

B Further results 161

B.1 Total adiabatic pressure drops . . . 161
B.2 Total two-phase flow pressure drops under uniform heating . . . 163
B.3 Two-phase flow channel pressure drops . . . 165
B.4 Two-phase heat transfer coefficient with 3D heat spreading . . . 168

C Existing heat transfer prediction methods compared with the current results 173

C.1 A composite heat transfer correlation of Bertsch et al. (2009) . . . 173
C.2 Flow pattern-based model of Costa-Patry et al. (2012) . . . 175
C.2.1 Three-zone model of Thome et al. (2004) . . . 176
C.2.2 Unified heat and flow model for annular flows of Cioncolini and Thome (2011) including entrainment prediction method of Cioncolini et al. (2009) 182
C.2.3 Modification to the original heat transfer prediction methods . . . 184
Three-zone model of Thome et al. (2004) . . . 184
Annular flow model of Cioncolini and Thome (2011) . . . 185
C.3 Validation of Matlab implementations . . . 186

D Bibliography 189

Curriculum Vitae 201

List of Figures

2.1 Visualization of the 4'052 μm test section at a high mass velocity: (a) without, and (b) with the orifice insert. Figure extracted from Park et al. (2009). 26

3.1 (a) Schematic of the refrigerant flow loop, and (b) photograph of the experimental flow boiling test facility with the optical system (Szczukiewicz et al., 2012b). . . 30

3.2 (a) Bottom part of the test section manifold, (b) front-side of the PCB board with HSEC8-130-01-S-DV-A edge connector, and (c) back-side of the PCB board with heaters and RTDs connectors. 31

3.3 (a) An example of an IR camera calibration curve for a given pixel on the sensor (Szczukiewicz et al., 2012a), and (b) probability density function for the reference temperature of 10.8 °C over a 3'621 length sample captured at 60 Hz. 32

3.4 Comparison of: (a) the pre- and post-experimental calibration curves for the pixel $P_{(15,16)}$ of the IR camera's sensor array (Szczukiewicz et al., 2012b), and (b) the calibration curves of the middle pixel of the IR camera's sensor array obtained for 4 different test sections. 33

3.5 Schematic of the test section assembly (Sabry et al., 2011). 34

3.6 (a) 100 x 100 μm^2 channels with the inlet restrictions of the expansion ratio of $e_{in,rest} = 2$, and (b) back-side of the silicon evaporator with the serpentine microheaters and RTDs. 35

3.7 Photograph of the surface roughness profile of the inlet restriction having the expansion ratio of $e_{in,rest} = 2$. 36

3.8 Photographs of: (a) 100 x 100 μm^2 channels, and (b) the surface profile of the channel bottom wall. 37

3.9 Snapshots of the high-speed flow visualization and the time-averaged IR temperature maps of the test section's base provided by the two-phase flow boiling of R245fa flowing in the micro-evaporators with and without any inlet restrictions for $G_{ch} = 2'035\,\mathrm{kg\,m^{-2}\,s^{-1}}$ and $q_b = 36.5\,\mathrm{W\,cm^{-2}}$. 39

4.1 Summary of the current experimental campaign, where × denotes the test case. . 41

4.2 Schematic of the test section. 43

4.3 Single-phase flow heat losses in function of the Reynolds number for the base heat flux varying from 1.9 to 2.4 $\mathrm{W\,cm^{-2}}$ and the inlet liquid subcooling ranging between 4.8 and 6.4K. 43

4.4 Measurements of: (a) total pressure drop, Δp_{total}, and (b) local IR temperatures, T_{IR}, with and without illumination for two-phase flow of R236fa flowing in the test section with the inlet restrictions of $e_{in,rest} = 2$ for the channel mass flux varying from 715 to 2'275 $\mathrm{kg\,m^{-2}\,s^{-1}}$ and the dissipated base heat flux of 24.6 $\mathrm{W\,cm^{-2}}$ (Szczukiewicz et al., 2012a,b). 44

4.5 Comparison of the experimental Nusselt numbers with those predicted by the Shah and London (1978) formula for laminar developing flow for $100 < \mathrm{Re} < 1'000$ with a uniform heat flux boundary condition in the test section with the inlet restrictions of $e_{in,rest} = 2$. The heat losses have been estimated from Fig. 4.3 and removed. Total MAE = 27.5 %. 45

4.6 Experimental Nusselt numbers versus those predicted by Shah and London (1978) formula method for laminar developing flow of R1234ze(E) flowing in the test section with the inlet restrictions of $e_{in,rest} = 2$ under a uniform heat flux boundary condition (Szczukiewicz et al., 2012a,b). 46

4.7 Thermocouple response at: (a) the inlet, T_{in}, and (b) the outlet, T_{out} manifold's plenums corresponding to the change of the base heat flux. 47

4.8 Sectional view of the micro-evaporator. 50

4.9 Diabatic two-phase flow pressure gradients. 53

4.10 Two-phase flow of R236fa in the half-heated test section ($e_{in,rest} = 4$) for the channel mass flux of $G_{ch} = 2'077\,\mathrm{kg\,m^{-2}\,s^{-1}}$ and the dissipated base heat flux of $q_b = 52.6\,\mathrm{W\,cm^{-1}}$: (a) flow pattern, and (b) IR temperature map. 55

4.11 Getting the standard deviations of the pixel intensity values over time and a selected example of the obtained results. 56

4.12 Spatial derivatives of: (a) the lateral-temperature at the channel location of $z = 10\,\mathrm{mm}$, and (b) the temperature along the centerline in the flow direction for the two-phase flow of R236fa flowing in the half-heated test section ($e_{in,rest} = 2$) for $G_{ch} = 2'087 \pm 0.5\%\,\mathrm{kg\,m^{-2}\,s^{-1}}$ and q_b ranging from 23.9 to 43.1 $\mathrm{W\,cm^{-1}}$. 57

4.13 Fluid temperature along a microchannel, based on Lee and Garimella (2008). . . 61

4.14 Control volume for heat conduction schemes. 63

4.15 Grid independence through the thickness of the test section for (a) 5 selected pixels of the IR camera's sensor array applying: (b) 2D, and (c) 3D heat conduction schemes under the two-phase flow of R236fa in the micro-evaporator with the inlet restrictions of $e_{in,rest} = 4$, $G_{ch} = 2\text{'}099\,\mathrm{kg\,m^{-2}\,s^{-1}}$ and $q_b = 16.9\,\mathrm{W\,cm^{-1}}$. 65

4.16 IR temperatures selected for the heat transfer data analysis. Two-phase flow IR temperature map for R236fa flowing in the test section with the inlet restrictions of $e_{in,rest} = 4$ for $G_{ch} = 1903\,\mathrm{kg\,m^{-2}\,s^{-1}}$ and $q_b = 43.4\,\mathrm{W\,m^{-2}}$. The blue square indicates an array of IR temperatures considered in heat transfer analysis. 66

5.1 Two-phase flow operational map for R245fa in the micro-evaporator with the $50\,\mu$m-wide, $100\,\mu$m-deep, and $100\,\mu$m-long inlet restrictions ($e_{in,rest} = 2$). 68

5.2 Two-phase flow operational map for R236fa in the micro-evaporator with the $50\,\mu$m-wide, $100\,\mu$m-deep, and $100\,\mu$m-long inlet restrictions ($e_{in,rest} = 2$). 69

5.3 Two-phase flow operational map for R1234ze(E) in the micro-evaporator with the $50\,\mu$m-wide, $100\,\mu$m-deep, and $100\,\mu$m-long inlet restrictions ($e_{in,rest} = 2$). 70

5.4 Two-phase flow operational map for R245fa in the micro-evaporator without any inlet restrictions ($e_{in,rest} = 1$). 71

5.5 Two-phase flow operational map for R236fa in the micro-evaporator with the $75\,\mu$m-wide, $100\,\mu$m-deep, and $100\,\mu$m-long inlet restrictions ($e_{in,rest} = 1.33$). . . . 72

5.6 Two-phase flow operational map for R236fa in the micro-evaporator with the $25\,\mu$m-wide, $100\,\mu$m-deep, and $100\,\mu$m-long inlet restrictions ($e_{in,rest} = 4$). 73

5.7 Some vapor bubbles flashed at the channel inlet for R236fa flowing in $e_{in,rest} = 4$, $G_{ch} = 896\,\mathrm{kg\,m^{-2}\,s^{-1}}$, $q_b = 20.7\,\mathrm{W\,cm^{-2}}$. 76

5.8 Simplified experimental test matrix for R245fa flowing within the test section without any inlet restrictions ($e_{in,rest} = 1$) and with the $50\,\mu$m-wide, $100\,\mu$m-deep, and $100\,\mu$m-long micro-orifices ($e_{in,rest} = 2$). 78

5.9 Simplified experimental test matrix for R236fa flowing within the 3 test sections ($e_{in,rest} = 1.33$, 2, and 4). 79

5.10 Simplified experimental test matrix for $e_{in,rest} = 2$ and the 3 fluids: R245fa, R236fa, R1234ze(E). 80

5.11 Two-phase flow operating regimes observed in the test section with the $50\,\mu$m-wide, $100\,\mu$m-deep, and $100\,\mu$m-long inlet restrictions ($e_{in,rest} = 2$). 82

5.12 Temporal non-uniformity of the two-phase flow of R236fa inside the microchannels with the expansion ratio of $e_{in,rest} = 2$, $G_{ch} = 300\,\mathrm{kg\,m^{-2}\,s^{-1}}$, $q_b = 9.6\,\mathrm{W\,cm^{-2}}$: (a) 0 s, (b) 0.1 s, (c) 0.2 s, and (d) 0.3 s. 84

5.13 Flashed vapor bubbles of R236fa. 85

5.14 Standard deviations of the pixel intensity values of the image sequences over time provided by the two-phase flow of R245fa flowing in the test section with the inlet restrictions of the expansion ratio of $e_{in,rest} = 2$. 86

5.15 Reversibility of the two-phase flow of R245fa in $100 \times 100\,\mu\mathrm{m}^2$ microchannels with the inlet restrictions of the expansion ratio of $e_{in,rest} = 2$, $G_{ch} = 1643\,\mathrm{kg\,m^{-2}\,s^{-1}}$, $q_b = 29\,\mathrm{W\,cm^{-2}}$. 87

5.16 Time-averaged temperature flow pattern maps for $e_{in,rest} = 2$. 89

5.17 Temporal temperature fluctuations for pixels: (a) $P_{(50,20)}$, (b) $P_{(20,50)}$, (c) $P_{(50,80)}$, and (d) $P_{(80,80)}$. 94

5.18 (a) Minimum junction temperature of the micro-evaporator's base ($T_{IR,min}$), (b) maximum junction temperature of the micro-evaporator's base ($T_{IR,max}$), (c) maximum base heat flux (q_b), and (d) corresponding total pressure drop ($\triangle p_{total}$) for all the test cases, where *0* indicates the cases which were not tested. 96

6.1 Adiabatic single-phase flow pressure drops as a function of the channel Reynolds number for: (a) R245fa in 2 test sections with $e_{in,rest} = 1$ and 2, (b) R236fa in 3 test sections ($e_{in,rest} = 1.33$, 2, and 4), and (c) fluids R245fa, R236fa, and R1234ze(E) flowing in the test section with $e_{in,rest} = 2$. 100

6.2 Single-phase flow inlet restriction pressure losses for R236fa in the test section with the inlet restrictions of $e_{in,rest} = 4$. 102

6.3 Adiabatic pressure gradients for: (a) R236fa in $e_{in,rest} = 4$, and (b) R1234ze(E) in $e_{in,rest} = 2$. 103

6.4 Total two-phase pressure drops of R236fa in the test section with the expansion ratio of $e_{in,rest} = 4$ in terms of the outlet vapor quality, x_{out}. In general, the difference between the channel mass flux, G_{ch}, for an individual data point in a particular curve and the reported nominal value is less than ±3.15% of the latter. 105

6.5 Total diabatic pressure drop dependence on the dissipated base heat flux for: (a) $G_{ch} = 1'105 \pm 5.4\%\,\mathrm{kg\,m^{-2}\,s^{-1}}$, and (b) $G_{ch} = 2'102 \pm 1.7\%\,\mathrm{kg\,m^{-2}\,s^{-1}}$. 106

6.6 Average test section's base temperature dependence on: (a) the total diabatic pressure drop, and (b) corresponding base heat flux for the channel mass flux of $G_{ch} = 2'102 \pm 1.7\%\,\mathrm{kg\,m^{-2}\,s^{-1}}$. The fitted curves consider point no. $3-5$ for the single-phase flow followed by two-phase flow without back flow operating regime and points no. $6-13$ for the flashing two-phase flow without back flow operating regime (see Fig. 6.5). 108

6.7 Schematic of the pressure drop change within the device, where the flow direction is from left to right (based on Schneider et al. (2007)). One needs to notice that the pressure drop in the inlet, $\Delta p_{in,rest}$, and the outlet, $\Delta p_{out,rest}$, sections are simplified here to be linear. 109

6.8 (a) Δp_{total} versus x_{out}, and (b) $\Delta p_{out,rest}$ versus $x_{ch,end}$ for the two-phase flow of R236fa flowing in the half-heated micro-evaporator with the inlet restrictions of $e_{in,rest} = 4$. The difference between the channel mass flux for an individual data point and the reported nominal value is within ±2.0% of the latter. Experimental results were selected based on flow visualization. 112

6.9 (a) Δp_{total} versus x_{out}, and (b) $\Delta p_{out,rest}$ versus $x_{ch,end}$ for the two-phase flow of R1234ze(E) flowing in the half-heated micro-evaporator with the inlet restrictions of $e_{in,rest} = 2$. The difference between the channel mass flux for an individual data point and the reported nominal value is within ±2.16% of the latter. Experiments were conducted without visual observation, thus all the data were considered. . . 113

6.10 Outlet restriction pressure drop ratios for: (a) R236fa in $e_{in,rest} = 4$, and (b) R1234ze(E) in $e_{in,rest} = 2$. 114

6.11 $\Delta p_{out,rest}$ curve fitting for: (a) R236fa in $e_{in,rest} = 4$, and (b) R1234ze(E) in $e_{in,rest} = 2$. 116

6.12 Δp_{ch} for R236fa flowing within the micro-evaporator with the inlet restrictions of $e_{in,rest} = 2$. 117

6.13 Δp_{ch} for R236fa flowing within the micro-evaporator with the inlet restrictions of $e_{in,rest} = 4$. 118

6.14 (a) Δp_{ch}, and (b) $\Delta p_{ch} / \Delta p_{total}$ ratio for R236fa flowing within the micro-evaporator with the inlet restrictions of $e_{in,rest} = 2$. 119

6.15 (a) $\Delta p_{in,rest} / \Delta p_{total}$, and (b) $\Delta p_{out,rest} / \Delta p_{total}$ ratios for R236fa flowing within the micro-evaporator with the inlet restrictions of $e_{in,rest} = 2$. 120

6.16 Δp_{ch} for the flashing two-phase flow without back flow operating regime for R236fa flowing within the micro-evaporator with the inlet restrictions of $e_{in,rest} = 2$ and 4. 121

6.17 Comparison of measured and predicted values of (a) Δp_{ch}, and (b) corresponding $T_{fl,sat}$ for the flashing two-phase flow without back flow operating regime for R236fa flowing in the test section with the inlet restrictions of $e_{in,rest} = 2$, $G_{ch} = 1'471\,\mathrm{kg\,m^{-2}\,s^{-1}}$, $q_b = 48.2\,\mathrm{W\,cm^{-2}}$. 123

6.18 Prorated fluid temperature for R236fa flowing in the test section with the inlet restrictions of $e_{in,rest} = 4$, $G_{ch} = 1'692\,\mathrm{kg\,m^{-2}\,s^{-1}}$, $q_b = 47.8\,\mathrm{w\,cm^{-2}}$ for the experimental pressure drop of 46.3 kPa. 125

7.1 Flow pattern map for R236fa in the micro-evaporator with the inlet restriction of $e_{in,rest} = 2$. 129

7.2 Transitions for stable flows of R236fa in the micro-evaporator with the inlet restriction of $e_{in,rest} = 2$. 130

7.3 Validation of the 3D heat spreading implementation (flow is from left to right): (a) heat flux map at the root of the fins, q_{ft}, and (b) lateral average heat flux distribution along the channel length. 131

7.4 Two-phase flow of R1234ze(E) in the test section with the inlet restrictions of $e_{in,rest} = 2$ for $G_{ch} = 1'705\,\mathrm{kg\,m^{-2}\,s^{-1}}$ and $q_b = 32\,\mathrm{W\,cm^{-2}}$: (a) temperature map at the base of the silicon substrate, T_{IR}, and (b) lateral averages of base and footprint temperatures obtained assuming 1D and 3D heat conduction. The area inside the blue square indicates the array of IR temperatures considered in heat transfer analysis. 132

7.5 Two-phase flow of R1234ze(E) in the test section with the inlet restrictions of $e_{in,rest} = 2$ for $G_{ch} = 1'705\,\mathrm{kg\,m^{-2}\,s^{-1}}$ and $q_b = 32\,\mathrm{W\,cm^{-2}}$: (a) actual heat flux at the root of the fins along the channel length, (b) local wall heat transfer coefficients, α_w, obtained using the 1D and 3D conduction schemes in function of local vapor quality, x, and (c) vapor quality along the length of the channel. . 133

7.6 The flashing two-phase flow without back flow operating regime of R236fa in the micro-evaporator with the inlet restrictions of $e_{in,rest} = 4$ for $G_{ch} = 2'096\,\mathrm{kg\,m^{-2}\,s^{-1}}$ and $q_b = 47\,\mathrm{W\,cm^{-2}}$: (a) wall heat transfer coefficient, α_w, and (b) video image of flow. 135

7.7 Two-phase wall heat transfer coefficient as a function of local vapor quality for R236fa flowing in the test section with the inlet restrictions of $e_{in,rest} = 2$ for $q_w = 175\,\mathrm{kW\,m^{-2}}$. 137

7.8 Two-phase wall heat transfer coefficient as a function of local vapor quality for R236fa flowing in the test section with the inlet restrictions of $e_{in,rest} = 4$ for $q_w = 171\,\mathrm{kW\,m^{-2}}$. 137

7.9 Two-phase wall heat transfer coefficient as a function of local vapor quality for R236fa flowing in the test section with the inlet restrictions of $e_{in,rest} = 2$ for $G_{ch} \approx 1'500\,\mathrm{kg\,m^{-2}\,s^{-1}}$. 138

7.10 Two-phase wall heat transfer coefficient of R245fa, R236fa, and R1234ze(E) flowing in $e_{in,rest} = 2$, $q_w = 205.8 \pm 3\%\,\mathrm{kW\,m^{-2}}$, $G_{ch} = 1'483 \pm 1.5\%\,\mathrm{kg\,m^{-2}\,s^{-1}}$. 139

7.11 Two-phase wall heat transfer coefficient as a function of local vapor quality for R236fa in the test section with the inlet restrictions of $e_{in,rest} = 2$ and 4 for $G_{ch} = 2'081\,\mathrm{kg\,m^{-2}\,s^{-1}}$ and $q_w = 173\,\mathrm{kW\,m^{-2}}$. 140

7.12 Predicted α_w versus the current experimental results for R236fa in the test section with the inlet restrictions of $e_{in,rest} = 4$ for $G_{ch} = 1'525\,\mathrm{kg\,m^{-2}\,s^{-1}}$ and $q_w = 155.3\,\mathrm{kW\,m^{-2}}$: (a) Costa-Patry and Thome (2012) with $x_{buffer} = \pm x_{exit}/5$, and (b) new buffer $x_{buffer} = \pm 2x_{CB-AF}$. 142

7.13 Comparison of the experimental local heat transfer coefficients, α_w, of R236fa flowing in $e_{in,rest} = 2$ with the: (a) Costa-Patry and Thome (2012), and (b) Bertsch et al. (2009) prediction methods. 143

7.14 Comparison of the experimental local heat transfer coefficients, α_w, of R236fa flowing in $e_{in,rest} = 4$ with the: (a) Costa-Patry and Thome (2012), and (b) Bertsch et al. (2009) prediction methods. 145

7.15 Comparison of the experimental local heat transfer coefficients, α_w, of R245fa flowing in $e_{in,rest} = 2$ with the: (a) Costa-Patry and Thome (2012), and (b) Bertsch et al. (2009) prediction methods. 146

7.16 Comparison of the experimental local heat transfer coefficients, α_w, of R1234ze(E) flowing in $e_{in,rest} = 2$ with the: (a) Costa-Patry and Thome (2012), and (b) Bertsch et al. (2009) prediction methods. 147

7.17 Comparison of the experimental and predicted local heat transfer coefficients applying a new vapor quality buffer of $x_{buffer} = \pm 2x_{CB-AF}$ to the flow pattern-based model of Costa-Patry and Thome (2012). The lines in the graph correspond to the local change in vapor quality for a single experiment. 148

B.1 Adiabatic pressure gradients for R236fa in the test section with the inlet restrictions of $e_{in,rest} = 1.33$. 161

B.2 Adiabatic pressure gradients for R236fa in the test section with the inlet restrictions of $e_{in,rest} = 2$. 162

B.3 Adiabatic pressure gradients for R245fa in the test section with the inlet restrictions of $e_{in,rest} = 2$. 162

B.4 Δp_{total} versus x_{out} for R236fa in the test section of $e_{in,rest} = 1.33$, where G_{ch} for an individual data point might vary ±10% of the reported nominal value of the curve. 163

B.5 Δp_{total} versus x_{out} for R245fa in the test section of $e_{in,rest} = 2$, where G_{ch} for an individual data point might vary ±10% of the reported nominal value of the curve. 164

B.6 Δp_{total} versus x_{out} for R236fa in the test section of $e_{in,rest} = 2$, where G_{ch} for an individual data point might vary ±5.36% of the reported nominal value of the curve. 164

B.7 Δp_{total} versus x_{out} for R1234ze(E) in the test section of $e_{in,rest} = 2$, where G_{ch} for an individual data point might vary ±3.33% of the reported nominal value of the curve. 165

B.8 Δp_{ch} for R236fa flowing within the micro-evaporator with the inlet restrictions of $e_{in,rest} = 1.33$. 166

B.9 Δp_{ch} for R245fa flowing within the micro-evaporator with the inlet restrictions of $e_{in,rest} = 2$. 166

B.10 Δp_{ch} for R1234ze(E) flowing within the micro-evaporator with the inlet restrictions of $e_{in,rest} = 2$. 167

B.11 α_w versus x for R245fa flowing in the test section with the inlet restrictions of $e_{in,rest} = 2$ for $q_w = 172\,\mathrm{kW\,m^{-2}}$. 168

B.12 α_w versus x for R1234ze(E) flowing in the test section with the inlet restrictions of $e_{in,rest} = 2$ for $q_w = 175\,\mathrm{kW\,m^{-2}}$. 169

B.13 α_w versus x for R1234ze(E) flowing in the test section with the inlet restrictions of $e_{in,rest} = 2$ for $q_w = 192\,\mathrm{kW\,m^{-2}}$. 169

B.14 α_w versus x for R236fa flowing in the test section with the inlet restrictions of $e_{in,rest} = 4$ for $G_{ch} \approx 2'100\,\mathrm{kg\,m^{-2}\,s^{-1}}$. 170

B.15 Two-phase wall heat transfer coefficient of R245fa, R236fa, and R1234ze(E) flowing in $e_{in,rest} = 2$, $q_w \approx 175\,\mathrm{kW\,m^{-2}}$, $G_{ch} \approx 1'900\,\mathrm{kg\,m^{-2}\,s^{-1}}$. 170

B.16 Two-phase wall heat transfer coefficient of R245fa, R236fa, and R1234ze(E) flowing in $e_{in,rest} = 2$, $q_w \approx 210\,\mathrm{kW\,m^{-2}}$, $G_{ch} \approx 1'900\,\mathrm{kg\,m^{-2}\,s^{-1}}$. 171

C.1 Multi-microchannel two-phase flow heat transfer coefficient versus vapor quality for R236fa and $G_{ch} = 823\,\mathrm{kg\,m^{-2}\,s^{-1}}$. Figure extracted from Costa-Patry and Thome (2011). 175

C.2 A triplet of liquid slug, an elongated bubble and a vapor slug. Figure extracted from Thome et al. (2004) 176

C.3 Schematic representation of annular two-phase flow. Figure extracted from Cioncolini and Thome (2011) 183

C.4 Schematic representation of the cross-sectional area A split among the phases. Figure extracted from Cioncolini et al. (2009). 184

C.5 Schematic of the transition from film evaporation to vapor convection in the dry zone. Figure extracted from Thome et al. (2004) 185

C.6 Validation of the Matlab implementation of the three-zone model of Thome et al. (2004) using the global parameters: (a) the results available in the literature, and (b) the simulated heat transfer coefficients. 187

List of Tables

2.1 Correlations used in Chapter 6 for comparison of measured and predicted pressure drop values. 10

2.2 Selected small single-channel studies involving flow visualization. 23

2.3 Some previous experimental studies on the two-phase flow visualization in multi-microchannel evaporators. 25

4.1 Refrigerant saturation properties at 31.5 °C. 48

4.2 Operating conditions and experimental uncertainties for the two-phase flow experiments under uniform heat flux. 49

5.1 Representative images of the two-phase flow operating regimes. 75

5.2 Width-wise time-averaged temperature standard deviations for the 8 representatives of the two-phase flow operating regimes. 88

5.3 Standard deviations of the temperature over time for the 8 representatives of the two-phase flow operating regimes. 93

5.4 Detailed summary of the experimental campaign including the minimum and maximum ($T_{IR,min}$ and $T_{IR,max}$) junction temperatures of the micro-evaporator's base, the maximum dissipated base heat flux (q_b), and the corresponding total pressure drops ($\triangle p_{total}$). 97

6.1 Operating conditions and experimental uncertainties for the *half-heating* tests. . 110

6.2 Parameters and goodness of fit for the $\Delta p_{out,rest}$ curve fitting. 115

6.3 Comparison of the experimental results with the correlations described in Chapter 2 considering the flashing two-phase flow without back flow operating regime. 124

7.1 Test conditions segregated by type of flow regime. 128

7.2 MAEs [%] for local two-phase heat transfer coefficients of R245fa, R236fa, and R1234ze(E) in $e_{in,rest} = 2$ and 4. 144

Nomenclature

Roman Letters

A	cross-sectional area	$[\mathrm{m}^2]$
a	aspect ratio	[-]
a, b, m	parameters in the $\Delta p_{out,rest}$ curve fitting	[-]
B	heater width	[m]
Bo	boiling number	[-]
Bond	Bond number	[-]
C_f	friction factor	[-]
Co	confinement number	[-]
c_p	constant-pressure specific heat	$[\mathrm{J\,kg^{-1}\,K^{-1}}]$
D_h	channel hydraulic diameter	[m]
D_t	thermal diffusivity	$[\mathrm{m^2\,s^{-1}}]$
D_t^+	dimensionless thermal diffusivity	[-]
D_{tube}	tube diameter	[m]
d	thickness	[m]
E	heat emission	[W]
e	expansion ratio	[-]
e_{LF}	entrained liquid fraction	[-]
F	enhancement factor	[-]
Fr	Froude number	[-]
f	Fanning friction factor	[-]

f	pair frequency in the three-zone model of Thome et al. (2004)	[Hz]
G	mass flux	[$\mathrm{kg\,m^{-2}\,s^{-1}}$]
g	gravity	[$\mathrm{m\,s^{-1}}$]
H	depth	[m]
h	enthalpy	[$\mathrm{J\,kg^{-1}}$]
h_{lv}	latent heat of vaporization	[$\mathrm{J\,kg^{-1}}$]
I	current	[A]
j	superficial velocity	[$\mathrm{m\,s^{-1}}$]
$K(\infty)$	incremental pressure drop number	[-]
k	thermal conductivity	[$\mathrm{W\,m^{-1}\,K^{-1}}$]
L	length	[m]
M	mass flow rate	[$\mathrm{kg\,s^{-1}}$]
MAE	mean absolute error	[%]
M_{mol}	molecular mass	[$\mathrm{kg\,kmol^{-1}}$]
m	fin parameter	[-]
N	number of channels	[-]
$\mathrm{Nu_z}$	Nusselt number	[-]
n	natural number	[-]
P	perimeter	[m]
$P_{(x,y)}$	pixel (x, y) of infra-red camera's sensor array	[-]
PDF	probability density function	[-]
Pe	Peclet number	[-]
Pr	Prandtl number	[-]
p	pressure	[Pa]
Q	heat flow rate	[W]
q	heat flux	[$\mathrm{W\,m^{-2}}$]
R	radius	[m]

R^+	dimensionless radius	[-]
Re	Reynolds number	[-]
R_p	surface roughness parameter according to DIN 4762	[μm]
RSD	relative standard deviation	[%]
R^2	goodness of fit	[-]
S	infra-red camera sensing signal	[-]
S	suppression factor	[-]
STD	standard deviation of temperature measurement	[K]
T	temperature	[°C]
$T_{out,sat}$	outlet saturation temperature	[°C]
t	time	[s]
U	velocity	[$\mathrm{m\,s^{-1}}$]
V	voltage drop across the heater	[V]
v	specific volume	[$\mathrm{m^3\,kg^{-1}}$]
W	width	[m]
We	Weber number	[-]
X	Lockhart-Martinelli parameter	[-]
X, Y, Z	Cartesian coordinates	[m]
x	vapor quality	[-]
y	direction perpendicular to the flow direction	[m]
ZS	zero stability in flow rate	[$\mathrm{kg\,s^{-1}}$]
z	distance from the channel entrance	[m]
z^*, z^+	non-dimensional length	[-]

Greek Letters

α	heat transfer coefficient	[$\mathrm{W\,m^{-2}\,K^{-1}}$]
Γ	mass flow rate	[$\mathrm{kg\,s^{-1}}$]
Γ_{lf}	liquid mass flow rate	[$\mathrm{kg\,s^{-1}}$]

Γ_{lf}^{+}	dimensionless liquid mass flow rate	[-]
γ	liquid droplet hold up	[-]
ΔE	heat loss	[%]
Δp	pressure drop	[Pa]
ΔT_s	wall superheat	[K]
$\Delta T_{in,sub}$	inlet liquid subcooling	[K]
Δt	time step	[s]
δ	thickness	[m]
ε	emissivity	[-]
ε_{tp}	void fraction	[-]
η	fin efficiency	[-]
λ_{cond}	axial conduction number	[-]
μ	dynamic viscosity	[Pa s]
ν	kinematic viscosity	[$\mathrm{m^2\,s^{-1}}$]
ξ	singular pressure loss coefficient	[-]
ρ	density	[$\mathrm{kg\,m^{-3}}$]
$\bar{\rho}$	homogeneous density	[$\mathrm{kg\,m^{-3}}$]
σ	surface tension	[$\mathrm{N\,m^{-1}}$]
τ	pair period in the three-zone model of Thome et al. (2004)	[s]
τ	shear stress	[$\mathrm{N\,m^{2}}$]
φ	heat flux ratio	[-]
$\overset{i}{\Sigma}$	prefix indicating summation over a sample of i elements	[-]
Φ	two-phase flow multiplier	[-]

Subscripts

AD	adiabatic
amb	ambient
ave	average

B	back
b	base
$buffer$	buffer
CV	control volume
c	core
ch	channel
$cont$	contraction
$conv, tp$	convective heat transfer
$crit$	critical
D	down
dp	pressure drop
dry	dry
e	equivalent
el	electrical
end	end
$exit$	exit
$\exp$	expansion
F	front
FB	flow boiling
f	fin
fd	fully developed
$film$	film
fl	fluid
fr	friction
ft	footprint
h	heater
IR	infra-red

in	inlet
$interface$	interface
L	left
lam	laminar
l	liquid
ld	load
lf	liquid film
lo	liquid only
max	maximum
$meas$	measured
mf	manifold
min	minimum
mol	molecular
NB	nucleate boiling
opt	optimum value
out	outlet
Px	Pyrex
p	pair
pl	plenum
$pred$	predicted
R	right
r	reduced
rad	radiation
ref	reference
$rest$	restriction
Si	silicon
sat	saturation

$slit$	slit
sg	singular
sp	single-phase
sub	subcooled
sur	surface
$tape$	tape
$total$	total
tp	two-phase
$tp, 0$	transition to two-phase flow
ts	test section
tt	turbulent – turbulent
$turb$	turbulent
U	up
v	vapor
vo	vapor only
w	wall
(x, y)	pixel's coordinates, where $(0, 0)$ corresponds to the bottom left corner of the IR camera sensor array
0	initial
1D	X conduction
2D	XZ conduction
3D	XYZ conduction

Abbreviations

AF	Annular Flow
CB	Coalescing Bubble
CB – AF	Coalescing Bubble to Annular Flow Transition
CBA	Coalescing Bubble to Annular Flow Transition

CHF	Critical Heat Flux
CMOS	Complementary Metal-Oxide-Semiconductor
CMOSAIC	3D Stacked Architectures with Interlayer Cooling project
CPU	Central Processing Unit
DRIE	Deep Reactive Ion Etching
IB	Isolated Bubble
IB – CB	Isolated Bubble to Coalescing Bubble Transition
IGBT	Insulated-Gate Bipolar Transistor
NIDAQ	National Instrument Data Acquisition System
NIST	National Institute of Standards and Technology
PCB	Printed Circuit Board
PIV	Particle Image Velocimetry
RIE	Reactive Ion Etching
RTD	Resistance Temperature Detector
SoC	System on Chip
TIM	Thermal Interface Material
TSV	Through-Silicon Via
UNFCCC	the United Nations Framework Convection on Climate Change
μPIV	Micro Particle Image Velocimetry
3D – IC	Three-Dimensional Integrated Circuit

Chapter 1

Introduction and research motivation

The micro-electronics industry with its scaling engine slowing is now searching for a new effective and *green*/Kyoto friendly[1] solution to extent the Complementary Metal-Oxide-Semiconductor (CMOS) performance trends over the next decades. Three-dimensional integrated circuit (3D-IC) stacked architecture with interlayer cooling, where the internal channels necessarily require a low aspect ratio and a size of $100\,\mu$m or even smaller, is an excellent opportunity to continue the progress relative to Moore's law (Moore, 1965). As a result, the **CMOSAIC - 3D Stacked Architectures with Interlayer Cooling** project intends to provide a high-performance 3D stacked computer chip that will compress almost 10^{12} nm-sized functional units into $1\,\mathrm{cm}^3$ with a 10 to 100 fold higher connectivity than otherwise possible (Sabry et al., 2011). To achieve this, an aggressive new 3D integration technology needs to be developed in order to remove very high heat fluxes dissipated by the stacked microprocessor chips, while minimizing the thermal stresses imposed on the architecture and achieving a microprocessor design with high-performance computing characteristics. However, due to high costs and difficulties in designing and fabricating such 3D systems, the cooling of individual layers needs to be tested beforehand in order to determine their optimal geometries and operation assuming no interaction between each layer. The present experimental study, as a part of the **CMOSAIC** project, investigates a single layer of such a 3D stack in order to acquire a database of heat transfer coefficients and pressure drops that supported by visual observation of flow stability will be later on used as an input for designing a practical multi-tier computer chip.

In 3D-IC systems, the layers are placed one on top of each other and are connected using vertical copper leads, known as through-silicon vias (TSVs), which reduce the distance for locally transporting data from one layer to another. Shortening the average distance between components within a stack improves the performance, makes the process faster, more efficient and generates less Joule heating. Nonetheless, the thermal considerations become essential in high density system integration. The existing air-cooling methods are judged to be inadequate for removing continuously increasing heat fluxes produced by CPUs regarding its cooling capacity in respect to the given temperature limit of 85 °C for CPUs while dissipating an average heat flux of about $100-150\,\mathrm{W\,cm^{-2}}$ and targeting the fluid temperature between 30 and 40 °C.

---

[1] Kyoto Protocol, adopted in 1997 and entered into force in 2005, is an international agreement to the United Nations Framework Convention on Climate Change (UNFCCC, 1997), aiming to stabilize the atmospheric concentration of greenhouse gases (GHG).

Agostini et al. (2007) presented a comprehensive state-of-the-art review of high heat flux cooling technologies including liquid jet impingement, single-phase liquid cooling, and two-phase flow boiling in copper or silicon micro-geometries. Recently, Marcinichen et al. (2010) and many other researchers proposed the multi-microchannel two-phase refrigerant evaporation as an alternative to water cooling and a *green* solution for cooling of computer blade servers and clusters, which might have up to 64 blades per rack cabinet, as well as their memories. The application of two-phase cooling strategies introduces a greater degree of complexity in the modelling and design of such systems compared to single-phase techniques. However, these difficulties are off set by the great increase in heat transfer coefficients provided by the two-phase microchannel evaporators that utilize the latent energy of the refrigerant to remove heat, providing better axial temperature uniformity and reduced coolant flow rates, and thus much less pumping power, as stated by Marcinichen et al. (2011). Moreover, different approaches of liquid cooling thermal management accounting for static and dynamic job scheduling in multiprocessor systems on chips (SoCs) are now discussed to reduce hot spots and to achieve a uniform temperature distribution on the 3D stack of computer chips (Coskun et al., 2008a,b, 2009).

A full understanding of two-phase flow boiling and heat transfer phenomena in microdevices, particularly flow instabilities, vapor back flow and flow maldistribution has yet to be mastered, thus creating a bottle neck in their commercial exploitation and indicating the need for continued research. In order to meet such an urgent demand, the current research project focuses on the two-phase flow of dielectric fluids, namely R245fa, R236fa, and R1234ze(E), which evaporate along the miniaturized channels, and they provide low pressures, compatibility with electrical environments in case of leakage, high efficiency, low toxicity, and saturation temperatures close to ambient.

The motivation behind the global trend towards miniaturization of electronics devices within the micro-electronics industry is associated with the reduced material and refrigerant-charge requirements that lower the cost, as well as the efficiency improvement when compared with the conventional or macroscale channel sizes. Besides that, the electronics devices are expected to be as thin as possible, thus the depth of the channels and, consequently, the thickness of the 3D stacked chip becomes a key factor. Hence, low aspect ratio channels appear to offer significant advantages in addressing heat removal challenges and potentially lead to a practical 3D-IC system. Several different micro-evaporators have been experimentally investigated in the present study, each of them composed of 67 channels having $100\,\mathrm{x}\,100\,\mu\mathrm{m}^2$ cross-sectional areas.

In order to study phase change phenomena in such channels, unlike single point measurements from thermocouples, the infra-red (IR) temperature measurement technique is employed here for instantaneous non-intrusive spatio-temporal temperature visualization over the entire micro-evaporator area and is coupled with high-speed two-phase flow visualization. As an important part of this investigation, a novel in-situ *pixel by pixel* technique was proposed and developed to calibrate the raw IR images, thus converting them into accurate two-dimensional temperature fields of the micro-evaporator's surface. Extensive experimental tests were run and will be compared to the existing prediction methods.

This manuscript is organized in the following way:

- Chapter 1: Introduction and research motivation
- Chapter 2: State-of-the-art review on microscale two-phase flows and heat transfer
- Chapter 3: Experimental set-up
- Chapter 4: Experiments, operating conditions, and data reduction
- Chapter 5: Two-phase flow and temperature visualizations
- Chapter 6: Pressure drop
- Chapter 7: Two-phase flow heat transfer
- Chapter 8: Concluding remarks and recommendations for further investigations.

Chapter 2

State-of-the-art review on microscale two-phase flows and heat transfer

Recently, the range of applications for the two-phase flows in miniaturized channels has been widened considerably, extending over a new generation of electronics devices, cooling systems, compact heat exchangers, etc. Multi-microchannel two-phase flow cooling is a promising solution to continue the CMOS performance trends of scalable integrated architectures (i.e. CPUs) over the next few decades (Marcinichen et al., 2010), and this field is the focus of the present experimental campaign. This chapter presents a number of representative theoretical, numerical and experimental studies related to the current research, addressing channel size effects, two-phase pressure drops, IR temperature measurements of heat transfer coefficients, flow boiling tests, axial conduction effects, and flow visualization.

2.1 Channel size

In spite of a large number of papers published in the single- and two-phase flows fields, many questions concerning macro-to-microchannel distinction criterion, channel classification and channel geometry still remain pending. In 1996, Mishima and Hibiki (1996) noted that more experiments are required to reproduce the effect of tube diameter on the important flow characteristics. A lack of such data and knowledge is enhanced by the continuous reduction in channel size driven by the micro-electronics and power electronics micro-evaporator applications. Several convective heat transfer studies, aiming to determine the contribution of the channel size and other two-phase flow aspects, are cited below.

Hetsroni et al. (2001, 2003, 2005) in one of the plenary studies concluded that geometrical parameters, such as hydraulic diameter, manifold's material and design significantly influenced microchannel two-phase flow. In their experiments, the hydraulic diameter varied between 103 and 129 μm.

Agostini et al. (2003) studied the influence of hydraulic diameter on the flow boiling heat transfer of R134a in parallel rectangular minichannels with hydraulic diameters of 0.77 and 2.01 mm. The heat transfer coefficient increased by a factor of ~1.74 when decreasing the hydraulic diameter, probably caused by the thinning of the liquid layer due to the bubble confinement. On the other hand, they pointed out that the early dryout occurred and the critical quality decreased from 0.43 to 0.19 for the diameter of 0.77 mm. The effect of channel confinement on two-phase flow patterns, liquid film stratification, heat transfer and critical heat flux (CHF) was also investigated by Ong and Thome (2011a,b). New channel classifications in terms of the confinement number, Co, were proposed. The lower threshold of macroscale flow and the upper threshold of symmetric microscale flow were, respectively, set to $Co = 0.3 - 0.4$ and $Co \approx 1$. The transition region was distinguished between those thresholds. In relation to the work of Hetsroni et al. (2001, 2003, 2005), Agostini and Bontemps (2005) and Karayiannis et al. (2010) reported an enhancement of flow boiling heat transfer in small channels, compared to conventional tubes. Also, Su et al. (2005) made the same observation in case of narrow channels. The increase of heat transfer coefficient for low values of vapor quality with decreasing channel diameter is associated with the initial film thickness, as explained by Dupont and Thome (2005) based on the three-zone model of Thome et al. (2004). For larger values of vapor quality, however, the three-zone model predicts the heat transfer coefficient to decrease.

Mishima and Hibiki (1996) concluded that the reliability of measured values is less with decreasing tube diameter, while Agostini et al. (2006) stated that numerous differences between micro- and macrochannels might be due to inaccurate dimensional measurements in microscale. Agostini et al. (2008d) also noted a surface roughness effect on heat transfer at low to medium vapor qualities in the slug flow regime.

Chung and Kawaji (2004) focused on two-phase flow characteristic of a nitrogen gas and water mixtures in circular channels with diameters raging from 50 to 530 μm. Their experiments showed that the flow patterns in the 250 and 530 μm-diameter channels were similar to those appearing in channels of ~1 mm in size. Instead, in channels having diameters of 50 or 100 μm, only slug flow was observed, explained to be associated with viscous and surface tension effects on the liquid flow. Moreover, the two-phase flow multiplier became independent of the mass flux when the channel diameter decreases. Their research was extended by Kawahara et al. (2005) in order to demonstrate the effects of channel diameter and liquid properties on void fraction in adiabatic two-phase flows through the channels with diameters ranging from 50 to 251 μm. Their conclusion was that the void fraction changes drastically between 251 and 100 μm-diameter channels.

Saitoh et al. (2005) investigated flow boiling heat transfer of R-134a in tubes with inner diameters ranging from 0.51 to 3.1 mm. They showed that the homogeneous pressure drop model gave better results comparing to the Lockhart and Martinelli (1949) correlation, when the internal diameter decreases. In their 0.51 mm-diameter tube, the flow instabilities were successfully suppressed, but dryout appeared at lower values of vapor quality than for larger tubes. A significant flow stability improvement in microchannels in respect to their larger counterparts was also observed by Bhide et al. (2009). Saitoh et al. (2007) modified the Chen (1966) correlation for the flow boiling heat transfer by including the Weber number in order to account for the effect of tube diameter. The proposed correlation provided good agreement with their experimental data for a wide range of tube diameters.

Scaling effects on flow in microchannels are discussed by Morini (2006) and Kandlikar (2010). Morini (2006) performed a comprehensive analysis of the viscous dissipation, conjugate heat transfer, and entrance effects on the mean Nusselt numbers for single-phase flows. The author developed a model to predict the temperature rise along the microchannel due to viscous heating, being a function of the Reynolds number, hydraulic diameter, microchannel length, and the Poiseuille number. Moreover, the viscous dissipation effect in microchannels was negligible for low values of the Reynolds number. Whilst, for the large Reynolds numbers, it tends to reduce the mean Nusselt numbers, when the hydraulic diameter decreases. The viscous heating is not important for macrotubes. More details on the conjugate heat transfer and entrance effects are given in Section 2.5. Kandlikar (2010) performed a scaling analysis of the forces dominating in microscale two-phase flow, namely surface tension and evaporation momentum forces. It was found that the elongated bubble/slug flow pattern, associated with transient conduction/microconvection, plays an important role in microchannels.

Harirchian and Garimella (2008, 2009a,b) tested 7 different microchannel heat sinks in order to resolve the effects of channel dimensions and mass flux on the flow boiling of FC-77. The channels had the depth of $400\,\mu$m and the width ranging from 100 to $5'850\,\mu$m. As expected, Harirchian and Garimella (2008) showed that pressure drop increased with increasing mass flux and decreasing channel width at fixed wall heat flux. For a mass flux of $250\,\mathrm{kg\,m^{-2}\,s^{-1}}$, the reported wall temperatures were lower for smaller channels, thus the amount of heat that could be dissipated increased with decreasing the width of the channel. The nucleate boiling mechanism was cited to be prevalent in all the cases except for the 100 and $250\,\mu$m-wide channels, which was then overcame by convective boiling mechanism with decreasing channel width and mass flux. Harirchian and Garimella (2009a) confirmed these observations by means of simultaneous flow and temperature visualizations. Furthermore, the authors demonstrated the effect of channel width on the flow regime transition based on flow regime maps. The flow patterns in the 100 and $250\,\mu$m-wide channels were similar to each other and differed comparing to the wider channels. In general, when the channel width increases, the bubbly flow and the intermittent churn/wispy-annular flow are replaced, respectively, by the slug flow and the intermittent churn/annular flow. After all, further research revealed that the microchannel cross-sectional area was the predominant parameter, leading to the change of the governing mechanism from the convective to the nucleate flow boiling for channels with the cross-sectional area bigger than $0.089\,\mathrm{mm}^2$ (Harirchian and Garimella, 2009b).

Global tendency towards miniaturization is the main driver for continuing microscale two-phase flow research. Many aspects, however, still need to be explained in order to provide a full understanding of the effect of channel size on two-phase flow characteristic. Such a knowledge will grease the wheels to develop more reliable prediction methods that can be used for designing new generation microchannel heat spreaders.

2.2 Two-phase pressure drop

Pressure drop is a predominant parameter in two-phase flow characterization, thus it has been extensively explored since the well-known correlation of Lockhart and Martinelli (1949). Their model was devised based on the limited smooth-tube data for annular flow regime, as pointed out by Chisholm and Laird (1958). Several two-phase flow frictional pressure drop correlations, used in Chapter 6 for comparison of measured and predicted pressure drop values, are briefly discussed here and the governing equations are given in Table 2.1.

Many of the existing two-phase flow frictional pressure drop models use the Chisholm (1967) two-phase flow multipier formulation:

$$\Phi_l^2 = 1 + \frac{C}{X} + \frac{1}{X^2} \tag{2.1}$$

where C varies from 5 to 20, depending on the flow regime of each phase (Chisholm, 1967). The Lockhart and Martinelli (1949) parameter is defined as:

$$X = \sqrt{\frac{\Delta p_l}{\Delta p_v}} \tag{2.2}$$

where Δp_l and Δp_v are, respectively, the frictional pressure losses of either liquid or vapor flowing separately in the channel. The following equations apply here:

$$\Delta p_l = 4 f_l \frac{L_{ch}}{D_h} \frac{(1-x)^2}{2\rho_l} G_{ch}^2 \tag{2.3}$$

$$\Delta p_v = 4 f_v \frac{L_{ch}}{D_h} \frac{x^2}{2\rho_v} G_{ch}^2 \tag{2.4}$$

Substituting Eqs. (2.3) and (2.4) into Eq. (2.2), the Lockhart and Martinelli (1949) parameter can be expressed as:

$$X = \sqrt{\frac{f_l}{f_v} \frac{(1-x)^2}{x^2} \frac{\rho_v}{\rho_l}} \tag{2.5}$$

Muller-Steinhagen and Heck (1986) suggested a simple two-phase flow frictional pressure drop correlation. The pressure drop due to friction is defined as a function of vapor quality. The correlation is applied in pipes under constant heat flux conditions, when $\mathrm{Re} > 100$ and $B > A$.

Mishima and Hibiki (1996) introduced a new equation to calculate two-phase flow frictional pressure loss based on their experimental data of air-water flows in glass and aluminum capillary tubes with inner diameters from 1 to 4 mm. Neglecting the accelerational pressure drop and subtracting the gravitational pressure loss, the pressure drop due to friction is given in terms of the modified parameter of Chisholm (1967) defined as a function of tube diameter by Eq. (2.13) in Table 2.1.

Similar to the prediction method of Mishima and Hibiki (1996), the correlation of Lee and Garimella (2008) is formulated in terms of the Chisholm (1967) two-phase flow multiplier, where the parameter C is defined by Eq. (2.15).

Cioncolini et al. (2009) developed a new annular flow model to predict the two-phase flow frictional pressure drop, while using the Lockhart and Martinelli (1949) method for the isolated bubble regime. Costa-Patry et al. (2011a) showed that this method gave the best prediction in the isolated bubble (IB) and coalescing bubble (CB) regimes identified using the flow pattern map of Ong and Thome (2009). The entrained liquid fraction, e_{LF}, is calculated based on Eq. (2.24), where the exponents $b_0 - b_9$ are given in terms of the liquid film Reynolds number (Cioncolini et al., 2009) defined as follows:

$$\mathrm{Re}_{lf} = (1 - e_{LF})\,(1 - x)\,\frac{G_{ch} D_h}{\mu_l} \tag{2.6}$$

Recently, the model of Cioncolini et al. (2009) was modified by implementing a predictor-corrector scheme (Cioncolini and Thome, 2012) to calculate entrained liquid fraction, e_{LF}, given by the following expression:

$$e_{LF} = \left(1 + 279.6 We_c^{-0.8395}\right)^{-2.209} \tag{2.7}$$

In the homogeneous model, both of the phases are considered to flow as a single-phase flow with mean fluid properties. The derivation and the usability of the model are discussed by Collier and Thome (1994).

Table 2.1: Correlations used in Chapter 6 for comparison of measured and predicted pressure drop values.

Reference	Governing equations
Muller-Steinhagen and Heck (1986)	$\Delta p_{fr} = G\left(1-x\right)^{1/3} + Bx^3$ (2.8) where $G = A + 2\left(B-A\right)x$ (2.9) and $A = 4 f_l \dfrac{G_{ch}^2}{2\rho_l D_h}$ (2.10) $B = 4 f_v \dfrac{G_{ch}^2}{2\rho_v D_h}$ (2.11)
Mishima and Hibiki (1996)	$\Delta p_{fr} = \Delta p_l \Phi_l^2$ (2.12) where Φ_l^2 is given by Eq. (2.1) with $C = 21\left(1 - e^{-0.319 D_h}\right)$ (2.13)
Lee and Garimella (2008)	$\Delta p_{fr} = \Delta p_l \Phi_l^2$ (2.14) where Φ_l^2 is given by Eq. (2.1) with $C = 2566 G_{ch}^{0.5466} D_h^{0.8819}\left(1 - e^{-319 D_h}\right)$ (2.15)

Continued on next page

Table 2.1 – *Continued from previous page*

Reference	Governing equations
Cioncolini et al. (2009)	$\Delta p_{fr} = 2 f_{tp} \frac{G_c^2}{\rho_c D_h} \quad (2.16)$ where microscale two-phase friction factor is defined as: $f_{tp} = 0.0196 We_c^{-0.372} \mathrm{Re}_{lf}^{0.318} \quad (2.17)$ $G_c = \frac{4}{\pi} \frac{\left[x + e_{LF}\left(1-x\right)\right] M_{ch}}{D_c^2} \quad (2.18)$ $\rho_c = \left(1-\varepsilon_c\right)\rho_l + \varepsilon_c \rho_v \quad (2.19)$ and $\varepsilon_c = \frac{\varepsilon_{tp}}{\varepsilon_{tp} + \gamma\left(1-\varepsilon_{tp}\right)} \quad (2.20)$ $We_c = \frac{G_c^2 D_c}{\rho_c \sigma} \quad (2.21)$ $D_c \approx \sqrt{\varepsilon_{tp} + \gamma - \varepsilon_{tp}\gamma} \quad (2.22)$ $\gamma = e_{LF} \frac{\varepsilon_{tp}}{1-\varepsilon_{tp}} \frac{1-x}{x} \frac{\rho_v}{\rho_l} \quad (2.23)$ $\frac{e_{LF}}{1-e_{LF}} = 10^{b_0} \rho_l^{b_1} \rho_v^{b_2} \mu_l^{b_3} \mu_v^{b_4} \sigma^{b_5} D_h^{b_6} j_l^{b_7} j_v^{b_8} g^{b_9} \quad (2.24)$ where j_l and j_v are the superficial liquid and vapor velocities: $j_l = \frac{\left(1-x\right) G_{ch}}{\rho_l} \quad (2.25)$ $j_v = \frac{x G_{ch}}{\rho_v} \quad (2.26)$ The void fraction, ε_{tp}, is determined based on the expression of Woldesemayat and Ghajar (2007).

2.3 Infra-red camera measurements applied to microchannels

An observable move towards nano-technology, particularly in convective heat transfer studies, requires new developments and innovations in measurement techniques. Temperature sensors that need to be embedded onto a surface or placed into a flowing fluid might considerably affect the resulting temperature and/or heat flow path. Moreover, many of them become inappropriate for temperature measurements in scale-down electronics devices with respect to numerous difficulties in their utilization.

In contrast, non-intrusive instantaneous spatio-temporal temperature measurement techniques, such as liquid crystals (Farina, 1995) or infra-red (IR) thermography (Carlomagno and Cardone, 2010), have gained a great attention since the change of the century. Due to remarkable advances in IR detector technology (Rogalski, 2002), IR thermography, providing a time response on the order of tens of milliseconds, has been employed by many researchers, including biochemical (Kakuta et al., 2009) and biological (Kakuta et al., 2011; Krebs et al., 2010) applications. In addition to the technique itself, its calibration is an important aspect that has been widely explored, for instance: Kim et al. (2012); Ochs et al. (2009); Rainieri and Pagliarini (2002). This literature survey presents some applications of the IR temperature measurement technique to study single- and two-phase flows inside mini- and microchannels.

SCHMIDT and co-workers (2000 – 2007)

The onset of nucleate boiling of deionized and degassed water flowing in a 1.5 mm internal diameter tube was the focus of Hapke et al. (2000, 2002) and Boye et al. (2007). They investigated flow boiling of water and *n*-heptane in rectangular microchannels with sizes ranging from 300 to 700 μm. Their work was extended by Diaz et al. (2006) and further on by Diaz and Schmidt (2007a,b), including different geometries, sizes, and fluids to study flow conditions, flow boiling regions and mechanisms, as well as stability of operational modes.

In above-mentioned studies, IR thermography was used for wall temperature measurements, from which the inner wall temperatures were calculated applying the classical one-dimensional heat conduction approach. In order to improve the accuracy of the IR temperature measurements, the test sections were painted black, providing an emissivity of $\sim$0.95. Afterwards, the local heat transfer coefficients could be determined. The IR camera was calibrated against a reference temperature, being measured either with the thermocouple embedded on the wall of the test section under a no flow condition or by running water flow within the test loop and referring to the average value of inlet and outlet temperatures. Microchannel flow boiling instabilities associated with low ratio of hydraulic diameter to bubble size were revealed based on the temperature oscillations of the silicon test section.

HETSRONI et al. (2001 – 2011)

Hetsroni and co-workers have significantly contributed in establishing an IR temperature measurement technique in heat transfer experimental investigations, involving single macro- and micro-, as well as multi-microchannels (Hetsroni et al., 2011). They focused on the triangular parallel multi-microchannels down to hundreds of microns in size. The number of channels varied from 13 to 26. The channels were etched in a 530 μm-thick silicon substrate, which was afterwards anodically bonded to a 500 μm-thick transparent Pyrex cover plate for visual flow inspection. Simultaneously, IR thermography was applied to monitor the temperature of the heated back surface of the test section with an accuracy of ±1 °C, obtained by increasing the emissivity of the observed surface. Different options including matt black paint, graphite, and matt black adhesive tape were discussed to achieved this. It is worthwhile mentioning that the given temperature limit of 85 °C for CPUs was not respected in their experiments.

Hetsroni et al. (2001) investigated vapor-water two-phase flow under uniform and non-uniform heat flux conditions using two types of heaters. The heating elements were sputtered onto the back-side of the silicon substrate that minimizes the contact resistance between the wall and the heater. Noticeable temperature irregularities across the uniformly heated chip's wall were found due to hydraulic instabilities within the test section and those irregularities were significantly enhanced for non-uniform heating. Hetsroni et al. (2002) studied the effects of mass velocity and vapor quality on the flow boiling heat transfer of Vertrel XF. They showed that temporal temperature and pressure fluctuations correspond to each other and cause a reduction in heat transfer. Hetsroni et al. (2009) proved that the heat transfer coefficient increases with increasing liquid velocity and decreasing with increasing air velocity. This paper highlights the significant discrepancies between experimental results obtained for micro- and conventional channels. Geometrical parameters, such as hydraulic diameter, as well as the manifold's material and design, appeared to have a profound influence on the air-water and steam-water two-phase flow heat transfer in microchannel heat sinks (Hetsroni et al., 2001, 2003). Air-water flow patterns varied among the channel within the test section. In steam-water flow, the periodic wetting and rewetting phenomena were suggested. Hetsroni et al. (2005) reported also on the *explosive* vaporization of water; in the other words – bubbles bursting; in microchannels with periodic wetting and dryout behaviour. This mechanism was explained in more detail for water and ethanol by Hetsroni et al. (2006).

XU et al. (2005, 2006)

Xu et al. (2005, 2006) applied IR thermography to observe thermal oscillations at the surface of the silicon test sections tested. Their IR camera was calibrated to ±0.4 °C. In particular, Xu et al. (2005) examined flow boiling of acetone in 10 parallel triangular microchannels, each having a hydraulic diameter of 155.4 μm. The test section was made of a 530 μm-thick silicon wafer bonded to a 410 μm-thick transparent Pyrex cover plate that enabled visual flow inspection. In order to mimic the heat generated by active components in a CPU chip, a thin platinum film was deposited onto the back-side of the silicon wafer, providing uniform heating. As mentioned by Hetsroni et al. (2001), use of an IR camera requires the surface emissivity to be close to 1.0. Therefore, the heated area was covered by a thin layer of black lacquer with an emissivity of 0.94, improving an accuracy of IR temperatures. Three zones of a full boiling cycle: (i) liquid refilling stage, (ii) bubble nucleation, growth and coalescence stage, and (iii) transient annular flow stage, were distinguished and the transient boundaries between them were given. Similar observations were made in the intercrossed array of 10 triangular microchannels of the same hydraulic diameter and 5 transverse trapezoidal microchannels of 212 μm in depth (Xu et al., 2006). However, they mentioned that the recording rate of the IR image system was too low to observe the flow patterns in greater detail.

PATIL and NARAYANAN (2006)

Patil and Narayanan (2006) utilized IR thermography to spatial resolved temperature measurements in a 13 mm-long, 50 μm-wide, and 135 μm-deep silicon microchannel under a constant heat input. Water was the test fluid. Both the wall and fluid temperatures near the channel wall (described in detail by Patil and Narayanan (2005)) were measured, depending on the opacity of the channel wall. The IR camera calibration for quantitative temperature measurements was done in respect to the intensity maps during water flow at the temperature of 23.5 °C.

HARDT et al. (2007)

An experimental investigation of flow boiling of 2-propanol and water in $50 \,\mathrm{x}\, 50\,\mu\mathrm{m}^2$ cyclo olefin polymer (COP) and $30 \,\mathrm{x}\, 30\,\mu\mathrm{m}^2$ silicon (Si) parallel microchannels was performed by Hardt et al. (2007). The number of channels was respectively 300 or 16. An IR camera was used for remote temperature measurements over the COP test section with a standard deviation ±0.08K at 30 °C. The IR camera was calibrated using a thermocouple that had an accuracy of ±1.5K.

BARBER et al. (2009, 2011)

Barber et al. (2009) studied flow boiling instabilities of *n*-pentane in a single, rectangular microchannel having a hydraulic diameter of 727 μm under uniform heating by means of an IR camera and a high-speed flow visualization camera. Therefore, simultaneous heating, as well as temperature and flow visualizations were possible. The heat transfer coefficients were determined based on the IR temperatures that were accurate to within ±1 °C. They showed that the temporal temperature and pressure oscillations are interdependent. Thin liquid film evaporation, entrainment, slug flow, bubble nucleation, dryout, etc., were investigated. More details one the bubble dynamics and are given by Barber et al. (2011).

CHAUVET et al. (2010)

The evaporation rate in a square capillary tube was investigated by means of an IR camera coupled with an ombroscopy visualisation technique by Chauvet et al. (2010). The IR temperature measurement uncertainty was estimated to be ±0.05 – 0.1K. The liquid film dynamics, affected by capillary, gravity and viscous forces, were then described in by a simple model. It was shown that geometrical parameters, such as roundness, etc., can significantly change the heat transfer performance.

WALSH et al. (2010)

Walsh et al. (2010) used an IR camera to study single-phase and plug-slug flow behaviours in the entrance and fully developed flow regions inside a single minichannel having an internal diameter of 1.5 mm under a constant wall heat flux boundary condition. The outer surface of the test section was painted by a matt black paint, thus providing the surface emissivity of 0.95.

Moreover, in order to minimize the reflection effects, the tested tube was placed in a black box. The IR camera calibration was done for three temperatures within the test loop by running single-phase flow tests with a flow rate that ensured the heat losses due to natural convection was negligible.

KIM and co-workers (2012)

Unlike point and average measurements, Kim et al. (2012) and Kommer et al. (2012) applied IR thermography into microgravity convective heat transfer experiments. The authors performed simultaneous flow and temperature visualizations during flow boiling of FC-72 within a single 6.0 mm diameter silicon channel under a range of gravity levels and determined a velocity threshold, at which heat transfer becomes independent of gravity (Kommer et al., 2012). Their test section was coated with a thin IR opaque film providing an emissivity of 0.90±0.01.

Thus, use of IR cameras has become more common in the past few years and it will be applied in the present thesis implementing some new calibration schemes (to be described in Chapter 3).

2.4 Flow boiling heat transfer

The application of the two-phase flow cooling strategies introduces a greater degree of complexity in the modelling and design of such systems compared to single-phase flow techniques. However, these difficulties are offset by the great increase in heat transfer coefficients provided by two-phase evaporators that utilize the latent energy of the refrigerant to extract heat. As a result of this enhanced thermal performance, better axial temperature uniformity and reduced coolant flow rates, and thus pumping powers, are obtained. Therefore, flow boiling heat transfer has been extensively analyzed since the 1960's in order to determine the impact of particular factors, such as geometry, dimensions, channel orientation, fluid properties, flow velocity, saturation temperature, subcooling, etc. on the process itself.

Over the past several years, single microchannel tubes have been the subject of fundamental studies. Today, however, multi-microchannels have gained particular attention in the micro-electronics and power electronics industries due to the tremendous challenge of removing continuously increasing heat fluxes dissipated by CPUs. The large amount of experimental work, theory and empirical design equations was reviewed by Thome (2004, 2006), Cheng et al. (2008), and recently by Thome and Consolini (2010). A comprehensive state-of-the-art of high heat flux cooling technology is presented by Agostini et al. (2007). Besides the LTCM[1] lab, Hetsroni et al. (2001, 2002, 2003, 2005, 2006, 2009), Xu et al. (2005, 2006), and Harirchian and Garimella (2008, 2009a,b) have contributed broadly to the field of multi-microchannel two-phase flow cooling. What was found to be useful is cited below concerning selected experimental investigations with 2D silicon micro-evaporators by the other groups first and then followed by

---

[1] Heat and Mass Transfer Laboratory, École Polytechnique Fédérale de Lausanne

LTCM's experience:

- Jiang et al. (2001) tested a transparent microchannel heat sink, which was fabricated by bonding a Pyrex glass cover plate to a silicon wafer. The chip, $10\,\mathrm{x}\,20\,\mathrm{mm}^2$ in size, was designed as an integrated system, comprising either 34 or 35 microchannels with triangular cross-sectional areas. Anodic bonding technology was used to create the test module. From the observed flow patterns, the authors distinguished three stable boiling modes. Moreover, they investigated the dependence of the flow regime on the input power level. Local nucleate boiling dominated in the microchannels at low input powers. Then, as the power level was increased, a stable annular flow was established. In contrast to macrochannels, no bubbly flow regime was detected (which however contrasts with their conclusion that nucleate boiling dominated at low vapor qualities). Also, neither bubbly nor slug flow was found in microchannels with diameters from 25 to 60 μm (Zhang et al., 2002).

- Wu and Cheng (2003a,b, 2004) carried out an experimental investigation of convective heat transfer and pressure drop of water flowing in silicon parallel microchannels of trapezoidal cross-sectional areas. The number of channels varied from 8 to 15. The alternative two-phase/single-phase flow was observed. Simultaneous periodic wall temperatures accompanied by inlet and outlet water temperature and pressure oscillations were reported. Pressure drop and flow boiling instabilities were assessed by Wu et al. (2006). The authors associated these instabilities with contradictory results found in the literature by Wang et al. (2008).

- Chen and Garimella (2006) focused on flow boiling heat transfer of FC-77 in 24 silicon microchannels, each with a $389\,\mu\mathrm{m}\,\mathrm{x}\,389\,\mu\mathrm{m}$ cross-sectional area and heated by 25 individual heating elements. Visual observation of flow regimes showed that bubbly flow was dominant at low heat fluxes. At higher heat fluxes wispy-annular and churn flows were observed. The heat transfer coefficient drop and strong fluctuations of wall temperature at high heat fluxes due to the partial wall dryout were reported (probably due to flow instabilities). The heat transfer coefficient and pressure drop in fully developed flow boiling were found to be independent of flow rate in the tested range of experimental conditions.

- Lee and Garimella (2008) used deionized water to study saturated flow boiling heat transfer and pressure drop in 400 μm-deep silicon microchannels. The channel width varied from 102 μm to 997 μm. New heat transfer coefficient and pressure drop models were invented and compared with existing prediction methods. As a result, satisfactory agreement was achieved.

- Schneider et al. (2007) studied convective heat transfer of non-cavitating and cavitating flow of R-123 in silicon multi-microchannels having a hydraulic diameter of 227 μm. In order to initiate cavitation (actually flashing) and enhance heat transfer, 20 μm-wide and 200 μm-long rectangular micro-orifices were installed at the entrance of each channel. The heat transfer coefficient for flashing flow was as much as 84% higher in comparison to non-flashing flow. They concluded that the two-phase flashing flow is dominated by the convective boiling, while for the non-flashing flow, it was hypothesized to be either the nucleate boiling or convective boiling depending on vapor quality.

- The experiments of Bogojevic et al. (2009, 2011) concentrated on flow boiling instabilities of water flowing in a silicon heat sink under uniform and non-uniform heating. The test section was composed of 40 parallel channels having a hydraulic diameter of 194 μm and a length of 15 mm. Bogojevic et al. (2009) demonstrated the existence of different flow regimes in different channels along the transverse direction. Inlet liquid subcooling was found to have an influence on the stability and uniformity of wall temperature, which improved for higher liquid inlet temperatures. They confirmed the observation of Hetsroni et al. (2001) that non-uniform heating enhances the microchannel flow boiling instabilities.
- Bertsch et al. (2009) proposed a heat transfer correlation for saturated flow boiling applying a superposition of nucleate boiling and convection contributions and taking into account the effect of channel size. The model was developed based on a database from 14 studies from literature, which included 12 different fluids, vertical and horizontal channels (both single and multiple) with diameters ranging from 0.16 to 2.92 mm and confinement numbers from 0.3 to 4.0. The authors reported that the correlation is in a good agreement with the experimental results, even though different trends were observed throughout. More details on the equations are given in Appendix C.
- More recently, Harirchian and Garimella (2012) presented a new flow regime map for FC-77, flowing in parallel silicon microchannels. A wide range of channel dimensions and experimental conditions was considered to develop this map, but only one fluid at one saturation temperature were tested, i.e. no variation in fluid physical properties. Slug, confined annular, bubbly, and alternating churn/annular/wispy-annular flows were distinguished and the models for predicting the heat transfer coefficients were given in each regime. In order to predict the liquid film thickness in the elongated bubble, the three-zone model of Thome et al. (2004) was modified. The channel locations where the flow transformed from bubbly to slug and consequently to annular flow were determined, and then the pressure drop for each regime occurring along the channel was separately calculated. Unlike the empirical correlations, the regime-based pressure drop prediction methods appeared to provide more reliable results, but only for this one fluid at one T_{sat}.

Thanks to the LTCM lab's experience with two-phase flow research, noticeable advances in the field have been established. A brief review is presented below.

In 2002, Jacobi and Thome (2002) proposed a simple analytical two-zone model of thin-film evaporation into elongated bubbles and demonstrated that it was the dominant heat transfer mechanism in microchannels in comparison to conventional macrochannel nucleate pool boiling mechanism, explaining the heat flux influence usually attributed by others to be evidence of nucleate boiling. Thome et al. (2004) modified the previous two-zone model to predict the time-averaged local heat transfer coefficients. The new three-zone model treats evaporation of elongated bubbles in microchannels as a cyclic passage of: a liquid slug, an evaporating elongated bubble, and a vapor slug, which is assumed to appear when the liquid film thickness near the bubble tail reaches the same order of magnitude as the surface roughness of the channel. The local heat transfer coefficients obtained from the three-zone model were compared to an experimental database including 1'591 data points (Dupont et al., 2004) from seven independent studies. As a result, 67% of the heat transfer data covering 7 different fluids were predicted within a ±30% tolerance band.

Agostini et al. (2008a,b,c,d) performed an experimental investigation of two-phase flow cooling of a silicon chip up to very high heat fluxes. Refrigerants, such as R236fa and R245fa, were used as the working fluids. 67 high depth-to-width aspect ratio of the microchannels with rectangular micro-orifices at the entrance to each channel were tested. The channels were 223 μm-wide, 680 μm-high and 20 mm-long. Agostini et al. (2008b) pointed out that the base temperature of the multi-microchannel heat sink could be kept below 52 °C while dissipating 255 $\mathrm{W\,cm^{-2}}$ with 10K of inlet subcooling and 90 kPa of pressure drop at a 25 °C of saturation temperature. They also reported that the cooling performance provided by two-phase flow cooling of such a chip is significantly better compared with single-phase liquid cooling at the same pumping power. Moreover, good performance of a split flow design with much lower pressure drop was demonstrated. Borhani et al. (2010) developed and applied a novel time strip technique to analyze the image sequences taken by a high-speed digital video camera during the flow boiling of R245fa in the test section of Agostini et al. (2008a,b,c,d). According to the authors, the conflicting results and the varied trends concerning heat transfer given by the literature might be explained by an intermittent dewetting-rewetting dryout mechanism of the liquid film trapped between the channel wall and the elongated bubble.

Park (2008) and Park and Thome (2010) presented a new saturated critical heat flux (CHF) database for multi-microchannel copper elements with low pressure refrigerants, namely R134a, R236fa, and R245fa. Two different heat sinks with either 20 or 29 high aspect ratio channels were tested against a wide range of mass and heat fluxes. The channels were 467 x 4'052 $\mu\mathrm{m}^2$ and 199 x 756 $\mu\mathrm{m}^2$, respectively. The comparison of the data with the available CHF methods showed good agreement for the predictions of Katto and Ohno (1984); Revellin and Thome (2008); Wojtan et al. (2006). The study involved a flow visual inspection in order to assess the effect of inlet orifices used for each channel (Park et al., 2009). The authors reported a substantial improvement of flow stability with the micro-orifices in place. Moreover, no back flow was observed and the flow uniformity was distinguishably better. The orifices caused an additional pressure drop and a consequent reduction of subcooling as well as in some cases also flashing. Therefore, the flow boiling was initiated at a lower heat flux, the wall-temperature distribution becomes more uniform and the wall-temperature overshoot for the onset of boiling is significantly reduced.

New tests with the split flow configuration (one inlet-two outlets) for the $199 \times 756\,\mu\text{m}^2$ channels were run by Mauro et al. (2010) with the refrigerants used by Park and Thome (2010). Lower pressure drops accompanied by higher CHFs were found for such a configuration compared with the single inlet/outlet system. Similarly, the correlations of Wojtan et al. (2006) and Katto and Ohno (1984) agreed well with the obtained CHF database for R134a, R236fa, and R245fa. The mean absolute errors (MAEs) for all the fluids were: 8.92% and 5.84%, respectively, within an error band of ±30%. The numerical model of Revellin and Thome (2008) provided the MAE of 14.2%. Thus, CHF in multiple microchannels with flow stabilized by inlet micro-orifices is now well predicted.

Ong and Thome (2009) investigated flow boiling heat transfer phenomenon of R134a, R236fa, and R245fa in a horizontal heated tube, which had a diameter of 1.03 mm. They classified the slug flow in microchannel systems into an isolated and coalescing bubble flow, which converts into an annular flow at higher vapor qualities. Heat flux dependence on heat transfer coefficients at low vapor qualities for those fluids was observed. Moreover, in the annular flow regime for low pressure fluids such as R236fa and R245fa, the convective boiling mechanism becomes dominant while vapor quality increases. The method proposed by Ong and Thome (2009) predicted relatively well the database of Arcanjo et al. (2010). Later on, the test facility of Ong and Thome (2009) was used in the experimental investigation of flow boiling of R1234ze(E) in 1.0 and 2.2 mm circular tubes (Tibirica et al., 2012). The heat transfer data bank of Tibirica et al. (2012) was well modelled by the model of Saitoh et al. (2007) that includes the effect of tube diameter. Ong and Thome (2011a,b) concentrated on the effect of channel confinement on two-phase flow patterns, liquid film stratification, heat transfer and critical heat flux (CHF). The confinement number, Co, was used as a new channel classification criterion, where the lower threshold of macroscale flow and the upper threshold of symmetric microscale flow are, respectively, $Co = 0.3 - 0.4$ and $Co \approx 1$.

The coalescing bubble flow during convective boiling heat transfer in micro-scaled systems was also studied by Consolini and Thome (2010), who presented a one-dimensional model for evaporation of confined bubbles. The model is based on the hypothesis of the thin film evaporation into elongated bubbles, as stated by Thome et al. (2004). Indeed, the comparison of the model to the experimental database revealed a conclusion that the film evaporation mechanism governs the heat transfer.

Costa-Patry et al. (2011a,b) focused on two-phase flow of R245fa and R236fa in 135 silicon multi-microchannels heated by 35 local heaters. The channels were $85\,\mu$m-wide, $560\,\mu$m-high, 12.7 cm-long, and separated by $46\,\mu$m-wide fins. As new experimental technique was developed in order to determine the outlet restriction pressure drop losses, which represented up to 30% of the total pressure loss through the micro-evaporator (but usually much less) and, thus, could not be neglected. The microchannel pressure drop experimental results were in a good agreement with the annular flow model of Cioncolini et al. (2009) used with the Lockhart and Martinelli (1949) method for the isolated bubble regime. Costa-Patry et al. (2011a) presented the heat transfer characteristics of before-mentioned fluids and showed the best prediction in the isolated bubble (IB) and coalescing bubble (CB) regimes identified using the flow pattern map of Ong and Thome (2009), which was given by the three-zone heat transfer model of Thome et al. (2004) for describing the evaporation process in miniaturized channels. Costa-Patry et al. (2010) and Costa-Patry et al. (2012) performed a series of experiments under hot spot conditions showing that the prediction methods of Thome et al. (2004) and Bertsch et al. (2009) are suitable also for non-uniform heat flux applications. Recently, Costa-Patry and Thome (2012) have presented a new flow pattern-based prediction method for heat transfer coefficient in microchannels. The three-zone model of Thome et al. (2004) and the Cioncolini and Thome (2011) annular flow model for convective boiling were joined applying a new heat flux-dependent transition from the coalescing elongated bubble to the annular flow. Appendix C presents the original models of Thome et al. (2004) and Cioncolini and Thome (2011), as well as the recent modifications introduced in Costa-Patry and Thome (2012).

Madhour et al. (2011) tested flow boiling of R134a at a saturation temperature of 63 °C, flowing in a copper heat sink with 100 parallel channels, where 35 local heaters and temperature sensors were utilized in their experiments. The temperature of the test section's base was below a given temperature limit of 85 °C with a maximum pressure drop of 94 kPa while dissipating over 180 $\mathrm{W\,cm^{-2}}$ of base heat flux. The reported base heat transfer coefficients were as high as 270 $\mathrm{kW\,m^{-2}\,K^{-1}}$.

Even with these many tests, more 2D multi-microchannel tests specifically targeted towards 3D-IC chips with interlayer cooling are needed and are the main subject of this thesis.

2.5 Axial conduction effects on heat transfer data

Due to many difficulties, axial heat conduction contribution associated with entrance effects is generally ignored in heat transfer studies (Davis and Cooper, 1969). Lin and Kandlikar (2012) showed that axial heat conduction in the fluid is negligible for air and water flow in microchannels for common cooling applications. On the contrary, axial heat conduction in the wall may be significant in developing flows and especially for non-uniform heat flux conditions. Beside dimensionless quantities, such as the Peclet number (Piva, 1996; Vick and Ozisik, 1981), dimensionless thickness, and thermal conductivity (Bilir, 1995), Peterson (1999) introduced the concept of the axial conduction number:

$$\lambda_{cond} = \frac{kA}{Mc_pL} \tag{2.27}$$

which was used by Maranzana et al. (2004) in their numerical analysis of convective heat transfer in rectangular mini- and microchannels.

Over the past several years, many numerical and experimental papers, concerning wall heat conduction in downscaled single channels appeared in the literature, for instance: Celata et al. (2006); Gamrat et al. (2005); Lelea (2007); Liu et al. (2007); Moharana et al. (2012); Muzychka and Yovanovich (2004). In respect to the focus of this study, a brief literature review on axial heat conduction problem in microchannel heat sinks for electronics packaging is presented.

Fedorov and Viskanta (2000) proposed a three-dimensional mathematical model to account for the flow and conjugate heat transfer in a microchannel-based silicon heat sink. The model, based on incompressible laminar Navier-Stokes equations, was evaluated against experimental data, providing a good agreement. The authors found that in some cases the Poiseuille flow assumption might not be accurate for the friction coefficient determination. Moreover, due to high conductivity of the silicon substrate, being in direct contact with flowing fluid, local heat transfer coefficients and the Nusselt numbers are erroneous if axial heat conduction effects in the channel wall are not taken into account. The heat spreading and heat conduction inside the silicon heat sink, as well as possible structural chip failure due to significant thermal stresses were mentioned to be crucial, and thus cannot be omitted in the analysis of such systems.

Tiselj et al. (2004) studied low-Re number heat transfer characteristics of water inside triangular silicon microchannels, each having a hydraulic diameter of 160 μm. Non-linear temperature distribution along the flow direction was observed. A negative temperature gradient between the wall and the bulk water temperatures, as well as a singular point along the Nu-profile indicated the change of the heat flux flow direction. Neglecting the dissipation effects, conventional Navier-Stokes equations were suggested to be applicable for describing the heat transfer under tested experimental conditions.

Morini (2006) performed a comprehensive analysis of the viscous dissipation, conjugate heat transfer, and entrance effects on the mean Nusselt numbers of single-phase flow is small channels. The viscous dissipation contribution is discussed in Section 2.1. Additionally, the entrance effects in tubes might be neglected if:

$$\frac{\mathrm{Re}\,\mathrm{Pr}\,D_h}{L} < 10 \tag{2.28}$$

and for the silicon walls, the conjugate wall-fluid effect can be ignored when the following condition is met:

$$\left(\frac{k_{Si}}{k_{fl}}\right)\left(\frac{D_h}{L}\right)\left(\frac{W_{ch}H_{ch}}{W_{ch}+H_{ch}}-1\right)\frac{1}{\mathrm{Re}\,\mathrm{Pr}} > 0.02 \tag{2.29}$$

Then, the following can be stated:

- for the low-Re flows, the mean Nusselt numbers are generally reduced, which is associated with a combined effect of the heat conduction along the solid walls and the internal convection, while

- for the high-Re flows, the mean Nusselt numbers are influenced by both the entrance effects and the viscous dissipation.

Cole and Cetin (2011) concluded that the conjugate heat transfer including axial conduction in the fluid and in the adjacent wall is crucial:

- for small length-over-height aspect ratio microchannels,
- for the small Pe numbers,
- for large ratios of wall thickness-to-channel height, and
- when the wall conductivity is high in respect to the thermal conductivity of the working fluid (see Eq. (2.29)).

Moharana et al. (2011) suggested that, besides the above-mentioned thermal conductivity, geometrical parameters, the Peclet, Nusselt, and Reynolds numbers, the Prandtl number, Pr, might play an important role in conjugate heat transfer situations and needs to be investigated.

Lin and Kandlikar (2012) pointed out that neglecting the effect of axial heat conduction, while reducing the experimental data, results in lower Nusselt numbers due to an increase in the local fluid temperature and a corresponding increase in the wall temperature. In order to account for this effect, the authors developed a new axial heat conduction model in the fully developed flow. The model provides good agreement with numerical and experimental data in terms of quantity and trends predicted.

2.6 Two-phase flow visualization

Flow patterns and flow pattern maps are commonly accepted to be important in heat transfer studies in both macro- and microscales, resulting in a variety of different types of transition boundaries between particular flow regimes. Cheng et al. (2008) and Thome (2010, in Chapter 20) provided a widespread compendium of visual observation of two-phase flow patterns. Table 2.2 presents selected experimental investigations, involving single-channel two-phase flow visualizations. The most typical flow pattern maps are constructed either in terms of superficial liquid and vapor velocities, $j_v - j_l$, or experimental conditions and vapor quality: $x - G$. Nonetheless, some others exist, for instance: , $G - q$ and $q - G$. As indicated, the two-phase flow visualization remains an active area of current research for fundamental studies.

Table 2.2: Selected small single-channel studies involving flow visualization.

Reference	Research details
Flow pattern map in respect to superficial liquid and vapor velocities, $j_v - j_l$	
Yang and Shieh (2001)	Tubes with inner diameters and lengths of, respectively: (i) 1.0 mm and 200 mm, (ii) 2.0 mm and 400 mm, as well as (iii) 3.0 mm and 600 mm
Serizawa et al. (2002)	Tubes of 20, 25, and 100 μm of inner diameter (for air-water flow) and tube of 50 μm diameter (for steam-water flow)
Huo et al. (2004) and Shiferaw et al. (2007)	Tubes with inner diameters and lengths of either (i) 4.26 mm and 500 mm or (ii) 2.01 mm and 211 mm
Revellin et al. (2006)	Tube with an inner diameter of 0.50 mm and a heated length of 70.70 mm
Shiferaw et al. (2009)	1.1 mm-diameter tube with a heated length of 150 mm
Fu et al. (2008)	Test section with an inner diameter of 1.931 mm, having a 100 mm heated section and a 50 mm adiabatic observation section
Zhang and Fu (2009)	Tubes of 0.531 and 1.042 mm inner diameters and a 100.0 mm heated sections
Martin-Callizo et al. (2010)	Tubes with an internal diameter of 1.33 mm and 235 mm in heated length
Saisorn et al. (2010)	600 mm-long mini-channel with a diameter of 1.75 mm
Galvis and Culham (2012)	Two 29.2 mm-long test sections with rectangular cross-sectional areas: either 198 x 241 or 378 x 471 μm^2
Flow pattern map with mass flux and vapor quality as coordinates, $x - G$	
Revellin et al. (2006)	Tube with an inner diameter of 0.50 mm and 70.70 mm in heated length
Fu et al. (2008)	Test section with an inner diameter of 1.931 mm, having a 100 mm heated section and a 50 mm adiabatic observation section
Zhang and Fu (2009)	Tubes of 0.531 and 1.042 mm inner diameters and a 100.0 mm heated section

Continued on next page

Table 2.2 – *Continued from previous page*

Reference	Research details
Ong and Thome (2009, 2011a)	Channels with length x diameter of, respectively, 478.0 mm x 1.03 mm, 713.4 mm x 2.2 mm, and 931.1 mm x 3.04 mm and 100 mm-long sight glass for flow visualization
Martin-Callizo et al. (2010)	Tubes with an inner diameter of 1.33 and 235 mm in heated length
Karayiannis et al. (2010)	Tubes with inner diameters and lengths of, respectively, (i) 4.26 mm and 500 mm, (ii) 2.88 mm and 300 mm, (iii) 2.01 mm and 211 mm, (iv) 1.10 mm and 150 mm, as well as (v) 0.52 mm and 100 mm
Saisorn et al. (2010)	600 mm-long channel with a diameter of 1.75 mm
Galvis and Culham (2012)	*See above*
Flow pattern map in respect to experimental conditions, either $G-q$ or $q-G$	
Celata et al. (2010)	100 mm-long microchannel with an inner diameter of 480 μm
Galvis and Culham (2012)	*See above*

Today, however, multi-microchannels have gained particular attention in the power electronics and micro-electronics and industries. Table 2.3 thus provides a summary of some previous experimental studies on the two-phase flow visualization in multi-microchannel evaporators. The number of parallel channels usually varies from 2 to over 60, although the two-phase flow visualisation usually involves from 1 up to only few channels.

Table 2.3: Some previous experimental studies on the two-phase flow visualization in multi-microchannel evaporators.

Reference	Overall number of channels	Number of channels being visualized
Hetsroni et al. (2001, 2002, 2003, 2005)	17, 21 or 26	below 20 (commonly 1)
Wu and Cheng (2003a, 2004)	8 or 15	1
Wu et al. (2006)	8	2
Wang et al. (2007, 2008)	8	from 1 to 5
Chen and Garimella (2006)	24	1
Harirchian and Garimella (2009a,b, 2010)	from 2 to 63	1
Bogojevic et al. (2009, 2011)	40	3 or 4, respectively
Park et al. (2009)	20	20

Among those, only the visualization performed by Park et al. (2009) was done for all the channels including inlet and outlet headers, as shown in Fig. 2.1. Hence, the goal of this research project was to carry out a 2D two-phase flow visualization, including all the channels, as well as inlet and outlet headers for a complete rather than partial view of the test section.

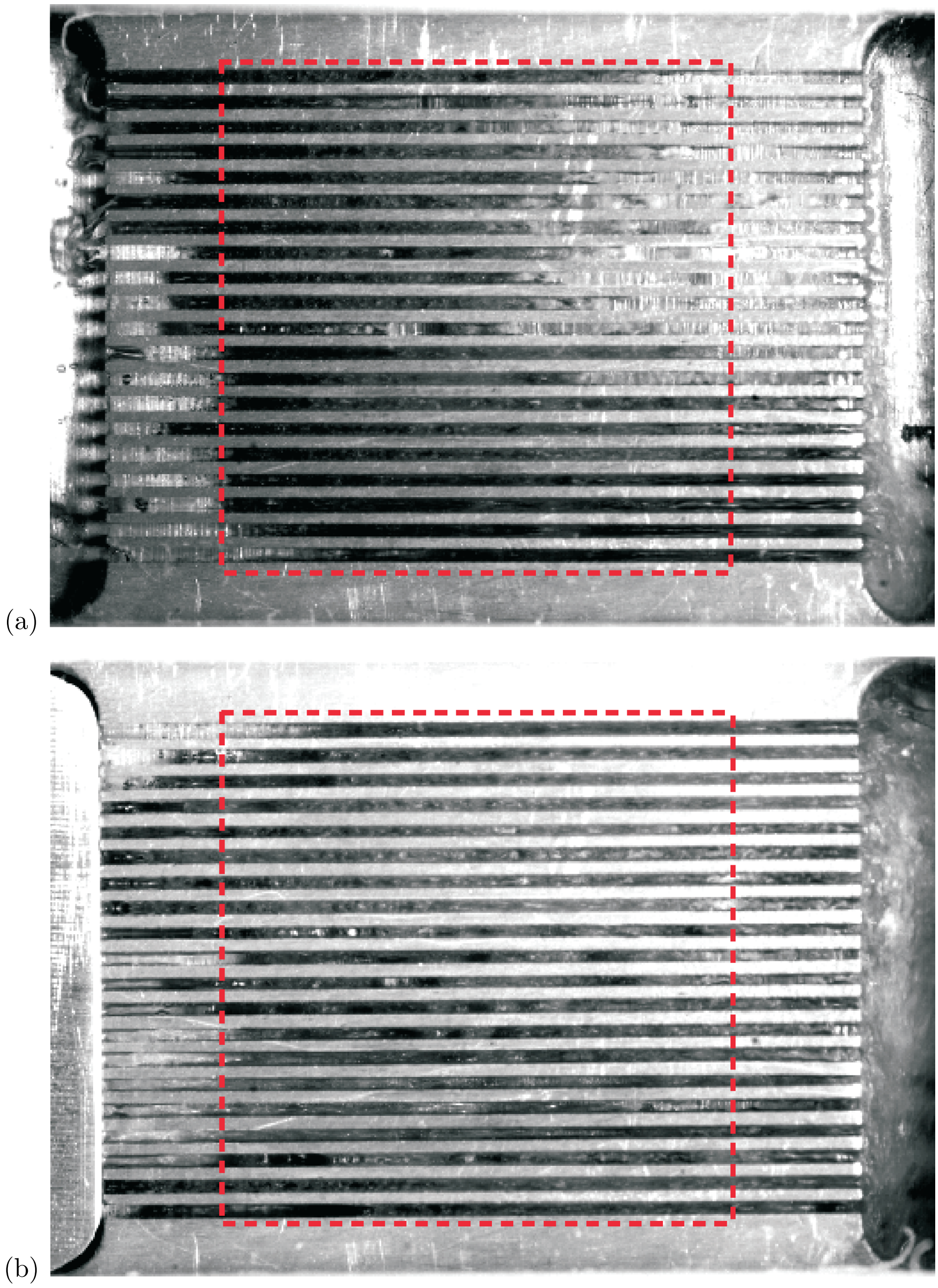

Figure 2.1: Visualization of the 4’052 μm test section at a high mass velocity: (a) without, and (b) with the orifice insert. Flow direction is from left to right. The heating area is denoted by a red dashed line. Bright areas in the channels represent a single-phase liquid (near inlet) or annular flow (near outlet), whereas darker areas represent two-phase bubble mixture. Figure extracted from Park et al. (2009).

2.7 Summary and problem statement

The present literature survey provides the following conclusions:

- Besides the point-wise temperature measurements, the use of IR thermography is recommended as a non-contact instantaneous spatio-temporal temperature measurement technique for the characterization of micro-evaporators cooling performance. Many of researchers highlighted the need to increase the emissivity of the observed surfaces to increase the signal-to-noise ratio and, thus, the accuracy of the IR thermography. Options discussed include matt black paint, graphite, and matt black adhesive tape.
- The present state-of-the-art review indicates that axial heat conduction, viscous dissipation, conjugate heat transfer and entrance effects are meaningful, and thus should not be neglected when reducing experimental data.
- Various studies dealing with visual inspection of flow patterns for a limited number of channels can be found in previous studies. Nonetheless, flow boiling instabilities in microchannels require an overall flow visualization of the test section, including the inlet and the outlet plenums, to see the entire process.

Therefore, the experimental investigation of the two-phase flow boiling in silicon micro-evaporators with a low depth-to-width aspect ratio of its microchannel and a $1\,\mathrm{cm}^2$ heated area has been undertaken. Refrigerants R245fa, R236fa, and R1234ze(E), all of which provide low pressure, compatibility with electrical environments in case of leakage, high efficiency, low toxicity, and saturation temperatures close to ambient, have been tested. Simultaneous flow and temperature visualizations have been conducted.

The present research project is expected to contribute to the realization of future high-performance 3D chip stacks with interlayer cooling, where the channels necessarily require a low aspect ratio and a size of $100\,\mu\mathrm{m}$ or even smaller.

Chapter 3

Experimental set-up

The present chapter describes the experimental flow boiling facility and the silicon multi-microchannel evaporators tested.

3.1 Flow boiling test facility

The existing experimental flow boiling test facility, built by Revellin (2005) and recently used by Ong (2010) to study the flow boiling and evaporation in single stainless steel tubes, was modified here to investigate two-phase flow in silicon multi-microchannel cold plates. It contains a closed loop of refrigerant, schematically presented in Fig. 3.1(a). An oil-free micropump coupled with a frequency controller is used to set the desired liquid flow rate, which is measured by a Coriolis mass flow meter with an accuracy of ±0.35% of the flow rate. Downstream of the flow meter, to assure the desired condition for the test section inlet, there are a pre-heater/subcooler and an electrical pre-heater. The test section, described in detail in the following subsection, is a silicon micro-evaporator with a transparent Pyrex cover plate.

The pre-heater and the test section are heated by applying direct DC current via two independent power sources. The voltage drop across the pre-heater and the test section, and the current (in-direct measurement) are measured via the National Instrument data acquisition system (NI DAQ). The micro-evaporator is inserted into a manifold, shown in Fig. 3.2(a), which is used to provide and remove fluid from the test section via the inlet and outlet manifold plenums. In order to prevent leakage, 500 μm-diameter O-rings are placed in the grooves around the manifold plenums. As well as providing mechanical support for the test section, this manifold provides optical access to both the top and bottom surfaces of the test section. The temperature of the refrigerant, as well as the pre-heater wall temperature, are measured by Thermocoax 0.25 mm K-type thermocouples calibrated to within ±0.1 °C. The absolute pressures at the inlet and outlet manifold plenums are measured by 10 bar absolute pressure sensors with a full-scale (FS) accuracy of ±0.1%. Moreover, the pressure drop between the inlet to outlet manifold plenums is obtained by a differential pressure sensor with a ±0.023% full-scale accuracy.

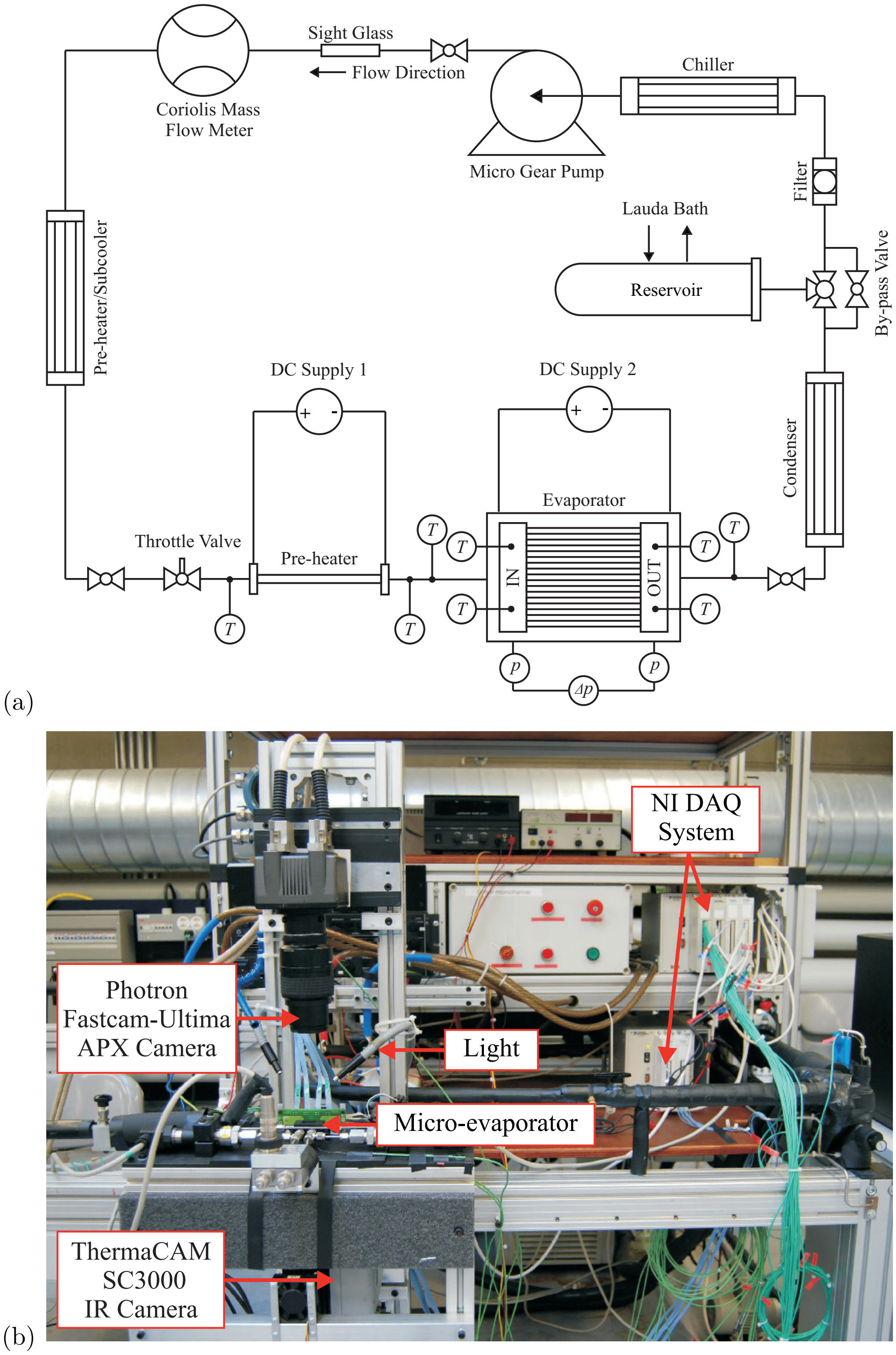
Sight Glass
Flow Direction
Coriolis Mass Flow Meter
Chiller
Micro Gear Pump
Filter
Lauda Bath
Reservoir
By-pass Valve
Pre-heater/Subcooler
DC Supply 1
DC Supply 2
+
-
Evaporator
Condenser
Throttle Valve
Pre-heater
IN
OUT
T
p
Δp
(a)
NI DAQ System
Photron Fastcam-Ultima APX Camera
Light
Micro-evaporator
ThermaCAM SC3000 IR Camera
(b)

Figure 3.1: (a) Schematic of the refrigerant flow loop, and (b) photograph of the experimental flow boiling test facility with the optical system (Szczukiewicz et al., 2012b).

After the working fluid passes through the test section, it is directed to the tube-in-tube type heat exchanger where it is condensed and subcooled. The reservoir containing the working fluid is used to control the saturation pressure in the refrigerant circuit by adjusting its temperature using a RK 20 KP LAUDA compact low-temperature thermostat. A 15 μm filter is installed on the facility to prevent any contaminants from entering the test section and blocking the microchannels.

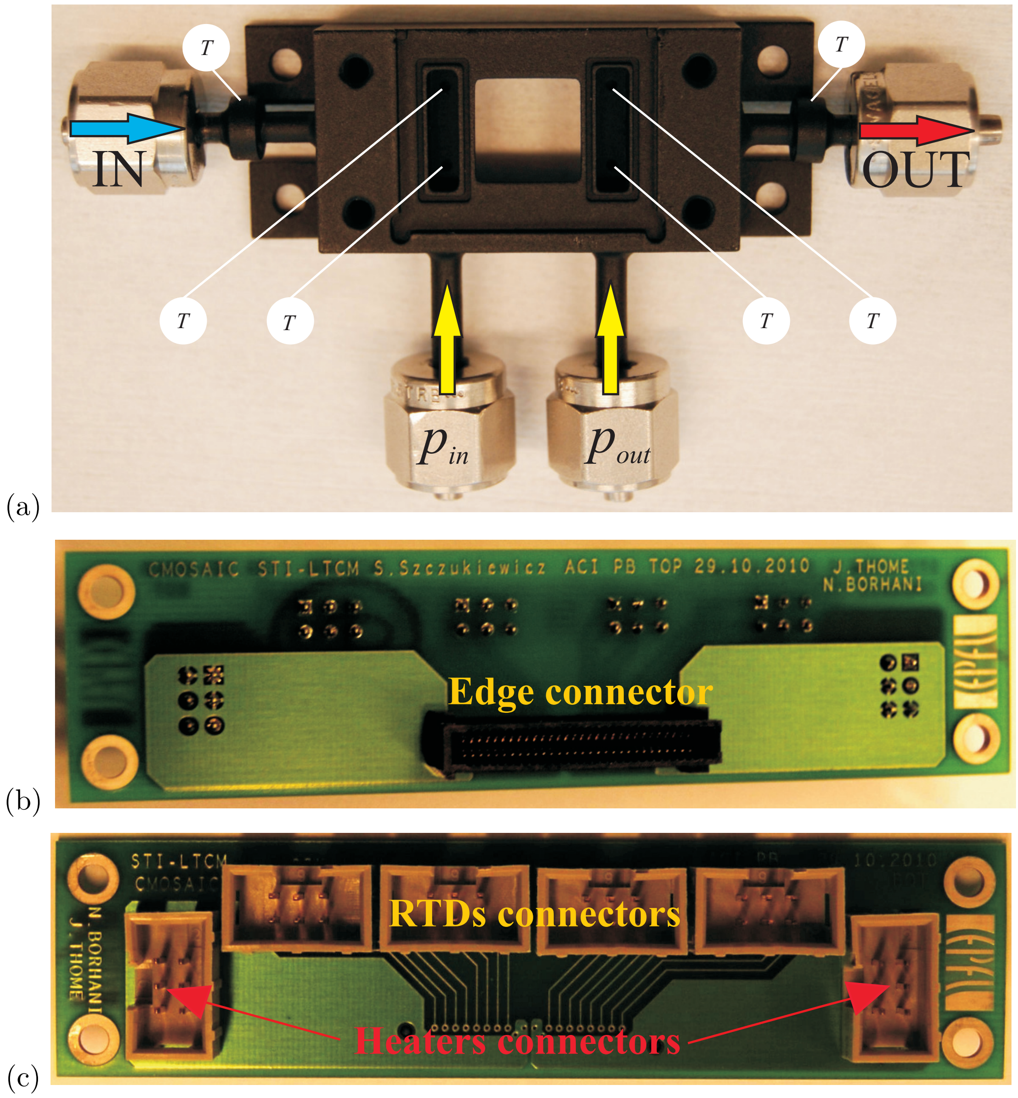
(a)
T
T
IN
OUT
T
T
T
T
p_{in}
p_{out}
(b)
CMOSAIC STI-LTCM S.Szczukiewicz ACI PB TOP 29.10.2010 J.THOME N.BORHANI
Edge connector
EPFL
(c)
STI-LTCM
CMOSAIC
N. BORHANI
J. THOME
RTDs connectors
Heaters connectors
EPFL

Figure 3.2: (a) Bottom part of the test section manifold, (b) front-side of the PCB board with HSEC8-130-01-S-DV-A edge connector, and (c) back-side of the PCB board with heaters and RTDs connectors.

The aim of the current research is to perform two-phase flow boiling and temperature visualizations over the entire micro-evaporator area. In order to do that, as depicted in Fig. 3.2(b), the experimental test facility is equipped with an optical system comprising two high-speed cameras: a Photron Fastcam-Ultima APX camera placed above the test section and a ThermaCAM SC3000 infra-red (IR) camera below. The Photron Fastcam-Ultima APX camera, having the highest spatial resolution of 1’024 x 1’024 pixels at 2’000 fps, was coupled with an AF Micro-Nikkor 105 mm 1:2.8D lens and an additional ring to increase magnification. An additional source of light is applied to illuminate the test section. The ThermaCAM SC3000 high-speed IR camera, having a maximum frame rate of 900 fps (presently operated at 60 Hz), was equipped with a close up lens LW 34/80, thus improving the measurement accuracy over the small target areas by excluding unwanted background (surrounding) temperatures.

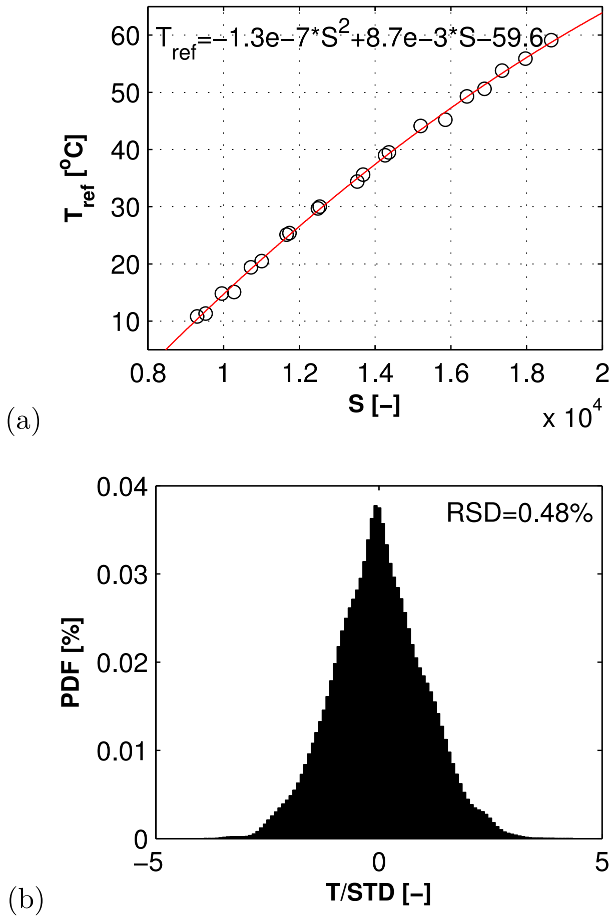

Figure 3.3: (a) An example of an IR camera calibration curve for a given pixel on the sensor (Szczukiewicz et al., 2012a), and (b) probability density function for the reference temperature of 10.8 °C over a 3’621 length sample captured at 60 Hz.

Use of IR thermography requires great attention to detail to get accurate temperature measurements without reflection, emissivity, and observation angle effects. Here, a novel in-situ *pixel by pixel* technique was developed to calibrate the raw IR image signals, S, thus converting them into two-dimensional temperature fields of the test section surface in a manner that avoids most such problems. In-situ IR camera calibration was performed with the flow loop by running single-phase liquid flow of a low-pressure refrigerant, namely R245fa, and keeping adiabatic conditions in the test section. While calibrating, the speed of the pump was set to nearly the maximum value to ensure uniform temperature distribution among the channels. The IR camera calibration was performed over the range of reference temperature, T_{ref}, from 10 and

60 °C with a temperature step of about 5 °C, where the reference temperature is the average value of the temperature measured at the inlet and outlet manifold plenums (see Fig. 3.2(a)). The IR camera calibration procedure was done in ascending and descending mode to check for hysteresis. Figure 3.3(a) presents an example of the IR camera calibration curve. Figure 3.3(b) illustrates the probability density function (PDF) for the same reference temperature over a 3'621 length sample captured at 60 Hz providing a relative standard deviation (RSD) of only 0.48%. The wall temperature during the calibration fluctuated within ± 0.1 °C at the reference temperature of 10.8 °C, giving the root mean squared (R_q) value of 0.17 °C. Thus, the present IR temperatures are accurate to within ±0.5 °C when calibrating over the range of reference temperatures between 10 and 60 °C. However, in the temperature range of the two-phase flow experiments, they are measured with an accuracy of ±0.2 °C, which provides a tenfold accuracy improvement compared to the manufacture's value of ±2 °C.

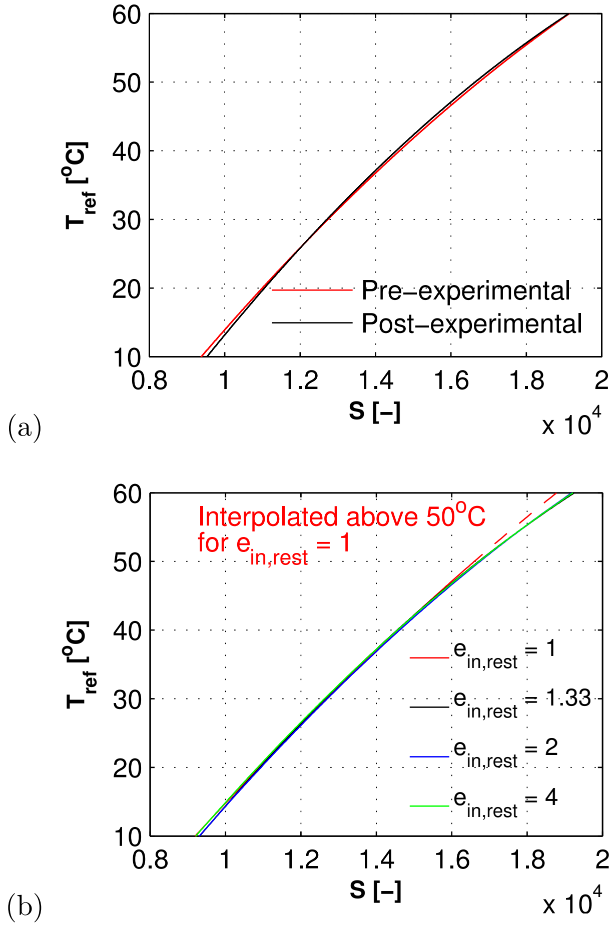

Figure 3.4: Comparison of: (a) the pre- and post-experimental calibration curves for the pixel $P_{(15,16)}$ of the IR camera's sensor array (Szczukiewicz et al., 2012b), and (b) the calibration curves of the middle pixel of the IR camera's sensor array obtained for 4 different test sections.

The comparison of the pre- and post-experimental calibration curves obtained for the pixel $P_{(15,16)}$ of the IR camera's sensor array, as well as the comparison of the the calibration curves for the middle pixel of the IR camera's sensor array and 4 different test sections revealed good agreement, as indicated in Fig. 3.4. The IR temperatures measured here that refer to junction temperatures commonly used in electronics devices, are thus accurate, repeatable, and reliable.

3.2 Micro-evaporators

The test section, described by Szczukiewicz et al. (2012a,b), had overall dimensions 25.4 x 28 mm^2. A 380 μm-thick double-side polished silicon wafer was anodically bonded to a 525 μm-thick transparent Pyrex cover plate. The schematic block diagram of the test section assembly is depicted in Fig. 3.5. The test section's fabricating process was as follows: (i) TiAl sputtering, (ii) TiAl Reactive Ion Etching (RIE), (iii) SiO_2 RIE and Si Deep Reactive Ion Etching (DRIE) for inlet/outlet openings, (iv) SiO_2 wet etching, (v) Si DRIE for microchannels, and (vi) silicon-Pyrex anodic bonding.

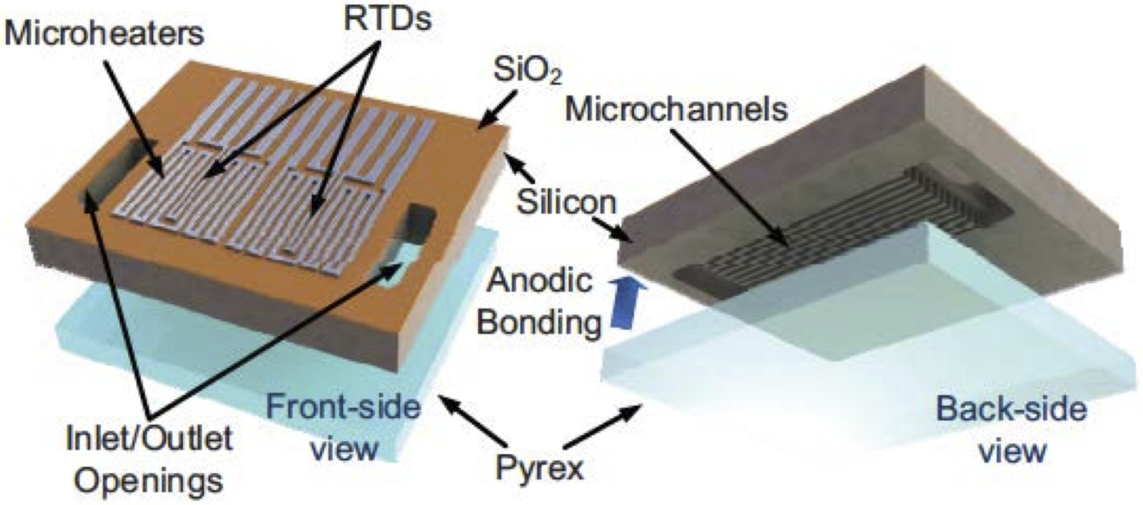

Figure 3.5: Schematic of the test section assembly (Sabry et al., 2011).

Tests revealed that the micro-evaporator was able to withstand absolute pressures up to 10 bars without bursting, thus indicating the high quality of the bonds. The channels, shown in Fig. 3.6(a), are 10 mm-long with a 100 x 100 μm^2 in cross section. The low aspect ratio of the channel:

$$a = \frac{H_{ch}}{W_{ch}} = 1 \tag{3.1}$$

minimizes the effect of flow stratification, due to the fact that the surface tension forces overcome the gravitational forces.

The surface roughness of the channel bottom wall was measured along its centerline using the non-contact optical phase shifting and white light vertical scanning interferometry technique,

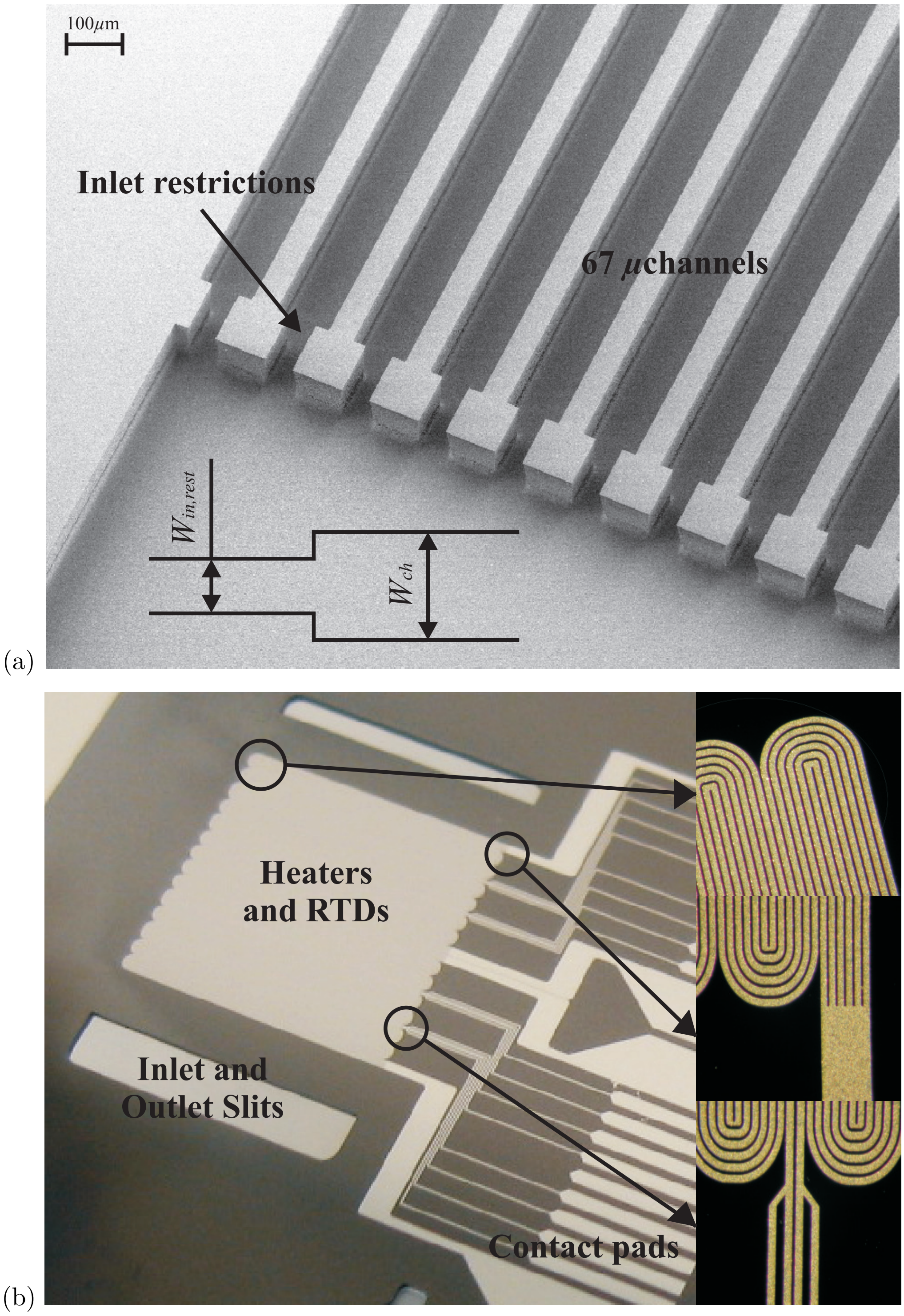
100μm
Inlet restrictions
67 μchannels
$W_{in,rest}$
W_{ch}
(a)
Heaters and RTDs
Inlet and Outlet Slits
Contact pads
(b)

Figure 3.6: (a) 100 x 100 μm^2 channels with the inlet restrictions of the expansion ratio of $e_{in,rest} = 2$, and (b) back-side of the silicon evaporator with the serpentine microheaters and RTDs.

which gave a root mean squared value of 90 nm. Figure 3.7 shows the photograph of the surface roughness profile of the inlet restriction having the expansion ratio of $e_{in,rest} = 2$. There were 67 channels separated by 50 μm-wide fins, which had a 1 cm^2 evaporating area representative of electronics devices (CPU, IGBT's, etc.). Therefore, in the present study, the heat flux will be expressed in W cm^{-2} when refereed to the micro-evaporator's base. The channels are not perfectly square; some curvatures exist in the channels' corners, as seen in Fig. 3.8. This is, however, neglected in the data reduction process.

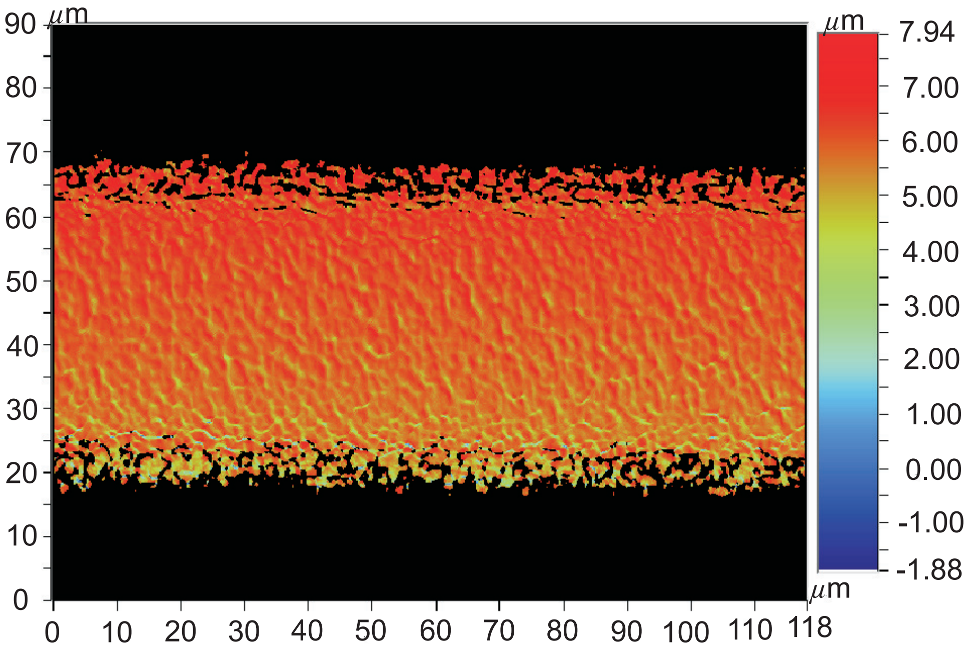

Figure 3.7: Photograph of the surface roughness profile of the inlet restriction having the expansion ratio of $e_{in,rest} = 2$.

The fluid entered and exited the test section headers via, respectively, 1 mm-wide inlet and 2 mm-wide outlet slits. Two independent serpentine microheaters, made from aluminium of 1.5 μm thickness, were sputtered onto the back-side of the micro-evaporator, as shown in Fig. 3.6(b), to simulate the power dissipated by active components in a 3D CMOS chip. Aluminium was chosen due to its compatibility with the machines in Clean Room[1] and relatively good resistance to delamination that might take place as the test section is cyclically heated during an experimental investigation. The heating path was split to 6 40 μm-wide strips with the distance in between them of 15 μm, chosen based on the penetration depth and checked against an electrical breakdown to prevent a short circuit. Also, 50 μm-wide 4-wire resistance temperature detectors (RTDs) were plated onto the back-side in between the heater coils. These were calibrated in the same way as the IR camera. DC current was applied to the micro-evaporator via a HSEC8-130-01-S-DV-A edge connector (SAMTEC) soldered to the PCB board. Figures 3.2(b) and (c) show the front- and back-side of the PCB. Then, this PCB was mounted on the side of the tested micro-evaporator.

---

[1] Center of Micronanotechnology, École Polytechnique Fédérale de Lausanne (CMI – EPFL)

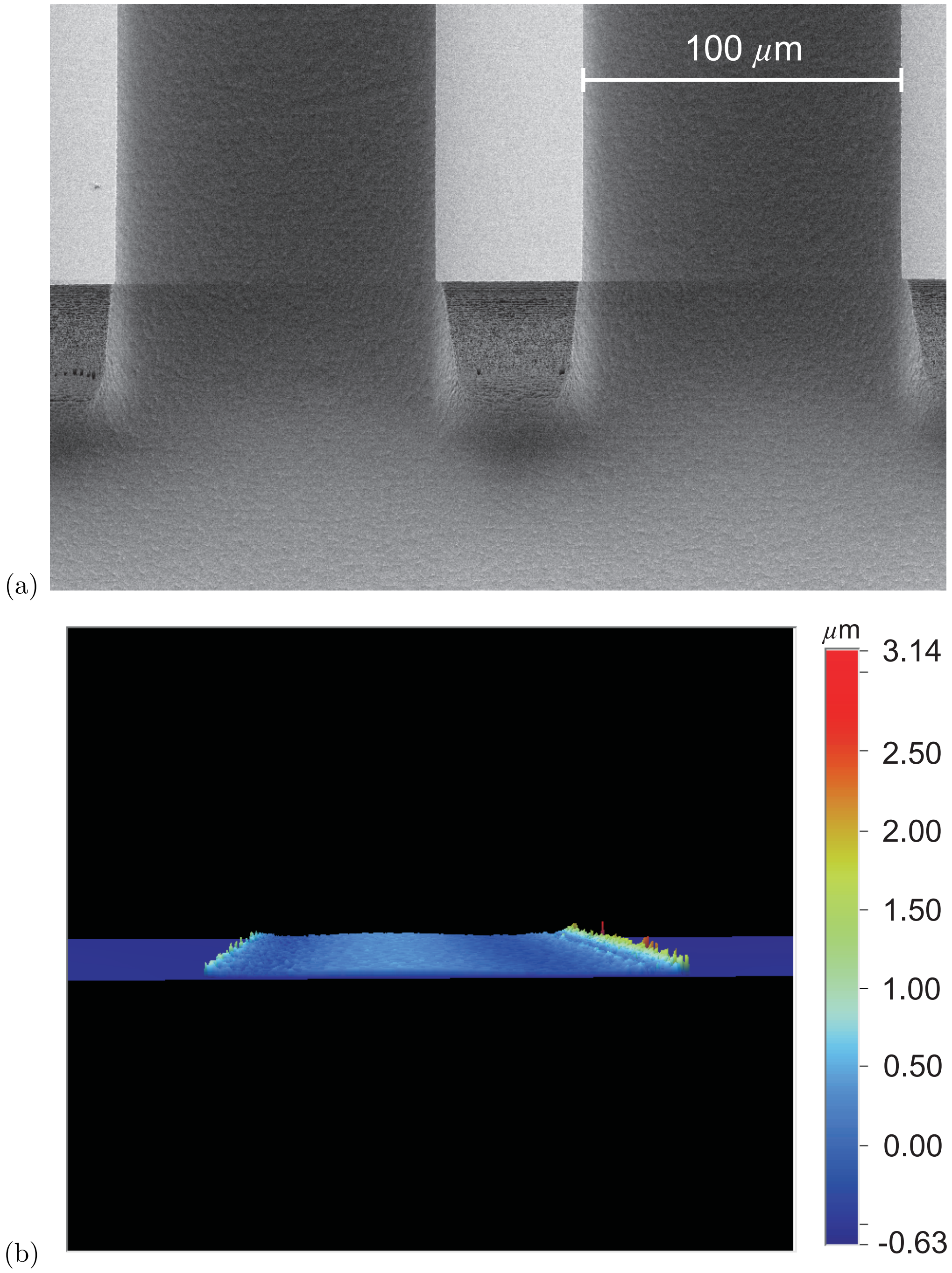
100 μm
(a)
μm
3.14
2.50
2.00
1.50
1.00
0.50
0.00
-0.63
(b)

Figure 3.8: Photographs of: (a) 100 x 100 μm^2 channels, and (b) the surface profile of the channel bottom wall.

As suggested by Hetsroni et al. (2001) and Xu et al. (2005), a high-emissivity black matt tape (ε_{tape} close to 1.0 within the present temperature range) was placed onto the back-side of the micro-evaporator to improve the accuracy of the IR temperature measurements and to minimize the IR transmissivity of the test section. The temperature distribution was uniform with the spatial derivative of the temperature less than ±0.09 °C/pixel.

Snapshots of the high-speed videos of flow visualization and the time-averaged IR temperature maps of the test section's base provided by the two-phase flow boiling of R245fa in two micro-evaporators, with and without inlet restrictions at the same experimental conditions are compared in Fig. 3.9. The flow direction is from left to right in all of presented images for both flow and temperature. As expected, observation of the two-phase flow with evaporation of R245fa in the micro-evaporator without any inlet restrictions revealed the presence of significant flow instabilities, such as parallel channel instability (Zhang et al., 2010, 2011), vapor back flow and non-uniform flow distribution among the channels. Wu and Cheng (2003a) pointed out that those phenomenon lead to high-amplitude and high-frequency temperature and pressure oscillations. Therefore, the rectangular restrictions were placed at the inlet of each channel, as suggested by Agostini et al. (2008c). Those restrictions of different expansion ratios ($e_{in,rest} = 1.33$, 2, and 4) and the channels were manufactured using the same procedure, thus they have the same depth. The expansion ratio downstream of the inlet restriction is defined as follows:

$$e_{in,rest} = \frac{W_{ch}}{W_{in,rest}} \tag{3.2}$$

The contour-type temperature maps, presented in Figs. 3.9(b) and 3.9(d), help to visually assess the temperature uniformity over the micro-evaporator area. For the test section with the inlet restrictions in Fig. 3.9(d), the wall-temperature distribution is much more uniform; in fact, only a small heat spreading effect is noticeable at the two lateral sides. Surprisingly, the contour lines of the temperature are smoother for the test section without any inlet restrictions where the flow instabilities take place, as illustrated in Fig. 3.9(b), the reason being is that these IR temperature maps are obtained by averaging the values over time and the vapor back flow appear to smooth the time-averaged temperature distribution. One needs to remember that the temperature fluctuations cannot be assessed here. Moreover, due to the unstable flow, the test section without any inlet restrictions failed before the experiment test matrix was successfully accomplished. As explained by Park et al. (2009), due to the flashing effect in the test section with the micro-orifices, the boiling starts at a lower heat flux, and thus the wall-temperature distribution becomes more uniform and the wall-temperature overshoot for the onset of boiling is circumvented by the vapor bubbles produced by the flashing. Therefore, inlet micro-orifices are very beneficial in order to prolong the lifetime and extend the stable operation of the future 3D interlayer cooling systems.

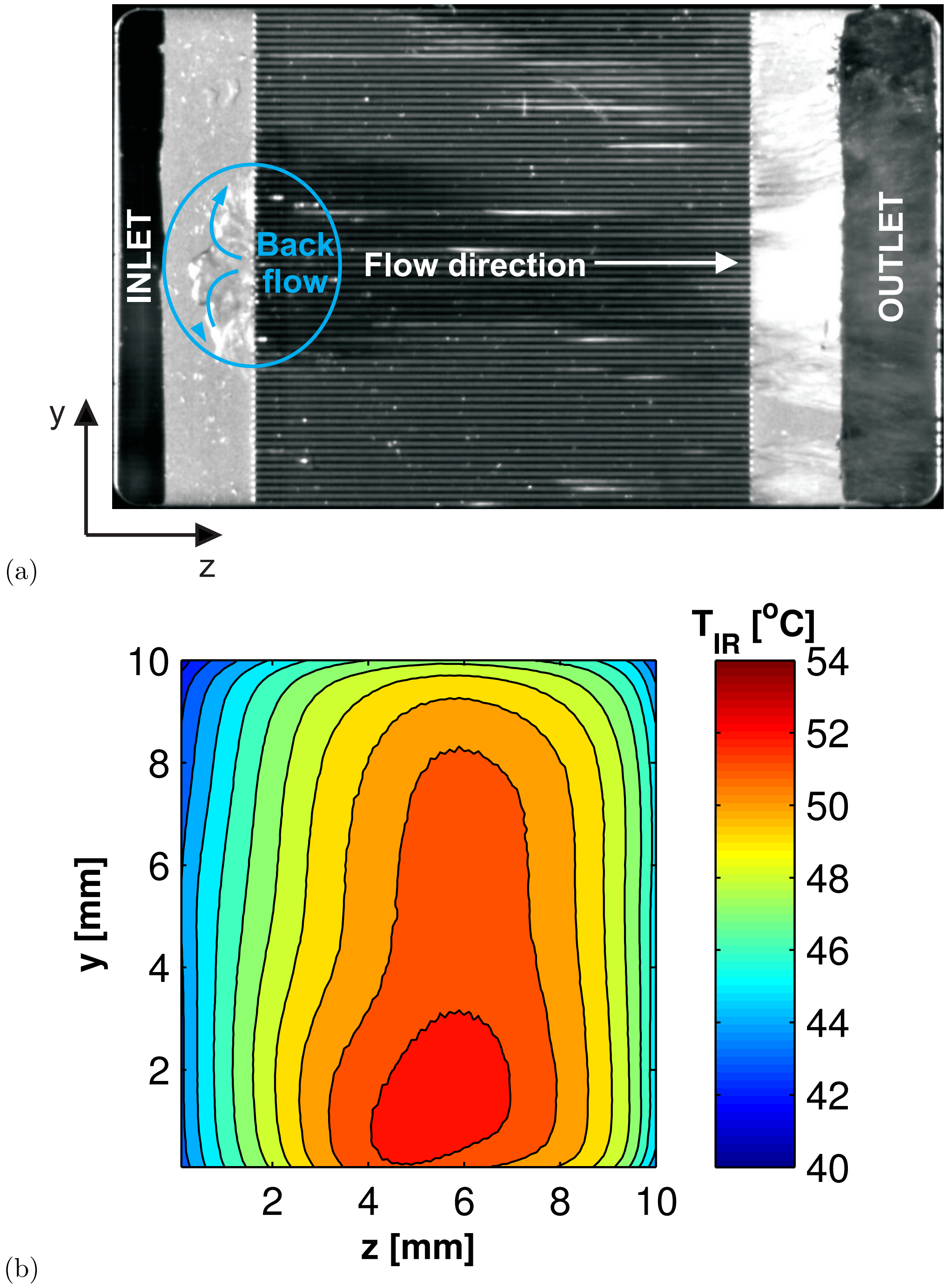

Figure 3.9: Snapshots of the high-speed flow visualization and the time-averaged IR temperature maps of the test section's base provided by the two-phase flow boiling of R245fa for $G_{ch} = 2\text{'}035\,\mathrm{kg\,m^{-2}\,s^{-1}}$ and $q_b = 36.5\,\mathrm{W\,cm^{-2}}$: (a), (b) without any inlet restrictions, and (c), (d) with the 50 μm-wide, 100 μm-deep, and 100 μm-long inlet micro-orifices (Szczukiewicz et al., 2012b). The flow is from left to right. The figure continues over pp. 39 – 40.

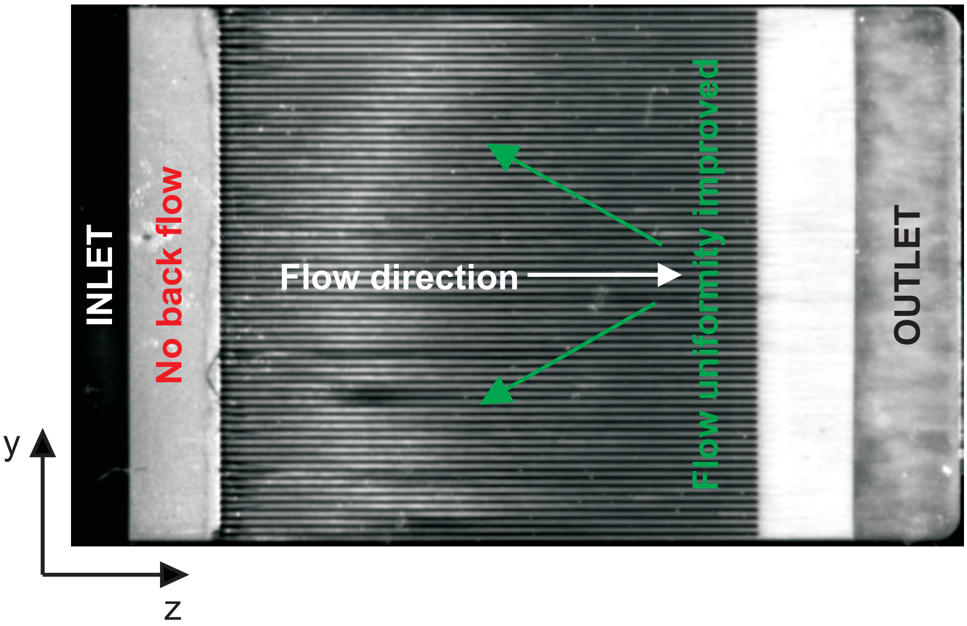
INLET
No back flow
Flow direction
Flow uniformity improved
OUTLET
y
z

(c)

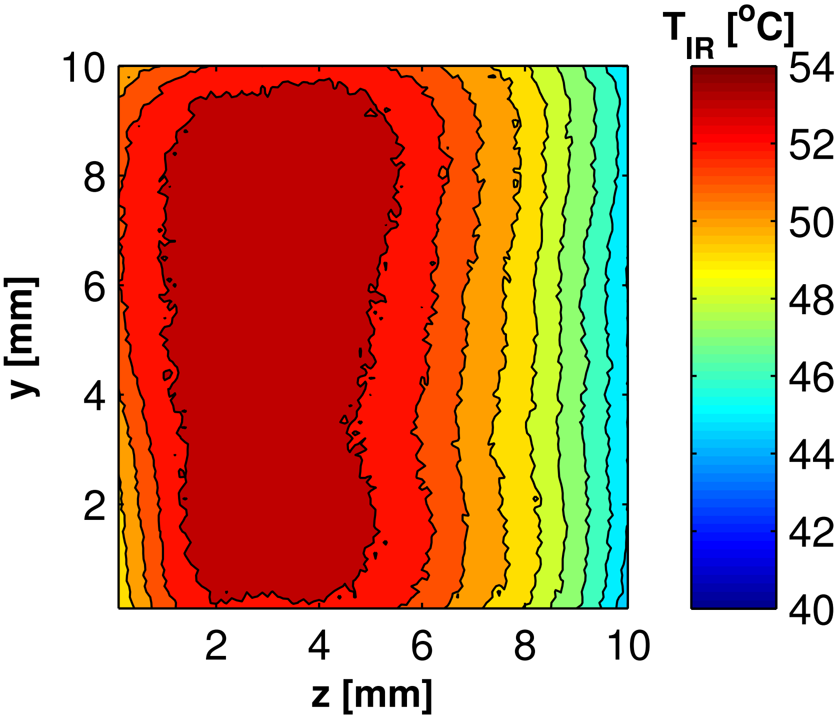

(d)

Figure 3.9: (continued) Snapshots of the high-speed flow visualization and the time-averaged IR temperature maps of the test section's base provided by the two-phase flow boiling of R245fa for $G_{ch} = 2\text{'}035\,\mathrm{kg\,m^{-2}\,s^{-1}}$ and $q_b = 36.5\,\mathrm{W\,cm^{-2}}$: (a), (b) without any inlet restrictions, and (c), (d) with the $50\,\mu$m-wide, $100\,\mu$m-deep, and $100\,\mu$m-long inlet micro-orifices (Szczukiewicz et al., 2012b). The flow is from left to right. The figure continues over pp. 39 − 40.

Chapter 4

Experiments, operating conditions, and data reduction

This chapter focuses on the experimental campaign and the data reduction procedures.

4.1 Experiments

Figure 4.1 presents the summary of the current experimental investigation. Its test matrix included 2 low-pressure refrigerants, R245fa and R236fa, as well as 1 medium-pressure new refrigerant R1234ze(E) flowing in 4 different test sections, both with ($e_{in,rest} = 4$, 2, and 1.33) and without any inlet restrictions ($e_{in,rest} = 1$).

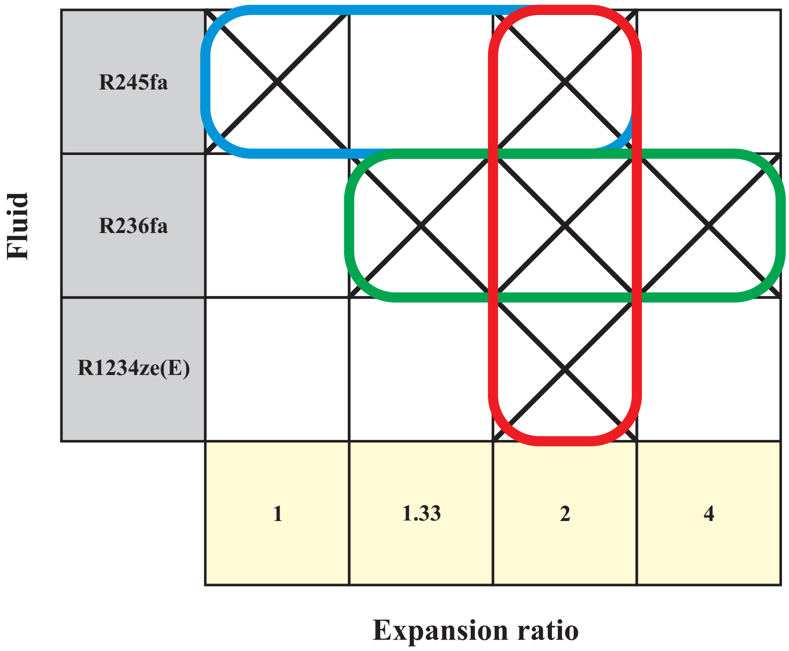

Figure 4.1: Summary of the current experimental campaign, where × denotes the test case.

The following comparisons are then possible:

- **cyan** – for R245fa flowing inside 2 test sections ($e_{in,rest} = 1$ and 2),
- **green** – for R236fa flowing inside 3 test sections ($e_{in,rest} = 1.33$, 2, and 4), and
- **red** – for $e_{in,rest} = 2$ tested for 3 fluids: R245fa, R236fa, and R1234ze(E).

4.1.1 Single-phase flow tests

Single-phase flow energy balances of the test section for various heat fluxes, channel mass fluxes, and inlet fluid subcoolings was performed in order to estimate the heat loss to the surrounding environment. The heat loss within the micro-evaporator to the fluid, shown schematically in Fig. 4.2, is equal to:

$$\Delta E = \frac{Q_{el} - M c_{p,l} \left(T_{out} - T_{in}\right)}{Q_{el}} \cdot 100\% \tag{4.1}$$

where: Q_{el} is the total electrical power supplied to the device, M is the fluid flow rate (measured by the Coriolis mass flow meter), c_{pl} is a liquid specific heat at a constant pressure, and T_{in} and T_{out} are the fluid temperatures at the inlet and the outlet manifold's plenums given as:

$$T_{in} = \frac{T_1 + T_2}{2} \tag{4.2}$$

and

$$T_{out} = \frac{T_3 + T_4}{2} \tag{4.3}$$

The fluid temperature in the loop was kept low to maintain single-phase flow. The measurements were taken once the operational steady state conditions were achieved. Figure 4.3 demonstrates the results of the single-phase (liquid) flow energy balance for the base heat flux varying from 1.9 to 2.4 $\mathrm{W\,cm^{-2}}$ and the inlet liquid subcooling ranging between 4.8 and 6.4K. **One needs to notice that all two-phase heat transfer tests were run at base heat fluxes of ~6 $\mathrm{W\,cm^{-2}}$ or higher.** The heat losses are indicative for low heat fluxes and channel mass fluxes, which is probably due to an insufficient measurement accuracy for those experimental test conditions. As expected, the heat loss decreases with increasing the mass velocity. Moreover, the single-phase flow tests showed that the heat loss decreases rapidly with increasing heat input, mass flow rate, and inlet fluid subcooling. **As a result, since for the maximum heat flux of 2.4 $\mathrm{W\,cm^{-2}}$ in Fig. 4.3, the effective heat loss is ~3%, so it was always ~3% or less for the two-phase flow tests.** In general, the heat loss was negligible relative to the heat fluxes that will be used in the two-phase flow tests. When significant, though, it was correlated in terms of the boiling and the Reynolds numbers, the average temperature of the micro-evaporator's surface, and the ambient temperature, respectively, Bo, Re, $T_{IR,ave}$, and T_{amb}. The above-mentioned dimensionless numbers are:

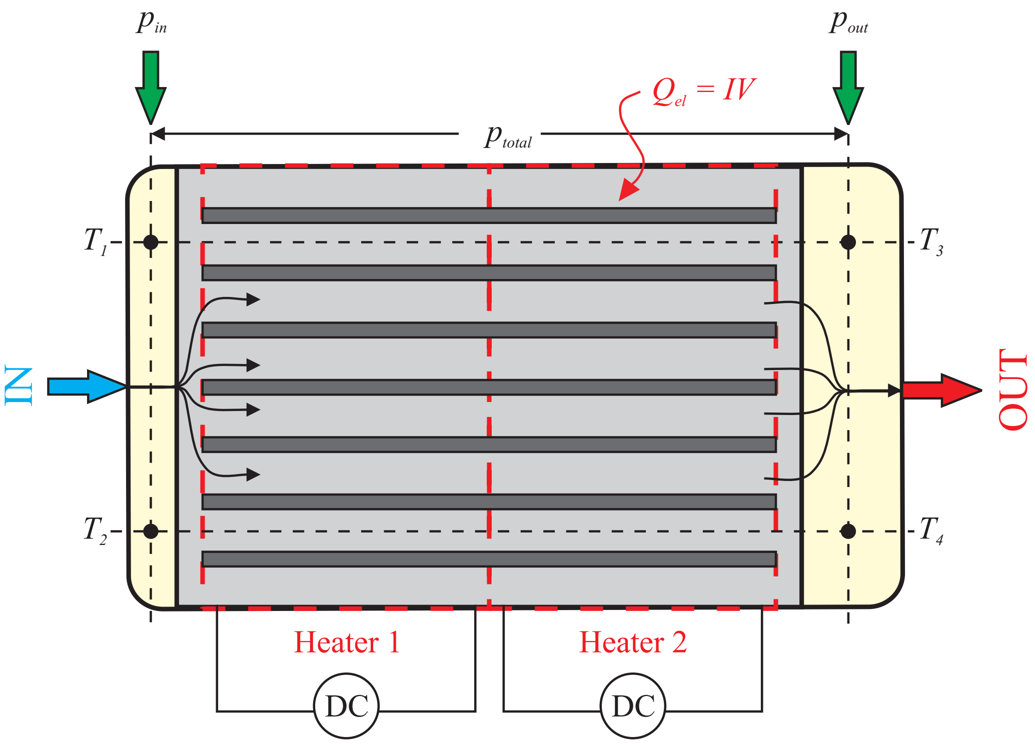
p_{in}
p_{out}
$Q_{el} = IV$
p_{total}
T_1
T_2
T_3
T_4
IN
OUT
Heater 1
Heater 2
DC
DC

Figure 4.2: Schematic of the test section.

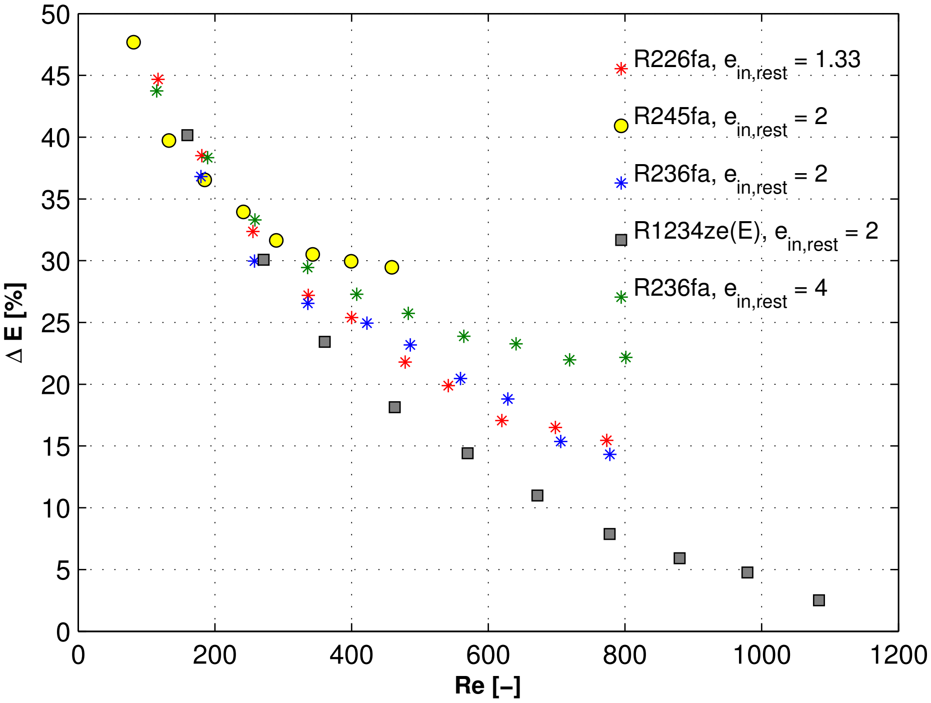

Figure 4.3: Single-phase flow heat losses in function of the Reynolds number for the base heat flux varying from 1.9 to 2.4 $\mathrm{W\,cm^{-2}}$ and the inlet liquid subcooling ranging between 4.8 and 6.4K.

$$Bo = \frac{q_b}{G_{ch} h_{lv}} \tag{4.4}$$

and

$$\mathrm{Re} = \frac{G_{ch} D_h}{\mu} \tag{4.5}$$

Since the $\varepsilon_{tape} \approx 1$ in the present temperature range, the Stefan-Boltzmann's law for a black body exposed to the surrounding with a known temperature, T_{amb}, is used to estimate the heat emission by radiation, E_{rad}. As a result, it is lower than 0.023 W. Therefore, the heat losses are mainly due to conduction down the wiring between the microheater and the power supply.

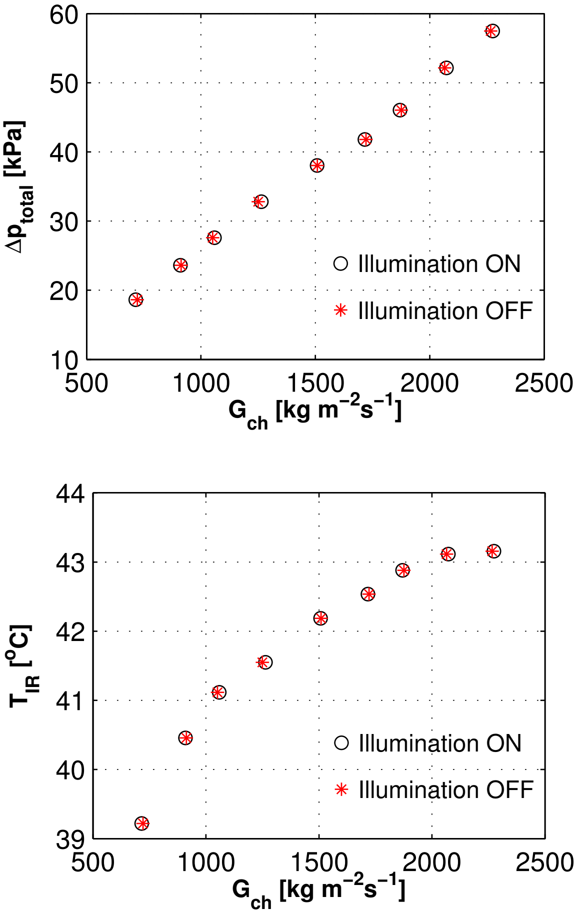

(a)

(b)

Figure 4.4: Measurements of: (a) total pressure drop, Δp_{total}, and (b) local IR temperatures, T_{IR}, with and without illumination for two-phase flow of R236fa flowing in the test section with the inlet restrictions of $e_{in,rest} = 2$ for the channel mass flux varying from 715 to 2'275 kg m^{-2} s^{-1} and the dissipated base heat flux of 24.6 W cm^{-2} (Szczukiewicz et al., 2012a,b).

The flow boiling experiments were performed above the T_{amb}. The input from the light used for the test section's illumination, measured with the Laser Power Meter Spectra-Physics 407a, was on an order of about 1% of the total heat flux supplied to the device. Moreover, as indicated in Fig. 4.4, the comparison of the two-phase flow total pressure drop of R236fa and local IR temperatures of the micro-evaporator's surface ($e_{in,rest} = 2$) for the channel mass flux varying from 715 to 2'275 $\mathrm{kg\,m^{-2}\,s^{-1}}$ and the dissipated base heat flux of 24.6 $\mathrm{W\,cm^{-2}}$ in both cases, with and without illumination, revealed very good agreement. Hence, the heat gain was assumed to be negligible. The tests without illumination were repeated 15 days after the one with the light turned on, which also proved good measurement reproducibility of the two-phase flow boiling experiments.

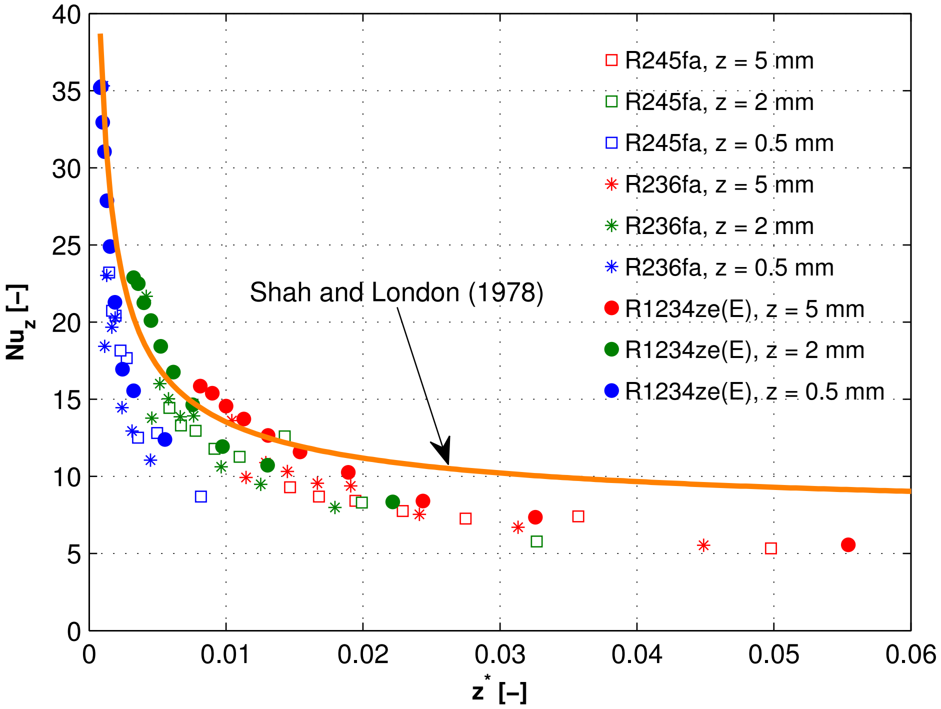

Figure 4.5: Comparison of the experimental Nusselt numbers with those predicted by the Shah and London (1978) formula for laminar developing flow for $100 < \mathrm{Re} < 1'000$ with a uniform heat flux boundary condition in the test section with the inlet restrictions of $e_{in,rest} = 2$. The heat losses have been estimated from Fig. 4.3 and removed. Total MAE = 27.5 %.

Prior to the flow boiling experiments, it is important to perform pre-validation tests to prove that the set-up is able to accurately measure some single-phase liquid heat transfer coefficients. Such tests were performed for subcooled refrigerant flows in the tested micro-evaporators. Several different longitudinal distances, $z = 0.5$, 2.0, and 5.0 mm, were analyzed. The experimental Nusselt numbers, Nu_z, calculated assuming one-dimensional (1D) heat conduction, were compared with those predicted by the Shah and London (1978) formula for laminar developing flow with a uniform heat flux boundary condition. Figure 4.5 illustrates the experimental Nusselt numbers versus the prediction method of Shah and London (1978) in function of a non-dimensional length:

$$z^* = \frac{\pi}{4} \frac{z}{\mathrm{Re}\,\mathrm{Pr}\,D_h} \tag{4.6}$$

Furthermore, the following definitions of dimensionless numbers are employed:

$$\mathrm{Nu_z} = \frac{\alpha(z)D_h}{k} \tag{4.7}$$

$$\mathrm{Pr} = \frac{c_p\mu}{k} \tag{4.8}$$

The Reynolds number is given by Eq. (4.5).

In Fig. 4.6, some discrepancies are seen for high Reynolds numbers, the reason being is that the prediction method does not consider downstream effects of the micro-orifices at the entrance, which enhances the heat transfer with increasing the mass velocity, and thus the experimental Nusselt numbers are higher than the predicted ones. Moreover, three-dimensional (3D) heat spreading is not taken into account when performing the validation, which may affect heat transfer results, as shown by Costa-Patry et al. (2012). The discrepancies seen for low Reynolds numbers are due to an insufficient experimental accuracy for such test conditions and the fact that the experimental facility was built to carry out two-phase flow experiments. For a test set-up for two-phase flow experiments, not a single-phase laminar tests, this comparison is reasonable.

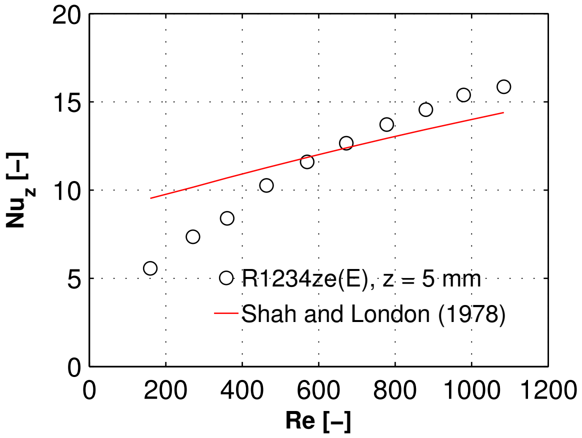

Figure 4.6: Experimental Nusselt numbers versus those predicted by Shah and London (1978) formula method for laminar developing flow of R1234ze(E) flowing in the test section with the inlet restrictions of $e_{in,rest} = 2$ under a uniform heat flux boundary condition (Szczukiewicz et al., 2012a,b).

4.1.2 Two-phase flow tests

Firstly, the test facility was evacuated by a vacuum pump for at least 12 hours. After filling it with the test fluid, the visual inspection through the sight glass, illustrated in Fig. 3.1(a), and the transparent cover plate in the test section was performed showing that non-condensable gases were not present in the test loop for all liquid flow tests. Moreover, it was confirmed by pressure and temperature monitoring within the test loop. The saturation pressure in the refrigerant circuit was set by adjusting the temperature in the RK 20KP LAUDA thermostat connected to the refrigerant tank. Once established, the mass velocity was set through the frequency controller acting on the micropump. Afterwards, the desired fluid subcooling in the test section's inlet was set by means of the pre-heater/subcooler; however, the electrical pre-heater could be also used to do this. Heat flux was then applied to the heater to initiate the transition to two-phase flow in the micro-evaporator. The experiments were performed at a constant heat flux, increased with a step of ∼4 W cm^{-2}, whereas the mass flux was gradually increased in steps of ∼200 kg m^{-2} s^{-1}. The frequency response of the IR camera was lower that the frequency of the bubble growth in the microchannels, and thus the measurements were limited to steady state conditions. The temperature, pressure, and voltage data were acquired by using the NI DAQ with a sampling rate of 1 kHz over 1 minute and then averaged.

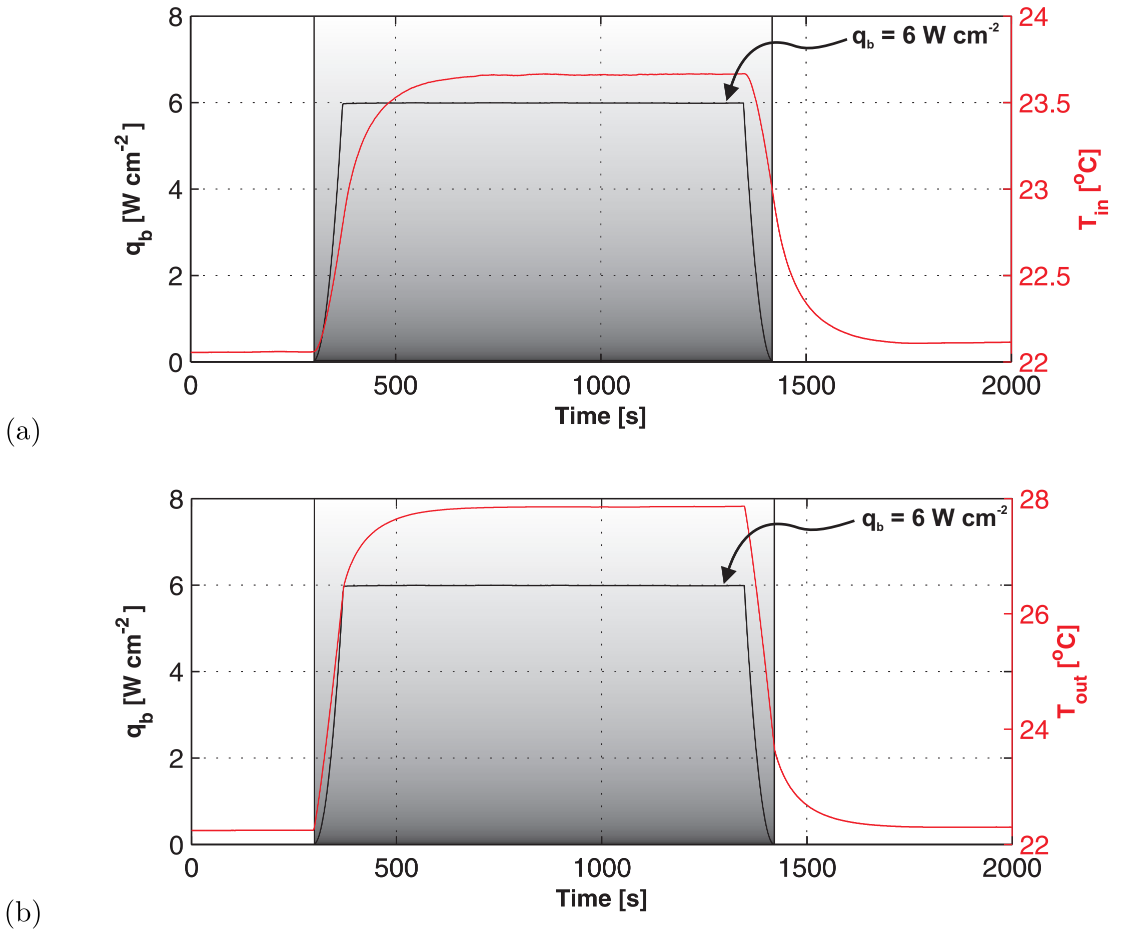

(a)

(b)

Figure 4.7: Thermocouple response at: (a) the inlet, T_{in}, and (b) the outlet, T_{out} manifold's plenums corresponding to the change of the base heat flux.

In order to estimate the relaxation time, in which an operational steady state is reached irrespective of its initial state, various tests were performed by increasing one of the parameters and observing the others. Figure 4.7 shows the change of temperatures recorded at the inlet and the outlet manifold's plenums in response to the change of the base heat flux. As illustrated, the test facility reached stable operation within ~10 minutes. However, due to the experimental protocol, the time of 30 minutes between two test conditions was applied for all the experiments.

4.2 Fluids

The properties of the test fluids, namely R245fa, R236fa, and R1234ze(E), were obtained with the REFPROP 8.0 software, the National Institute of Standards and Technology (NIST) Standard Reference Database 23. Table 4.1 presents the refrigerant saturation properties evaluated at 31.5 °C, which provided a range of pressures suitable for the silicon multi-microchannels.

Table 4.1: Refrigerant saturation properties at 31.5 °C.

Parameter	Unit	R245fa	R236fa	R1234ze(E)
p	kPa	187.5	336.8	592.4
ρ_l	$\mathrm{kg\,m^{-3}}$	1320.7	1337.6	1137.6
ρ_v	$\mathrm{kg\,m^{-3}}$	10.7	22.6	31.6
h_l	$\mathrm{kJ\,kg^{-1}}$	241.1	239.2	242.9
h_v	$\mathrm{kJ\,kg^{-1}}$	427.5	381.2	404.9
h_{lv}	$\mathrm{kJ\,kg^{-1}}$	186.4	142.0	162.0
μ_l	$\mu\mathrm{Pa\,s}$	375.2	263.2	187.4
μ_v	$\mu\mathrm{Pa\,s}$	10.5	11.1	12.8
k_l	$m\mathrm{W\,m^{-1}\,K^{-1}}$	86.1	70.9	60.7
k_v	$m\mathrm{W\,m^{-1}\,K^{-1}}$	13.4	13.3	16.3
σ	$m\mathrm{N\,m^{-1}}$	13.2	9.3	7.7

4.3 Operating conditions

The geometrical specifications, experimental parameters, and uncertainties for the uniform heat flux tests are given in Table 4.2. A similar table for the two-phase flow experiments in the half-heated test sections (those in which only the heater of the first half of the test section was turned on) is shown in Chapter 6. The uncertainties of the measured values were obtained through the equipment calibrations, while the uncertainties of the derived parameters were calculated using the method developed by Kline and McClintock (1953). Appendix A includes the equations used in the error propagation. For all the tests, the outlet saturation temperature and the inlet liquid subcooling were within 31.5±1 °C and 5.7±1.5K, respectively. Therefore, they will not be reported throughout the manuscript.

Table 4.2: Operating conditions and experimental uncertainties for the two-phase flow experiments under uniform heat flux.

Parameter	Unit	Value	Uncertainty
N	-	67	-
L_h	μm	9’765	±5
B	μm	10’000	±5
d_{Si}	μm	380	±10
d_{Px}	μm	525	±10
d_h	μm	1.5	±0.075
H_{ch}	μm	100	±3
W_{ch}	μm	100	±3
W_f	μm	50	±3
$L_{in,rest}$	μm	100	±3
$H_{in,rest}$	μm	100	±3
$W_{in,rest}$	μm	25, 50, 75, and 100	±5
$e_{in,rest}$	-	4, 2, 1.33, and 1	±0.5 – 0.04
a	-	1	0.04
$\Delta T_{in,sub}$	K	5.7	±1.5
$T_{out,sat}$	°C	31.5	±1
T_{fl}	°C	28.9 – 44.7	±0.1
T_{IR}	°C	29.4 – 57.1	±2 (±0.2[a])
p_{out}	kPa	188 – 597	±1
$p_{ch,end}$	kPa	177 – 632	±3.8
Δp_{total}	kPa	2 – 122	±1
$\Delta p_{in,rest}$	kPa	1.2 – 31.9	±1
$\Delta p_{out,rest}$	kPa	(–25.9) – 32.9	±3.9
Δp_{ch}[b]	kPa	(–2.5) – 73.4	±4.2
G_{ch}	$\mathrm{kg\,m^{-2}\,s^{-1}}$	283 – 2’370	4.5%[c]
I	A	3.99 – 23.4	±0.65%
V	V	0.52 – 2.51	±0.53%
q_b	$\mathrm{W\,cm^{-2}}$	1.9 – 48.6	3%
q_w	$\mathrm{W\,cm^{-2}}$	10.8 – 23.4	3%
x_{out}	-	0 – 0.54	0.05
$x_{ch,end}$	-	0 – 0.54	0.05
α_w	$\mathrm{kW\,m^{-2}\,K^{-1}}$	10.1 – 38.9	±15%

---

[a] Including only steady flows.

[b] All the data points included. The negative channel pressure drops might be associated with an estimation of the inlet and the outlet pressure restriction losses as well as the accuracy of the differential pressure sensor at low values of Δp.

[c] The uncertainty in G_{ch} takes into account a variation of channel dimensions within one test section that was estimated to be $\pm 3\,\mu$m.

4.4 Data reduction procedure

The nomenclature, used in this study, is defined in Fig. 4.8.

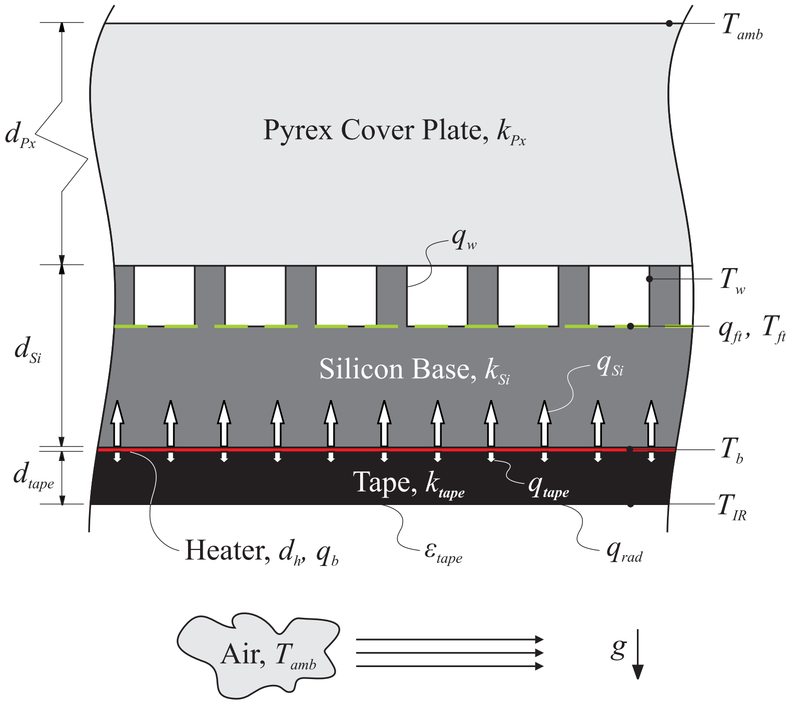
T_{amb}
d_{Px}
Pyrex Cover Plate, k_{Px}
q_w
T_w
q_{ft}, T_{ft}
d_{Si}
Silicon Base, k_{Si}
q_{Si}
T_b
d_{tape}
Tape, k_{tape}
q_{tape}
T_{IR}
Heater, d_h, q_b
ε_{tape}
q_{rad}
Air, T_{amb}
g

Figure 4.8: Sectional view of the micro-evaporator.

4.4.1 Channel mass flux

Assuming flow uniformity within the test section, the channel mass flux is calculated as:

$$G_{ch} = \frac{M}{N W_{ch} H_{ch}} \tag{4.9}$$

where M is the total mass flow rate in kg s^{-1} feeding N channels, each with a width of W_{ch} and a height of H_{ch}.

4.4.2 Pressures

In the current research, due to numerous technical difficulties, the pressure drop was measured between the inlet and the outlet manifold's plenums, although some methods of more local pressure measurements within microchannels are available in the literature. For instance, Kohl et al. (2005) employed integrated multiple pressure-sensitive membranes for pressure measurements inside a single microchannel down to 25 μm. In case of multi-microchannels, however, the applicability of such a single-channel method was not feasible.

The total pressure drop, Δp_{total}, is composed of several pressure gradients due to flow contraction, Δp_{cont}, and flow expansion, $\Delta p_{\exp}$, as well as the channel pressure drop (refer to Fig. 3.2(a), 3.5, and 3.6(a)):

$$\begin{aligned}\Delta p_{total} = \Delta p_{cont,1} + \Delta p_{cont,2} + \Delta p_{cont,3} + \Delta p_{\exp,1} \\ +\Delta p_{ch} \\ +\Delta p_{\exp,2} + \Delta p_{\exp,3} + \Delta p_{\exp,4}\end{aligned} \tag{4.10}$$

In the present study, the fluid enters the test section subcooled, thus the single-phase flow inlet restriction pressure losses due to flow contraction are computed according to Lee and Garimella (2008):

- inlet manifold's plenum – inlet slit

$$\Delta p_{cont,1} = \left[1 - \left(\frac{A_{in,slit}}{A_{mf}}\right)^2 + K_{cont,1}\right] \frac{G^2_{in,slit}}{2\rho_l} \tag{4.11}$$

where

$$K_{cont,1} = 0.0088 \left(\frac{H_{in,slit}}{W_{in,slit}}\right)^2 - 0.1785 \left(\frac{H_{in,slit}}{W_{in,slit}}\right) + 1.6027 \tag{4.12}$$

- inlet slit – test section's plenum

$$\Delta p_{cont,2} = \left[1 - \left(\frac{A_{ts,pl}}{A_{in,slit}}\right)^2 + K_{cont,2}\right] \frac{G^2_{ts,pl}}{2\rho_l} \tag{4.13}$$

where

$$K_{cont,2} = 0.0088 \left(\frac{H_{ts,pl}}{W_{ts,pl}}\right)^2 - 0.1785 \left(\frac{H_{ts,pl}}{W_{ts,pl}}\right) + 1.6027 \tag{4.14}$$

- test section's plenum – N orifices

$$\Delta p_{cont,3} = \left[1 - \left(\frac{NA_{in,rest}}{A_{ts,pl}}\right)^2 + K_{cont,3}\right] \frac{G^2_{in,rest}}{2\rho_l} \tag{4.15}$$

where

$$K_{cont,3} = 0.0088 \left(\frac{H_{in,rest}}{W_{in,rest}}\right)^2 - 0.1785 \left(\frac{H_{in,rest}}{W_{in,rest}}\right) + 1.6027 \tag{4.16}$$

Knowing the saturation pressure at the end of the orifice, the vapor quality at this location is determined as:

$$x = \frac{h_{in} - h_{out}}{h_{lv}} \tag{4.17}$$

where: h_{in} and h_{out} are the enthalpies of the saturated liquid at the inlet and the outlet of the orifice, and h_{lv} is the latent heat of vaporization. Therefore, the pressure recovery due to the flow expansion into the channel, $\Delta p_{exp,1}$, is:

- for single-phase flow

$$\Delta p_{\exp,1-sp} = -2 \times 1.33 \left(\frac{A_{in,rest}}{A_{ch}}\right) \left[1 - \left(\frac{A_{in,rest}}{A_{ch}}\right)\right] \frac{G_{in,rest}^2}{2\rho_l} \tag{4.18}$$

- for two-phase flow

$$\Delta p_{\exp,1-tp} = \left[\frac{A_{in,rest}}{A_{ch}} \left(\frac{A_{in,rest}}{A_{ch}} - 1\right)\right] \left(1 - x\left(L_{in,rest}\right)\right)^2 \left[1 + \frac{C}{X_{tt}} + \frac{1}{X_{tt}^2}\right] \frac{G_{in,rest}^2}{2\rho_l} \tag{4.19}$$

where X_{tt} is the Lockhart and Martinelli (1949) parameter for turbulent – turbulent flow and C varies from 5 to 20, depending on the flow regime of each phase.

The single-phase flow pressure recovery due to the fluid expansion from the channel to the outlet manifold's plenum is determined step by step using the following equations:

- N channels – test section's plenum

$$\Delta p_{\exp,2} = -2 \times 1.33 \left(\frac{NA_{ch}}{A_{ts,pl}}\right) \left[1 - \left(\frac{NA_{ch}}{A_{ts,pl}}\right)\right] \frac{G_{ch}^2}{2\rho_l} \tag{4.20}$$

- test section's plenum – outlet slit

$$\Delta p_{\exp,3} = -2 \times 1.33 \left(\frac{A_{ts,pl}}{A_{out,slit}}\right) \left[1 - \left(\frac{A_{ts,pl}}{A_{out,slit}}\right)\right] \frac{G_{ts,pl}^2}{2\rho_l} \tag{4.21}$$

- outlet slit – outlet manifold's plenum

$$\Delta p_{\exp,4} = -2 \times 1.33 \left(\frac{A_{out,slit}}{A_{mf}}\right) \left[1 - \left(\frac{A_{out,slit}}{A_{mf}}\right)\right] \frac{G_{out,slit}^2}{2\rho_l} \tag{4.22}$$

Those components are grouped as:

- the inlet restriction pressure losses

$$\Delta p_{in,rest} = \Delta p_{cont,1} + \Delta p_{cont,2} + \Delta p_{cont,3} + \Delta p_{\exp,1} \tag{4.23}$$

- the outlet restriction pressure losses

$$\Delta p_{out,rest} = \Delta p_{\mathrm{exp},2} + \Delta p_{\mathrm{exp},3} + \Delta p_{\mathrm{exp},4} \tag{4.24}$$

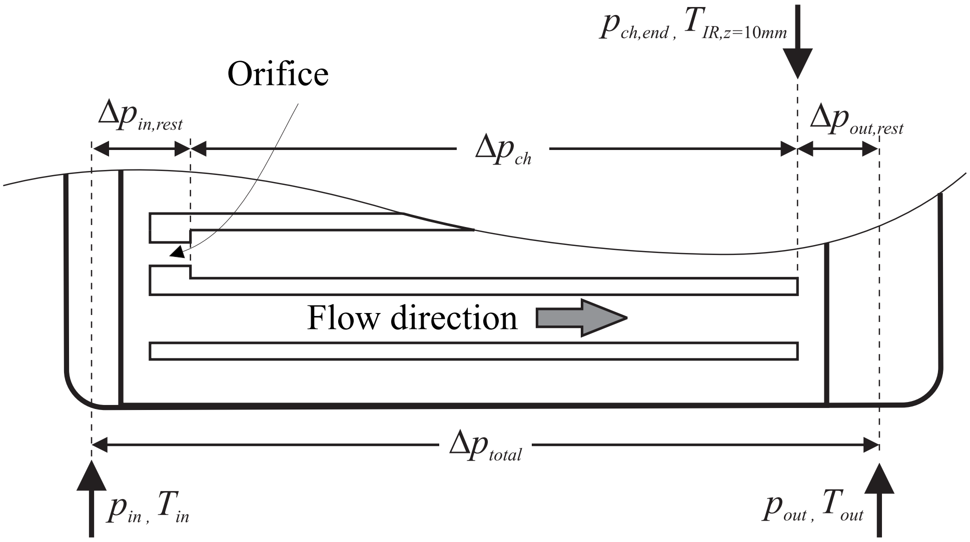

Figure 4.9: Diabatic two-phase flow pressure gradients.

Then, as shown in Fig. 4.9, the diabatic two-phase flow channel pressure drop is calculated by subtracting the inlet and the outlet restriction pressure losses from the total experimentally measured pressure drop as:

$$\Delta p_{ch} = \Delta p_{total} - \Delta p_{in,rest} - \Delta p_{out,rest} \tag{4.25}$$

where: $\Delta p_{in,rest}$ and $\Delta p_{out,rest}$ are specified by Eqs. (4.23) and (4.24), respectively.

The single-phase flow frictional pressure drop along a single channel is determined using:

$$\Delta p_{fr} = 4f\frac{G_{ch}^2}{2\rho_l}\frac{L_{ch}}{D_h} \tag{4.26}$$

where f is the Fanning friction factor for hydrodynamically developing flow (in the present study the Re of the liquid in the channels was always below 2'000) evaluated based on the Shah and London (1978) interpolation formula:

$$f \cdot \mathrm{Re} = 3.44\left(z^+\right)^{-0.5} + \frac{K(\infty)/(4z^+) + f_{fd}\mathrm{Re} - 3.44\,(z^+)^{-0.5}}{1 + C\,(z^+)^{-2}} \tag{4.27}$$

where

$$z^+ = \frac{z}{\mathrm{Re}D_h} \tag{4.28}$$

For rectangular channels with an aspect ratio of a, the f is calculated from Eq. (4.29) (Thome, 2010, in Chapter 4).

$$f \cdot \mathrm{Re} = \left[\frac{3.44}{\left(z^{+}\right)^{-0.5}} + \frac{24 + K\left(\infty\right)/z^{+} - 3.44\left(z^{+}\right)^{-0.5}}{1 + C\left(z^{+}\right)^{-2}} \right] G\left(a\right) \tag{4.29}$$

where

$$G\left(a\right) = 1 - 1.3553a + 1.9467a^{2} - 1.7012a^{3} + 0.9564a^{4} - 0.2537a^{5} \tag{4.30}$$

The incremental pressure drop number $K\left(\infty\right)$ and the parameter C are 0.674 and 0.000029, respectively. The gravitational pressure drop is neglected due to the horizontal channel orientation.

The two-phase flow outlet restriction pressure loss, $\Delta p_{out,rest}$, is obtained by employing the method of Costa-Patry et al. (2011b). The $\Delta p_{out,rest}$ is expressed by:

$$\Delta p_{out,rest} = p_{ch,end} - p_{out} \tag{4.31}$$

knowing the absolute pressure measured in the outlet manifold's plenum, p_{out}, and the pressure at the outlet of the channel evaluated based on the vapor pressure curve at the lateral average value of the steady state IR adiabatic zone temperature measurements, $p_{ch,end}$, as illustrated in Fig. 4.10. In order to determine the $p_{ch,end}$, the power is applied only to the first microheater, as shown in Fig. 4.10(b), thus giving two-phase adiabatic flow at the channel outlets ($z = 10\,\mathrm{mm}$) of known vapor quality. Ideally, if the channel ends are not affected by a conjugate effect, the local base temperature at the channel exit during the two-phase flow could be assumed to be the local fluid saturation temperature. Then, presuming that the two-phase flow pattern does not affect the pressure drop, the results obtained in the half-heated test section and correlated based on the outlet experimental conditions might be extended to the uniform heat flux experiments.

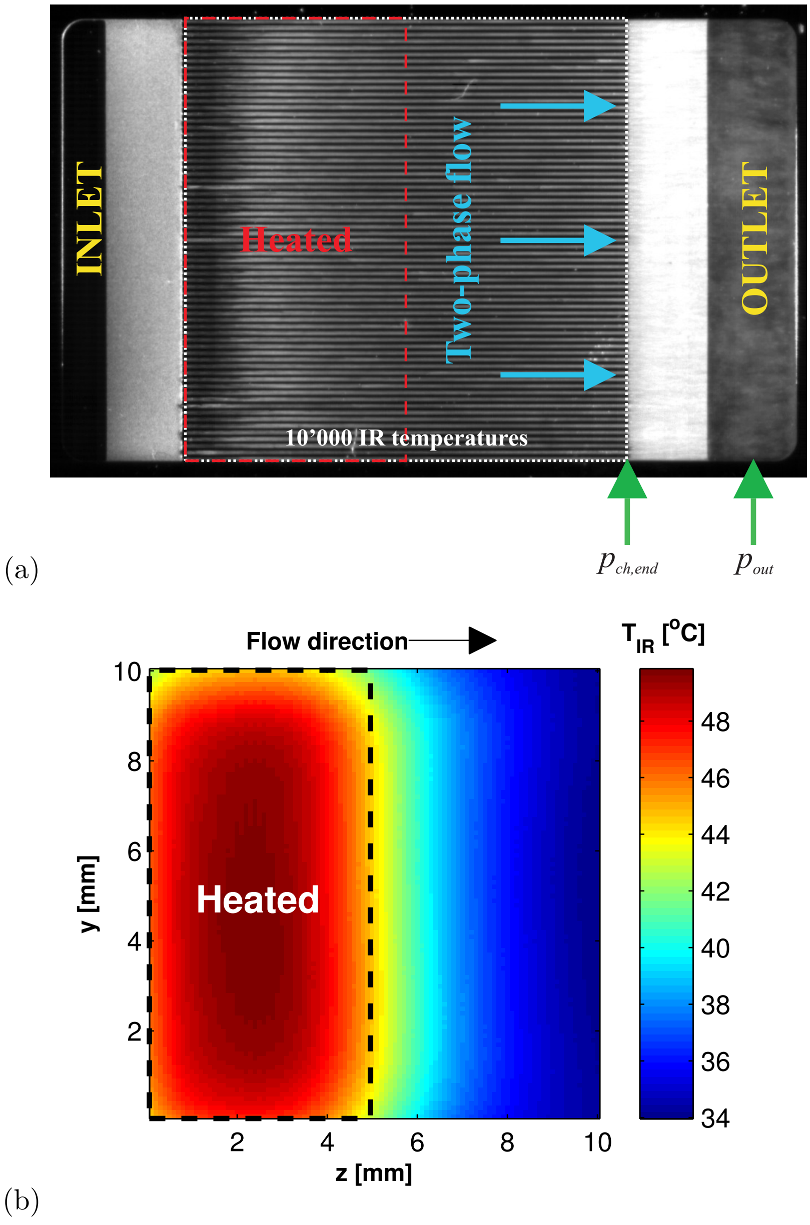

Figure 4.10: Two-phase flow of R236fa in the half-heated test section ($e_{in,rest} = 4$) for the channel mass flux of $G_{ch} = 2'077\,\mathrm{kg\,m^{-2}\,s^{-1}}$ and the dissipated base heat flux of $q_b = 52.6\,\mathrm{W\,cm^{-1}}$: (a) flow pattern, and (b) IR temperature map.

Firstly, a qualitative investigation of flow uniformity at the channel ends was performed considering a sample of 2'000 grayscale images of the two-phase flow patterns, captured with a frequency of 2'000 Hz over a time of 1 second. The standard deviations of the pixel intensity values over time were calculated, as depicted in Fig. 4.11 and displayed as a real image. Figure 4.11 contains an example of the results for the test case presented in Fig. 4.10. The horizontal black stripes are the fins with the channels in between them, where the black color corresponds to low and white to high standard deviations. Along the channel, the color changes from almost black (subcooled flow) to nearly white (transition to two-phase flow) and becomes gray at the exit, which represents a core of vapor flowing towards the outlet manifold's plenum. The fluid leaves all the channels as annular flow (vapor surrounded by a ring of liquid), which was confirmed by observing the original high quality video images.

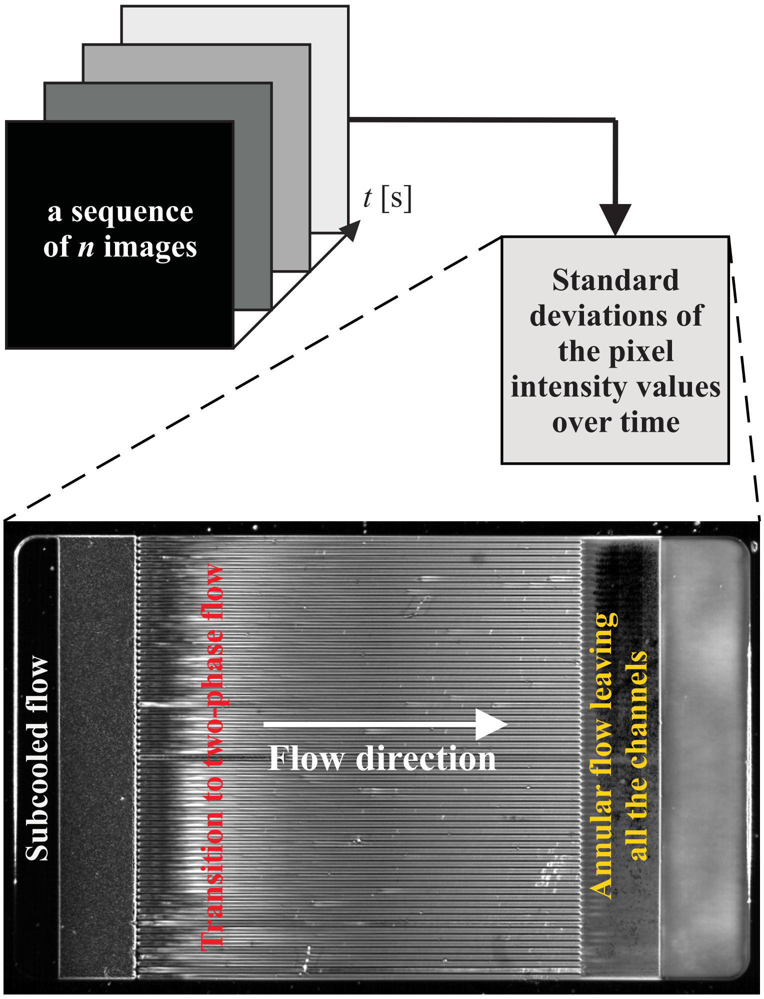
a sequence of *n* images
t [s]
Standard deviations of the pixel intensity values over time
Subcooled flow
Transition to two-phase flow
Flow direction
Annular flow leaving all the channels

Figure 4.11: Getting the standard deviations of the pixel intensity values over time and a selected example of the obtained results.

In addition to the flow uniformity, the lateral-temperature profiles at the channel ends ($z = 10\,\mathrm{mm}$) were analyzed. Their spatial derivatives for the channel mass flux of ∼2'087 $\mathrm{kg\,m^{-2}\,s^{-1}}$ and the base heat flux ranging between 23.9 and 43.1 $\mathrm{W\,cm^{-1}}$ during the two-phase flow of R236fa in the half-heated test section ($e_{in,rest} = 2$) are illustrated in Fig. 4.12(a).

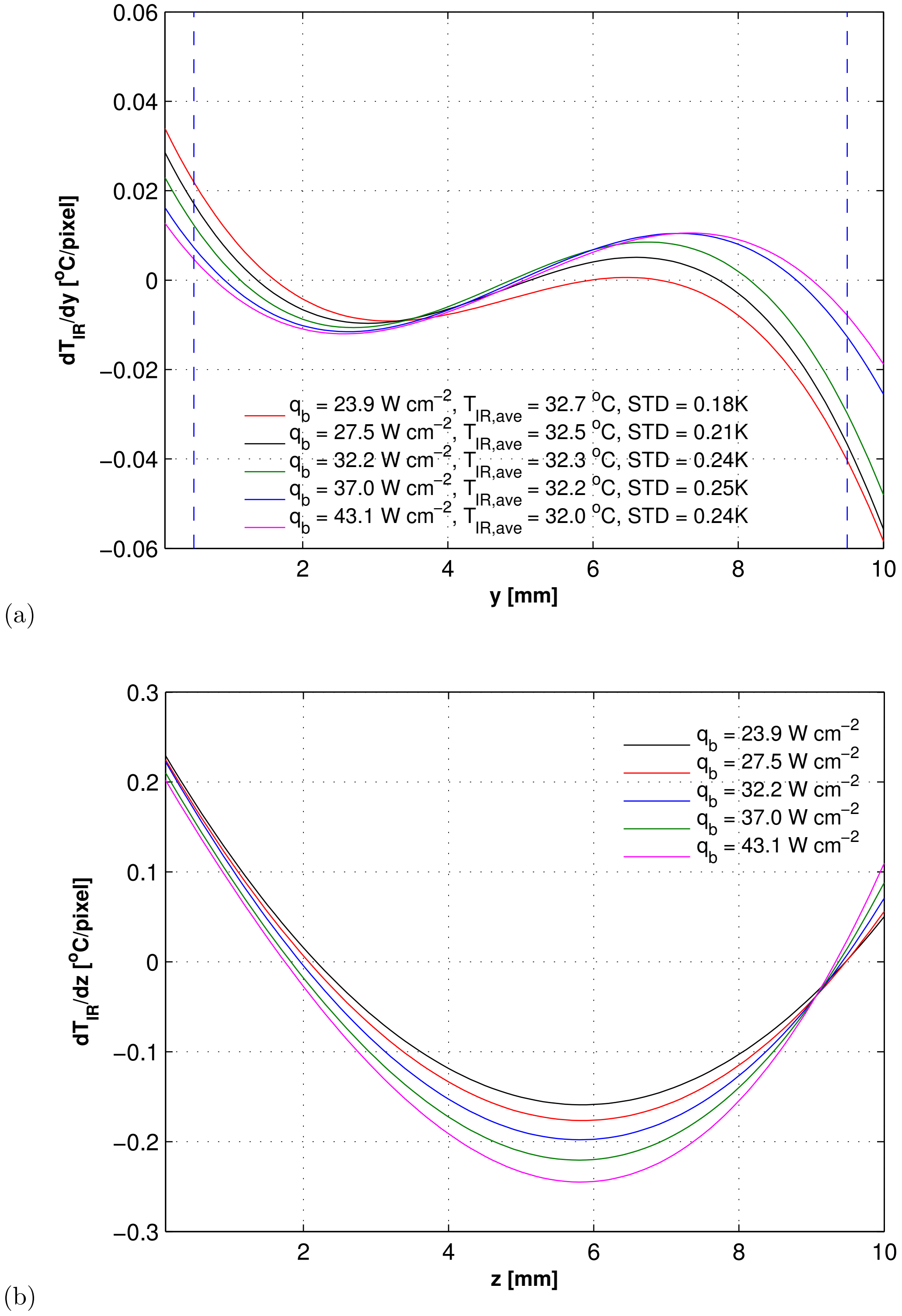

Figure 4.12: Spatial derivatives of: (a) the lateral-temperature at the channel location of $z = 10\,\mathrm{mm}$, and (b) the temperature along the centerline in the flow direction for the two-phase flow of R236fa flowing in the half-heated test section ($e_{in,rest} = 2$) for $G_{ch} = 2'087 \pm 0.5\%\,\mathrm{kg\,m^{-2}\,s^{-1}}$ and q_b ranging from 23.9 to $43.1\,\mathrm{W\,cm^{-1}}$.

Ten IR temperatures indicated by the vertical blue dashed lines (5 per each side) were excluded from the analysis because of the 5 mm-curvatures in the corners of the window for IR visualization (see Fig. 3.2(a)). Therefore, the average temperatures, $T_{IR,ave}$, and the temperature standard deviations, STD, provided in Fig. 4.12(a) were calculated based on 90 IR temperatures (removing 5 pixels from each side). The $T_{IR,ave}$ varies between 32.0 and 32.7 °C, and decreases with increasing the base heat flux, which is associated with decreasing the fluid saturation temperature in the two-phase flow region, as explained later in Fig. 4.13. For a certain q_b, the lateral temperature decreases with respect to the test section width, y, due to the heating coil connection being on the side at $y = 0$, as can be seen in Fig. 4.2, although the STDs are on an order of the accuracy of the IR camera's calibration.

The adiabatic zone at the channel ends was examined by plotting the spatial derivatives of the temperature along the centerline in the flow direction. For example, Fig. 4.12(b) demonstrates the results of such an analysis for the channel mass flux of ∼2'087 $\mathrm{kg\,m^{-2}\,s^{-1}}$ and the base heat flux ranging between 23.9 and 43.1 $\mathrm{W\,cm^{-1}}$ during the two-phase flow of R236fa in the micro-evaporator ($e_{in,rest} = 2$) powered only by the first heater. The curves follow the same trend regardless of the base heat flux imposed. Moreover, the gradients at the channel location of $z = 10$ mm are, in general, lower than 0.1 °C. Thus, the adiabatic conditions at the channel outlets were confirmed and the lateral average value of 90 IR local base temperature measurements at the longitudinal channel position of $z = 10$ mm could be assumed to be the local fluid saturation temperatures.

The inlet and the outlet restrictions pressure losses, as well as the resulting channel pressure gradients are presented in Chapter 6.

4.4.3 Base and wall heat fluxes

The total heat flux supplied to the device is defined as:

$$q_{ld} = \frac{Q_{el}}{L_h B} \tag{4.32}$$

where Q_{el} is the electrical power:

$$Q_{el} = IV \tag{4.33}$$

The definition of the base heat flux includes a ratio between the heat transferred to the working fluid and the total heat input:

$$q_b = \varphi \frac{IV}{L_h B} \tag{4.34}$$

where φ takes into account the voltage drop down the wiring between the heater and the power supply assuming the resistivity of the heater to be constant within the temperature range of the two-phase flow experiments as well as the heat losses to ambient if significant, as mentioned earlier in Section 4.1.1.

The total base heat flux splits into two, as presented in Fig. 4.8, and it is a sum of the heat transferred to the silicon substrate and to the black matt tape, used for IR temperature measurements:

$$q_b = q_{Si} + q_{tape} \tag{4.35}$$

The q_{tape} is balanced by the heat emission by radiation from the surface covered with the high-emissivity matt black tape over the surface area, q_{rad}. The heat emission by radiation, E_{rad}, is determined based on the Stefan-Boltzmann's law for a blackbody ($\varepsilon_{tape} \approx 1$ in the present temperature range) exposed to the surroundings of known temperature, T_{amb}. In Eq. (4.35), the q_{tape} is usually lower than 0.05% of the q_b, so it is postulated to be negligible.

The wall heat flux, q_w, is estimated using the fin efficiency formula for $(N-1)$ parallel rectangular fins with adiabatic tips:

$$q_w = q_{Si} \frac{N\left(W_f + W_{ch}\right) - W_f}{2\left(N-1\right)\left(H_{ch} + 0.5W_f\right)\eta + NW_{ch}} \tag{4.36}$$

where

$$\eta = \frac{\tanh\left(m\left(H_{ch} + 0.5W_f\right)\right)}{m\left(H_{ch} + 0.5W_f\right)} \tag{4.37}$$

$$m = \sqrt{\frac{2\alpha_w\left(L_{ch} + W_f\right)}{k_{Si}L_{ch}W_f}} \tag{4.38}$$

The temperature of the test section's base in the lateral direction and the temperature across the fin thickness, as explained by Incropera et al. (2007) for 1D conduction, are assumed to be uniform. In general, the fin efficiency, η, is higher than 0.95.

4.4.4 Base and footprint temperatures

The base temperature is computed based on the following equation:

$$T_b = T_{IR} + \frac{q_{tape}d_{tape}}{k_{tape}} \tag{4.39}$$

where T_{IR} is measured by means of the IR camera with an accuracy of ±0.2 °C in the temperature range of the two-phase flow experiments. The tape thermal conductivity, k_{tape}, was measured experimentally by carrying out some steady state thermal conductivity measurements for temperatures between 20 and 60 °C corresponding to the range of the two-phase flow experiments. The temperature gradient through the tape is one order of magnitude smaller than the IR temperature measurement accuracy. Therefore, the second term in Eq. (4.39) can be neglected and the temperature observed by the IR camera is assumed to be the temperature of the test section's base, T_b.

Then, assuming 1D heat conduction from the silicon base to the root of the fins, the test section's footprint temperature, T_{ft}, is expressed as follows:

$$T_{ft} = T_{IR} - \frac{q_{Si} d_{Si}}{k_{Si}} \tag{4.40}$$

The thermal conductivity of silicon, k_{Si}, was evaluated based on a curve fitting of the experimental data of Shanks et al. (1963):

$$k_{Si} = 0.0007T^2 - 0.5416T + 157.39 \tag{4.41}$$

including its change as the temperature drops across the micro-evaporator's thickness.

4.4.5 Fluid temperature and inlet subcooling

For subcooled flow, the inlet of the channel after the inlet orifice is usually in the single-phase flow region, i.e. inlet enthalpy is below that of saturated liquid or is higher but with no flashing. Instead, for the flashing two-phase flow with and without back flow operating regimes, as explained further on in Chapter 5, the two-phase flow occupies the entire length of the channel, L_{ch}.

Figure 4.13 schematically depicts the fluid temperature along a microchannel assuming linear pressure drop, where the temperature gradient from the inlet to the outlet might be positive for single-phase liquid flow or negative for two-phase flow. For the subcooled flow, the local fluid temperature is obtained based on single-phase flow energy balance using the following equation:

$$T_{fl}(z) = T_{in} + \frac{B \sum\limits_{0}^{z} q_{Si} dz}{M c_{p,l}} \tag{4.42}$$

The subcooled length is calculated as follows:

$$L_{sub} = \frac{M c_{p,l}}{q_{Si} B} \left(T_{tp,0} - T_{in}\right) \tag{4.43}$$

where the subscript $tp, 0$ announces the transition to two-phase flow and the inlet liquid sub-

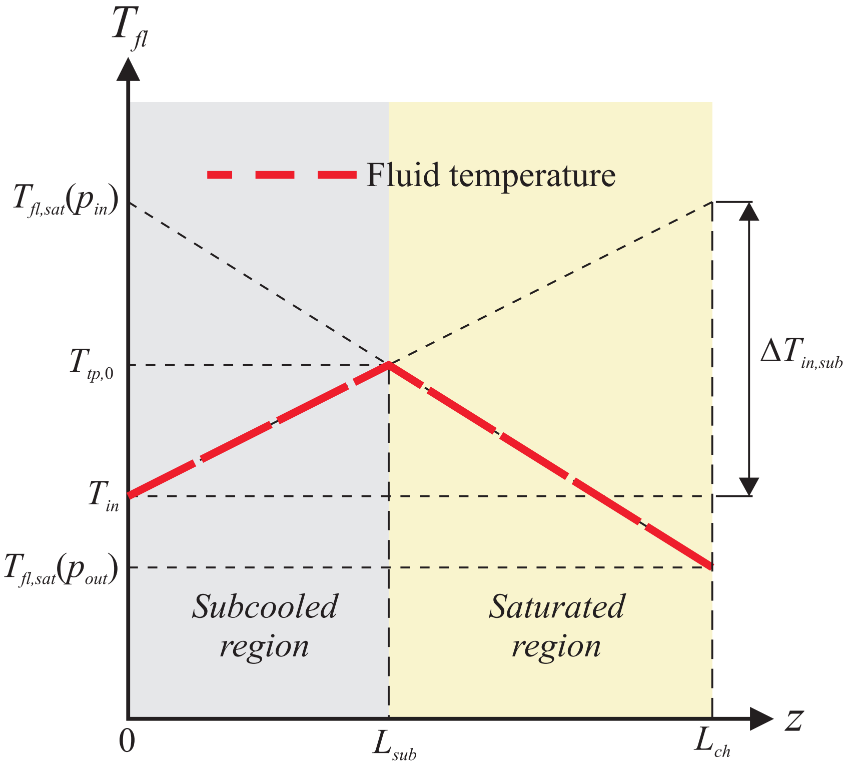
T_{fl}
Fluid temperature
$T_{fl,sat}(p_{in})$
$T_{tp,0}$
T_{in}
$T_{fl,sat}(p_{out})$
$\Delta T_{in,sub}$
Subcooled region
Saturated region
0
L_{sub}
L_{ch}
z

Figure 4.13: Fluid temperature along a microchannel, based on Lee and Garimella (2008).

cooling, $\Delta T_{in,sub}$, is estimated as:

$$\Delta T_{in,sub} = T_{fl,sat}\left(p_{in}\right) - T_{in} \tag{4.44}$$

where the fluid saturation temperature, $T_{fl,sat}$, is obtained from the vapor pressure curve at the p_{in}, and the T_{in} is an average of the temperatures measured by two thermocouples installed in the inlet manifold's plenum.

For the saturated region, the local fluid temperature along the channel, $T_{fl}(z)$, is calculated in 100 increments at the local pressure using the REFPROP 8.0 software based on the NIST Standard Reference Database 23 after subtracting the inlet restriction pressure losses, $\Delta p_{in,rest}$, from the absolute pressure at the inlet manifold's plenum.

4.4.6 Vapor quality

The mass flow rate and the net power supplied to the device are known, thus the local vapor quality is determined using an energy balance as follows:

$$x(z) = \frac{h(z) - h_l\left(p_{sat}\right)}{h_{lv}\left(p_{sat}\right)} \tag{4.45}$$

where: $h_{lv}(p_{sat})$ and $h_l(p_{sat})$ are the local latent heat of vaporization and the local liquid enthalpy, respectively, evaluated based on the local saturation pressure. The local enthalpy, $h(z)$ is given as follows:

$$h(z) = h_{in} + \frac{B \sum\limits_{0}^{z} q_{Si} dz}{M} \tag{4.46}$$

The variation of vapor quality along the microchannel length is calculated for each $dz = L_{ch}/100$.

4.4.7 Heat transfer coefficient

Assuming $\eta \approx 1$, the local wall heat transfer coefficient, $\alpha_w(z)$, is estimated using the following equation:

$$\alpha_w(z) = \frac{q_w(z)}{T_{ft}(z) - T_{fl}(z)} \tag{4.47}$$

Equations (4.36) – (4.38) and (4.47) are interdependent, and thus they are iteratively solved using a fixed-point method.

4.5 Heat conduction schemes

The present 1D heat conduction approach does not take into account heat spreading towards the colder surrounding regions that can be observed due to the variation in the local heat transfer coefficient with vapor quality along the channel, for instance, in Fig. 3.9 at the two lateral sides of the micro-evaporator. Costa-Patry (2011) noted that the lateral non-uniform heat flux distribution might change the local pressure drop and evaporation rates. Consequently, the calculated values of local wall temperatures and heat fluxes are influenced by the data reduction procedure. As indicated in Chapter 2, heat transfer calculations, taking into account axial heat conduction, viscous dissipation, conjugate heat transfer and entrance effects, are required. In order to minimize heat spreading effects, the two- (2D) and three-dimensional (3D) thermal conduction schemes of Costa-Patry (2011) are employed in the present study.

For a chosen control volume (CV), shown in Fig. 4.14, knowing the temperature and heat flux values at the test section's base, the energy balance yields:

$$Q_D + Q_L + Q_F + Q_U + Q_R + Q_B = 0 \tag{4.48}$$

where:

$$Q_D = q_D dxdydz \tag{4.49}$$

$$Q_L = k_{Si} dxdy \frac{T_L - T_{CV}}{dz} \tag{4.50}$$

$$Q_F = k_{Si} dxdz \frac{T_F - T_{CV}}{dy} \tag{4.51}$$

$$Q_R = k_{Si} dxdy \frac{T_R - T_{CV}}{dz} \tag{4.52}$$

$$Q_B = k_{Si} dxdz \frac{T_B - T_{CV}}{dy} \tag{4.53}$$

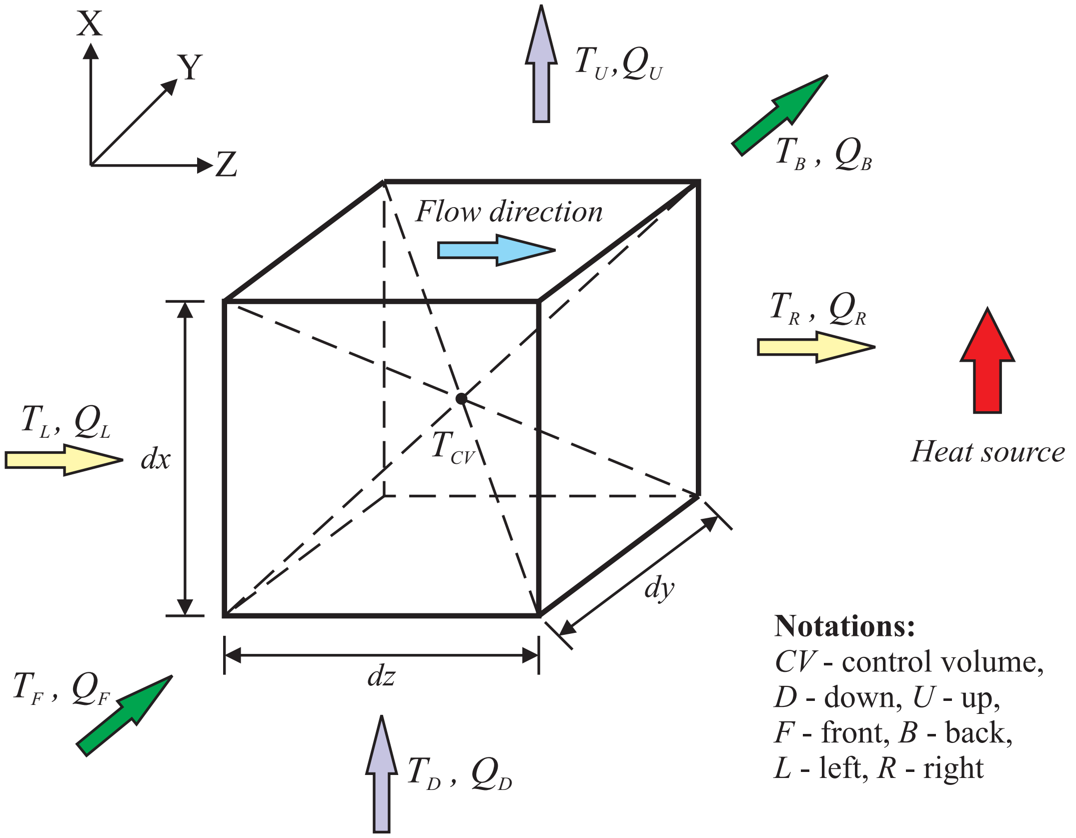
X
Y
Z
T_U, Q_U
T_B, Q_B
Flow direction
T_R, Q_R
T_L, Q_L
dx
T_{CV}
Heat source
dy
dz
T_F, Q_F
T_D, Q_D
Notations:
CV - control volume,
D - down, *U* - up,
F - front, *B* - back,
L - left, *R* - right

Figure 4.14: Control volume for heat conduction schemes.

Then, assuming the external walls of the silicon test section to be adiabatic, the various nodes are linked with each other, such that: $Q_L(n) = -Q_R(n-1)$, $Q_F(n) = -Q_B(n-1)$, and $Q_D(n) = -Q_U(n-1)$, where n is a natural number indicating the layer's number. In Eq. (4.49), q_D is the heat flux transferred to the current control volume from the one below. For the first CV, $q_D = q_b$. In the 2D heat conduction scheme, then $Q_F = Q_B = 0$.

The change of k_{Si} across the test section's thickness, with respect to the temperature drop, is included by sub-dividing the silicon substrate into several layers. Grids with a layer thickness from 70 down to $0.2\,\mu$m were examined to ensure its independence. Figure 4.15(b) and 4.15(c) demonstrate the mean relative errors (MAE) using different grids for 5 selected pixels of the IR camera's sensor array, which are shown in Fig. 4.15(a), and applying the 2D and 3D conduction schemes, respectively. The MAE, defined by Eq. (6.12), decreases with decreasing the thickness dx; in the other words – increasing the number of layers. As a result, a sandwich of 140 layers having the thickness of $2\,\mu$m, provided the MAE below 0.01%. Therefore, it was chosen for heat transfer calculations, also for 1D thermal conduction.

Each layer consists of 10'000 pixel elements, corresponding to the IR local temperature measurements. Thus, the control volumes are $100\,\mu$m-long (dz), $100\,\mu$m-wide (dy), and $2\,\mu$m-thick (dx). The energy balance is performed one step at a time and moving to the next layer up to the top of the silicon substrate. In Chapter 7, the temperature pixels influenced by the edge effects will be excluded, in effect taking a matrix of 90 x 90, as shown in Fig. 4.16. More detail regarding heat transfer data processing will be noted there.

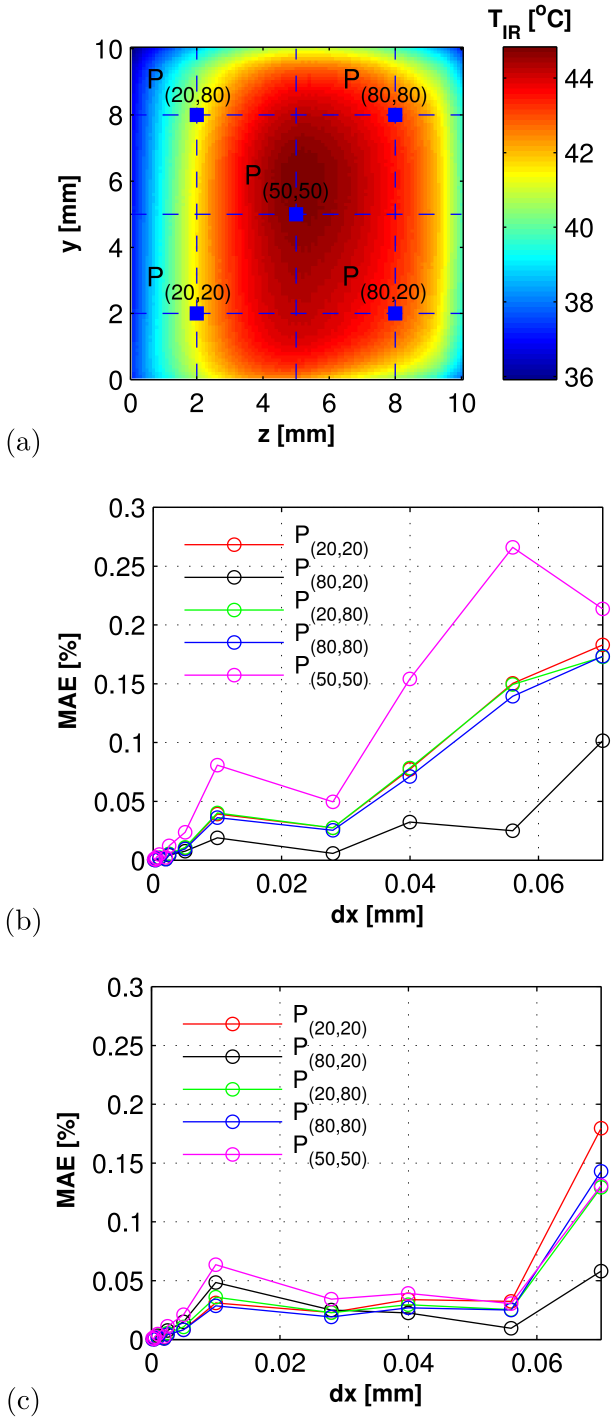

Figure 4.15: Grid independence through the thickness of the test section for (a) 5 selected pixels of the IR camera's sensor array applying: (b) 2D, and (c) 3D heat conduction schemes under the two-phase flow of R236fa in the micro-evaporator with the inlet restrictions of $e_{in,rest} = 4$, $G_{ch} = 2'099\,\mathrm{kg\,m^{-2}\,s^{-1}}$ and $q_b = 16.9\,\mathrm{W\,cm^{-1}}$.

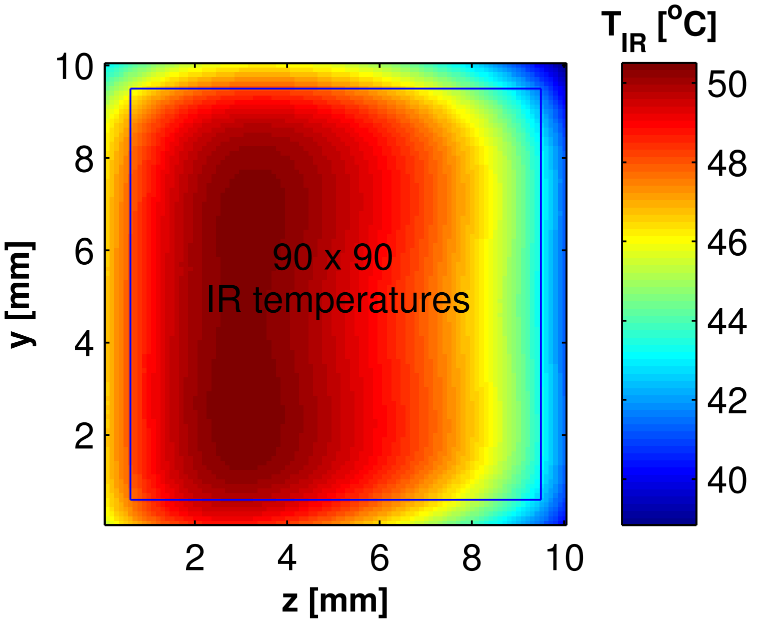

Figure 4.16: IR temperatures selected for the heat transfer data analysis. Two-phase flow IR temperature map for R236fa flowing in the test section with the inlet restrictions of $e_{in,rest} = 4$ for $G_{ch} = 1903\,\mathrm{kg\,m^{-2}\,s^{-1}}$ and $q_b = 43.4\,\mathrm{W\,m^{-2}}$. The blue square indicates an array of IR temperatures considered in heat transfer analysis.

The following convention in notations will be used lather in the thesis:

- 1D – one-dimensional heat conduction (axis X),
- 2D – two-dimensional heat conduction (axes XZ), and
- 3D – three-dimensional heat conduction (axes XYZ).

Chapter 5

Two-phase flow and temperature visualizations

Visual investigation into the two-phase flow dynamics in the multi-microchannels was carried out by means of a high-speed digital camera with the spatial resolution of 1’024 x 768 pixels at 2’000 fps over a 4 second period with a field of view that includes the channels as well as the inlet and outlet plenums of the test section and their slits. As illustrated earlier in Fig. 3.9, the single-phase liquid in the channel near the entrance and the annular flow downstream in the channel are represented by the dark areas, where the two-phase flow mixture (bubbly and slug flows) appears brighter with a very shiny liquid-vapor interface. As mentioned previously, the fluid flows from left to right in all the presented images.

The temperature visualizations were conducted by means of the high-speed infra-red (IR) camera with the spatial resolution of 320 x 240 pixels at 60 fps taken over a time of 1 minute. Due to technical issues, an array of 100 x 100 IR temperature pixels measurements covered the 1 cm x 1 cm heated area of the micro-evaporator. Thus, 600’000 individual temperatures are acquired per second (3.6 million for the 1 minute). The temperature data are obtained through the in-situ *pixel by pixel* calibration of the IR camera described in Chapter 3 that provides a tenfold accuracy improvement compared to the manufacture’s value in the temperature range of two-phase flow experiments.

5.1 Two-phase flow operational maps

In the current research, two-phase flow operational maps (Figs. 5.1 – 5.6) for 3 refrigerants, namely R245fa, R236fa, and R1234ze(E), flowing within the 4 multi-microchannel evaporators ($e_{in,rest} = 1$, 1.33, 2, and 4) were obtained. The points represent the tested operating conditions, such as the channel mass flux and the base heat flux, respectively G_{ch} and q_b being calculated from Eqs. (4.9) and (4.34). Such operational maps are very useful for defining the most advantageous operating conditions for stable flows, e.g. one can set a minimum operational mass flux at which flow is always going to be stable.

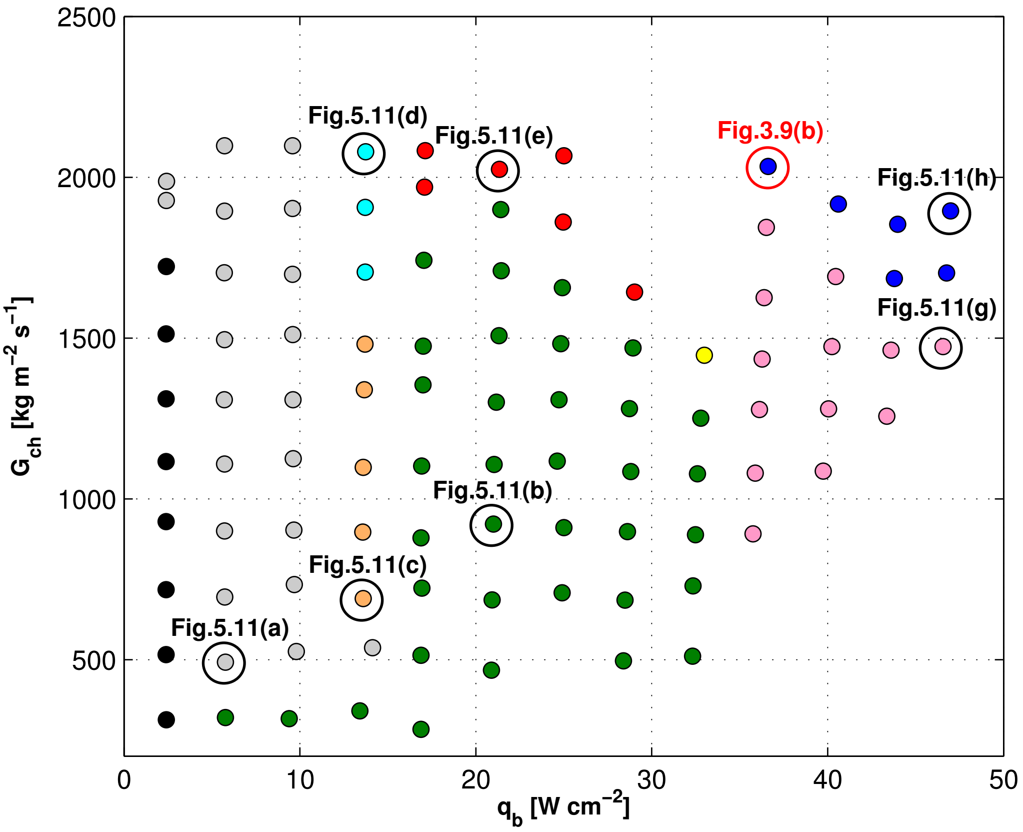

Figure 5.1: Two-phase flow operational map for R245fa in the micro-evaporator with the 50 μm-wide, 100 μm-deep, and 100 μm-long inlet restrictions ($e_{in,rest} = 2$), where: ⚫ - single-phase flow, ⚪ - single-phase flow in the test section with the vapor bubbles at the manifold's outlet plenum, 🟢 - single-phase flow followed by two-phase flow with back flow, 🟠 - unstable two-phase flow with back flow developing into jet flow, 🔵 - jet flow, 🔴 - single-phase flow followed by two-phase flow without back flow, 🟡 - two-phase flow with back flow triggered by bubbles formed in the flow loop before the test section, 🟣 - flashing two-phase flow with back flow, and 🔵 - flashing two-phase flow without back flow (the most desirable operating condition). The black circles indicate representative images of the operating regimes (shown later in Fig. 5.11). The data point marked by the red circle corresponds to the flow pattern shown earlier in Fig. 3.9(b).

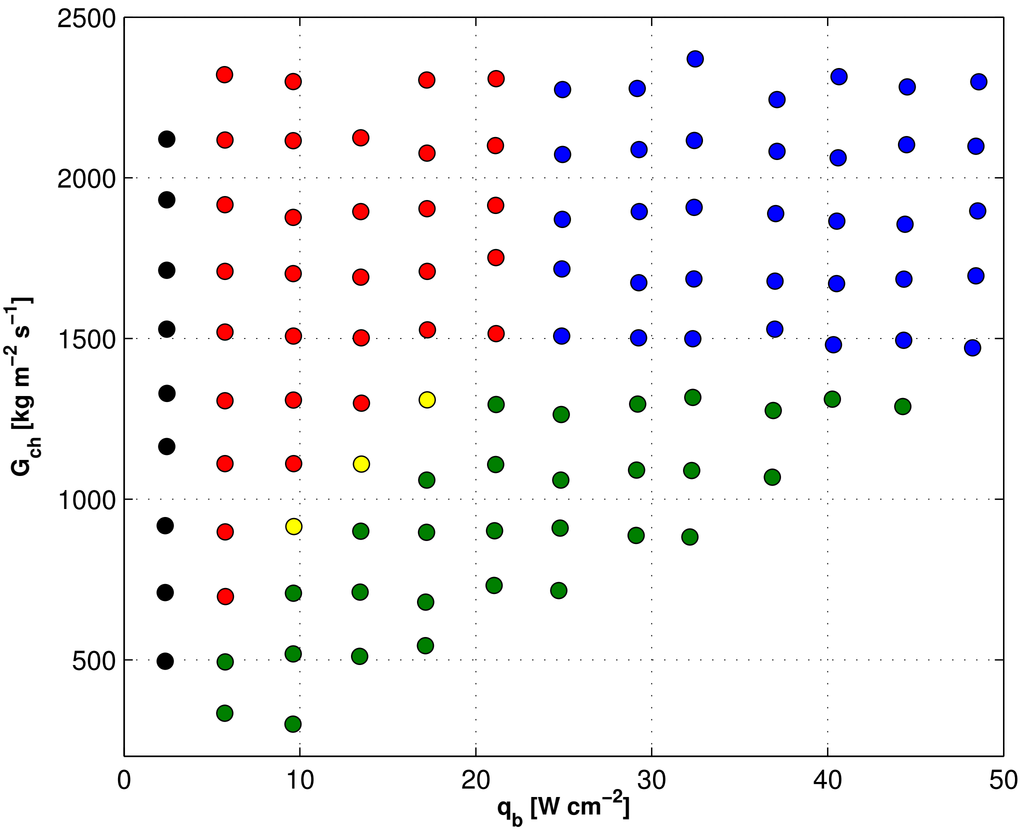

Figure 5.2: Two-phase flow operational map for R236fa in the micro-evaporator with the 50 μm-wide, 100 μm-deep, and 100 μm-long inlet restrictions ($e_{in,rest} = 2$), where: ● - single-phase flow, 🟢 - single-phase flow followed by two-phase flow with back flow, 🔴 - single-phase flow followed by two-phase flow without back flow, 🟡 - two-phase flow with back flow triggered by bubbles formed in the flow loop before the test section, and 🔵 - flashing two-phase flow without back flow (the most desirable).

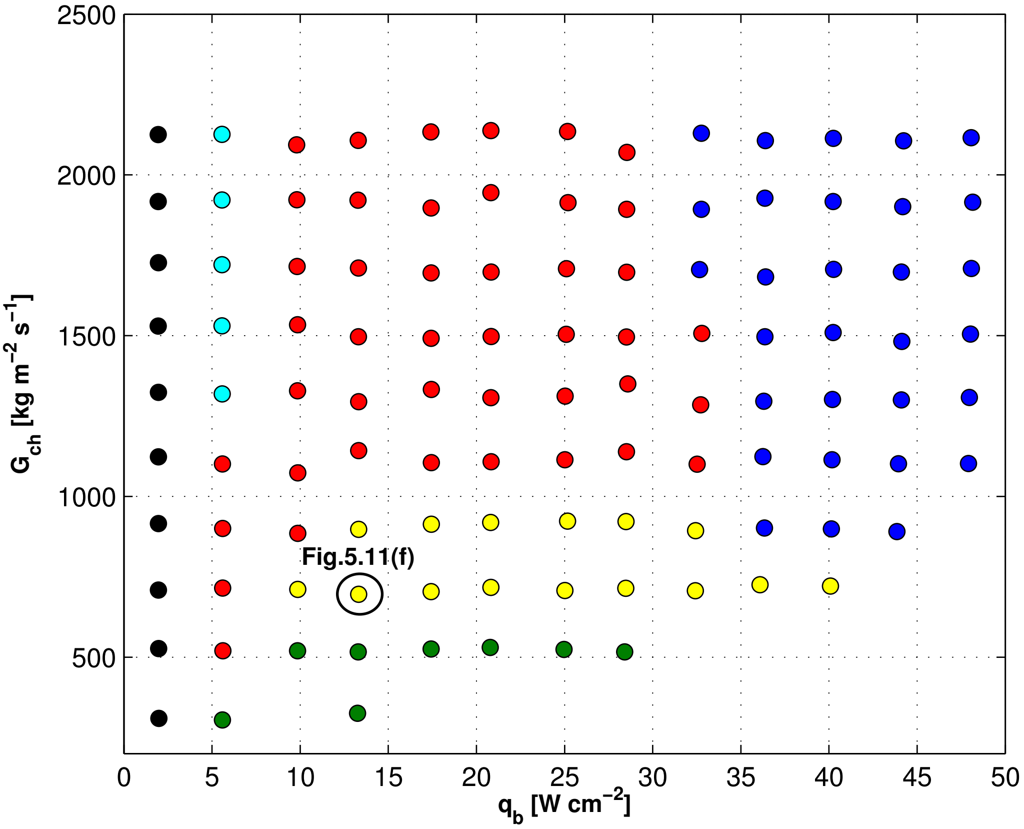

Figure 5.3: Two-phase flow operational map for R1234ze(E) in the micro-evaporator with the 50 μm-wide, 100 μm-deep, and 100 μm-long inlet restrictions ($e_{in,rest} = 2$), where: ● - single-phase flow, ● - single-phase flow followed by two-phase flow with back flow, ● - jet flow, ● - single-phase flow followed by two-phase flow without back flow, ● - two-phase flow with back flow triggered by bubbles formed in the flow loop before the test section, and ● - flashing two-phase flow without back flow (the most desirable). The black circles indicate representative images of the operating regimes (see later in Fig. 5.11).

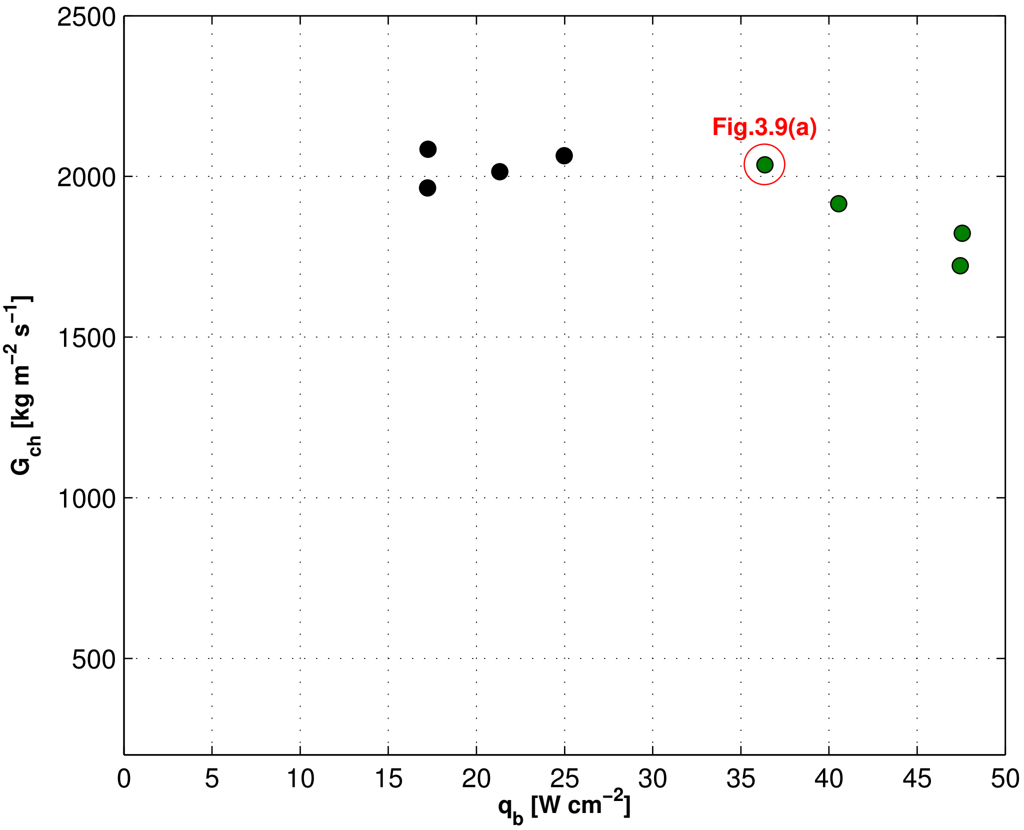

Figure 5.4: Two-phase flow operational map for R245fa in the micro-evaporator without any inlet restrictions ($e_{in,rest} = 1$), where: ● - single-phase flow, and ● - single-phase flow followed by two-phase flow with back flow. This two-phase flow operational map is based on a few selected data points before the test section burned out. The data point marked by the red circle corresponds to the flow pattern shown in Fig. 3.9(a).

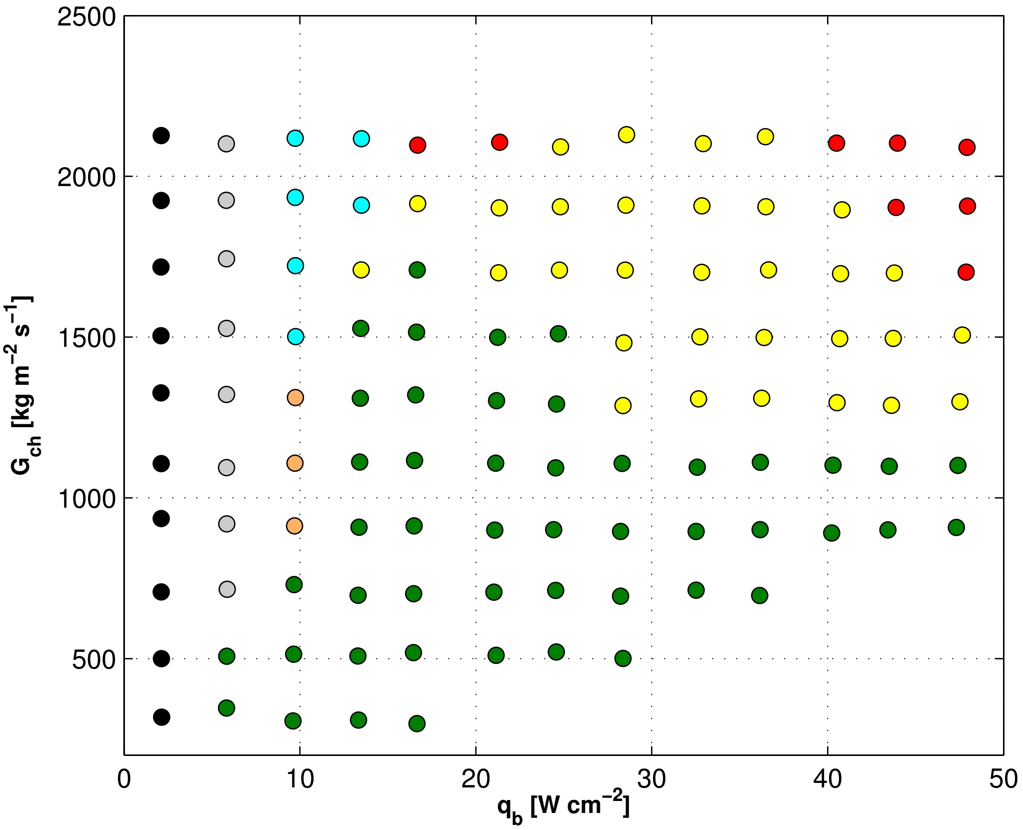

Figure 5.5: Two-phase flow operational map for R236fa in the micro-evaporator with the 75 μm-wide, 100 μm-deep, and 100 μm-long inlet restrictions ($e_{in,rest} = 1.33$), where: ⚫ - single-phase flow, ⚪ - single-phase flow in the test section with the vapor bubbles at the manifold's outlet plenum operating regime, 🟢 - single-phase flow followed by two-phase flow with back flow, 🟠 - unstable two-phase flow with back flow developing into jet flow, 🔵 - jet flow, 🔴 - single-phase flow followed by two-phase flow without back flow, and 🟡 - two-phase flow with back flow triggered by bubbles formed in the flow loop before the test section. The most desirable flow was not observed with this orifice size.

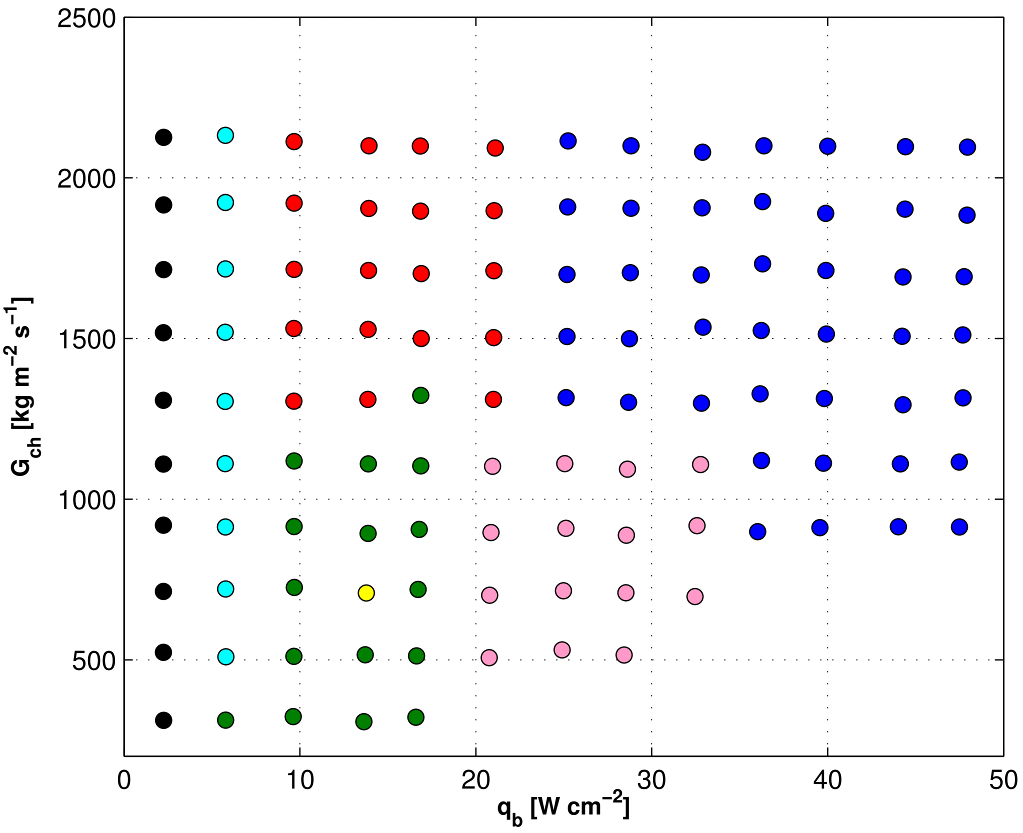

Figure 5.6: Two-phase flow operational map for R236fa in the micro-evaporator with the 25 μm-wide, 100 μm-deep, and 100 μm-long inlet restrictions ($e_{in,rest} = 4$), where: ● - single-phase flow, ● - single-phase flow followed by two-phase flow with back flow, ● - jet flow, ● - single-phase flow followed by two-phase flow without back flow, ● - two-phase flow with back flow triggered by bubbles formed in the flow loop before the test section, ● - flashing two-phase flow with back flow, and ● - flashing two-phase flow without back flow (the most desirable).

Some of these operational maps were obtained based on the results of Szczukiewicz et al. (2012a,b), who reported on the two-phase flow of R245fa, R236fa and R1234ze(E) in the micro-evaporator with the 50 μm-wide, 100 μm-deep, and 100 μm-long micro-orifices ($e_{in,rest} = 2$). The authors distinguished 8 different operating regimes: (i) single-phase flow in the test section with the vapor bubbles at the manifold's outlet plenum, (ii) single-phase flow followed by two-phase flow with back flow, (iii) unstable two-phase flow with back flow developing into jet flow, (iv) jet flow (two-phase flow is initiated only in few channels; vapor phase is pushed out of the channel creating a jet), (v) single-phase flow followed by two-phase flow without back flow (desirable operating regime), (vi) two-phase flow with back flow triggered by bubbles formed in the flow loop before the test section, (vii) flashing two-phase flow with back flow, and (viii) flashing two-phase flow without back flow (most desirable operating regime).

Their data were used to developed the two-phase flow operational maps shown in Figs. 5.1 – 5.3, where the following colors represent:
⚫ - single-phase flow,
⚪ - single-phase flow in the test section with the vapor bubbles at the manifold's outlet plenum (i),
🟢 - single-phase flow followed by two-phase flow with back flow (ii),
🟠 - unstable two-phase flow with back flow developing into jet flow (iii),
🔵 - jet flow (iv),
🔴 - single-phase flow followed by two-phase flow without back flow (v),
🟡 - two-phase flow with back flow triggered by bubbles formed in the flow loop before the test section (vi),
🟣 - flashing two-phase flow with back flow (vii), and
🔵 - flashing two-phase flow without back flow (viii).

The black circles in Figs. 5.1 and 5.3 indicate the representatives of the above-mentioned operating regimes illustrated later in Fig. 5.11 and described in the following subsection. Table 5.1 provides more details on each of those data points.

Moreover, the results for the other micro-evaporators ($e_{in,rest} = 1$, 1.33 and 4) are added here in order to provide a comprehensive view on the two-phase multi-microchannel phenomena (Figs. 5.4 – 5.6). The exact transition parameters between these states are not known (they are in between test conditions), and thus they are not indicated on the maps. The notations from (i) to (viii) will be used later on to refer to particular operating regimes. As mentioned above, the micro-evaporator without any inlet restrictions failed before its tests were successfully accomplished. Therefore, in Fig. 5.4, there are only 8 points on its map. This two-phase flow operational map is based on the selected data points. In some conditions in Fig. 5.6, vapor bubbles could be flashed at the channel inlet, as indicated by a red circle in Fig. 5.7(a). However, when comparing Fig. 5.7(b) to the temperature patterns in Fig. 5.16(g) and 5.16(h), the temperature trends are different (Section 5.2). Therefore, these experimental points could not be categorized as flashing two-phase flow (neither operating regime (vii) nor (viii)).

Table 5.1: Representative images of the two-phase flow operating regimes.

Operating regime	Fluid	$e_{in,rest}$	G_{ch}	q_b	Two-phase flow operating map	Two-phase flow pattern	IR temperature map
		-	$\mathrm{kg\,m^{-2}\,s^{-1}}$	$\mathrm{W\,cm^{-2}}$			
single-phase flow in the test section with the vapor bubbles at the manifold's outlet plenum (i)	R245fa	2	492	5.8	Fig. 5.1	Fig. 5.11(a)	Fig. 5.16(a)
single-phase flow followed by two-phase flow with back flow (ii)	R245fa	2	922	21.0	Fig. 5.1	Fig. 5.11(b)	Fig. 5.16(b)
unstable two-phase flow with back flow developing into jet flow (iii)	R245fa	2	690	13.9	Fig. 5.1	Fig. 5.11(c)	Fig. 5.16(c)
jet flow (iv)	R245fa	2	2'079	13.7	Fig. 5.1	Fig. 5.11(d)	Fig. 5.16(d)
single-phase flow followed by two-phase flow without back flow (v)	R245fa	2	2'025	21.4	Fig. 5.1	Fig. 5.11(e)	Fig. 5.16(e)
two-phase flow with back flow triggered by bubbles formed in the flow loop before the test section (vi)	R1234ze(E)	2	695	13.3	Fig. 5.3	Fig. 5.11(f)	Fig. 5.16(f)
flashing two-phase flow with back flow (vii)	R245fa	2	1'473	46.5	Fig. 5.1	Fig. 5.11(g)	Fig. 5.16(g)
flashing two-phase flow without back flow (viii)	R245fa	2	1'895	47.0	Fig. 5.1	Fig. 5.11(h)	Fig. 5.16(h)

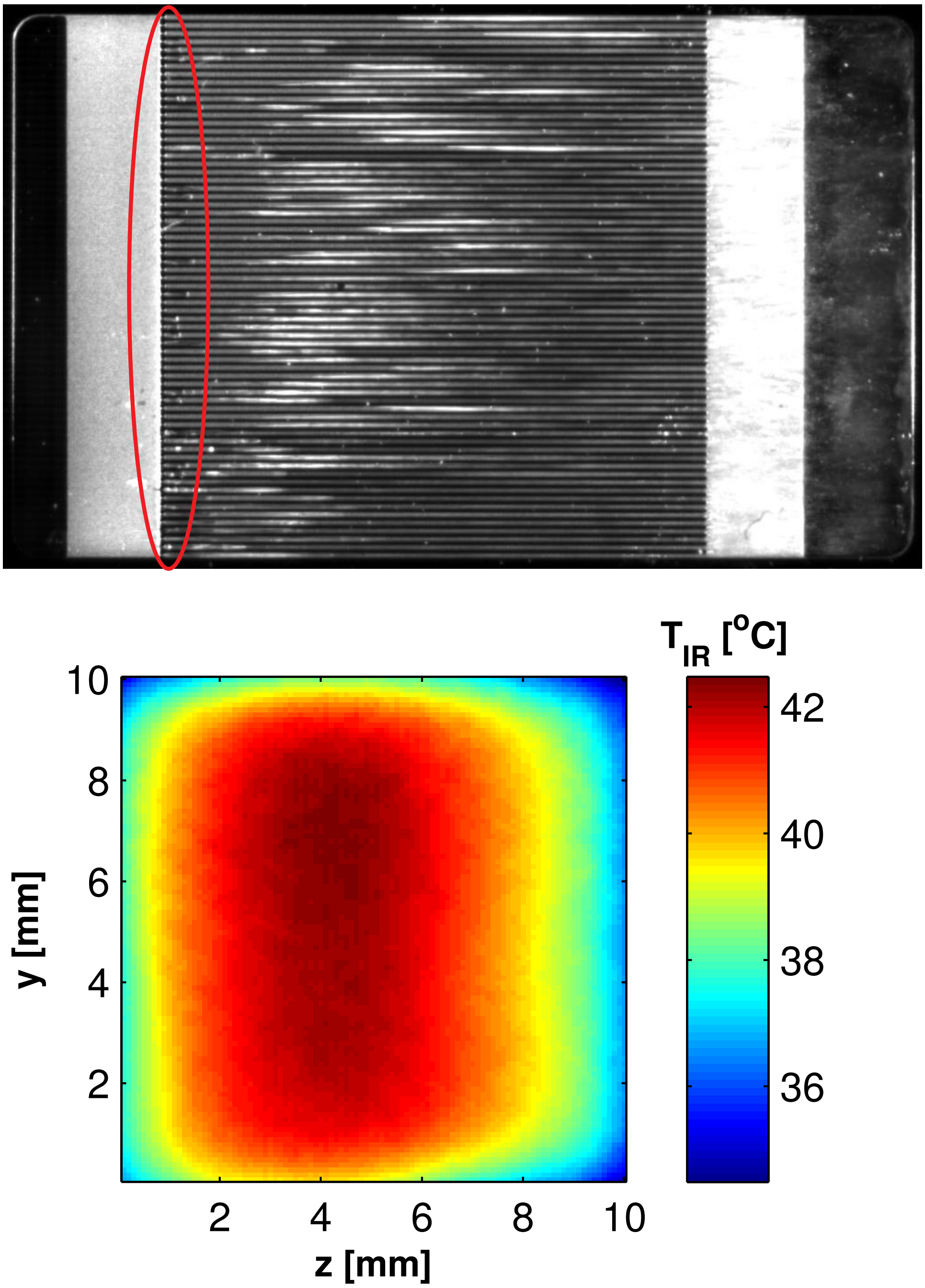

(a)

(b)

Figure 5.7: Some vapor bubbles flashed at the channel inlet for R236fa flowing in $e_{in,rest} = 4$, $G_{ch} = 896\,\mathrm{kg\,m^{-2}\,s^{-1}}$, $q_b = 20.7\,\mathrm{W\,cm^{-2}}$: (a) snapshot from the high-speed video of the two-phase flow, and (b) corresponding thermal map.

The following observations have been made:

- **`R245fa flowing within the 2 test sections` ($e_{in,rest} = 1$ `and 2`)**

  Figures 5.1 and 5.4 show the two-phase flow operational maps for R245fa flowing within the 2 test sections: one without any inlet restrictions and the second one with the inlet micro-orifices of the expansion ratio of $e_{in,rest} = 2$. As can be seen in Fig. 5.8, the boiling starts at a lower heat flux when using orifices. Furthermore, the (viii) operating regime was not observed in the test section without any inlet restriction.

- **`R236fa flowing within the 3 test sections` ($e_{in,rest} = 1.33$, `2, and 4`)**

  As shown in Fig. 5.5 in the range of the tested experimental conditions, neither (vii) nor (viii) operating regimes were observed for R236fa flowing within the test section with the inlet restrictions of the expansion ratio of $e_{in,rest} = 1.33$. These inlet restrictions do not provide enough pressure drop to generate some flashed bubbles at the beginning of the channels. For $e_{in,rest} = 2$ and 4, the zones where the operating regime (viii) was observed correspond to each other relatively well (Fig. 5.9). For $e_{in,rest} = 2$, this operating regime is observed above the channel mass fluxes of $\sim 1'500\,\mathrm{kg\,m^{-2}\,s^{-1}}$ and base heat fluxes higher than $\sim 24\,\mathrm{W\,cm^{-2}}$ (Fig. 5.2), whereas for $e_{in,rest} = 4$, the transition line moves to lower values of the mass flux (Fig. 5.6).

- **$e_{in,rest} = 2$ `and the 3 fluids: R245fa, R236fa, and R1234ze(E)`**

  For R236fa, the (viii) operating regime was observed for mass fluxes higher than $\sim 1'500\,\mathrm{kg\,m^{-2}\,s^{-1}}$ and base heat fluxes higher than $\sim 24\,\mathrm{W\,cm^{-2}}$, as depicted in Fig. 5.2. For R245fa, there were only 6 data points recorded that showed this operating regime (Fig. 5.1), whereas for R1234ze(E), the two-phase flow was stable for the mass fluxes higher than $\sim 900\,\mathrm{kg\,m^{-2}\,s^{-1}}$ and the base heat fluxes higher than $\sim 32\,\mathrm{W\,cm^{-2}}$ (Fig. 5.3). As presented in Fig. 5.10, the transition lines between particular operating regimes are fluid-dependent. The flow of R236fa was stable over a wider range of parameters and the transitions in between the operating regimes were more predictable, when comparing to R245fa and R1234ze(E).

As noted above, flashing two-phase flow without back flow is the most desirable operational condition. The second most favorable condition is the flashing two-phase flow with back flow along with the single-phase flow followed by two-phase flow without back flow.

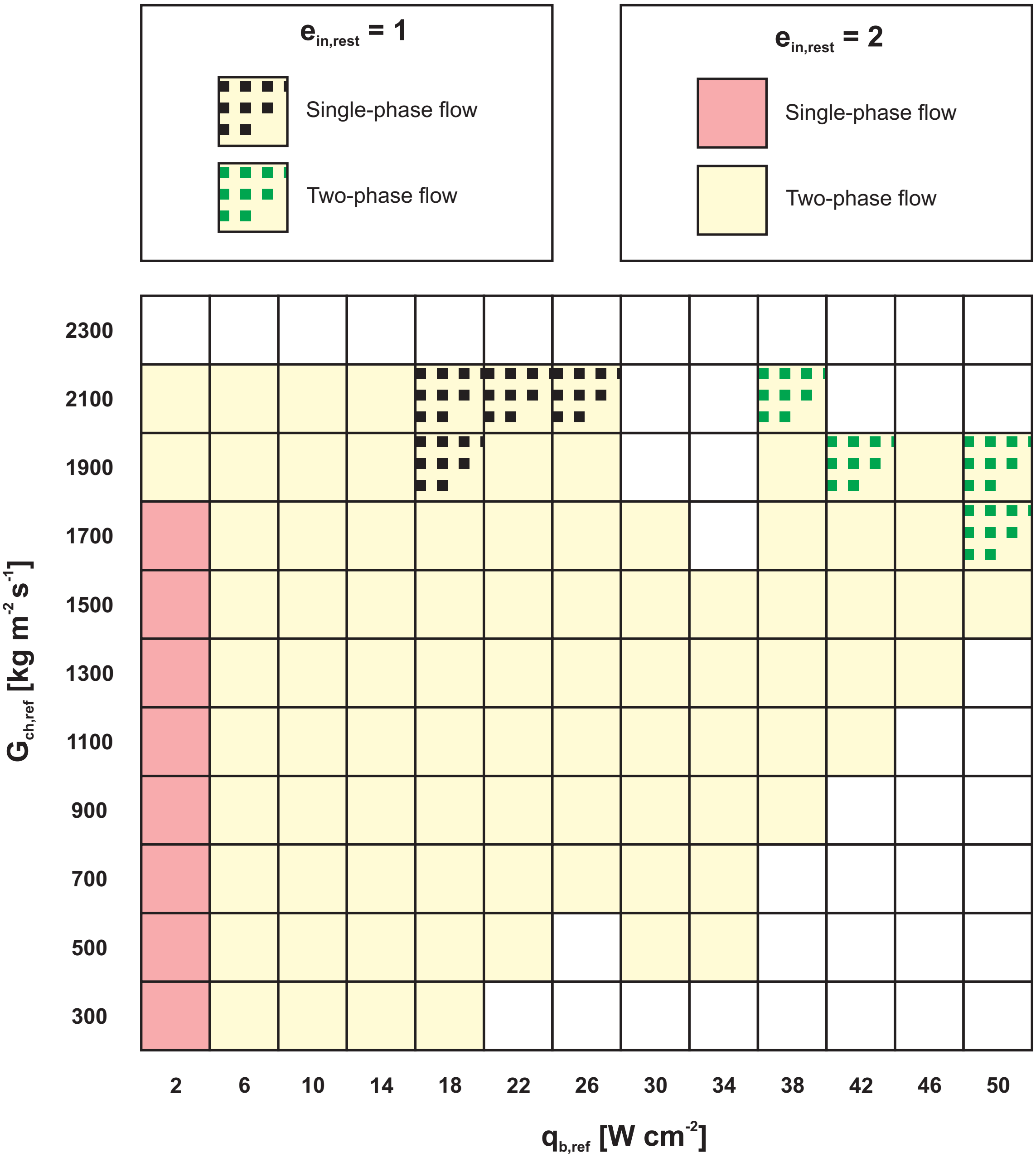

Figure 5.8: Simplified experimental test matrix for R245fa flowing within the test section without any inlet restrictions ($e_{in,rest} = 1$), and with the 50 μm-wide, 100 μm-deep, and 100 μm-long micro-orifices ($e_{in,rest} = 2$), where $G_{ch,ref}$ and $q_{b,ref}$ are the targeted channel mass flux and base heat flux, respectively. The white squares indicate cases that have not been tested.

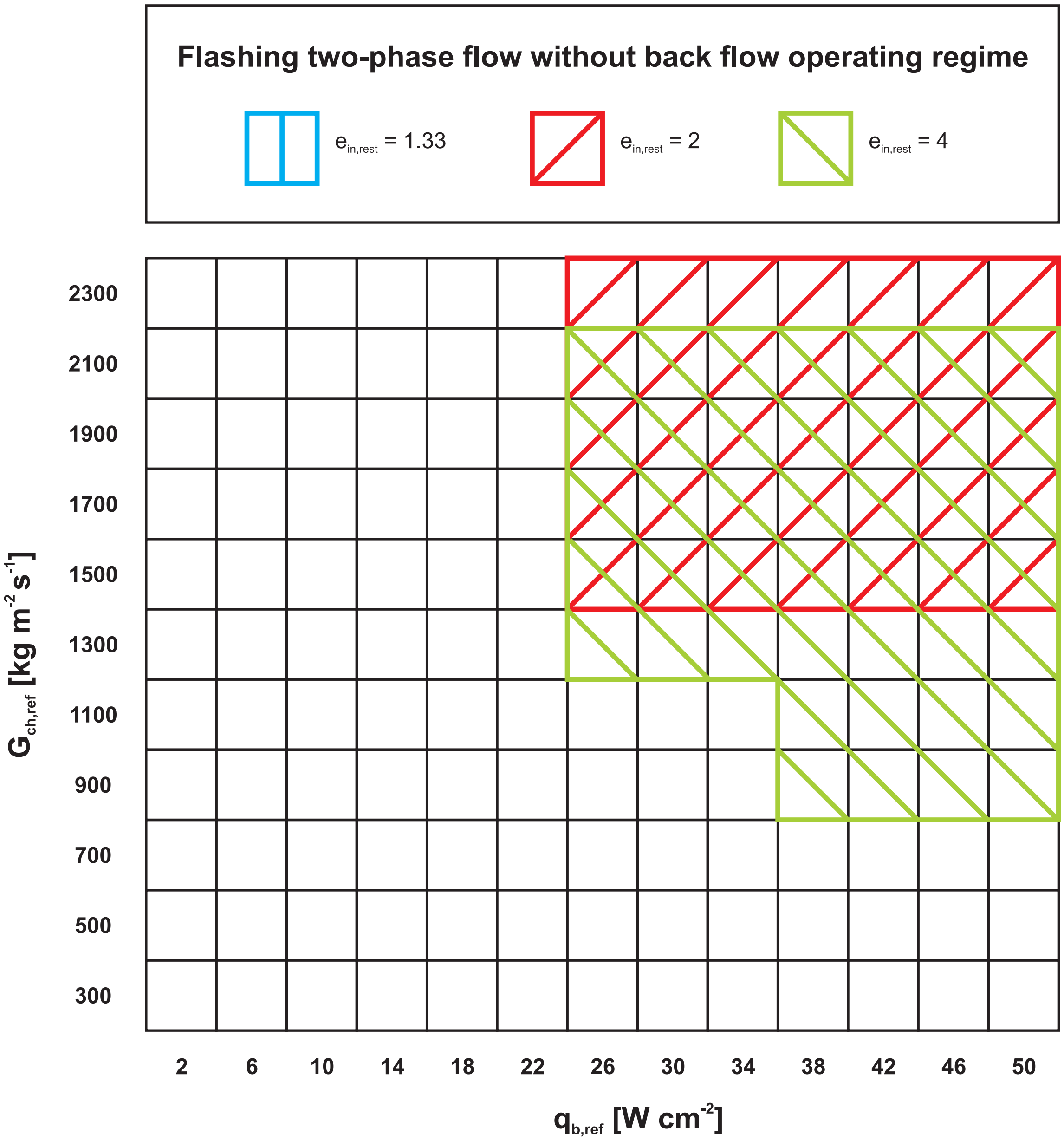

Figure 5.9: Simplified experimental test matrix for R236fa flowing within the 3 test sections ($e_{in,rest} = 1.33$, 2, and 4), where $G_{ch,ref}$ and $q_{b,ref}$ are the targeted channel mass flux and base heat flux, respectively. The flashing two-phase flow without back flow operating regime was not observed in the test section with the inlet restriction of the expansion ratio of $e_{in,rest} = 1.33$.

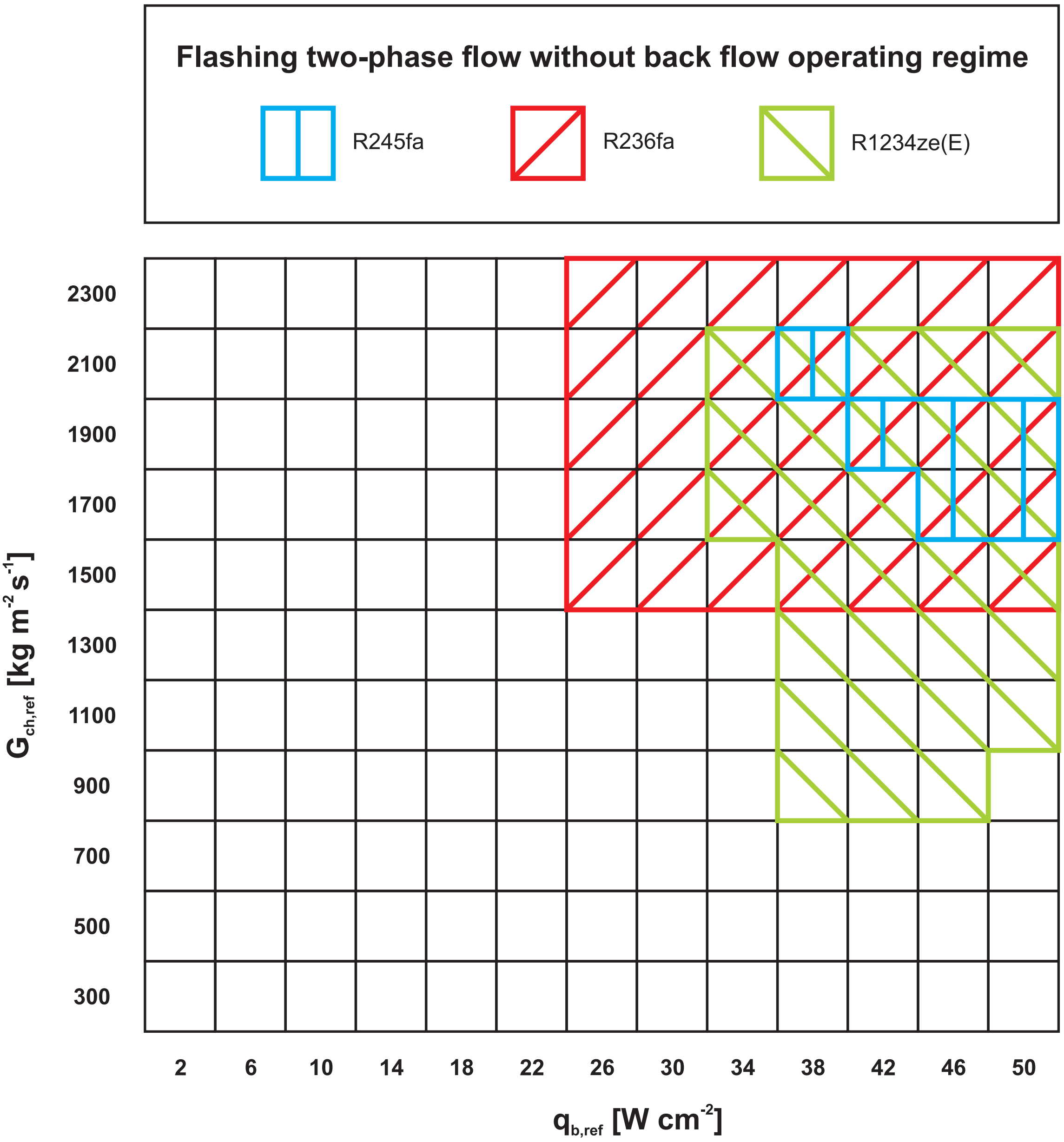

Figure 5.10: Simplified experimental test matrix for $e_{in,rest} = 2$ and the 3 fluids: R245fa, R236fa, R1234ze(E), where $G_{ch,ref}$ and $q_{b,ref}$ are the targeted channel mass flux and base heat flux, respectively.

5.2 Two-phase flow operating regimes

The flow remains in the single-phase flow regime in the micro-evaporator for the lowest base heat flux. In some conditions, bubbles are observed at the manifold's outlet plenum, whilst within the microchannels the flow stays in the single-phase regime, as seen in Fig. 5.11(a). The transition to two-phase flow in the test section is a very dynamic process and is highly unstable right after this occurs. The vapor bubbles come back to the inlet manifold and test section plenums. Therefore, the temporal (Fig. 5.12) and spatial (Figs. 5.11(b) and 5.11(c)) non-uniformity of the flow inside the channels is observed. Moreover, in Figs. 5.11(b), 5.11(c) and 5.11(g), the vapor back flow can be seen. For the jet flow operating regime (iii), which is an alternative repeatable in time, the flow transition from two-phase flow to jet flow is illustrated in Fig. 5.11(d). In case of the operating regime (iv), the two-phase flow is initiated only in a few channels and the vapor phase is pushed out of the channels creating liquid jets. The amount of vapor coming back to the inlet manifold's plenum decreases when increasing the mass flow rate while the heat flux is kept constant. The reverse flow from the boiling incipience is then suppressed by the inlet restrictions. However, the transition to two-phase flow does not happen at the same longitudinal positions in all the channels, as shown in Fig. 5.11(e). The flow in the upper channels is still single-phase, while two-phase flow has already appeared in the rest of the channels. The reason for this is the heat spreading into the copper manifold housing the test section, which consequently reduces the heat flux to the flow. Such cases, when the flow is not well distributed among the channels, are difficult to interpret since the flow behaviour is different in respective channels.

As the heat flux is further increased, the operating regimes (vii) and (viii) are obtained, as shown in Figs. 5.11(g) and 5.11(h). The flashing two-phase flow without back flow (viii) operating regime is the most desired operating regime for two-phase flow boiling in multi-microchannels. The two-phase flow is initiated from the beginning of the channel directly from flashed vapor bubbles. The bubble flow develops along the channel into slug and annular flows. Due to the flashing effect, the boiling starts at a lower value of heat flux, and thus the wall-temperature distribution becomes more uniform and the wall-temperature overshoot for the onset of boiling is circumvented (Park et al., 2009).

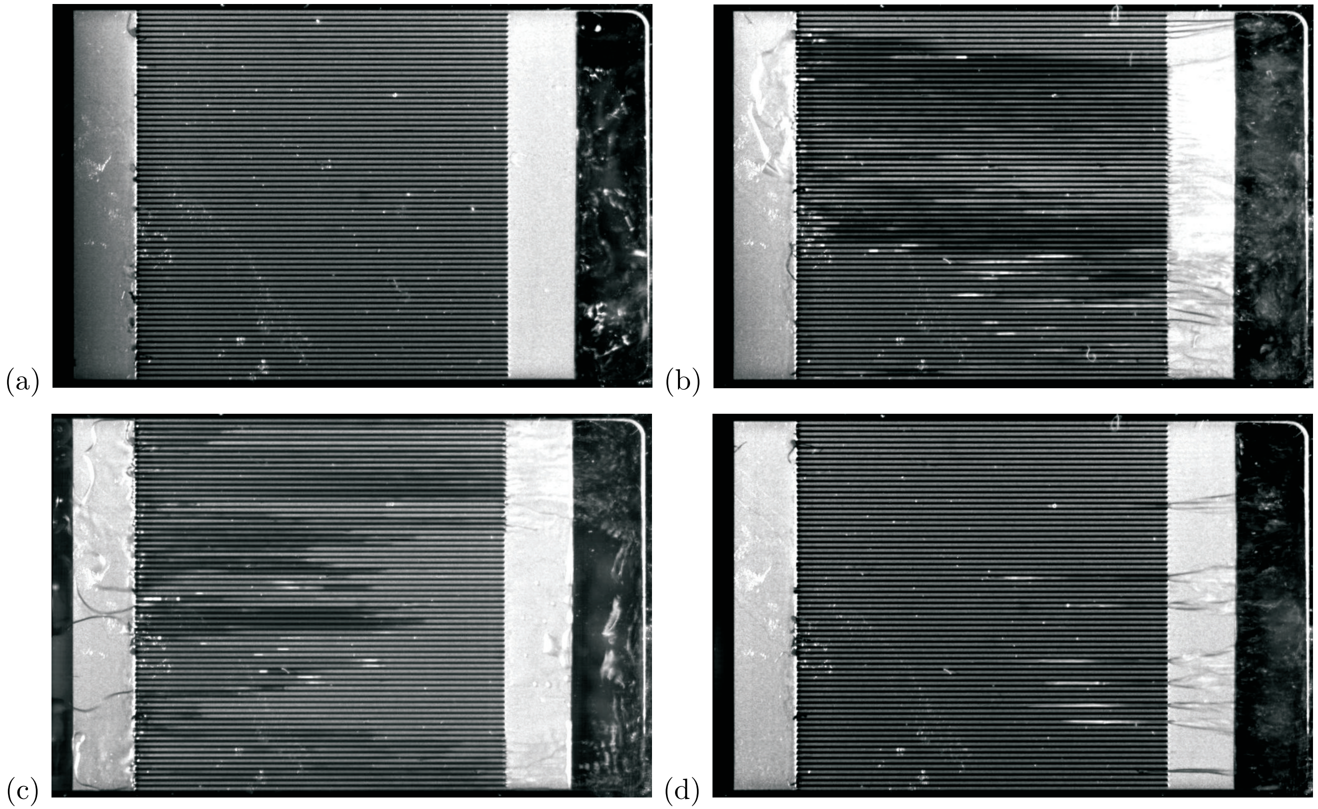

Figure 5.11: Two-phase flow operating regimes observed in the test section with the 50 μm-wide, 100 μm-deep, and 100 μm-long inlet restrictions ($e_{in,rest} = 2$): (a) single-phase flow in the test section with the vapor bubbles at the manifold's outlet plenum, (b) single-phase flow followed by two-phase flow with back flow, (c) unstable two-phase flow with back flow developing into jet flow, (d) jet flow, (e) single-phase flow followed by two-phase flow without back flow, (f) two-phase flow with back flow triggered by bubbles formed in the flow loop before the test section, (g) flashing two-phase flow with back flow, and (h) flashing two-phase flow without back flow. More details about the experimental conditions of each operating regime are given in Table 5.1. The figure continues over pp. 82 – 83.

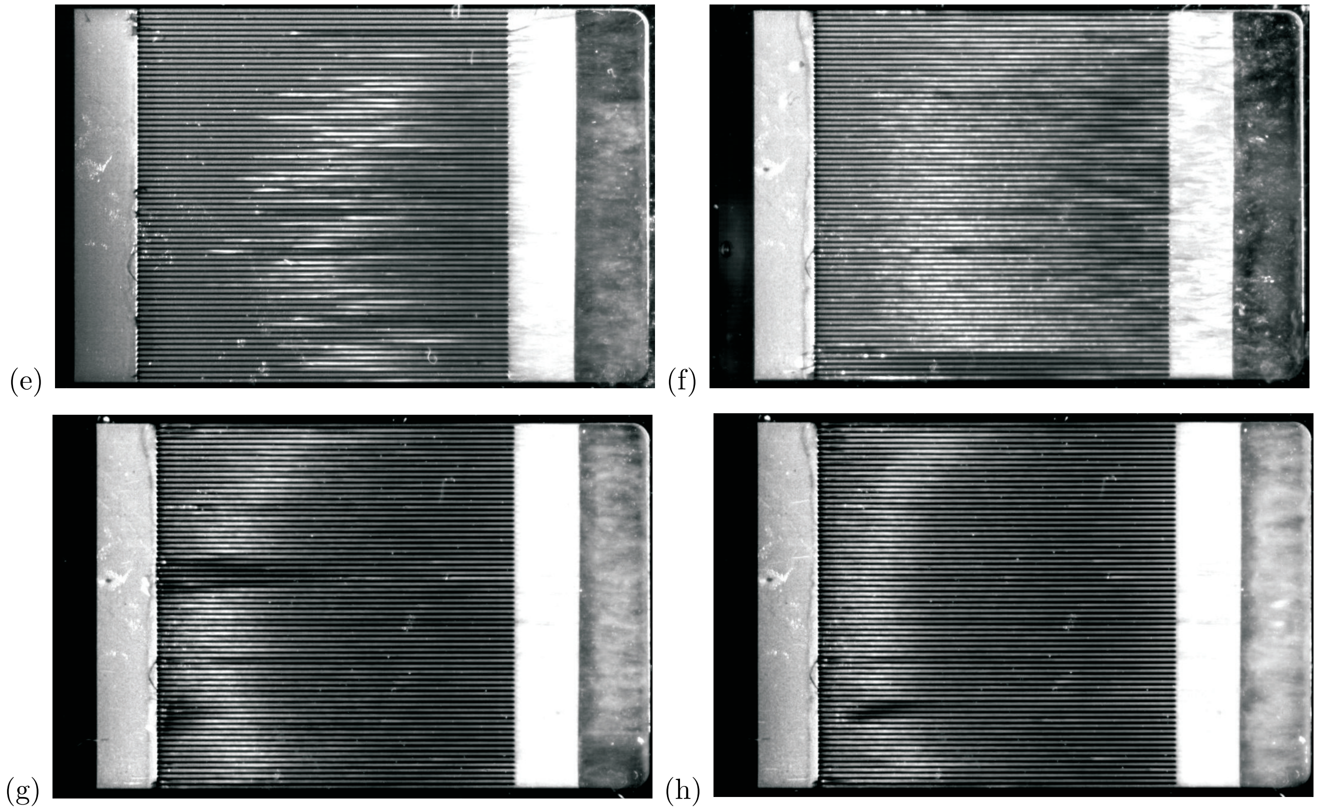

Figure 5.11: (continued) Two-phase flow operating regimes observed in the test section with the 50 μm-wide, 100 μm-deep, and 100 μm-long inlet restrictions ($e_{in,rest} = 2$): (a) single-phase flow in the test section with the vapor bubbles at the manifold's outlet plenum, (b) single-phase flow followed by two-phase flow with back flow, (c) unstable two-phase flow with back flow developing into jet flow, (d) jet flow, (e) single-phase flow followed by two-phase flow without back flow, (f) two-phase flow with back flow triggered by bubbles formed in the flow loop before the test section, (g) flashing two-phase flow with back flow, and (h) flashing two-phase flow without back flow. More details about the experimental conditions of each operating regime are given in Table 5.1. The figure continues over pp. 82−83.

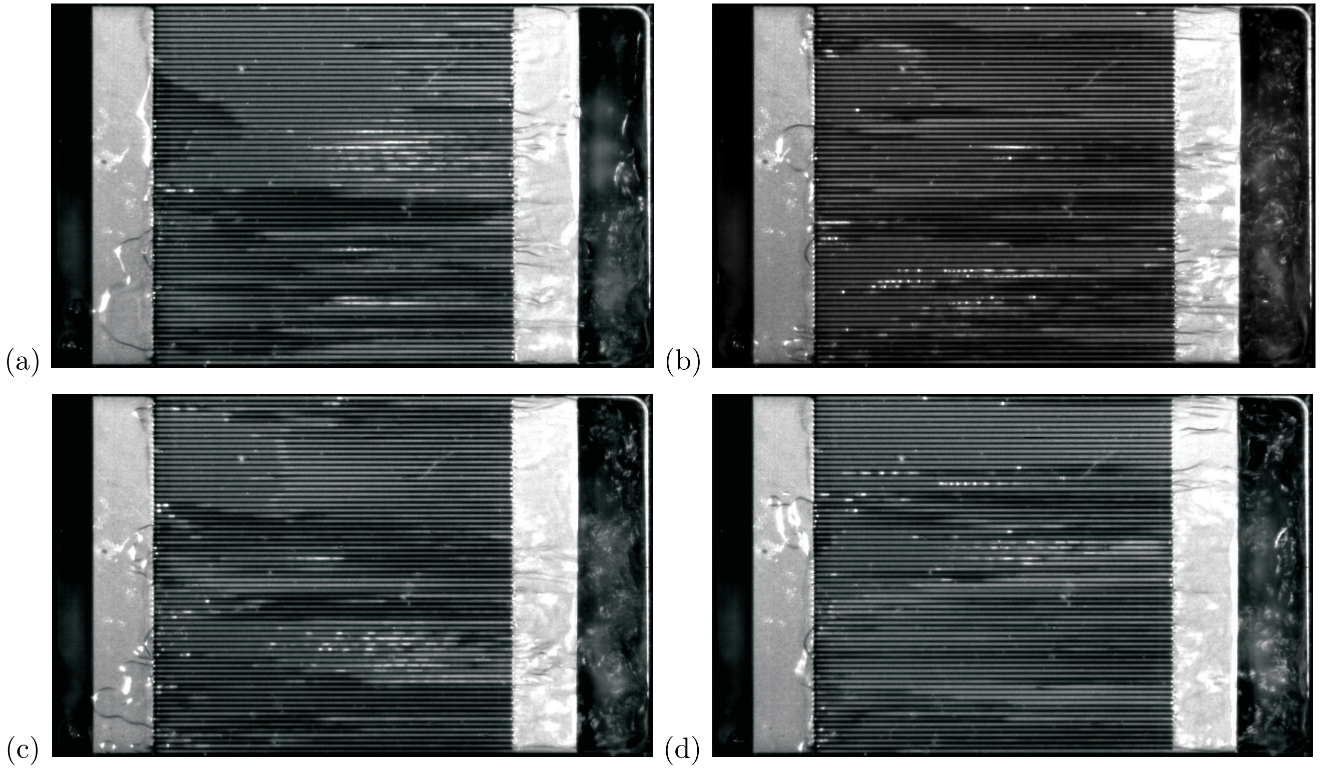

Figure 5.12: Temporal non-uniformity of the two-phase flow of R236fa inside the microchannels with the expansion ratio of $e_{in,rest} = 2$, $G_{ch} = 300\,\mathrm{kg\,m^{-2}\,s^{-1}}$, $q_b = 9.6\,\mathrm{W\,cm^{-2}}$: (a) 0 s, (b) 0.1 s, (c) 0.2 s, and (d) 0.3 s.

A time sequence of images in Fig. 5.13 illustrates some flashed bubbles are generated by the inlet restriction of the expansion ratio of $e_{in,rest} = 4$ (blue circle). They grow and become elongated further downstream (Fig. 5.13(b) and 5.13(c)). In Figs. 5.13(d) – 5.11(f), the situation repeats (red circle). Furthermore, some isolated bubbles formed in the piping before the test section pass through (Figs. 5.13(g) and 5.13(h)) without disturbing the flow in the micro-evaporator. In Fig. 5.13(j), no back flow was observed (yellow circle). Those bubbles are created through a combine effect of fluid pre-heating and geometrical components in the refrigerant loop. However, for some of the experimental conditions, back flow can be triggered by those bubbles (see Fig. 5.13(f) at left). This phenomenon did not have any significant effect on the two-phase flow in the test section and the back flow observed in these few cases (operating regime (vi)) was not comparable to that occurring in the operating regimes (ii), (iii) and (vii).

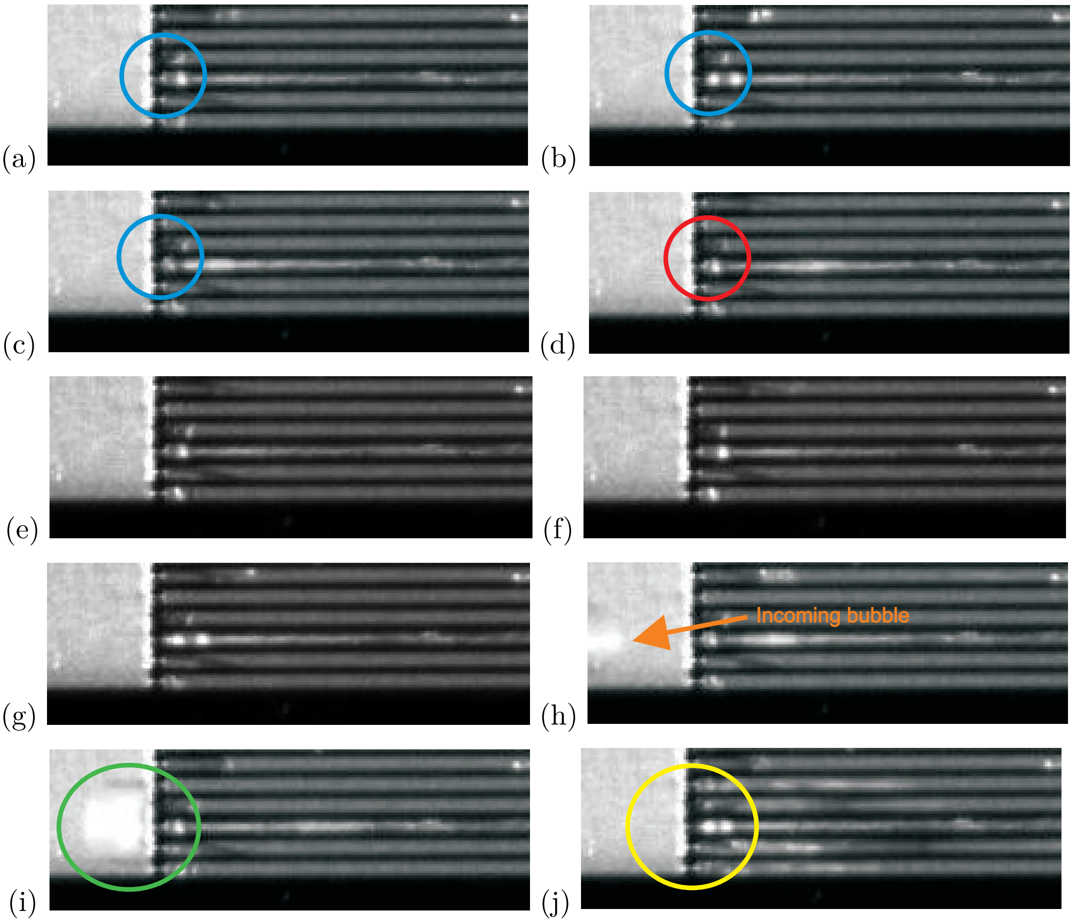

Figure 5.13: Flashed vapor bubbles of R236fa (white at left). Zoom-in into the inlet restriction of the expansion ratio of $e_{in,rest} = 4$, $G_{ch} = 1'311\,\mathrm{kg\,m^{-2}\,s^{-1}}$, $q_b = 13.9\,\mathrm{W\,cm^{-2}}$, $\Delta t = 0.001\,\mathrm{s}$.

Figure 5.14 illustrates the visual interpretation of the standard deviations obtained from 2'729 images of flow visualization for operating regimes (v) and (viii). The shiny areas correspond to the two-phase flow transition. In Fig. 5.13(a), the two-phase flow starts at different longitudinal distances among the channels, whereas, in the other case, the flow distributes uniformly with some flashed vapor bubbles at the channel inlets. The flow develops into annular flow faster in the middle channels. The flashing two-phase flow without back flow (viii) operating regime appeared to provide very good flow uniformity in time and space (refer to Fig. 3.9(b)). The flow was stable, and thus it is the most desirable operating condition.

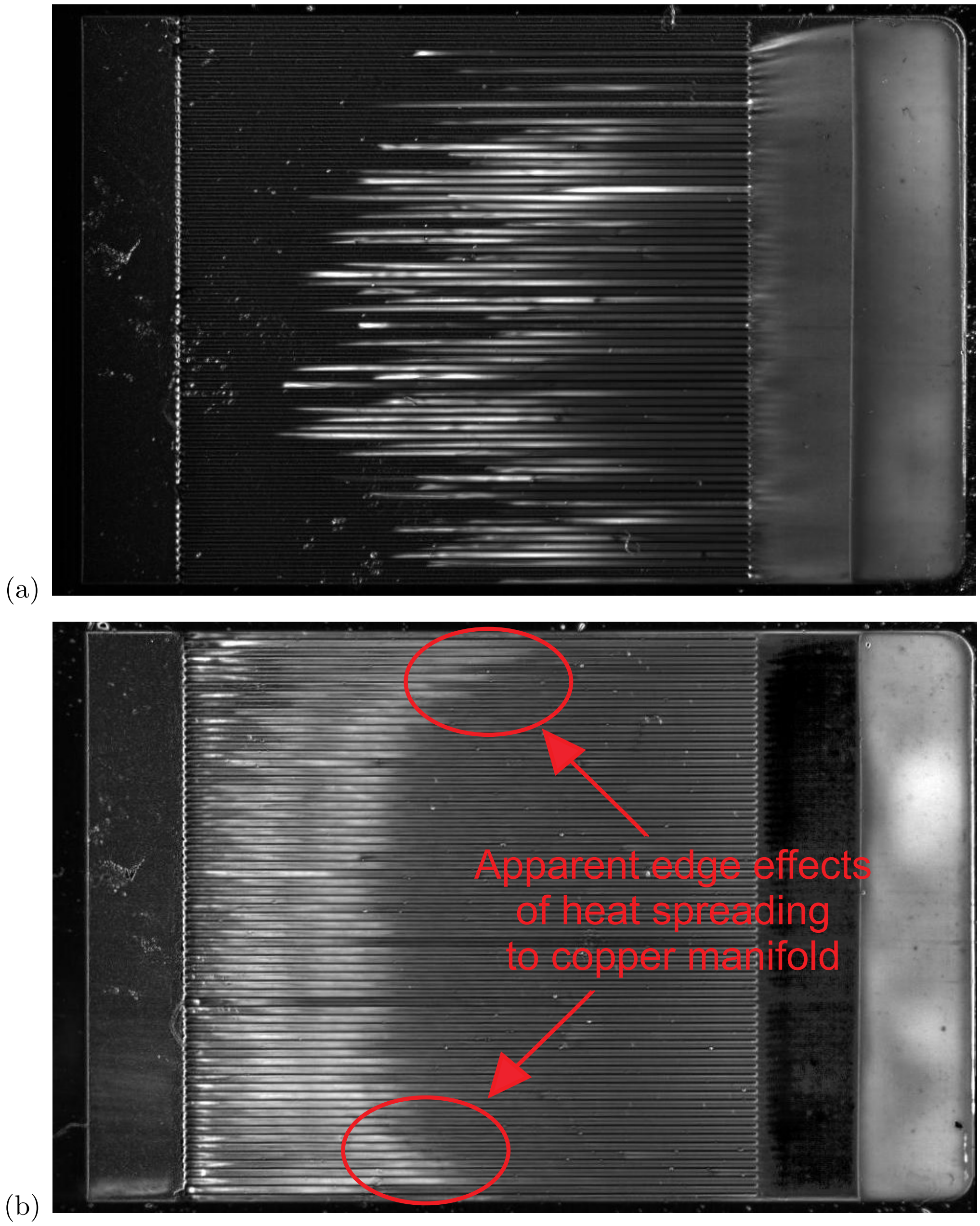

Figure 5.14: Standard deviation of the image sequences over time provided by the two-phase flow of R245fa flowing in the test section with the inlet restrictions of the expansion ratio of $e_{in,rest} = 2$ for: (a) single-phase flow followed by two-phase flow without back flow operating regime, $G_{ch} = 2’025\,\mathrm{kg\,m^{-2}\,s^{-1}}$, $q_b = 21.4\,\mathrm{W\,cm^{-2}}$ (desirable operating regime), and (b) flashing two-phase flow without back flow operating regime, $G_{ch} = 1’895\,\mathrm{kg\,m^{-2}\,s^{-1}}$, $q_b = 47\,\mathrm{W\,cm^{-2}}$ (the most desirable operating regime).

Due to the presence of the inlet orifices, the reversibility of two-phase flow in microchannels was observed. Figure 5.15 is a time strip of one channel over a time period of 0.025 s (Borhani et al., 2010). When the incoming subcooled flow transitions to two-phase flow, the bubbles being generated push the neighbouring fluid in all directions in spite of the flow direction, as previously reported by Park et al. (2009) (refer to flow recirculation in high aspect ratio microchannels). Since the boiling incipience happens close to the inlet, the flow tends to move towards the inlet and some reverse flow takes place. Nonetheless, the inlet restrictions block the vapor bubbles from going back into the inlet header and the subcooled single-phase flow helps the bubbles to move along the microchannels and leave the test section. The situation repeats periodically, and thus the wavy behaviour of the two-phase flow transition zone could be seen in time.

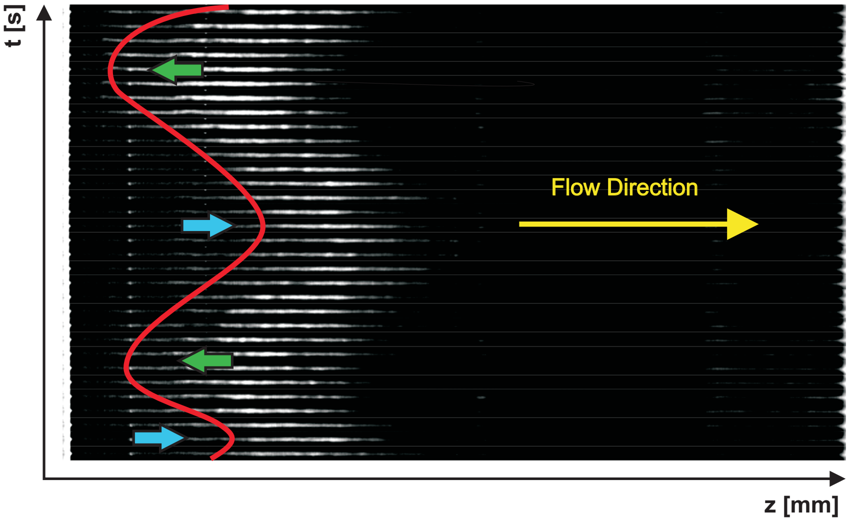

Figure 5.15: Reversibility of the two-phase flow of R245fa in 100 x 100 μm^2 microchannels with the inlet restrictions of the expansion ratio of $e_{in,rest} = 2$, $G_{ch} = 1643\,\mathrm{kg\,m^{-2}\,s^{-1}}$, $q_b = 29\,\mathrm{W\,cm^{-2}}$.

5.3 Temperature visualization

Figure 5.16 illustrates several temperature maps of the test section's base obtained for different two-phase flow operating regimes. For the operating regimes from (i) to (vi), the temperature increases along the channel and slightly decreases at the channel outlet. The temperature increase towards the outlet is characteristic for the single-phase flow. Whereas, for the operating regimes (vii) and (viii), the temperature decreases from inlet to outlet due to the drop in the saturation pressure of the fluid. Table 5.2 presents the width-wise temperature standard deviations (STD) for 4 longitudinal channel positions ($z = 2.0$, 4.0, 6.0, 8.0 mm from the inlet) for the 8 two-phase flow operating regimes from Fig. 5.16. The operating regimes (i) and (iv) provide the highest width-wise temperature standard deviations even up to 0.6K. In case of the operating regimes (ii), (iii), (vi), and (vii), the values of STD are relatively good; however, the two-phase flow is non-uniform and unstable with the vapor bubbles coming back to the inlet test section's and manifold's plenums. As showed, the temperature uniformity along with very good flow stability and flow distribution among the channels is the best for the operating regime (viii), for which, the calculated width-wise time-averaged temperature standard deviations are about $1-2\,\%$ of the local wall superheat, ΔT_s. In the end, the flashing two-phase flow without back flow operating regime (viii), depicted in Fig. 5.16(h), provided the best flow and temperature uniformity and is the most desirable operating regime. That confirms the statement of Park et al. (2009) that, due to the flashing effect, the wall-temperature distribution becomes more uniform.

Table 5.2: Width-wise time-averaged temperature standard deviations for the 4 longitudinal channel positions ($z=2.0$, 4.0, 6.0, $8.0\,\mathrm{mm}$) and the 8 representatives of the two-phase flow operating regimes presented in Fig. 5.16. More details about the experimental conditions of each operating regime are given in Table 5.1.

Operating regime	STD [K]			
z [mm]	2.0	4.0	6.0	8.0
single-phase flow in the test section with the vapor bubbles at the manifold's outlet plenum (i)	0.4	0.5	0.5	0.6
single-phase flow followed by two-phase flow with back flow (ii)	**0.2**	**0.1**	**0.2**	**0.2**
unstable two-phase flow with back flow developing into jet flow (iii)	**0.3**	**0.3**	**0.3**	**0.3**
jet flow (iv)	0.5	0.6	0.6	0.6
single-phase flow followed by two-phase flow without back flow (v)	**0.2**	**0.2**	**0.2**	**0.2**
two-phase flow with back flow triggered by bubbles formed in the flow loop before the test section (vi)	**0.2**	**0.2**	**0.2**	**0.2**
flashing two-phase flow with back flow (vii)	**0.2**	**0.2**	**0.3**	**0.3**
flashing two-phase flow without back flow (viii)	**0.3**	**0.2**	**0.2**	**0.2**

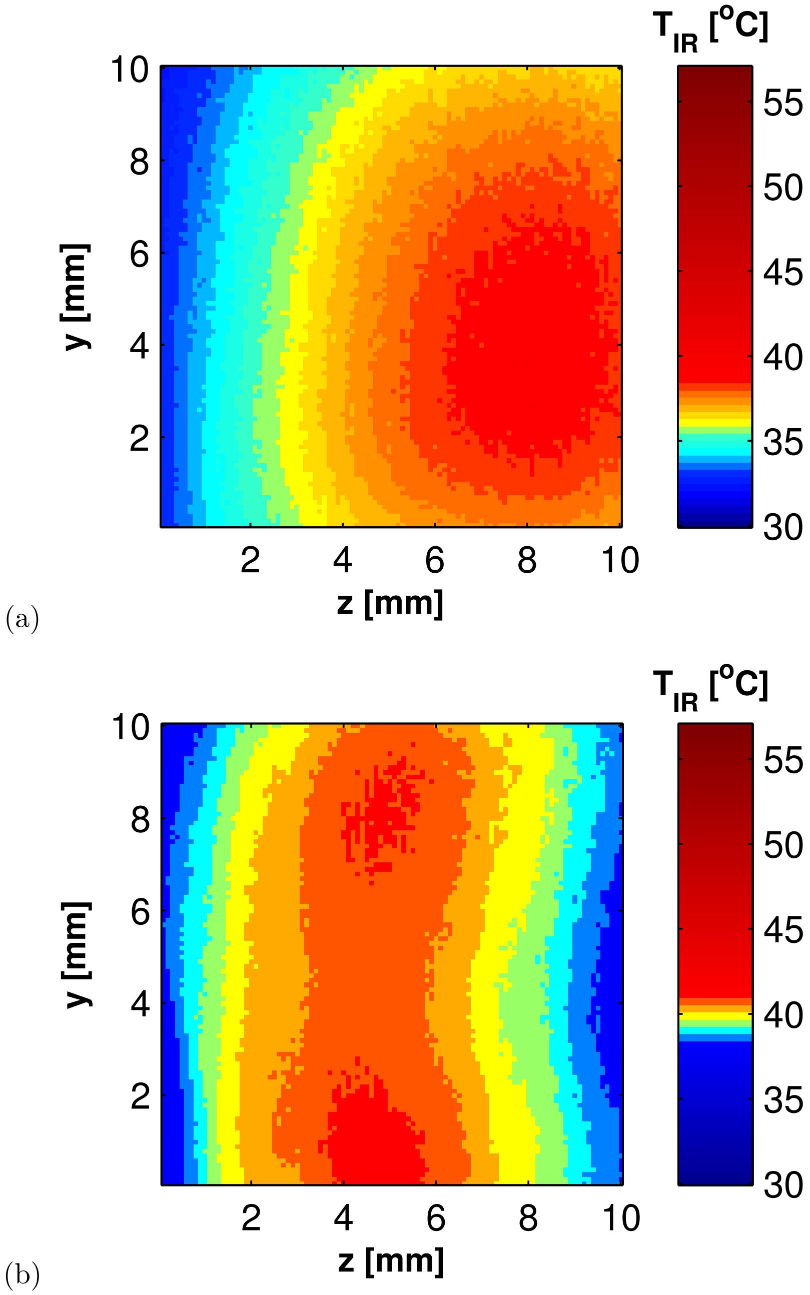

Figure 5.16: Time-averaged temperature flow pattern maps for $e_{in,rest} = 2$: (a) single-phase flow in the test section with the vapor bubbles at the manifold's outlet plenum, (b) single-phase flow followed by two-phase flow with back flow, (c) unstable two-phase flow with back flow developing into jet flow, (d) jet flow, (e) single-phase flow followed by two-phase flow without back flow, (f) two-phase flow with back flow triggered by bubbles formed in the flow loop before the test section, (g) flashing two-phase flow with back flow, and (h) flashing two-phase flow without back flow. More details about the experimental conditions of each operating regime are given in Table 5.1. The figure continues over pp. 89 – 92.

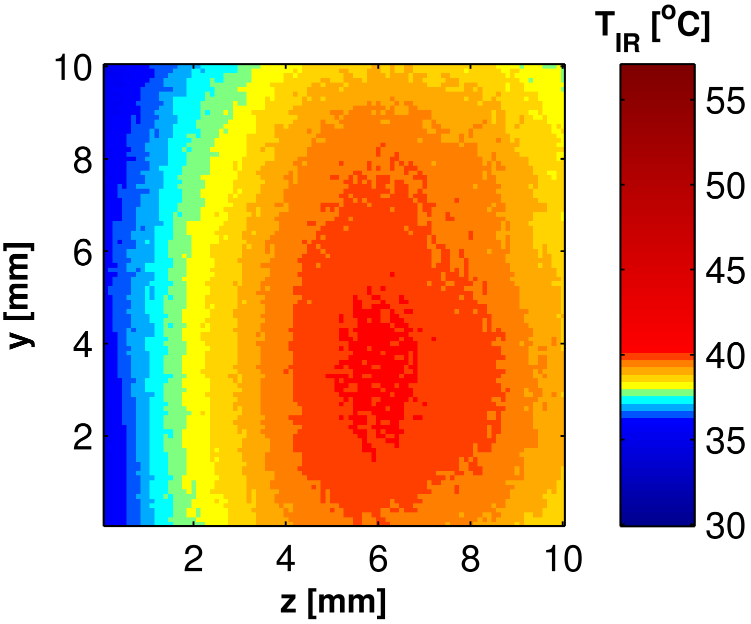

(c)

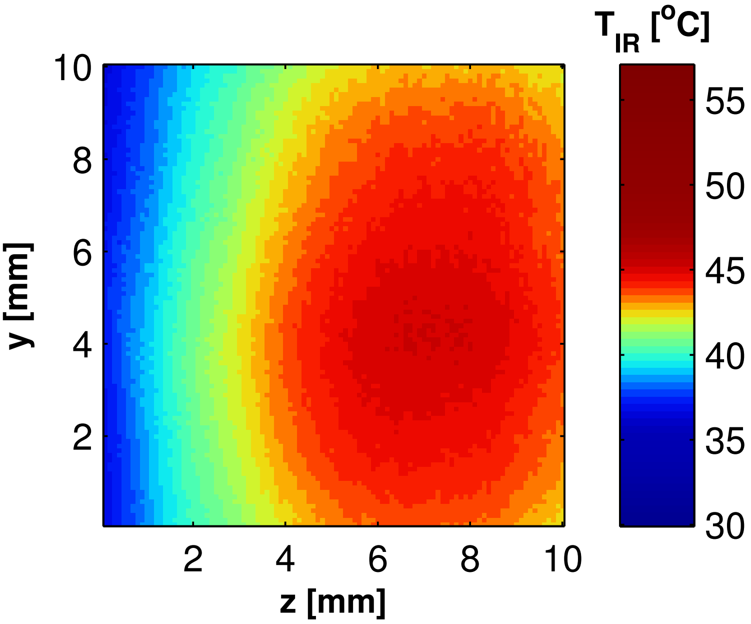

(d)

Figure 5.16: (continued) Time-averaged temperature flow pattern maps for $e_{in,rest} = 2$: (a) single-phase flow in the test section with the vapor bubbles at the manifold's outlet plenum, (b) single-phase flow followed by two-phase flow with back flow, (c) unstable two-phase flow with back flow developing into jet flow, (d) jet flow, (e) single-phase flow followed by two-phase flow without back flow, (f) two-phase flow with back flow triggered by bubbles formed in the flow loop before the test section, (g) flashing two-phase flow with back flow, and (h) flashing two-phase flow without back flow. More details about the experimental conditions of each operating regime are given in Table 5.1. The figure continues over pp. 89 – 92.

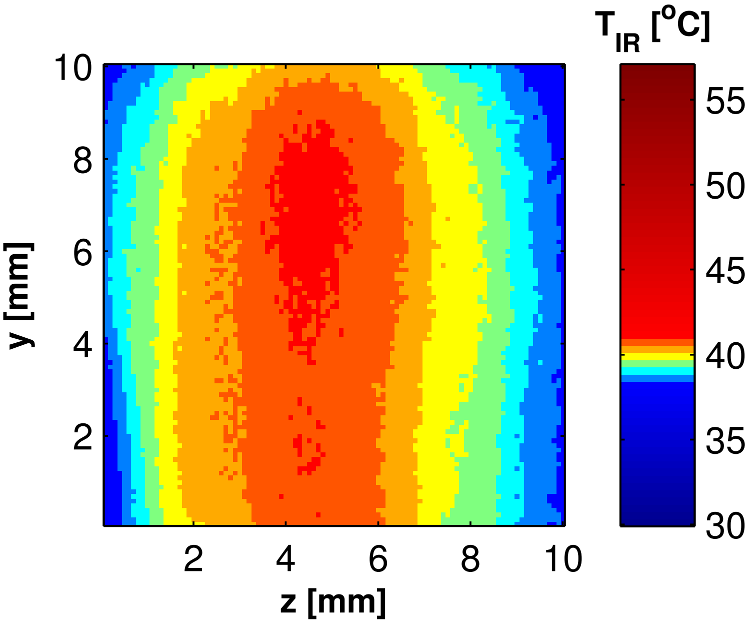

(e)

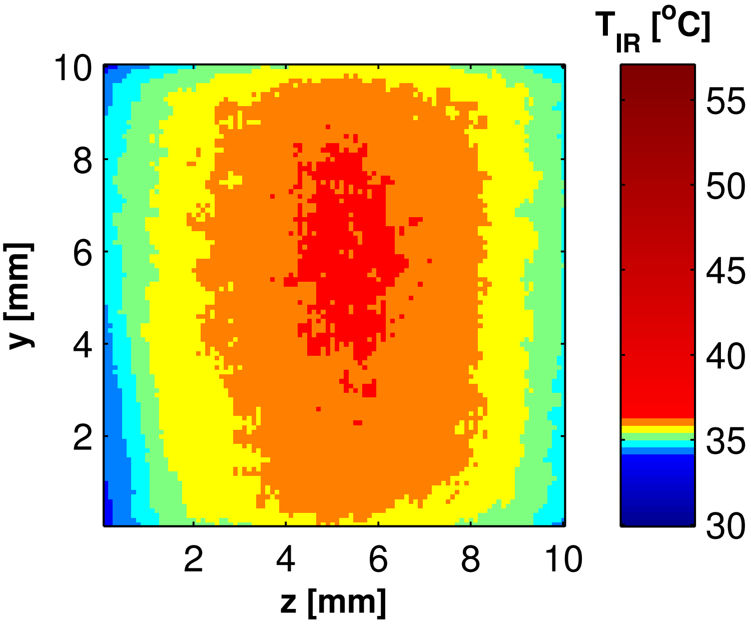

(f)

Figure 5.16: (continued) Time-averaged temperature flow pattern maps for $e_{in,rest} = 2$: (a) single-phase flow in the test section with the vapor bubbles at the manifold's outlet plenum, (b) single-phase flow followed by two-phase flow with back flow, (c) unstable two-phase flow with back flow developing into jet flow, (d) jet flow, (e) single-phase flow followed by two-phase flow without back flow, (f) two-phase flow with back flow triggered by bubbles formed in the flow loop before the test section, (g) flashing two-phase flow with back flow, and (h) flashing two-phase flow without back flow. More details about the experimental conditions of each operating regime are given in Table 5.1. The figure continues over pp. 89 – 92.

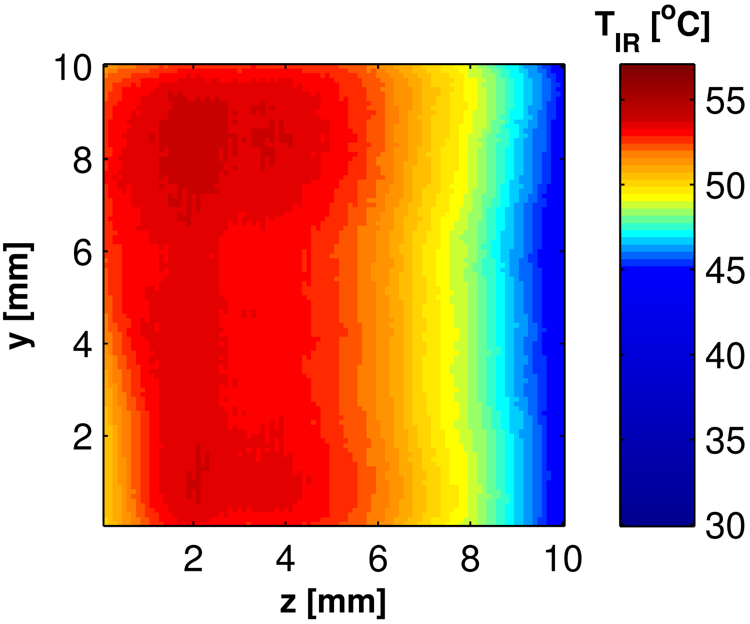

(g)

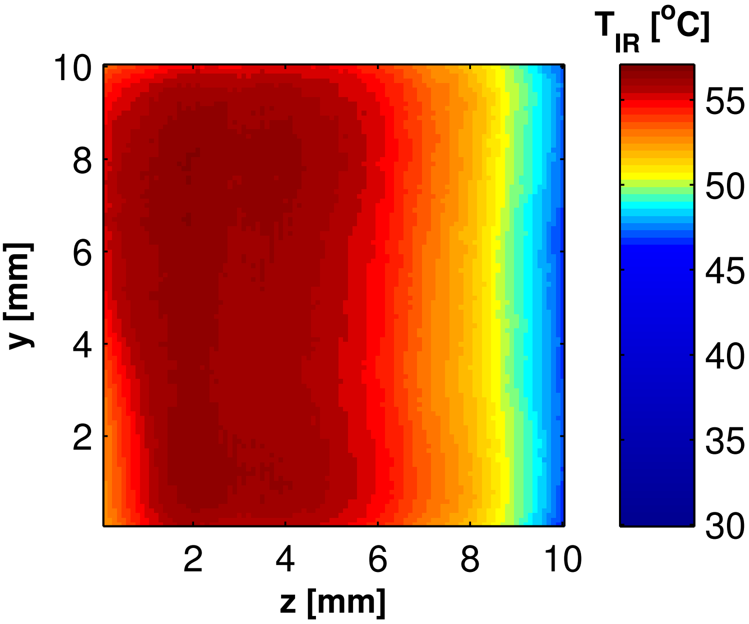

(h)

Figure 5.16: (continued) Time-averaged temperature flow pattern maps for $e_{in,rest} = 2$: (a) single-phase flow in the test section with the vapor bubbles at the manifold's outlet plenum, (b) single-phase flow followed by two-phase flow with back flow, (c) unstable two-phase flow with back flow developing into jet flow, (d) jet flow, (e) single-phase flow followed by two-phase flow without back flow, (f) two-phase flow with back flow triggered by bubbles formed in the flow loop before the test section, (g) flashing two-phase flow with back flow, and (h) flashing two-phase flow without back flow. More details about the experimental conditions of each operating regime are given in Table 5.1. The figure continues over pp. 89 – 92.

In order to investigate the temporal temperature fluctuations of the two-phase flow in the multi-microchannels, the temperature distributions of several pixels of the IR camera's sensor array for the representative two-phase flow operating regimes (refer to Fig. 5.11) are presented in Fig. 5.17. The colors used in here correspond to the ones used in the two-phase flow operational maps (Figs. 5.1 – 5.6). Additionally, Table 5.3 presents the standard deviations of the temperature (STD) for 3'200 data samples recorded at 60 Hz for those data points. As can be seen, the flashing two-phase flow (viii) operating regime provides the best flow and temperature stability in both, time and space (the spatial uniformity was discussed above). The temporal standard deviations in this case are about 0.3 % of the local wall superheat, ΔT_s, and an order of magnitude smaller than the accuracy of the IR camera. The standard deviations of the temperature for the (vii) operating regime are comparable, even though one needs to remember that vapor back flow occurs in this case. Whereas, for the (iii) operating regime, the temperature fluctuations over time were as high as 2 °C.

Table 5.3: Standard deviations of the temperature (STD) over 3'200 data points recorded at 60 Hz for the 4 pixels of the IR camera's sensor array and the 8 representatives of the two-phase flow operating regimes shown in Fig. 5.16. More details about the experimental conditions of each operating regime are given in Table 5.1.

Operating regime	STD [K]			
Pixel	$P_{(50,20)}$	$P_{(20,50)}$	$P_{(50,80)}$	$P_{(80,80)}$
single-phase flow in the test section with the vapor bubbles at the manifold's outlet plenum (i)	0.16	0.18	0.16	0.15
single-phase flow followed by two-phase flow with back flow (ii)	0.22	0.22	0.25	0.21
unstable two-phase flow with back flow developing into jet flow (iii)	**1.62**	**1.97**	**1.40**	**0.82**
jet flow (iv)	0.06	0.06	0.06	0.06
single-phase flow followed by two-phase flow without back flow (v)	0.16	0.25	0.21	0.16
two-phase flow with back flow triggered by bubbles formed in the flow loop before the test section (vi)	0.1	0.08	0.1	0.09
flashing two-phase flow with back flow (vii)	**0.07**	**0.07**	**0.06**	**0.06**
flashing two-phase flow without back flow (viii)	**0.04**	**0.05**	**0.04**	**0.04**

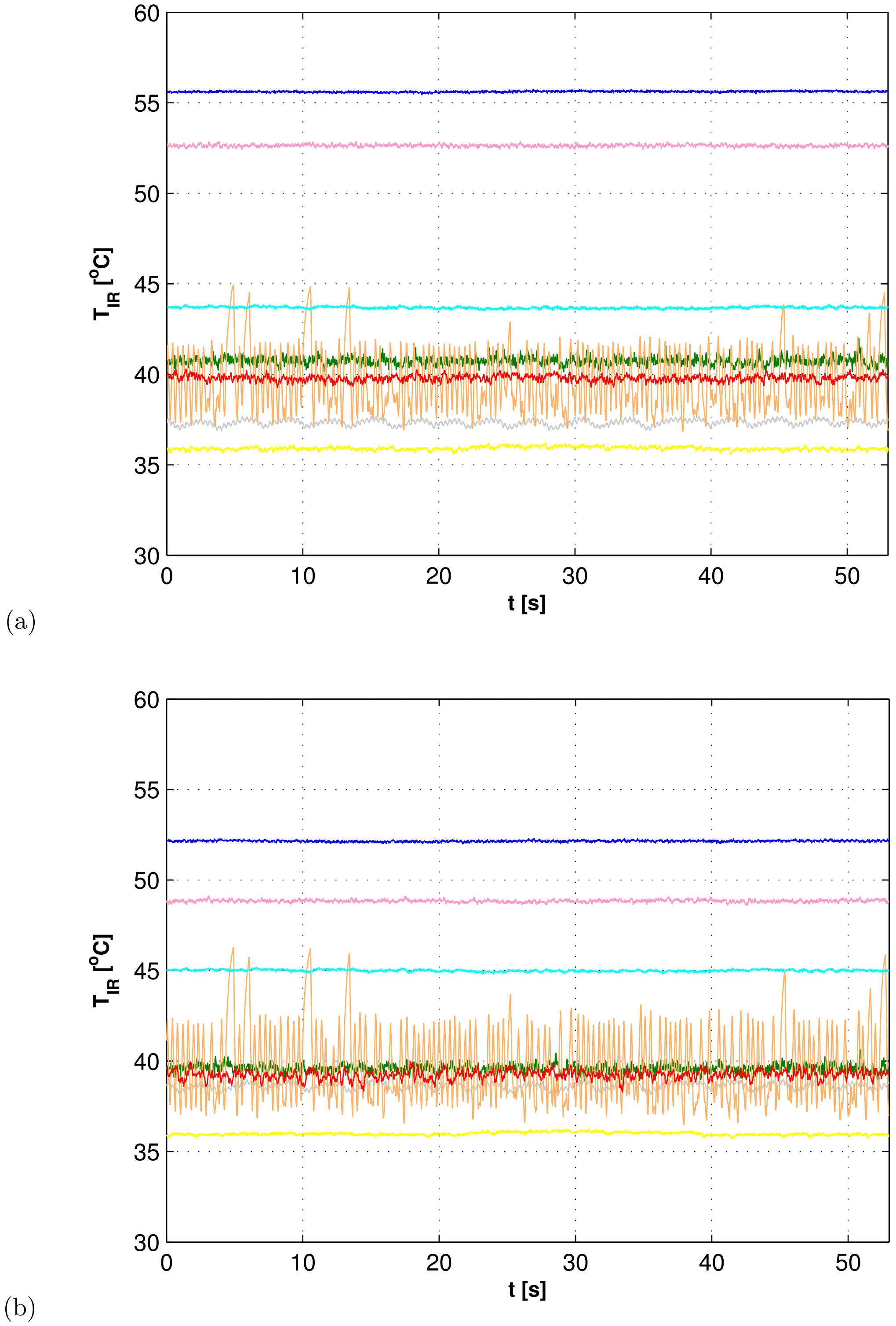

Figure 5.17: Temporal temperature fluctuations for pixel: (a) $P_{(50,20)}$, (b) $P_{(20,50)}$, (c) $P_{(50,80)}$, and (d) $P_{(80,80)}$, where: —— - single-phase flow in the test section with the vapor bubbles at the manifold's outlet plenum, —— - single-phase flow followed by two-phase flow with back flow, —— - unstable two-phase flow with back flow developing into jet flow, —— - jet flow, —— - single-phase flow followed by two-phase flow without back flow, —— - two-phase flow with back flow triggered by bubbles formed in the flow loop before the test section, —— - flashing two-phase flow with back flow, and —— - flashing two-phase flow without back flow. More details about the experimental conditions of each operating regime are given in Table 5.1. The figure continues over pp. 94 – 95.

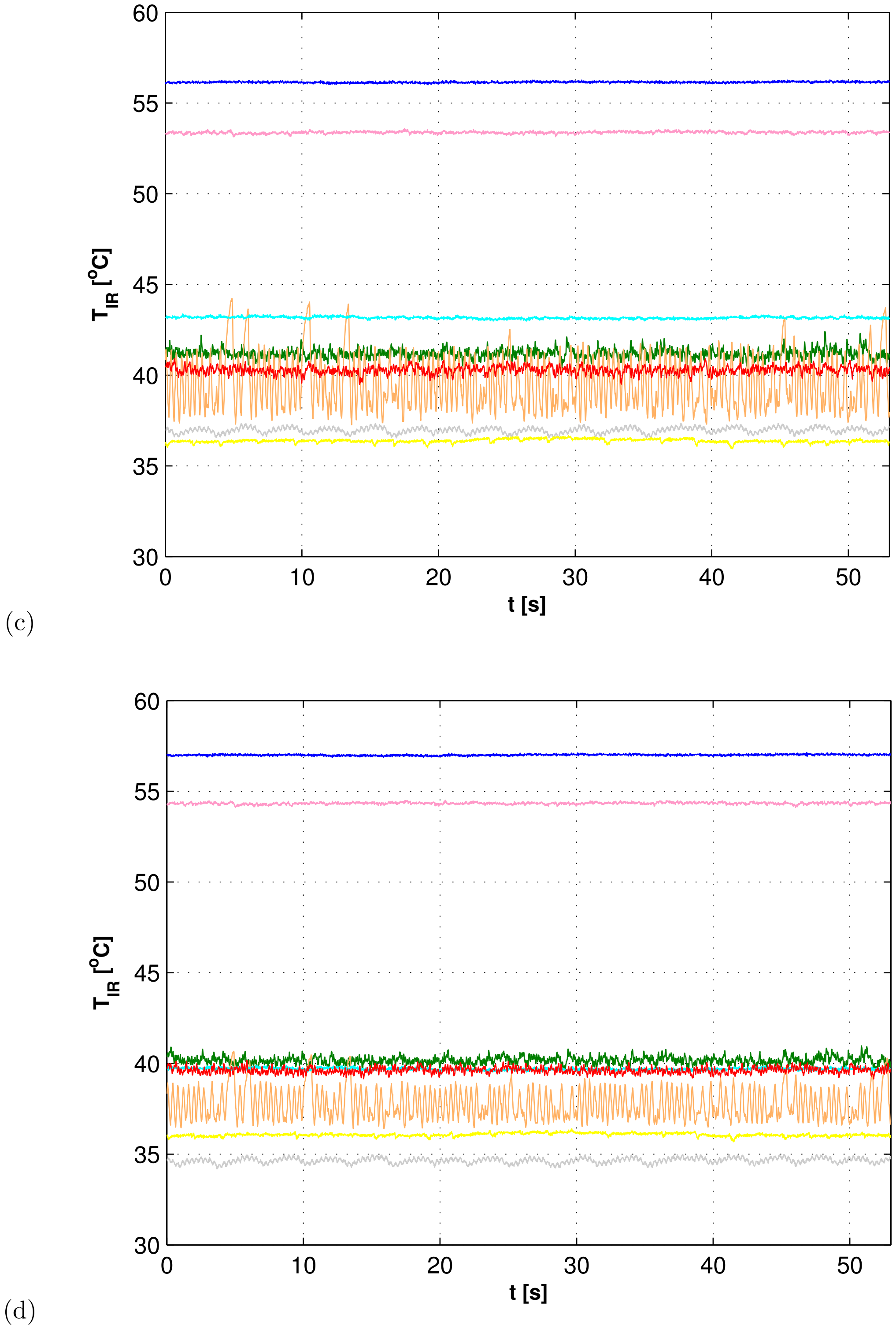

Figure 5.17: (continued) Temporal temperature fluctuations for pixels: (a) $P_{(50,20)}$, (b) $P_{(20,50)}$, (c) $P_{(50,80)}$, and (d) $P_{(80,80)}$, where: —— - single-phase flow in the test section with the vapor bubbles at the manifold's outlet plenum, —— - single-phase flow followed by two-phase flow with back flow, —— - unstable two-phase flow with back flow developing into jet flow, —— - jet flow, —— - single-phase flow followed by two-phase flow without back flow, —— - two-phase flow with back flow triggered by bubbles formed in the flow loop before the test section, —— - flashing two-phase flow with back flow, and —— - flashing two-phase flow without back flow. More details about the experimental conditions of each operating regime are given in Table 5.1. The figure continues over pp. 94 – 95.

Figure 5.18, supplemented by Table 5.4, shows the minimum and maximum junction temperatures of the micro-evaporator's base, respectively $T_{IR,min}$ and $T_{IR,max}$, the maximum dissipated base heat fluxes, q_b, as well as the corresponding maximum total pressure drops, $\triangle p_{total}$, for all the test cases. The maximum junction temperature of 57.1 °C was obtained while dissipating the base heat flux 47.6 W cm^{-2} with 63 kPa of total pressure drop (for the micro-evaporator without any inlet restriction) or 47.0 W cm^{-2} of the base heat flux with 106 kPa of total pressure drop (for the test sections with the micro-orifices). These are not however the critical heat fluxes, which were avoided here not to risk the burnout of the test sections.

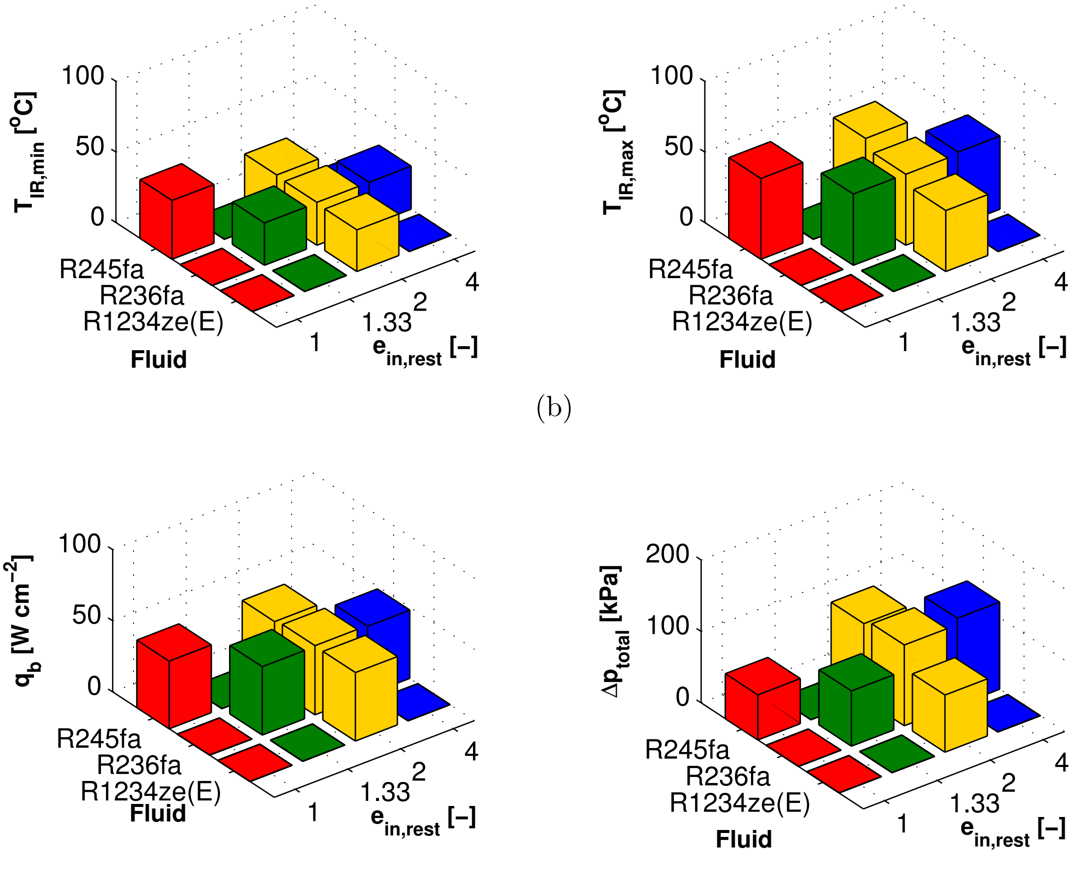

(a) (b)

(c) (d)

Figure 5.18: (a) Minimum junction temperature of the micro-evaporator's base ($T_{IR,min}$), (b) maximum junction temperature of the micro-evaporator's base ($T_{IR,max}$), (c) maximum base heat flux (q_b), and (d) corresponding total pressure drop ($\triangle p_{total}$) for all the test cases, where *0* indicates the cases which were not tested.

Table 5.4: Detailed summary of the experimental campaign including the minimum and maximum ($T_{IR,min}$ and $T_{IR,max}$) junction temperatures of the micro-evaporator's base, the maximum dissipated base heat flux (q_b), and the corresponding total pressure drops ($\triangle p_{total}$).

<table>
<tr><td colspan="5">$T_{IR,min}$ [°C]</td></tr>
<tr><td>$e_{in,rest}$</td><td>1</td><td>1.33</td><td>2</td><td>4</td></tr>
<tr><td>R245fa</td><td>41.5</td><td></td><td>31.2</td><td></td></tr>
<tr><td>R236fa</td><td></td><td>30.0</td><td>30.4</td><td>30.4</td></tr>
<tr><td>R1234ze(E)</td><td></td><td></td><td>29.4</td><td></td></tr>
<tr><td colspan="5">$T_{IR,max}$ [°C]</td></tr>
<tr><td>$e_{in,rest}$</td><td>1</td><td>1.33</td><td>2</td><td>4</td></tr>
<tr><td>R245fa</td><td>57.1</td><td></td><td>57.1</td><td></td></tr>
<tr><td>R236fa</td><td></td><td>50.4</td><td>50.3</td><td>51.8</td></tr>
<tr><td>R1234ze(E)</td><td></td><td></td><td>43.1</td><td></td></tr>
<tr><td colspan="5">q_b $[\mathrm{W\,cm^{-2}}]$</td></tr>
<tr><td>$e_{in,rest}$</td><td>1</td><td>1.33</td><td>2</td><td>4</td></tr>
<tr><td>R245fa</td><td>47.6</td><td></td><td>47.0</td><td></td></tr>
<tr><td>R236fa</td><td></td><td>47.9</td><td>48.6</td><td>47.9</td></tr>
<tr><td>R1234ze(E)</td><td></td><td></td><td>48.1</td><td></td></tr>
<tr><td colspan="5">$\triangle p_{total}$ [kPa]</td></tr>
<tr><td>$e_{in,rest}$</td><td>1</td><td>1.33</td><td>2</td><td>4</td></tr>
<tr><td>R245fa</td><td>63</td><td></td><td>106</td><td></td></tr>
<tr><td>R236fa</td><td></td><td>77</td><td>113</td><td>122</td></tr>
<tr><td>R1234ze(E)</td><td></td><td></td><td>80</td><td></td></tr>
</table>

5.4 Conclusions

- The importance of the overall visual inspection in multi-microchannel experiments to study phase change phenomenon has been shown.
- Three different micro-orifice expansion ratios ($e_{in,rest} = 1.33$, 2, and 4) have been tested and the obtained results were compared with the test section with no inlet restrictions.
- Micro-orifices having the expansion ratio of 2 and 4 successfully suppressed flow instability, vapor back flow and significantly improved flow uniformity among the channels in the range of the tested operating conditions. Hence, the use of micro-orifices is essential for two-phase cooling in the micro-electronics industry in order to ensure the stable operation of future 3D interlayer cooling systems.
- The two-phase flow experimental test conditions were categorized into 8 operating regimes, among which the flashing two-phase flow without back flow (viii) operating regime was found to provide the best flow and temperature uniformity in time and space. The transitions from one regime to another were fluid-dependent. Among the test fluids, refrigerant R236fa is proposed here to be used in the future 3D high-performance computer chips. The reason behind is that this fluid was stable over a wider range of experimental conditions and the transitions in between the operating regimes were more predictable compared to R245fa and R1234ze(E).
- The most advantageous operating conditions for stable flows, such as the flashing two-phase flow without back flow, can be tracked using the two-phase flow operational maps obtained for each test fluid and each micro-evaporator in terms of channel mass flux and dissipated base heat flux.
- The maximum junction temperature of 57.1 °C was obtained while dissipating the base heat flux $47.6\,\mathrm{W\,cm^{-2}}$ with 63 kPa of the total pressure drop (for the micro-evaporator without any inlet restriction) or $47.0\,\mathrm{W\,cm^{-2}}$ of the base heat flux with 106 kPa of the total pressure drop (for the test sections with the micro-orifices). For all the test cases the temperature was below the given temperature limit of 85 °C for CPUs, while dissipating half of the heat flux being targeted. Thus, further research is needed extending for higher heat fluxes and CHF tests. The fact that needs to be highlighted here is the following: the junction temperature of the micro-evaporator can still increase more than 25 °C before the given limit is reached.

Chapter 6

Pressure drop

The adiabatic and diabatic pressure drops for the micro-evaporator tests are presented here. The equations used for pressure drop calculations were introduced previously in Chapter 4. Besides quantifying these pressure drops themselves, they are used to determine the local saturation pressure / saturation temperature to back out the local two-phase heat transfer coefficients.

6.1 Adiabatic results

Prior to the flow boiling experiments, a series of adiabatic single-phase flow tests were performed for the range of channel mass fluxes corresponding to the two-phase flow experiments.

6.1.1 Total pressure drop

The purpose of this section is to determine the influence of the micro-orifice's expansion ratio, $e_{in,rest}$, and the fluid properties on the total adiabatic pressure drop, $\Delta p_{total,AD}$. Figure 6.1 illustrates the adiabatic pressure drops, measured between the inlet and the outlet manifold's plenums, as a function of the single-phase Reynolds number in the microchannels, Re.

As expected, the ascending trend of $\Delta p_{total,AD}$ is observed in Fig. 6.1 with increasing Re due to a rise in the surface shear stress, τ_{sur}. The total pressure drop increases when decreasing the micro-orifice's hydraulic diameter. In Fig. 6.1(a), for the Reynolds number of $\mathrm{Re} \approx 365$, the pressure drop of R245fa within the test section of $e_{in,rest} = 2$ is ~14% higher compared to the micro-evaporator without any inlet restrictions ($e_{in,rest} = 1$). Moreover, a noticeable pressure drop increase is seen between the expansion ratios of $e_{in,rest} = 2$ and 4. For instance for $\mathrm{Re} \approx 645$, the total adiabatic pressure drop of R236fa increases by a factor of ~2.78 when reducing the width of the orifice from 50 to 25 μm, as shown in Fig. 6.1(b). Potentially, the micro-evaporators might be slightly different due to the fabrication process, but this would have

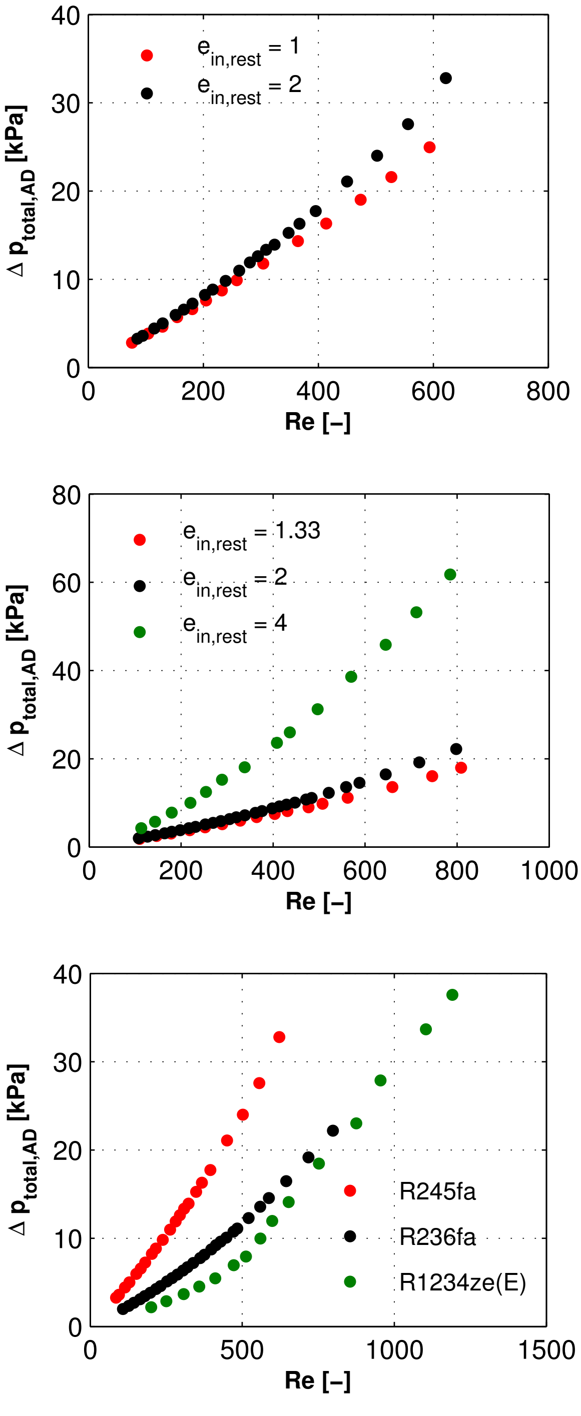

(a)

(b)

(c)

Figure 6.1: Adiabatic single-phase flow pressure drops as a function of the channel Reynolds number for: (a) R245fa in 2 test sections with $e_{in,rest} = 1$ and 2, (b) R236fa in 3 test sections ($e_{in,rest} = 1.33$, 2, and 4), and (c) fluids R245fa, R236fa, and R1234ze(E) flowing in the test section with $e_{in,rest} = 2$.

only a minor influence on the present comparison.

Figure 6.1(c) shows the influence of the fluid properties of the refrigerants at the saturation temperature of 31.5±1 °C. R245fa has the highest pressure drops because of its high liquid kinematic viscosity, ν_l, as listed in Table 4.1.

6.1.2 Inlet restriction pressure loss

The inlet restriction pressure losses, $\Delta p_{in,rest}$, are quantified here excluding the test case of R245fa flowing in the test section without any inlet restrictions ($e_{in,rest} = 1$) that failed (broke) before completing a full series of experiments.

Commonly, the singular pressure drop due to the flow contraction in the test section's inlet and the flow expansion in the test section's outlet are computed by modifying the expression given by White (1999) and Incropera et al. (2007):

$$\Delta p_{total} = \Delta p_{fr} + \Delta p_{sg} \tag{6.1}$$

where the subscripts fr indicates pressure gradient due to friction and sg denotes the singular pressure drop. The assumption that the outlet component is small relative to the one at the inlet yields the following:

$$\Delta p_{in,rest} = \Delta p_{total} - \Delta p_{fr} = \xi \frac{G_{in,rest}^2}{2\rho_l} \tag{6.2}$$

where ξ is the singular pressure loss coefficient according to the Idelcik (1999) definition. An example of the $\Delta p_{in,rest}$ curve fitting for R236fa in the test section with the inlet restriction of $e_{in,rest} = 4$ is shown in Fig. 6.2. As it can be seen, the value of ξ depends on the Reynolds number, $\mathrm{Re}_{in,rest}$, defined here with respect to the micro-orifice's cross-sectional area. Therefore, the coefficient ξ can be then correlated in terms of $\mathrm{Re}_{in,rest}$, as shown in Fig. 6.2.

Alternatively, the inlet restriction pressure losses can also be calculated as described in Chapter 4. It stands that the total adiabatic pressure drop, $\Delta p_{total,AD}$, is composed of:

- the inlet restriction pressure loss

$$\Delta p_{in,rest} = \Delta p_{cont,1} + \Delta p_{cont,2} + \Delta p_{cont,3} + \Delta p_{\mathrm{exp},1} \tag{6.3}$$

  where $\Delta p_{cont,1,2,3}$ are the pressure drops due to fluid contraction calculated step-wise from the inlet manifold's plenum through the slit, the test section's plenum to the inlet orifice and $\Delta p_{exp,1}$ is the pressure recovery due to fluid expansion into the channel.

- the channel pressure drop (the gravitational pressure drop is neglected due to the horizontal channel orientation)

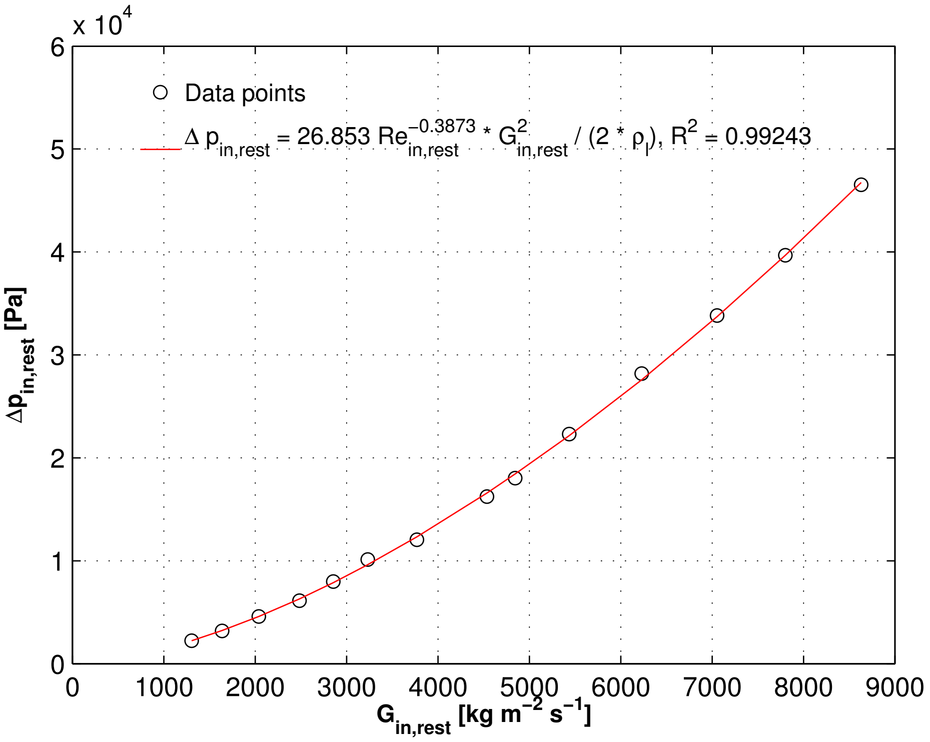

Figure 6.2: Single-phase flow inlet restriction pressure losses for R236fa in the test section with the inlet restrictions of $e_{in,rest} = 4$.

$$\Delta p_{fr} = 4f \frac{G_{ch}^2}{2\rho_l} \frac{L_{ch}}{D_h} \tag{6.4}$$

where f is the Fanning friction factor defined by Eq. (4.29).

- the outlet restriction pressure loss

$$\Delta p_{out,rest} = \Delta p_{\exp,2} + \Delta p_{\exp,3} + \Delta p_{\exp,4} \tag{6.5}$$

where $\Delta p_{exp,2,3,4}$ are the pressure recoveries due to fluid expansion from the outlet of the channel up to the outlet manifold's plenum.

Each component is calculated with the corresponding sign according to Eqs. (4.11) – (4.30) in Chapter 4. In Figs. 6.3 and B.1 – B.3 in Appendix B, vertical bar charts are used to compare the calculated values with the adiabatic total pressure drops, $\Delta p_{total,AD}$. Some discrepancies were found, which might be associated with the measurement accuracy as well as imperfections in obtaining the coefficients for contracting and expanding flows, K_{cont} and K_{exp}, respectively. As presented, the inlet restriction pressure losses tend to be significant, while the outlet single-phase flow pressure recovery, $\Delta p_{out,rest}$, are generally negligible compared to the other two.

The pressure drop due to the flow contraction, $\Delta p_{cont,1,2,3}$, and the pressure recovery due to the flow expansion, $\Delta p_{exp,2,3,4}$, are the single-phase flow components. Whereas, in most

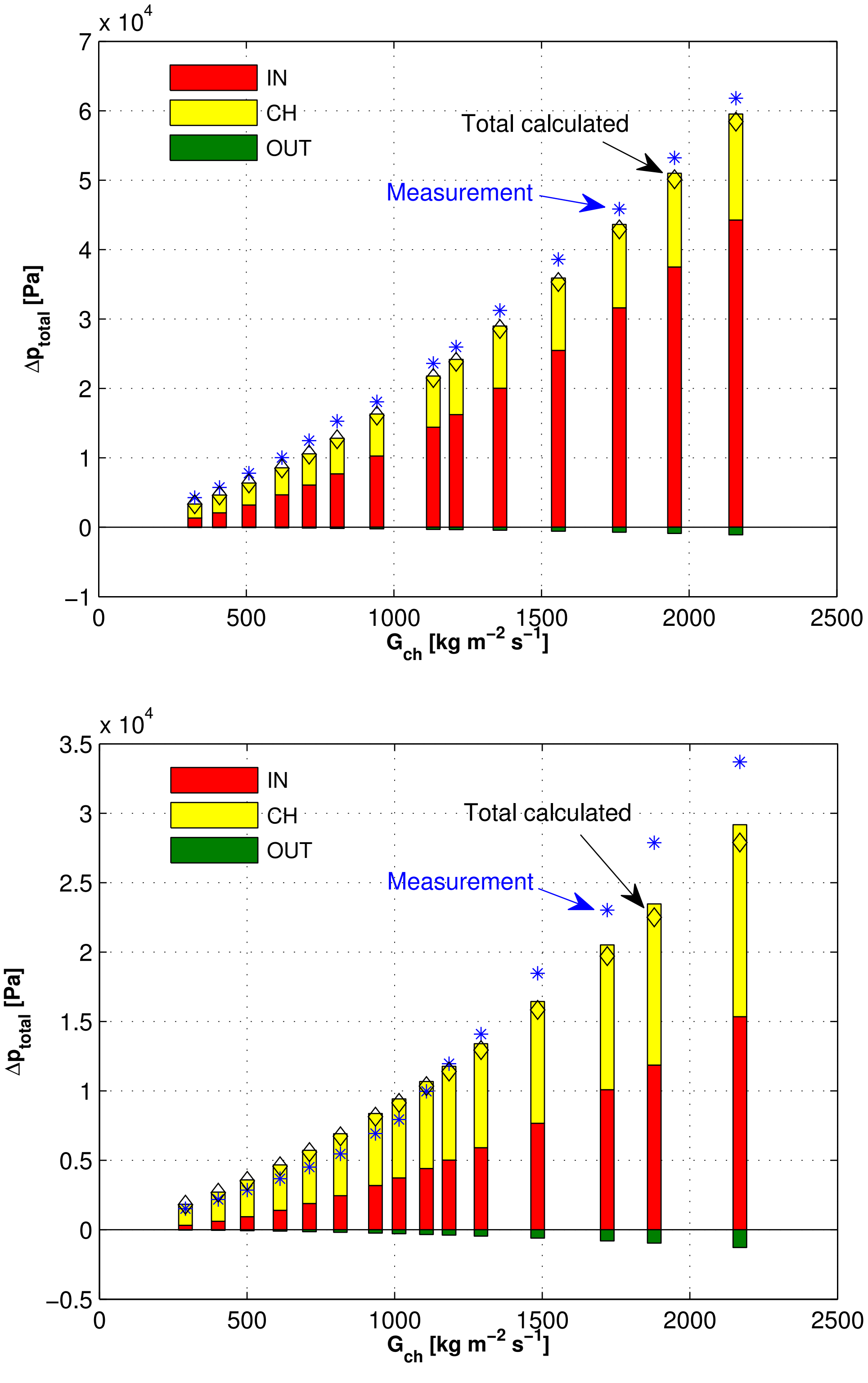

(a)

(b)

Figure 6.3: Adiabatic pressure gradients for: (a) R236fa in $e_{in,rest} = 4$, and (b) R1234ze(E) in $e_{in,rest} = 2$.

cases, due to the sudden flow contraction through the micro-orifice, $\Delta p_{exp,1}$ is a two-phase flow term (low values of vapor quality), depending on the size of the orifice and the experimental conditions, although no vapor could be observed in orifice's exit into channel since the flow expands into a bigger volume and the bubbles collapse. The single-phase flow along the length of the channel up to the outlet manifold's plenum was indicated using flow visualization videos. In order to compare the diabatic channel pressure drops, $\Delta p_{exp,1}$ needs to be separated from the value of Δp_{ch}. Therefore, the second method better suits the current study since it allows us to determine $\Delta p_{exp,1}$.

6.2 Diabatic results

Prior to data analysis, it should be mention that uniform distribution in all the channels is assumed in this study. Nonetheless, for some two-phase flow operating regimes, significant flow maldistribution, back flow and flow instabilities were observed, as was shown in Chapter 5. Some channels might be in two-phase flow regime, while others are occupied by single-phase liquid flow resulting in different channel flow resistances and thus mass fluxes. However, assuming uniform flow is the only feasible option here, since the flow rate in the individual channels cannot be measured. Moreover, in unsteady conditions, the total pressure drop is distinguishably affected by vapor back flow leading to high-amplitude and high-frequency temperature and pressure oscillations.

This experimental investigation was focused on the steady state operational conditions. Flow observations were performed with a digital video frequency of 2'000 fps, thus a governing phenomena could be observed. One needs to notice, however, that the sampling rate of the NI data acquisition system and the frequency of IR temperature measurements were lower than the one of the flow visualization camera. Therefore, the flow unsteadiness could be captured only to a limited extent via these measurements. Further investigation of flow instability is required to describe the underlying physics.

The nominal channel mass fluxes, reported in the graphs, are the averages of the values for each series of tests. The channel mass flux, G_{ch}, for an individual data point are within ±10% (often within ±4%) of the nominal value targeted for the corresponding series of tests.

6.2.1 Total pressure drop

The maximum total pressure drop of 122 kPa was obtained in the micro-evaporator with the expansion ratio of $e_{in,rest} = 4$ with two-phase flow of R236fa, as depicted in Fig. 6.4. The remaining pressure drop results are shown in Figs. B.4 – B.7 in Appendix B. In Fig. 6.4, the total two-phase pressure drop, Δp_{total}, coming from both frictional and acceleration pressure gradients, grows hugely with increasing q_b due to an increasing x_{out} (Jiang et al., 2002). The reason is that, in two-phase flow, vapor flowing along the channel with very high velocities accelerates the liquid phase, thus causing an additional pressure drop for the fluid. Moreover, the frictional pressure gradient increases due to the increasing shear stress between the two phases.

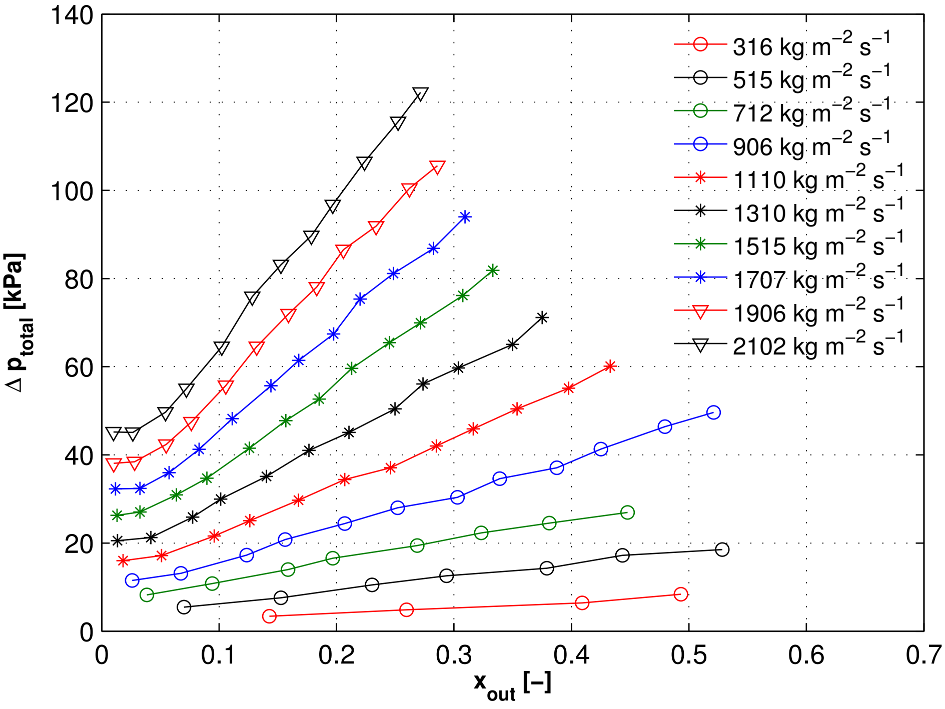

Figure 6.4: Total two-phase pressure drops of R236fa in the test section with the expansion ratio of $e_{in,rest} = 4$ in terms of the outlet vapor quality, x_{out}. In general, the difference between the channel mass flux, G_{ch}, for an individual data point in a particular curve and the reported nominal value is less than ±3.15% of the latter.

Figure 6.5 outlines the total diabatic pressure drop dependence on the dissipated base heat flux for the channel mass fluxes of 1'105 and 2'102 kg m^{-2} s^{-1}, where the pressure fluctuations were within the accuracy of the differential pressure sensor (that is, for a very stable flow). For single-phase flow in all the test cases, the total diabatic pressure drop first decreases with increasing heat input, q_b, because the liquid dynamic viscosity drops with rising temperature. The location of this transition depends on both the mass flux feeding the channels and the heat flux supplied to the micro-evaporator and is an indication of the transition from single- to two-phase flow operational regimes. Then, the pressure drop starts to take off, when the transition to the two-phase flow takes place in the test section, which is associated with an increase of the two-phase friction factor. The ascending trend of the total two-phase pressure drop, Δp_{total}, is observed with increasing vapor quality at the manifold's outlet plenum, x_{out}, as was observed in Fig. 6.4. It progresses approximately linearly regardless of the two-phase flow operating regimes. Furthermore, the pressure drop trend remains similar for the all the test fluids and micro-evaporators, while the value of Δp_{total} grows with increasing $e_{in,rest}$ and fluid viscosity for the same heat flux, q_b.

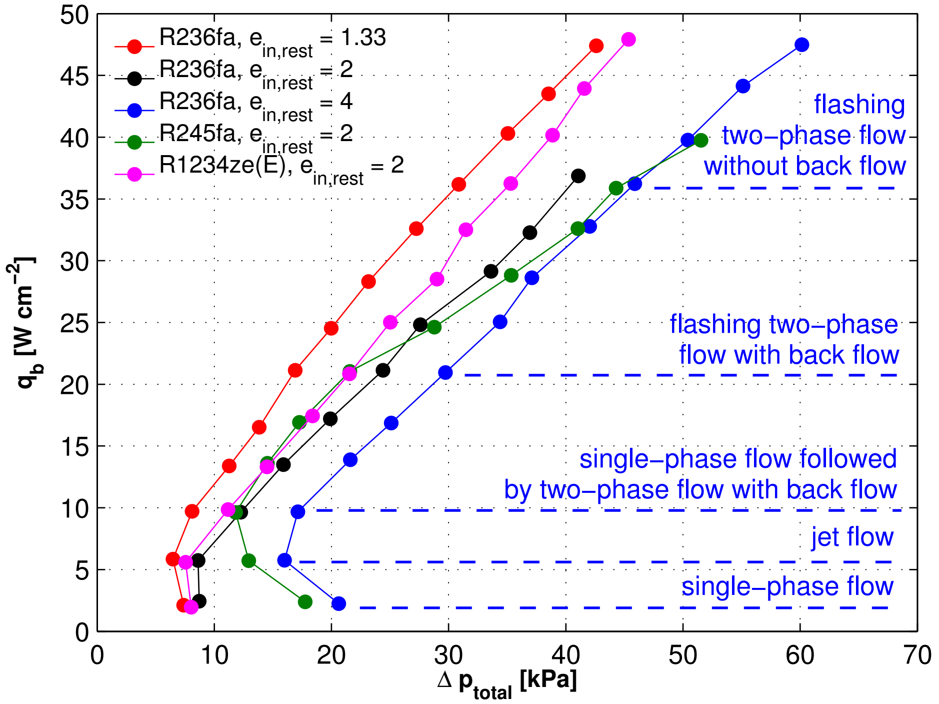

(a)

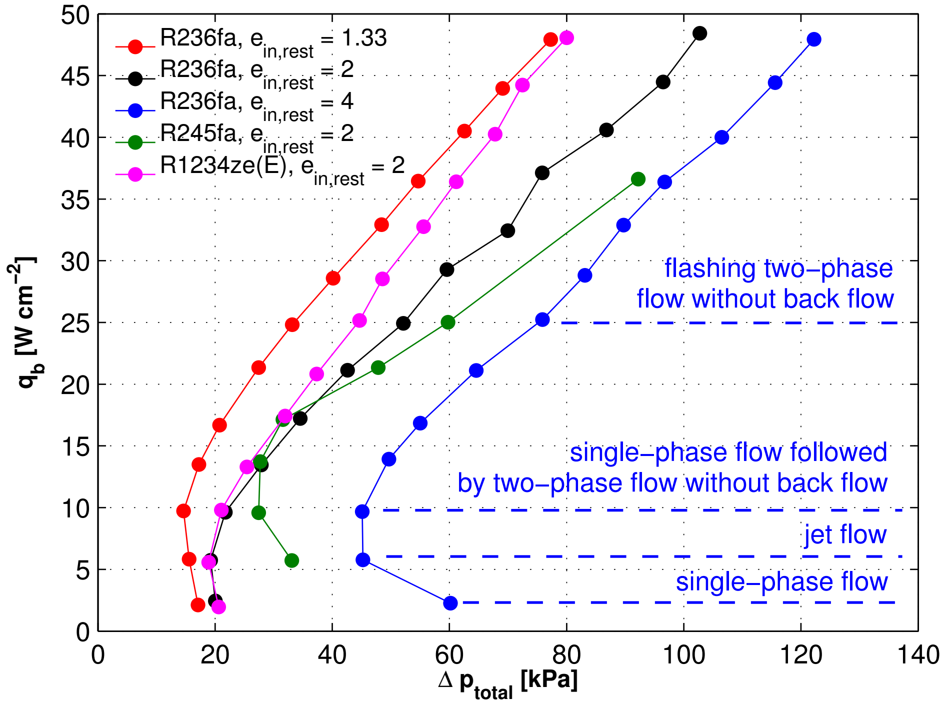

(b)

Figure 6.5: Total diabatic pressure drop dependence on the dissipated base heat flux for: (a) $G_{ch} = 1'105 \pm 5.4\% \, \mathrm{kg\,m^{-2}\,s^{-1}}$, and (b) $G_{ch} = 2'102 \pm 1.7\% \, \mathrm{kg\,m^{-2}\,s^{-1}}$.

Figure 6.6 displays the total diabatic pressure drop and the corresponding dissipated heat flux versus the average test section's base temperature for the channel mass flux of 2'102 $\mathrm{kg\,m^{-2}\,s^{-1}}$. In Fig. 6.6(a), the pressure drop slightly decreases and then climbs considerably as the average base test section's temperature increases with increasing heat flux, q_b. The fluid leaving the channels with a temperature close to the saturation temperature might be partially flashed and the bubbles produced at the manifold's outlet plenum cause the pressure to increase. Consequently the total pressure drop decreases, as marked in Fig. 6.6(a) by a black ellipsoid, in the case of R245fa flowing in the test section with the inlet restrictions of $e_{in,rest} = 2$ at low temperatures of the test section base. In Chapter 5, single-phase flow in the test section had some vapor bubbles at the manifold's outlet plenum for R245fa and R236fa flowing in the test sections with the inlet restriction of $e_{in,rest} = 2$ and 1.33, respectively. However, for the latter test case, the total pressure drop declines gently due to the lower value of vapor quality at the outlet manifold's plenum compared to R245fa.

Jiang et al. (2002) observed a linear increase of their chip's temperature with increasing input power in both single- and two-phase flow regimes with a change in the slope of the curve corresponding to the single-to-two-phase flow transition. Figure 6.6(b) confirms that the base temperature rises approximately linearly with increasing heat flux, although the two-phase flow operating regimes were found to have a significant impact on the slope of the $T_{IR,ave} - q_b$ curve. As can be seen, for R236fa flowing in the micro-evaporator of $e_{in,rest} = 4$, the slope of the curve changes from 2.0 for the single-phase flow followed by two-phase flow without back flow operating regime to 5.3 for the flashing two-phase flow without back flow operating regime (the representative images for those operating regimes were presented in Chapter 5). It can be seen that the linearity of the dependency is well improved for the latter case due to the enhancement of temporal temperature uniformity, as listed in Table 5.3. Similar observations were also made for the other test fluids and micro-evaporators, for which the flashing two-phase flow without back flow operating regime happened (for R245fa in $e_{in,rest} = 2$, R236fa in $e_{in,rest} = 2$ and 4, as well as R1234ze(E) in $e_{in,rest} = 2$). For R245fa flowing in the test section with the inlet restrictions of $e_{in,rest} = 2$ and $G_{ch} = 2'102 \pm 1.7\%\ \mathrm{kg\,m^{-2}\,s^{-1}}$, this operating regime was observed only for the base heat flux of $\sim$36.6 $\mathrm{W\,cm^{-2}}$, as indicated by a green circle in Fig. 6.6(b).

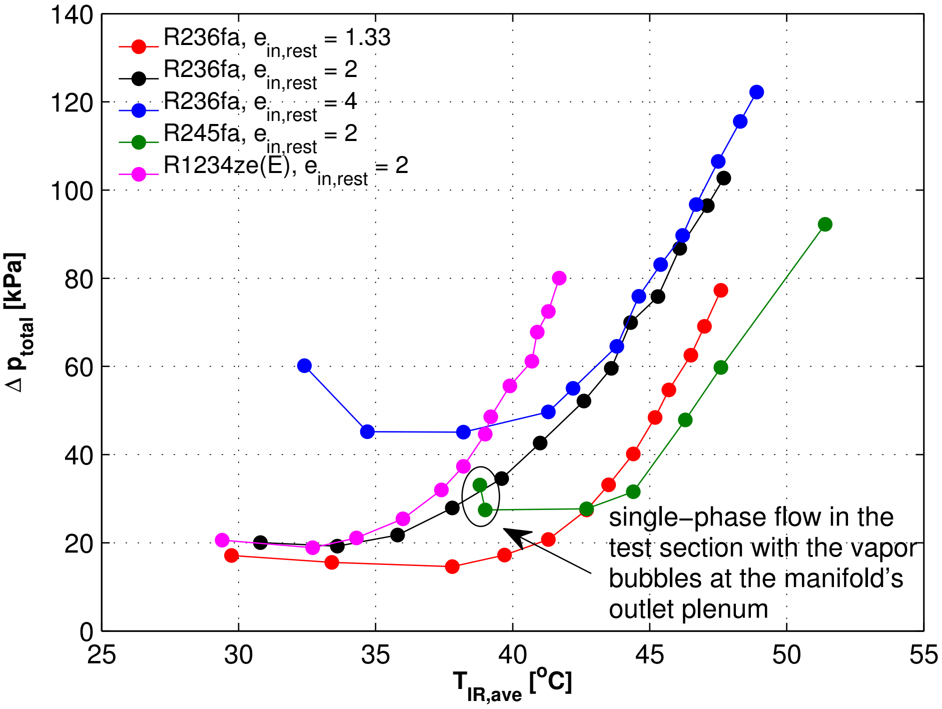

(a)

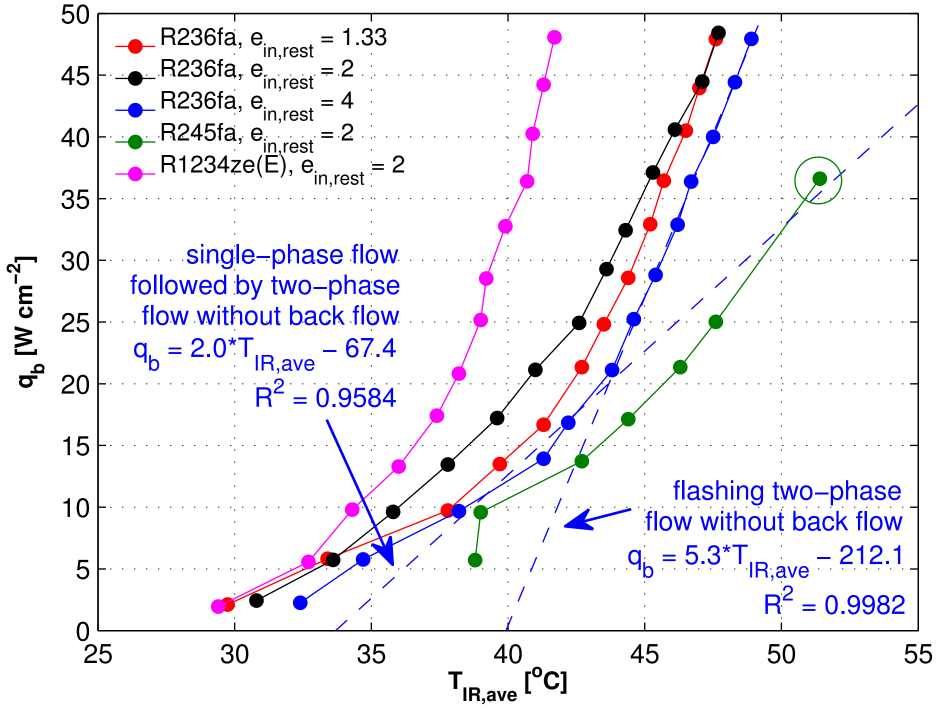

(b)

Figure 6.6: Average test section's base temperature dependence on: (a) the total diabatic pressure drop, and (b) corresponding base heat flux for the channel mass flux of $G_{ch} = 2'102 \pm 1.7\%\,\mathrm{kg\,m^{-2}\,s^{-1}}$. The fitted curves consider point no. 3−5 for the single-phase flow followed by two-phase flow without back flow operating regime and points no. 6−13 for the flashing two-phase flow without back flow operating regime (see Fig. 6.5).

6.2.2 Outlet restriction pressure loss

Costa-Patry et al. (2011b) found that the two-phase outlet restriction pressure losses ($\Delta p_{out,rest}$) in their silicon test section were up to 30% of the total pressure drop (Δp_{total}). Thus, it is important to determine the contribution of $\Delta p_{out,rest}$ in the Δp_{total} attributable to the outlet manifold's plenum for the eventual design of multi-microchannel evaporators, as shown in Fig. 6.7. Due to the complexity of the test section design, in most cases, the pressure drop up to the channel ends, $\Delta p_{ch,end}$, may be higher than Δp_{out} measured at the outlet manifold's plenum because of pressure recovery in the outlet (larger cross-sectional area deaccelerates the flow).

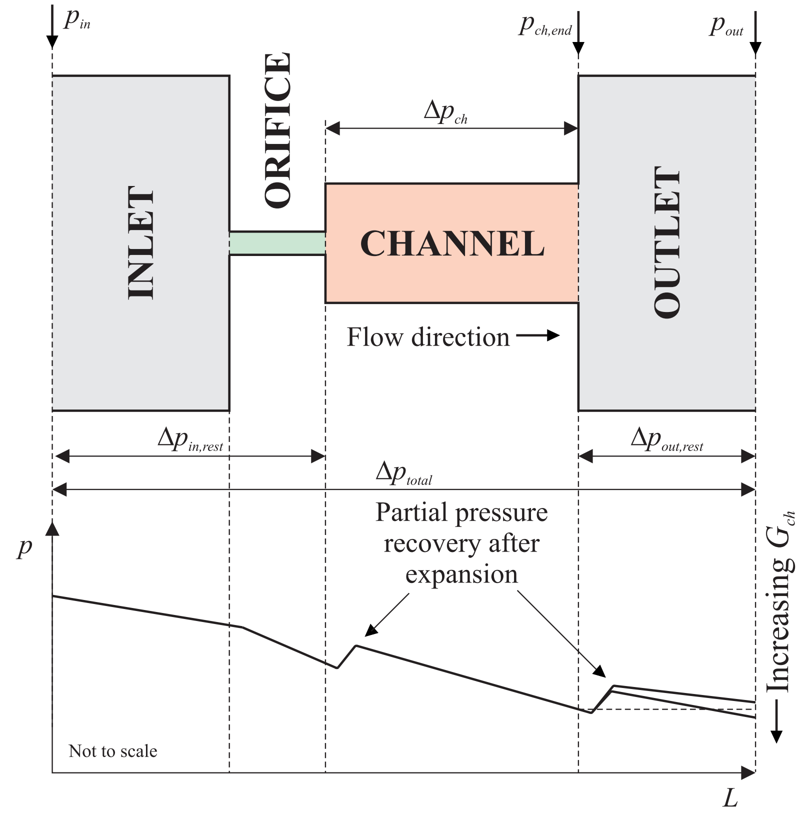
p_{in}
$p_{ch,end}$
p_{out}
ORIFICE
Δp_{ch}
INLET
CHANNEL
OUTLET
Flow direction
$\Delta p_{in,rest}$
$\Delta p_{out,rest}$
Δp_{total}
Partial pressure recovery after expansion
p
Increasing G_{ch}
Not to scale
L

Figure 6.7: Schematic of the pressure drop change within the device, where the flow direction is from left to right (based on Schneider et al. (2007)). One needs to notice that the pressure drop in the inlet, $\Delta p_{in,rest}$, and the outlet, $\Delta p_{out,rest}$, sections are simplified here to be linear.

In the present investigation, the values of $\Delta p_{out,rest}$ were determined experimentally using the method of Costa-Patry et al. (2011b). As described in Chapter 4, it is obtained as the difference between the saturation pressure at the end of the channels obtained from the local adiabatic saturation temperature measurement and the absolute pressure measured at the manifold's outlet plenum. The adiabatic conditions over the second half of the channels are obtained by shutting off the corresponding heater (*half-heating* experiments). Flow and temperature uniformities at the channel location of $z = 10\,\text{mm}$ need to be ensured, as demonstrated in Figs. 4.11 – 4.12 in Chapter 4.

In this manner, a data base of 560 points was acquired including the 3 test fluids flowing in the 3 micro-evaporators. Table 6.1 presents the operating conditions and experimental uncertainties for the *half-heating* experiments.

Table 6.1: Operating conditions and experimental uncertainties for the *half-heating* tests.

Parameter	Unit	Value	Uncertainty
G_{ch}	$\mathrm{kg\,m^{-2}\,s^{-1}}$	301 – 2’175	4.5%[a]
q_b	$\mathrm{W\,cm^{-2}}$	9.9 – 65.3	0.5%
$\Delta T_{in,sub}$	K	5.7	±1.5
$T_{out,sat}$	°C	31.7	±0.5
$T_{IR,z=10\mathrm{mm}}$	°C	30.6 – 36.2	±0.2
x_{out}	-	0.10 – 0.60	0.05
$x_{ch,end}$	-	0.06 – 0.59	0.05
Δp_{total}	kPa	3 – 103	±1
$\Delta p_{out,rest}$	kPa	$(-0.9)-30$[b]	±3.7
p_{out}	kPa	187 – 600	±1
$p_{ch,end}$	kPa	196 – 606	±3.6

---

[a] The $\Delta p_{out,rest}$ curve fitting is performed for each micro-evaporator separately, thus the uncertainty in G_{ch} takes into account a variation of channel dimensions within one test section that was estimated to be ±3 μm.

[b] Without considering the test case of R1234ze(E) in the micro-evaporator with the inlet restrictions of $e_{in,rest} = 2$, for which the $\Delta p_{out,rest}$ varied between (−20) and 8.7 kPa.

The tests were performed for R245fa and R236fa within the test sections with the expansion ratios of $e_{in,rest} = 1.33$, 2, and 4 including flow visualization and for R1234ze(E) inside the micro-evaporator with 50 μm-wide micro-orifices without visual inspection due to the fact that, in general, this fluid provides relatively high Reynolds numbers, and thus uniform flow distribution among the channels. An analysis of the two-phase flow visualization videos for R245fa and R236fa enabled confirmation of those conditions, for which the experimental assumptions were valid. For R1234ze(E) flowing in the test section with the expansion ratio of $e_{in,rest} = 2$, all the acquired data (94 points) were considered. Therefore, for this test fluid at low channel mass fluxes, the reliability of the measurement might be influenced by flow instabilities and flow maldistribution.

The present experimental results of $\Delta p_{out,rest}$ for R245fa and R236fa (the test cases supported by flow visualization) were compared with the correlation of Costa-Patry (2011), given by the following equation, which was developed based on the Collier and Thome (1994)'s relation for two-phase flow pressure recovery through a sudden expansion:

$$\Delta p_{out,rest} = \frac{G_{ch}^2}{\rho_l} \left(\frac{W_{ch}}{W_{in,rest}} \right)^{0.2274} x_{ch,end} \frac{\rho_l}{\rho_v} \tag{6.6}$$

As a result, 76.8% of data points were within an error band of ±50%, which is relatively good considering the fact that the minor pressure loss coefficients are usually strong functions of geometry parameters, which are different here. Figures 6.8 and 6.9 show the Δp_{total} and $\Delta p_{out,rest}$ results in the half-heated micro-evaporators versus the outlet vapor quality, x_{out}, and the vapor quality at the channel ends, $x_{ch,end}$, respectively. In Fig. 6.8(b), the $x_{ch,end}-\Delta p_{out,rest}$ curves including only the stable flows are very smooth, whereas for R1234ze(E) in $e_{in,rest} = 2$, the $\Delta p_{out,rest}$ values fluctuate and the curves for two different channel mass fluxes might overlap, as presented in Fig. 6.9(b). In Figs. 6.8(b) and 6.9(b), the $\Delta p_{out,rest}$ increases with increasing $x_{ch,end}$ and channel mass flux, G_{ch}. The two-phase flow tests revealed that the $\Delta p_{out,rest}$ can represent up to ∼46% of the Δp_{total} for R236fa in the half-heated test section with the 50 μm-wide micro-orifices.

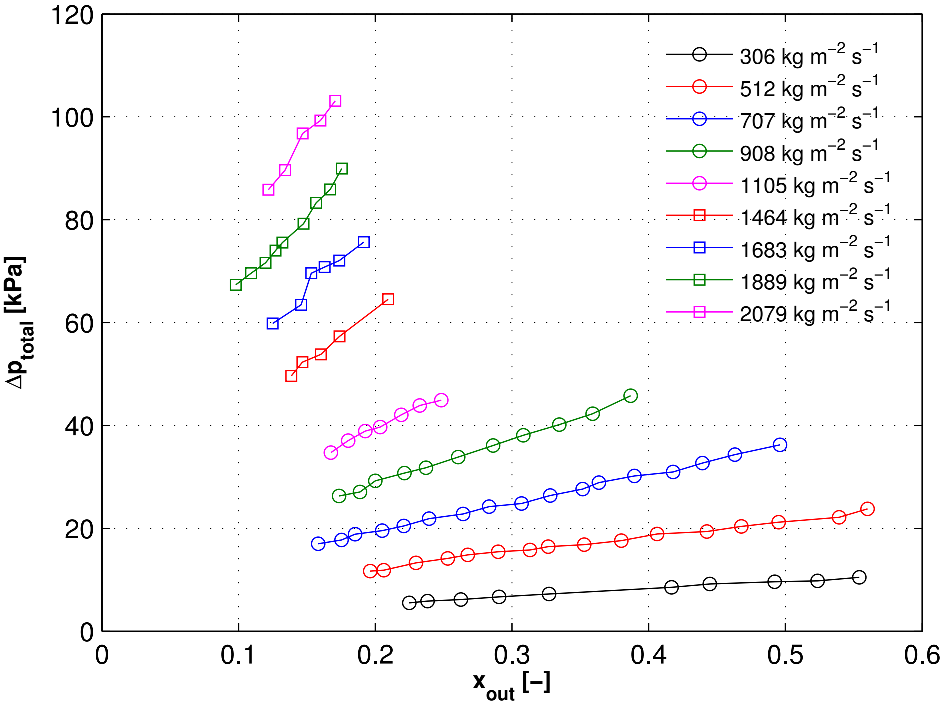

(a)

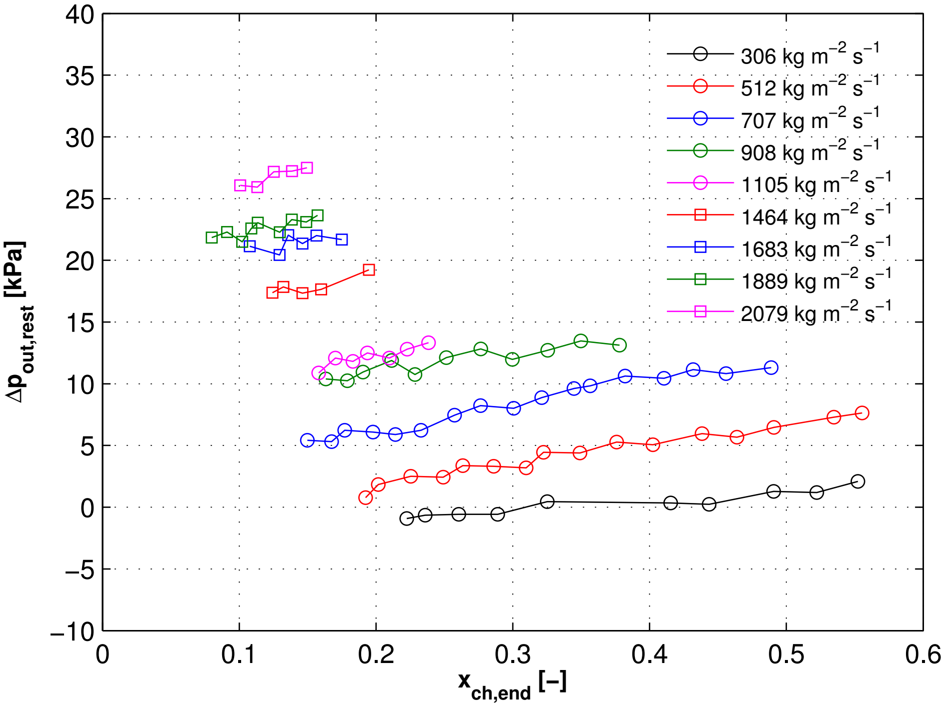

(b)

Figure 6.8: (a) Δp_{total} versus x_{out}, and (b) $\Delta p_{out,rest}$ versus $x_{ch,end}$ for the two-phase flow of R236fa flowing in the half-heated micro-evaporator with the inlet restrictions of $e_{in,rest} = 4$. The difference between the channel mass flux for an individual data point and the reported nominal value is within ±2.0% of the latter. Experimental results were selected based on flow visualization.

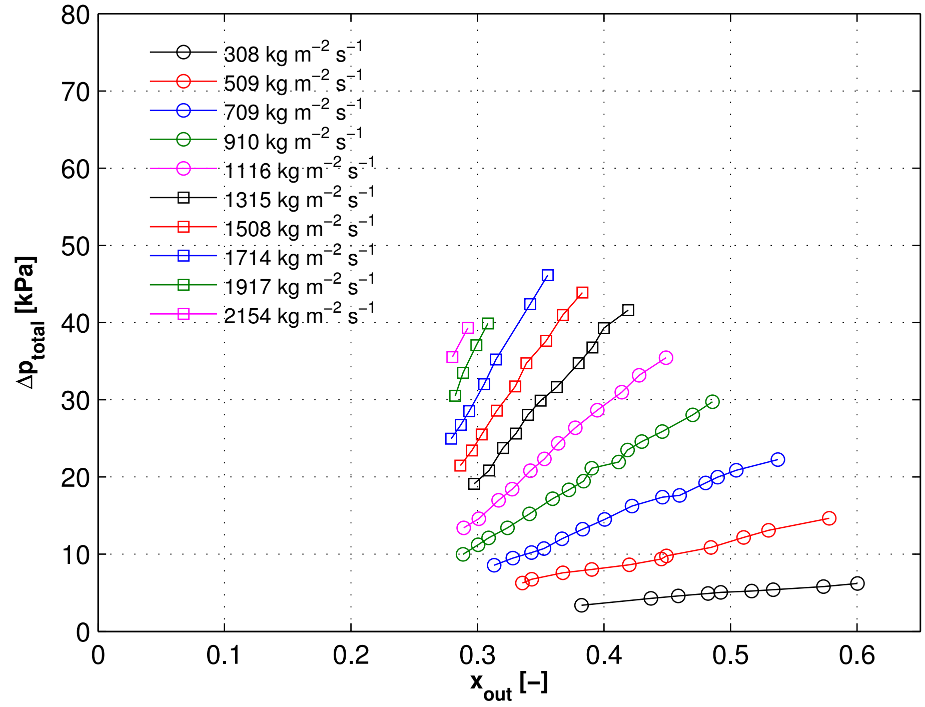

(a)

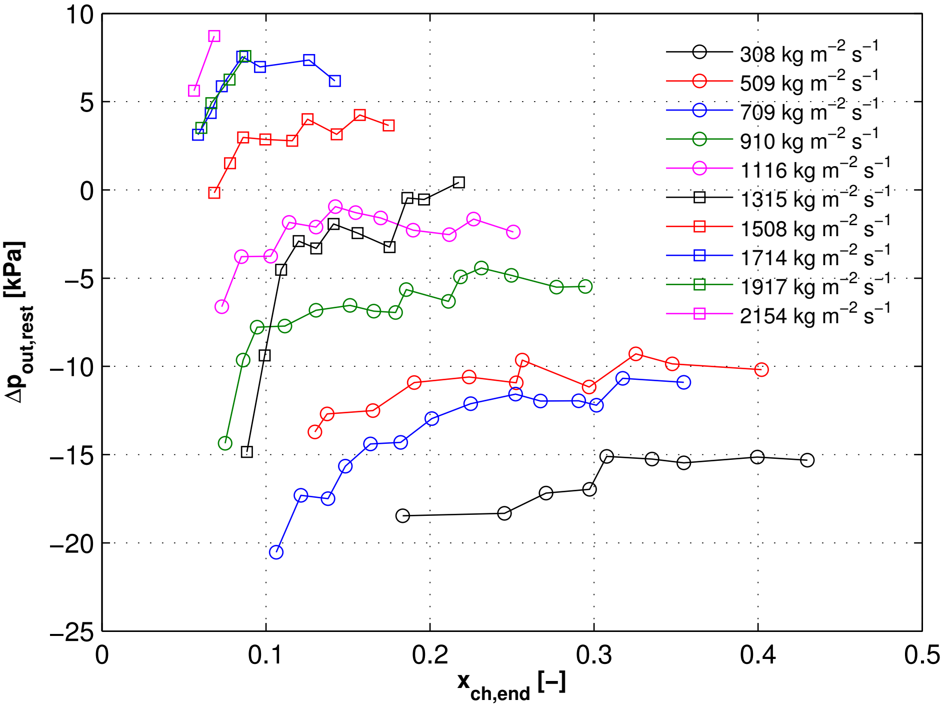

(b)

Figure 6.9: (a) Δp_{total} versus x_{out}, and (b) $\Delta p_{out,rest}$ versus $x_{ch,end}$ for the two-phase flow of R1234ze(E) flowing in the half-heated micro-evaporator with the inlet restrictions of $e_{in,rest} = 2$. The difference between the channel mass flux for an individual data point and the reported nominal value is within ±2.16% of the latter. Experiments were conducted without visual observation, thus all the data were considered.

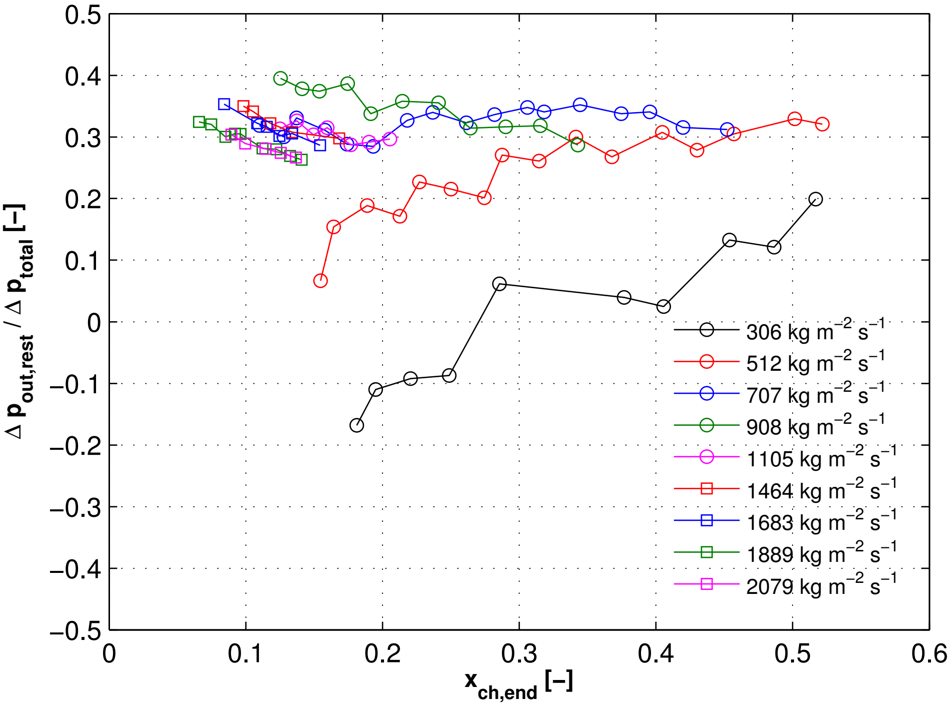

(a)

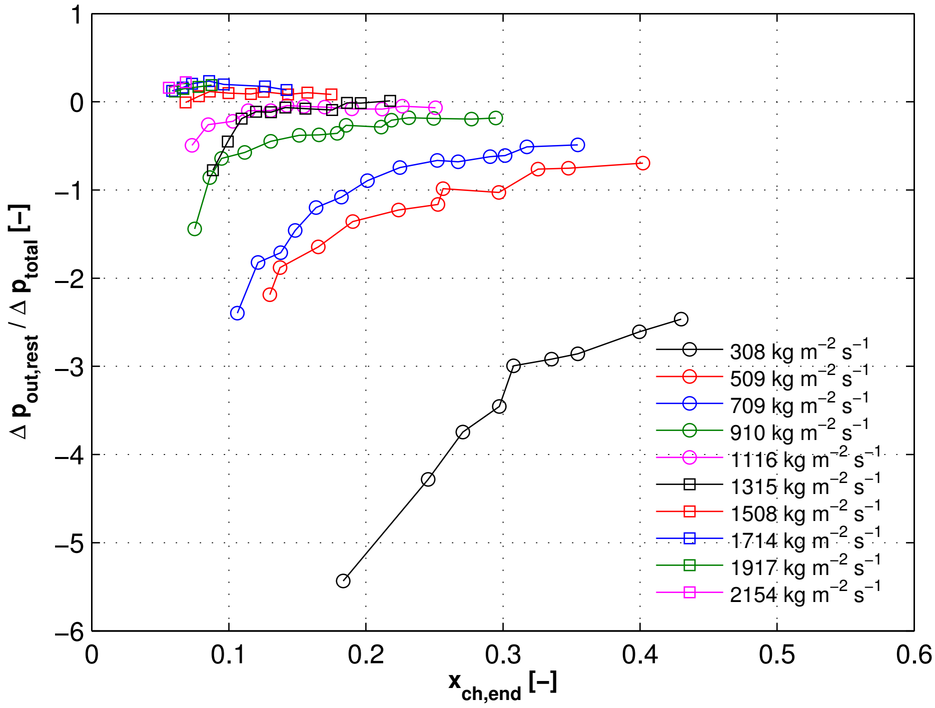

(b)

Figure 6.10: Outlet restriction pressure drop ratios for: (a) R236fa in $e_{in,rest} = 4$, and (b) R1234ze(E) in $e_{in,rest} = 2$.

As shown in Fig. 6.11, the experimental data were correlated based on the outlet conditions for each test case separately using the following equation:

$$\Delta p_{out,rest} = a\psi^{m} - b \tag{6.7}$$

where

$$\psi = x_{out}\left(G_{ch}/G_{ch,min}\right)^{4} \tag{6.8}$$

and the parameters: a, b, and m, as well as $G_{ch,min}$, are listed in Table 6.2, where $G_{ch,min}$ refers to the minimum channel mass flux. Firstly, one might spot that the reported parameters for R236fa in the test section with the inlet restrictions of $e_{in,rest} = 2$ differ considerably from the other test cases, which is associated with the range of experimental conditions tested in this case ($G_{ch,min}$). Secondly, the experimental data are well represented by the $\Delta p_{out,rest}$ correlations except for R1234ze(E) in the micro-evaporator with the inlet restrictions of $e_{in,rest} = 2$, for which the goodness of the fit, R^2, is the lowest. The scatter of the experimental data for R1234ze(E) in the micro-evaporator with the expansion ratio of $e_{in,rest} = 2$ in Fig. 6.11(b) is linked with the fact that no observations were taken to segregate and exclude the non-stable and / or non-uniform flows.

Table 6.2: Parameters and goodness of fit for the $\Delta p_{out,rest}$ curve fitting.

Fluid	$e_{in,rest}$	a	b	m	$G_{ch,min}$	R^2
	-	-	-	-	kg m^{-2} s^{-1}	-
R245fa	2	32'830	11'705	0.28079	1'089	0.97881
R236fa	1.33	3'618	2'219.3	0.53299	507	0.95531
	2	$2.9391 \cdot 10^{5}$	$2.8277 \cdot 10^{5}$	0.022199	911	0.96003
	4	11'364	9'261.9	0.1977	306	0.98661
R1234ze(E)	2	5'396.1	20'904	0.26935	308	0.85276

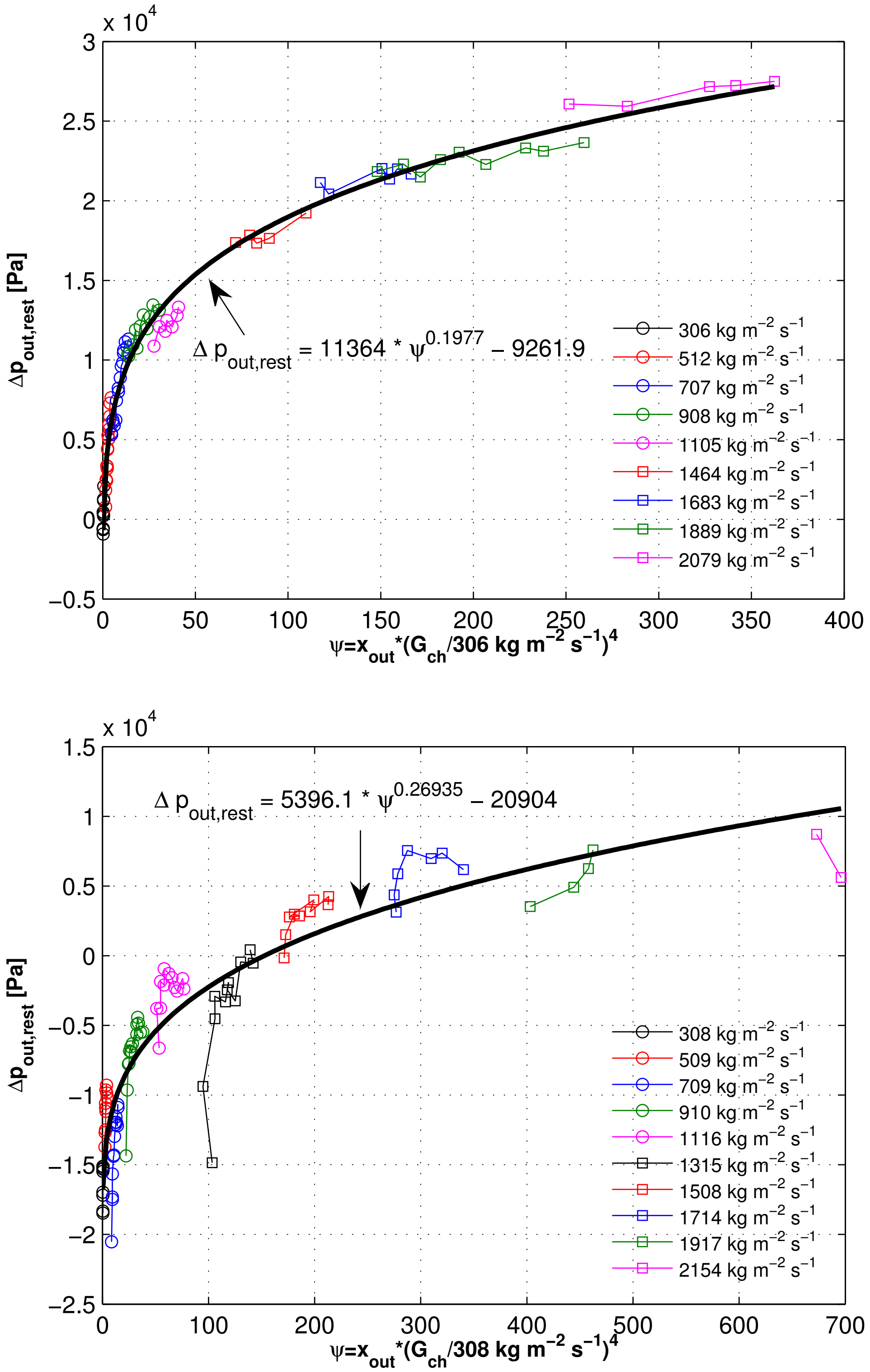

(a)

(b)

Figure 6.11: $\Delta p_{out,rest}$ curve fitting for: (a) R236fa in $e_{in,rest} = 4$, and (b) R1234ze(E) in $e_{in,rest} = 2$.

6.2.3 Channel pressure drop

Knowing the inlet, $\Delta p_{in,rest}$, and the outlet restriction pressure losses, $\Delta p_{out,rest}$, the channel pressure drops, Δp_{ch}, were obtained by subtracting those from the total pressure drops, Δp_{total}. The channel pressure drops are shown in Figs. 6.12, 6.13 and B.8 – B.10 in Appendix B. The maximum channel pressure drop of ~73.4 kPa was obtained for R236fa in the micro-evaporator of $e_{in,rest} = 2$ with the vapor quality at the channel ends of $x_{ch,end} \approx 23\%$, as presented in Fig. 6.12. It represents ~65% of the Δp_{total} for this test case. The remaining quantity is distributed between the inlet and the outlet restrictions, where the $\Delta p_{out,rest}$ is ~2x of the $\Delta p_{in,rest}$. The slightly negative values of $x_{ch,end}$ correspond to the single-phase flow in the test section with the vapor bubbles at the manifold's outlet plenum and the jet flow operating regimes in Fig. 6.13, where the negative channel pressure drops are probably associated with the estimation of the inlet and the outlet restriction pressure losses, as well as the accuracy of the differential pressure sensor at low values of Δp. These negative values always remained within the uncertainty of the measurement of Δp_{ch}.

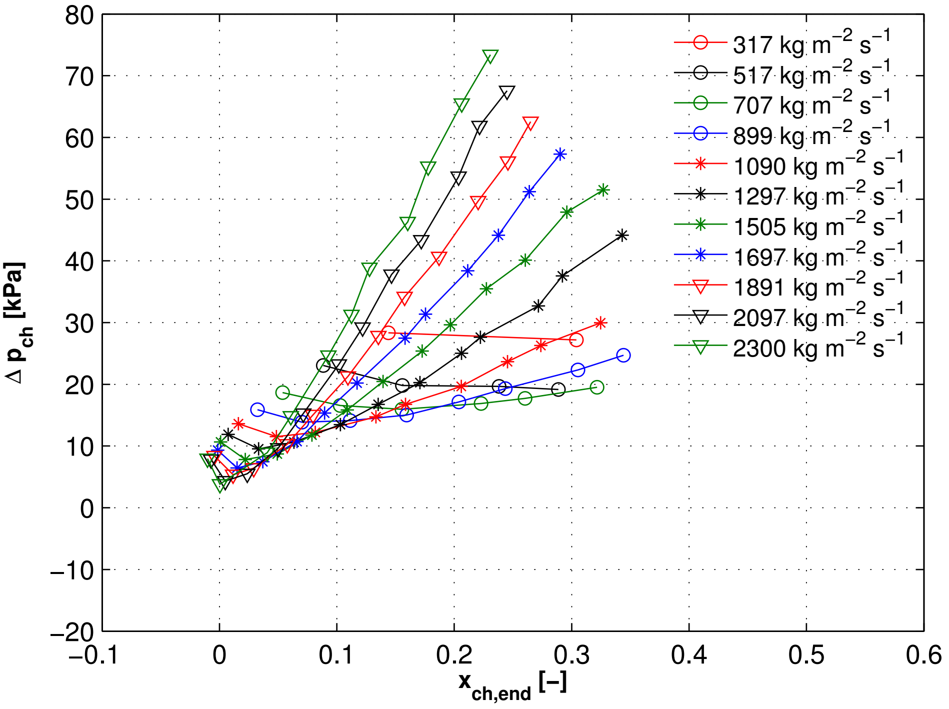

Figure 6.12: Δp_{ch} for R236fa flowing within the micro-evaporator with the inlet restrictions of $e_{in,rest} = 2$.

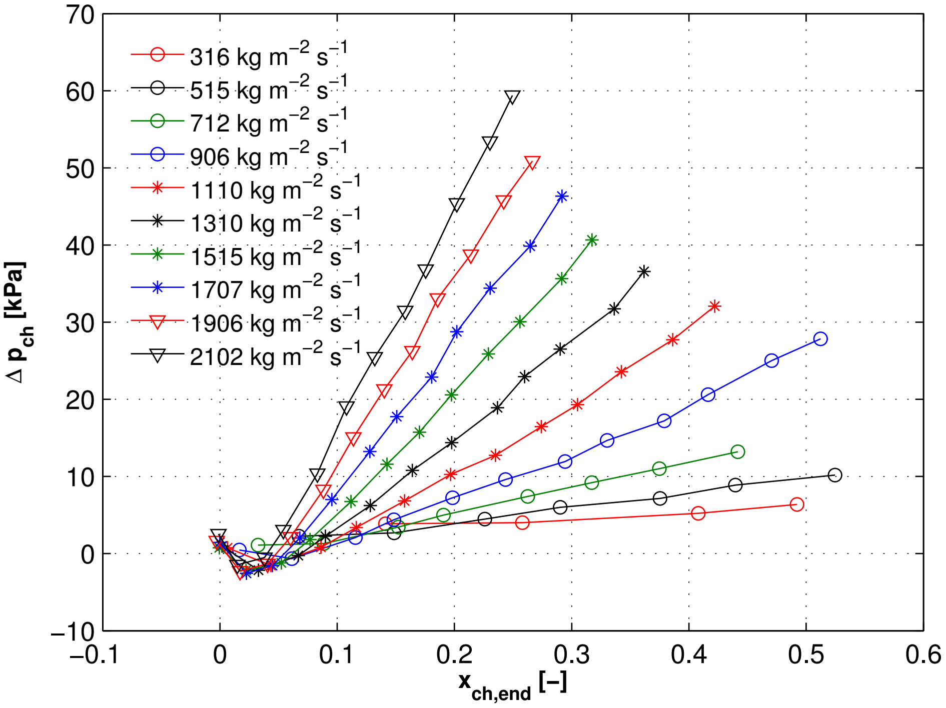

Figure 6.13: Δp_{ch} for R236fa flowing within the micro-evaporator with the inlet restrictions of $e_{in,rest} = 4$.

This research focuses on stable and uniform flows, therefore only the pressure drop data for the flashing two-phase flow without back flow operating regime are considered here. In Fig. 6.15, Δp_{ch} increases almost linearly with increasing $x_{ch,end}$ and follows the trend of Δp_{total}. As illustrated, the $\Delta p_{ch} \,/\, \Delta p_{total}$ ratio for this operating regime varies from ∼0.4 for low-$x_{ch,end}$ flows up to ∼0.7 as the vapor quality increases. The corresponding ratios of $\Delta p_{in,rest} \,/\, \Delta p_{total}$ and $\Delta p_{out,rest} \,/\, \Delta p_{total}$ are presented in Fig. 6.15. Generally, the pressure loss through the outlet is about twice of that at the inlet.

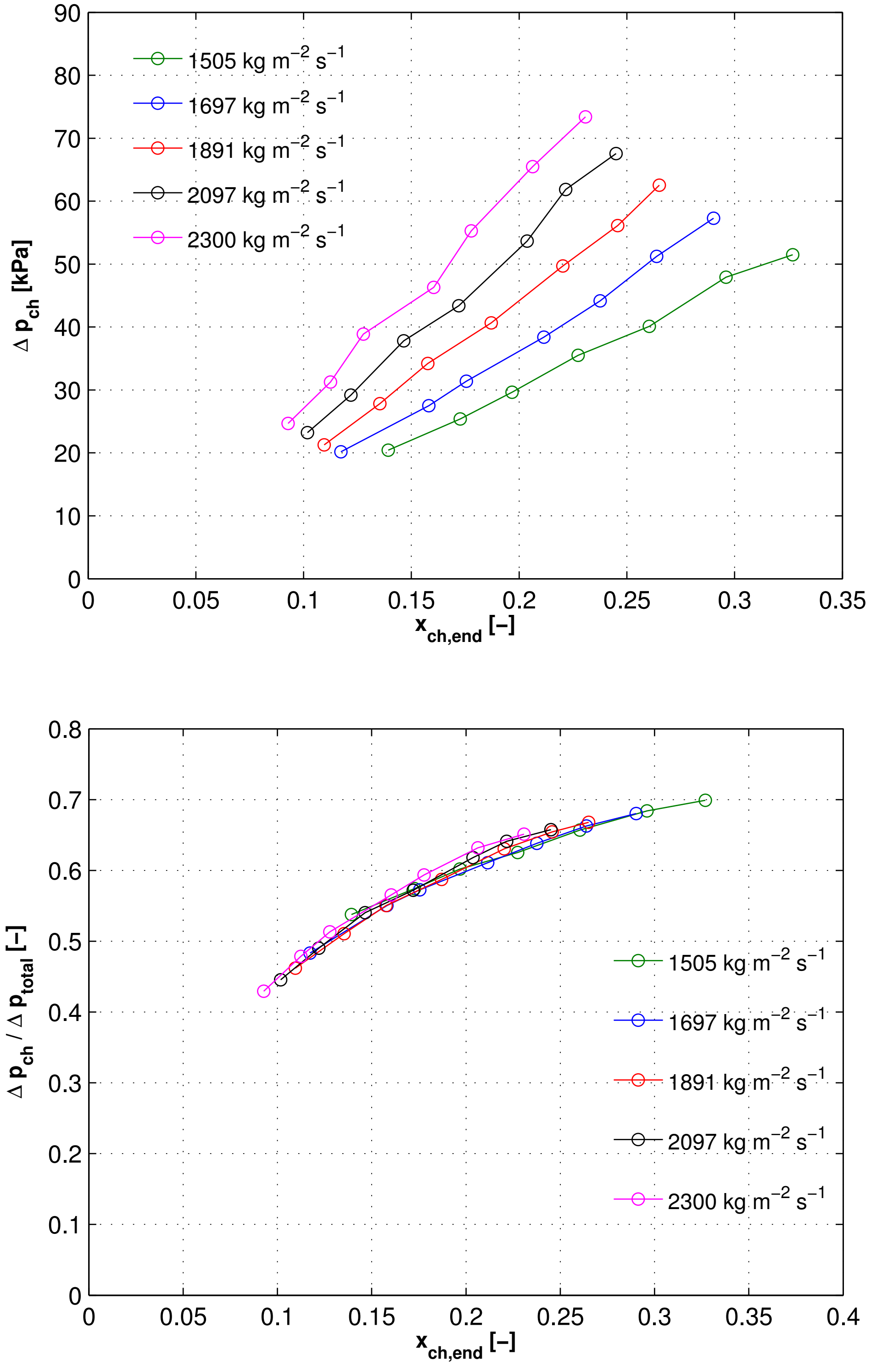

(a)

(b)

Figure 6.14: (a) Δp_{ch}, and (b) $\Delta p_{ch} \, / \, \Delta p_{total}$ ratio for R236fa flowing within the micro-evaporator with the inlet restrictions of $e_{in,rest} = 2$.

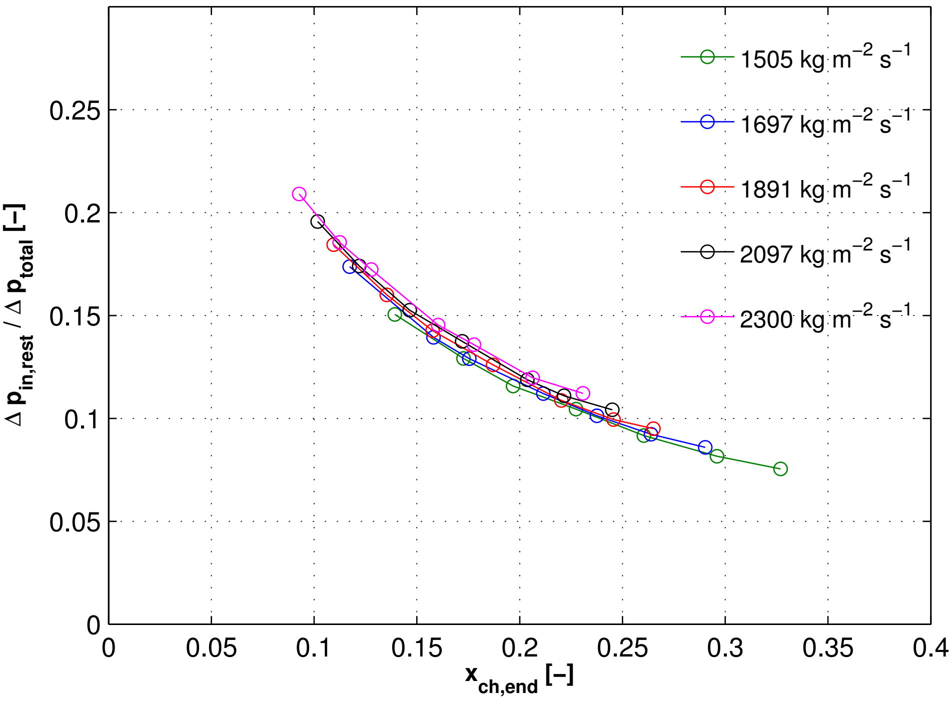

(a)

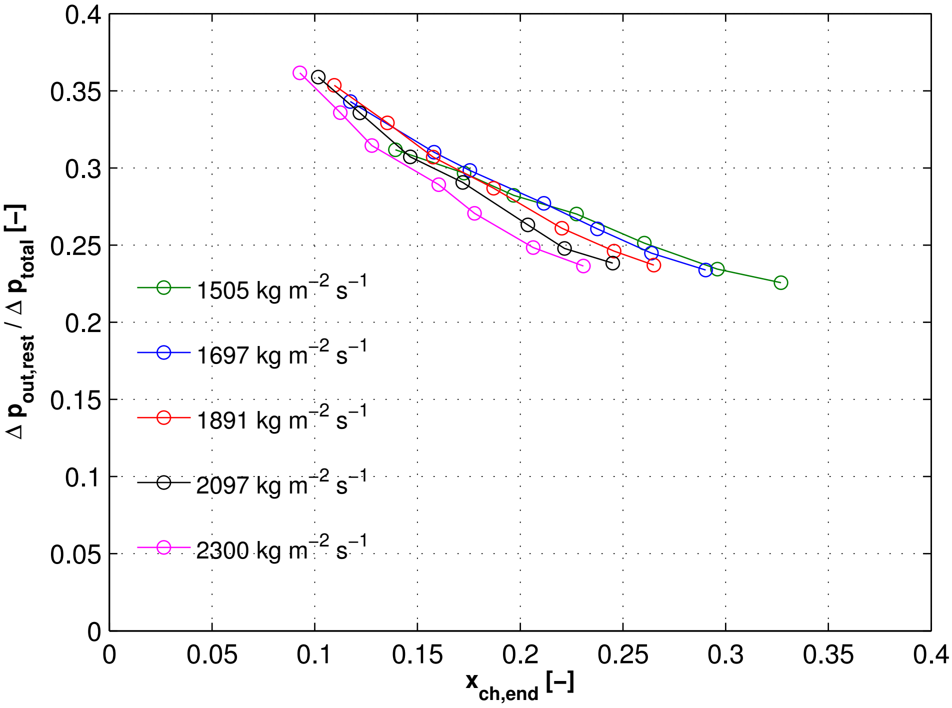

(b)

Figure 6.15: (a) $\Delta p_{in,rest} \, / \, \Delta p_{total}$, and (b) $\Delta p_{out,rest} \, / \, \Delta p_{total}$ ratios for R236fa flowing within the micro-evaporator with the inlet restrictions of $e_{in,rest} = 2$.

Conceptually, if the channel itself remains unchanged, the values of Δp_{ch} for the same value of $x_{ch,end}$ should also be the same. In Fig. 6.16, the channel pressure drops for R236fa flowing in the micro-evaporators with the inlet restrictions of $e_{in,rest} = 2$ and 4 are compared at two different mass fluxes for the flashing two-phase flow without back flow operating regime. A noticeable bias is seen between $e_{in,rest} = 2$ and 4 for the same G_{ch} associated with different two-phase flow patterns within a channel. High-speed flow visualization videos confirmed that the flashed bubbles coming into the channels affect the two-phase flow structure after the inlet orifice and consequently the channel pressure drop. The difference in the channel pressure drops for the two inlet orifices is notable but to some extension within their measurement error bands and the method for backing out these values. Moreover, as shown in Figs. 5.1 − 5.6 in Chapter 5, the expansion ratio of the micro-orifice has a significant effect on the overall operational stability of the micro-evaporator.

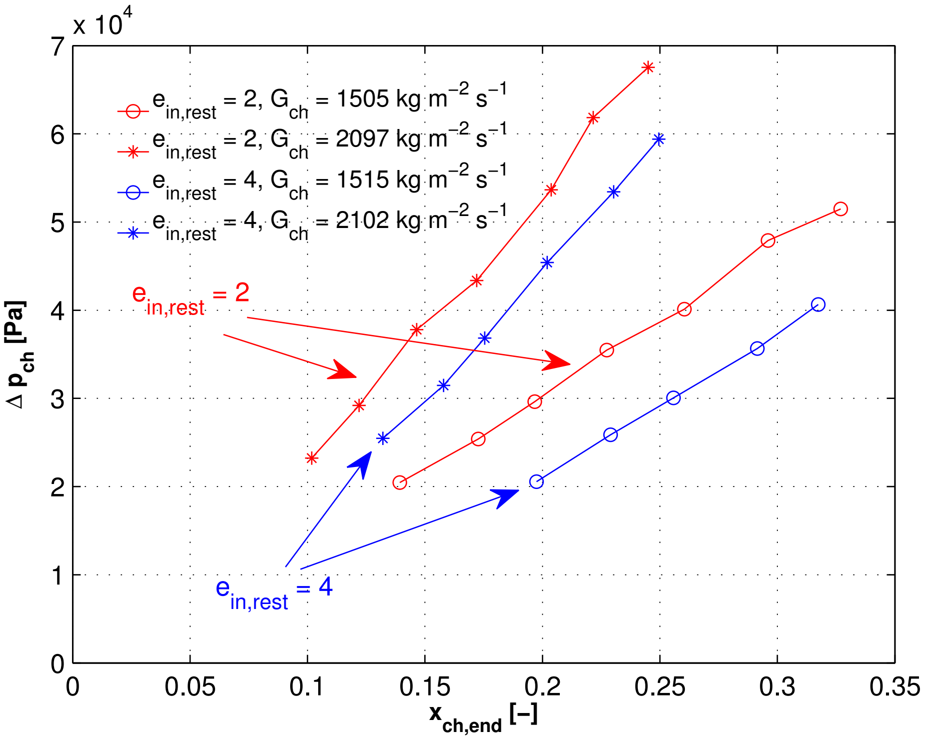

Figure 6.16: Δp_{ch} for the flashing two-phase flow without back flow operating regime for R236fa flowing within the micro-evaporator with the inlet restrictions of $e_{in,rest} = 2$ and 4.

6.3 Fluid temperature

Assuming a linear pressure drop over the length of the channel, the values of Δp_{ch} can be used to determine the local saturation temperature of the refrigerant along the channels, $T_{fl,sat}$, based on the vapor pressure curve. Then, the values of $T_{fl,sat}$ can be used to determine the local heat transfer coefficients. The alternative way to obtain $T_{fl,sat}$ is to apply a well-established two-phase flow pressure drop prediction method for the channels. Several of them, listed in Table 2.1 in Chapter 2, are compared to the experimentally obtained values of Δp_{ch}.

The examined two-phase pressure drop prediction methods were developed for different channel geometries, therefore the following definition of hydraulic diameter was employed:

$$D_h = \frac{4W_{ch}H_{ch}}{2W_{ch} + 2H_{ch}} \tag{6.9}$$

The homogeneous model was implemented using the fluid viscosity according to Cicchitti et al. (1960). The Cioncolini et al. (2009) annular pressure drop prediction method is not suitable for low vapor qualities, thus the Lockhart and Martinelli (1949) model was used for vapor qualities below the isolated bubble to coalescing bubble (IB - CB) transition of Ong (2010) given as follows:

$$x_{IB-CB} = 0.36\left(Co^{0.20}\right)\left(\frac{\mu_{vo}}{\mu_{lo}}\right)^{0.65}\left(\frac{\rho_{vo}}{\rho_{lo}}\right)^{0.9}\mathrm{Re}_{vo}^{0.75}Bo^{0.25}We_{lo}^{-0.91} \tag{6.10}$$

where

$$Co = \frac{\sqrt{\frac{\sigma}{g(\rho_l-\rho_v)}}}{D_h} \tag{6.11}$$

and the subscripts *vo* and *lo* refer to vapor only and liquid only, respectively.

Figure 6.17(a) presents one experimental example of the pressure trend over the length of the channel assuming a linear pressure drop between the inlet and the outlet of the channel after subtracting $\Delta p_{in,rest}$ and $\Delta p_{out,rest}$ along with several prediction methods considering a stable flow of R236fa flowing in the test section of the inlet restriction of $e_{in,rest} = 2$ for the channel mass flux of 1'471 $\mathrm{kg\,m^{-2}\,s^{-1}}$ and the dissipated base heat flux of 48.2 $\mathrm{W\,cm^{-2}}$ (the straight line illustrates the actual pressure drop for this set of conditions). The results shown in Fig. 6.17(a) include the momentum pressure drop calculated using the void fraction of Steiner (1993), as suggested by Thome (2010), if it was not specified by a respective model. The corresponding local saturation temperatures of the fluid are illustrated in Fig. 6.17(b). All the methods show the same *belly* shape of the saturation temperature profile. However, significant discrepancies at the exit of the channel can be seen between them. Generally, when comparing to the experimentally measured pressure drops, the models overpredict the value of Δp_{ch}, which will have a crucial effect on the determination of the heat transfer coefficients. For instance in Fig. 6.17(b), the saturation temperature at the end of the channel varies from ~28 °C for homogeneous model up to ~35 °C obtained for Lee and Garimella (2008) prediction method leading to a difference of ~50% in heat transfer coefficient at the $T_w \approx 42\,°\mathrm{C}$.

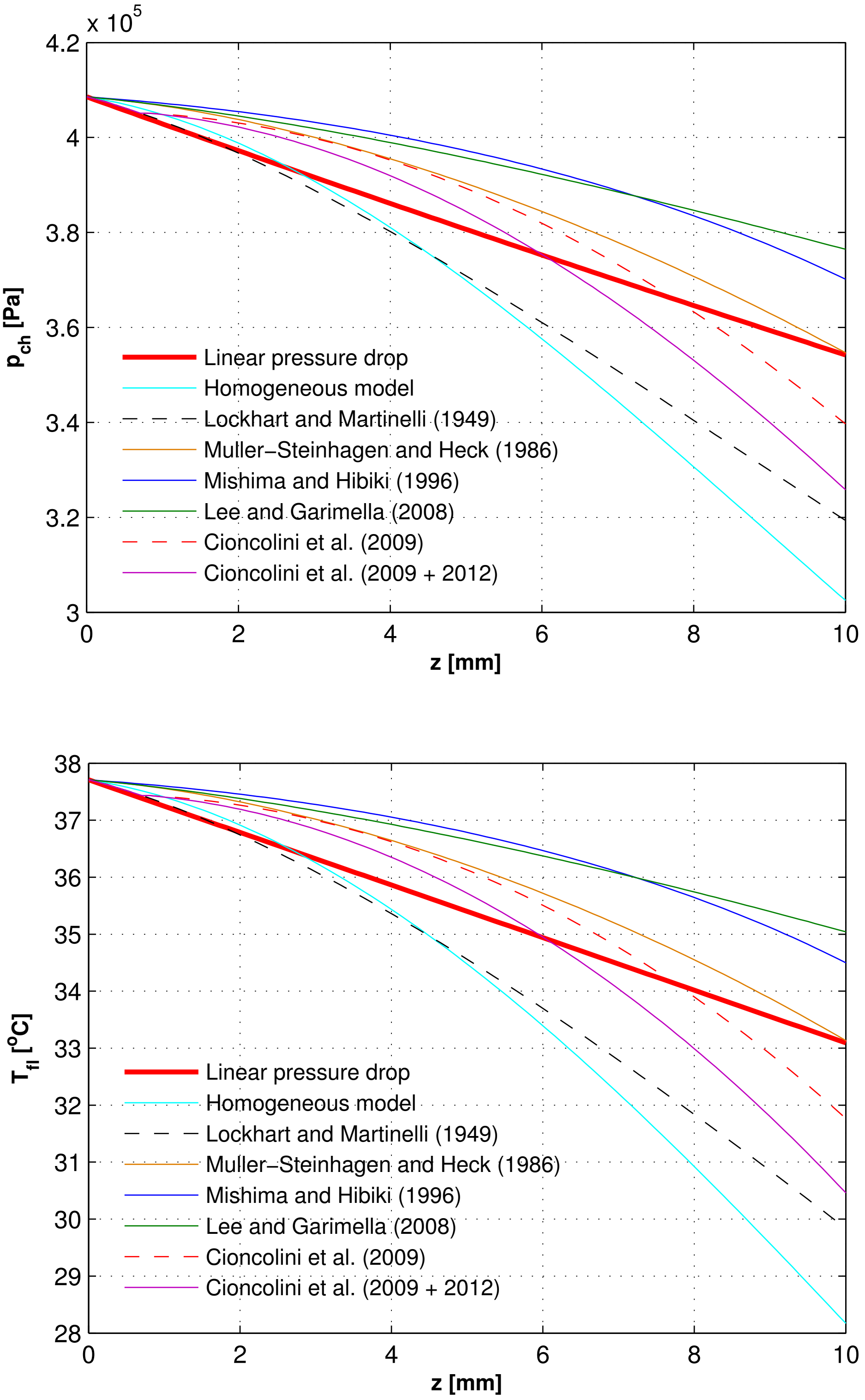

(a)

(b)

Figure 6.17: Comparison of measured and predicted values of (a) Δp_{ch}, and (b) corresponding $T_{fl,sat}$ for the flashing two-phase flow without back flow operating regime for R236fa flowing in the test section with the inlet restrictions of $e_{in,rest} = 2$, $G_{ch} = 1\text{'}471\,\mathrm{kg\,m^{-2}\,s^{-1}}$, $q_b = 48.2\,\mathrm{W\,cm^{-2}}$.

Table 6.3 lists the mean absolute errors, MAE [%], between the experimental and the predicted pressure drop values calculated based on:

$$MAE = \frac{1}{i} \overset{i}{\Sigma} \left| \frac{\Lambda_{meas} - \Lambda_{pred}}{\Lambda_{meas}} \right| \cdot 100\% \tag{6.12}$$

where Λ relates to the evaluated parameter and i is a number of data points. To eliminate the influence of flow instabilities and flow maldistribution, the present comparison was performed only for the flashing two-phase flow without back flow operating regime. This set of values should be taken only for qualitative comparison, since a dedicated set of results with direct measurements of Δp_{ch} would be required to do a more exact quantitative comparison.

Table 6.3: Comparison of the experimental results with the correlations described in Chapter 2 considering the flashing two-phase flow without back flow operating regime.

Fluid	R245fa	R236fa	R236fa	R1234ze(E)	MAE
$e_{in,rest}$ [-]	2	2	4	2	%
Homogeneous model	182.07	410.53	499.28	50.20	285.52
Lockhart and Martinelli (1949)	93.33	381.26	425.56	102.16	250.58
Muller-Steinhagen and Heck (1986)	47.52	165.20	167.55	27.35	101.91
Mishima and Hibiki (1996)	61.47	10.82	15.15	59.56	36.75
Lee and Garimella (2008)	19.65	172.24	171.42	26.10	97.35
Cioncolini et al. (2009)	54.91	212.48	222.48	19.86	127.43
Cioncolini et al. (2009) + Cioncolini and Thome (2012)	69.33	281.27	292.68	39.55	170.71

As demonstrated in Fig. 6.16, the two-phase flow patterns within the microchannel have a significant effect on the pressure drop. This effect is taken into account in the Cioncolini et al. (2009) prediction model that appears to give the intermittent values and it was found to be the best method in Costa-Patry (2011), who had a differential pressure transducer for direct measurement of Δp_{ch} in channels of similar width. Therefore, in the present study, the heat transfer data will be reduced using the Cioncolini et al. (2009)'s annular pressure drop prediction method with the Lockhart and Martinelli (1949) model for vapor qualities below the isolated bubble to coalescing bubble (IB-CB) transition of Ong (2010) and applying a ratio of the experimental and the predicted pressure drop values. An example of the prorated fluid temperature is shown in Fig. 6.18.

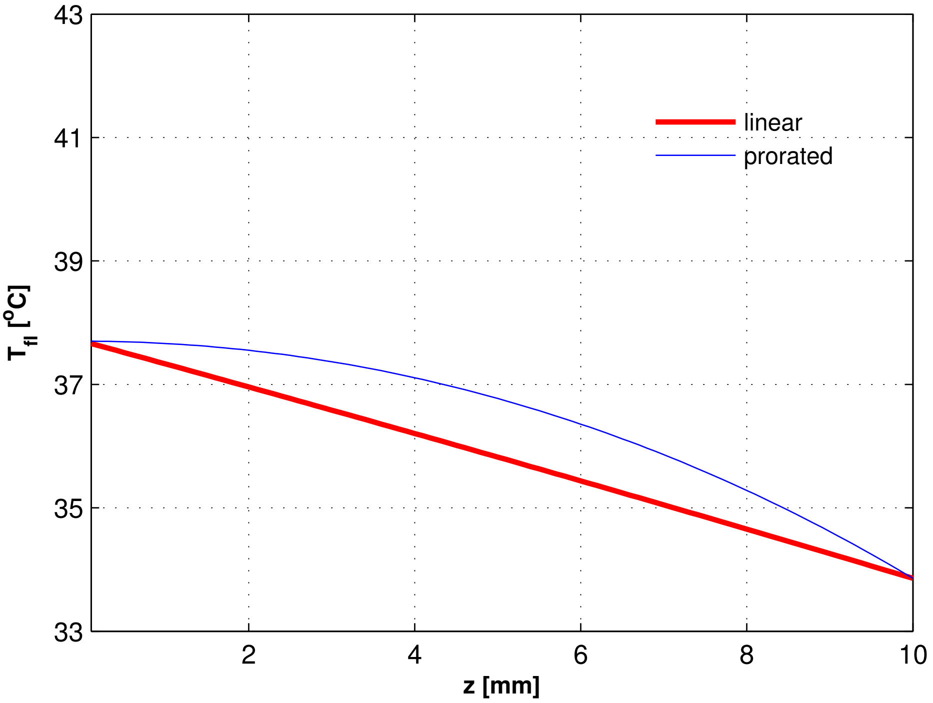

Figure 6.18: Prorated fluid temperature for R236fa flowing in the test section with the inlet restrictions of $e_{in,rest} = 4$, $G_{ch} = 1'692\,\mathrm{kg\,m^{-2}\,s^{-1}}$, $q_b = 47.8\,\mathrm{w\,cm^{-2}}$ for the experimental pressure drop of 46.3 kPa.

6.4 Conclusions

- The maximum two-phase pressure drop of $\Delta p_{total} = 122\,\mathrm{kPa}$ was obtained in the micro-evaporator with the expansion ratio of $e_{in,rest} = 4$ for two-phase flow of R236fa. The total pressure drop was found to be independent of the two-phase flow operating regimes.

- The inlet and outlet restriction pressure losses, respectively $\Delta p_{in,rest}$ and $\Delta p_{out,rest}$, need to be quantified in order to accurately simulate the hydraulic performance of microchannel evaporators and provide more reliable heat transfer data. In the present study, the single-phase flow inlet pressure losses were calculated and compared to the adiabatic experimentally measured pressure drops revealing good agreement. The pressure losses through the outlet restriction were determined experimentally using the method of Costa-Patry et al. (2011b) and correlated based on the outlet conditions separately for each micro-evaporator and each test fluid.

- The maximum channel pressure drop of $\Delta p_{ch} \approx 73.4\,\mathrm{kPa}$ was measured for two-phase flow of R236fa in the micro-evaporator with the inlet restriction of $e_{in,rest} = 2$ with the vapor quality at the channel ends of $x_{ch,end} \approx 23\%$. In general, the Δp_{ch} is ~65% of the total measured pressure drop as soon as the flashing two-phase flow without back flow operating regime occurs.

- The diabatic channel pressure drops, Δp_{ch}, for the same experimental conditions and the same fluid flowing in two different test sections (different inlet restrictions, while the size of the channel remains unchanged) are dependent on the two-phase flow pattern in the channel. There appears to be a downstream effect of the micro-orifices' impinging jet of vapor into the channel.
- The comparison of the experimentally measured two-phase channel pressure drops with the existing prediction methods revealed significant discrepancies. The flow-pattern-based pressure drop method of Cioncolini et al. (2009) for annular flow coupled with the Lockhart and Martinelli (1949) for the vapor qualities below the isolated bubble to coalescing bubble (IB-CB) transition of Ong (2010) will be used in heat transfer coefficient data reduction for obtaining local saturation temperature of the fluid.

Chapter 7

Two-phase flow heat transfer

The present chapter reports the time-averaged two-phase flow heat transfer results determined based on IR temperature measurements conducted across a heated area of the micro-evaporator's base. As explained in Chapter 4, in order to minimize the edge conduction effects, 5 pixels on each side (around the perimeter) are not taken into account, so that an array of 90 x 90 pixels is considered here. The data are reduced based on the 3D (axes XYZ) heat spreading model of Costa-Patry (2011) that takes into account the heat spreading towards the colder surrounding regions, due to the non-uniformity of the flow boiling heat transfer coefficients versus vapor quality, to obtain the actual local heat fluxes for then determining the local heat transfer coefficients. The comparison between heat transfer coefficients computed assuming 1D heat conduction and accounting for 3D heat spreading is also included here for comparison purposes. Prior to the heat transfer calculations, the IR signals were filtered by fitting a 4^{th} order polynomial curve to the temperature data in order to remove the high-frequency noise. The presented heat transfer data consider only the stable flows described in more details in Chapter 5 so as not to mix unstable results with stable data. The general trends are shown based on selected examples. The remaining results can be found in Appendix B.

7.1 Transitions for stable flows

The current study confirmed that the two-phase flow in multi-microchannels is sensitive to various flow instabilities and non-uniform flow distribution. Table 7.1 gives more details on the percentage of stable and unstable flows in the present database. Such phenomena were inhibited but not eradicated by placing restrictions at the inlet of each channel, which successfully suppressed back flow, eliminated flow instabilities, and considerably improved flow uniformity among the channels for relatively high heat fluxes and mass fluxes. Therefore, before analysing the heat transfer data, the operating boundaries for achieving stable flow need to be determined and quantified.

Table 7.1: Test conditions segregated by type of flow regime.

Operating regime	R245fa	R245fa	R236fa	R236fa	R236fa	R1234ze(E)
$e_{in,rest}$	1	2	1.33	2	4	2
single-phase flow (0)	50.0	8.1	8.8	8.3	8.9	8.9
single-phase flow in the test section with the vapor bubbles at the manifold's outlet plenum (1)	-	21.2	7.0	-	-	-
single-phase flow followed by two-phase flow with back flow (2)	50.0	36.4	42.1	27.8	14.0	7.1
unstable two-phase flow with back flow developing into jet flow (3)	-	5.1	2.6	-	-	-
jet flow (4)	-	3.0	5.3	-	8.0	4.5
single-phase flow followed by two-phase flow without back flow (5)	-	6.1	7.0	28.7	16.8	39.3
two-phase flow with back flow triggered by bubbles formed in the flow loop before the test section (6)	-	1.0	27.2	2.7	0.9	13.4
flashing two-phase flow with back flow (7)	-	13.0	-	-	13.3	-
flashing two-phase flow without back flow (8)	-	6.1	-	32.4	38.1	26.8
(5) + (7) + (8)	-	25.2	7.0	61.6	68.2	66.1

Figure 7.1 illustrates a $G_{ch}-x_{ch,end}$ plot of the test conditions for R236fa flowing in the test section with the inlet restrictions of $e_{in,rest}=2$, which corresponds to the two-phase flow operational map shown in Fig. 5.2 in Chapter 5. In Fig. 7.2, the two-phase operational regimes were superimposed on the $G_{ch}-x_{ch,end}$ flow pattern map. The green dots represent the experimental conditions for which there was single-phase flow followed by two-phase flow with back flow before changing to the one regime without back flow. Whereas, the blue dots indicate the range of $x_{ch,end}$ and G_{ch}, where flashing two-phase flow without back flow operating regime was observed. The remaining area corresponds to the single-phase flow followed by two-phase flow without back flow. The G_{ch} and q_b steps were not fine enough however to capture the exact transitions between the particular operating regimes.

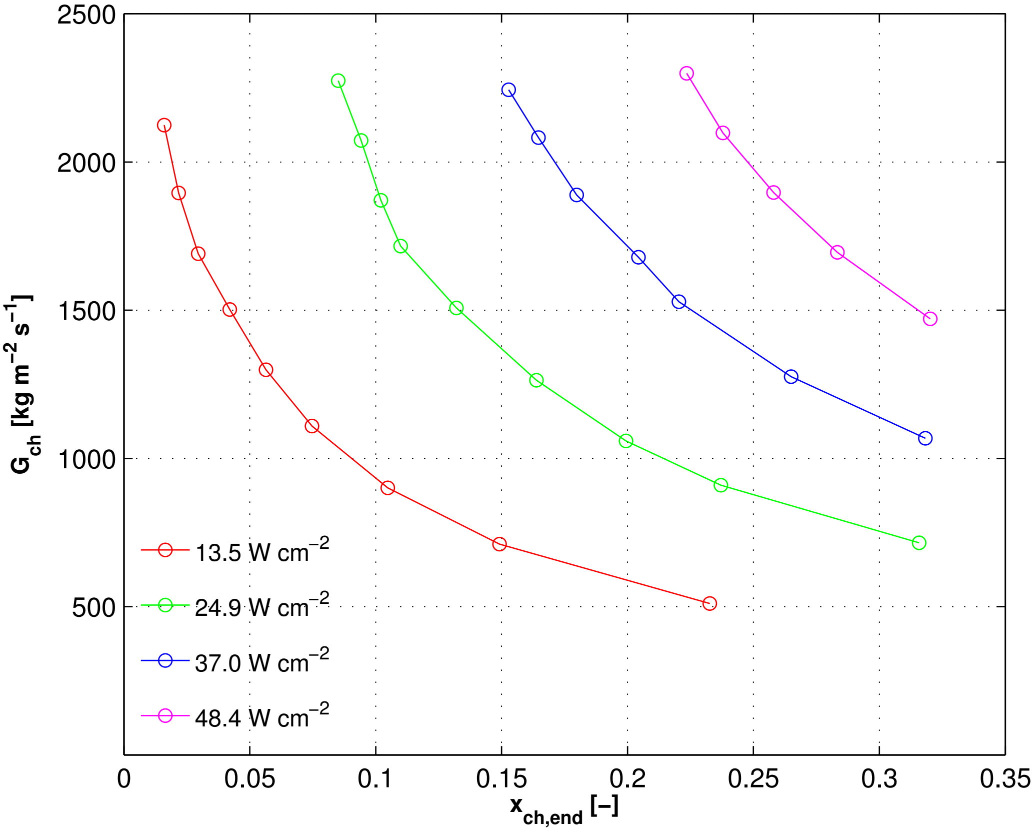

Figure 7.1: Flow pattern map for R236fa in the micro-evaporator with the inlet restriction of $e_{in,rest}=2$.

Taking this information from Fig. 7.1 and plotting these transitions in Fig. 7.2, for low channel mass fluxes the flow stability improves with decreasing $x_{ch,end}$. For higher G_{ch}, above ~1'500 $\mathrm{kg\,m^{-2}\,s^{-1}}$, the back flow was eliminated. The flashing two-phase flow without back flow regime was viewed with further increasing $x_{ch,end}$. For R236fa in the micro-evaporator with the inlet restrictions of $e_{in,rest}=2$, the flashing two-phase flow without back flow operating regime (the most desirable operating regime) occurs at $x_{ch,end}$ higher than ~8.0 − 13.5% and

$G_{ch} > 1'500\,\mathrm{kg\,m^{-2}\,s^{-1}}$, while for the other test sections and fluids, this operating regime is entered for the range of vapor qualities between 0.1 and 0.4. Generally, it moves to lower values of $x_{ch,end}$, when $G_{ch,end}$ increases. In the present chapter, only heat transfer results in the flashing two-phase flow without back flow operating regimes are evaluated and presented.

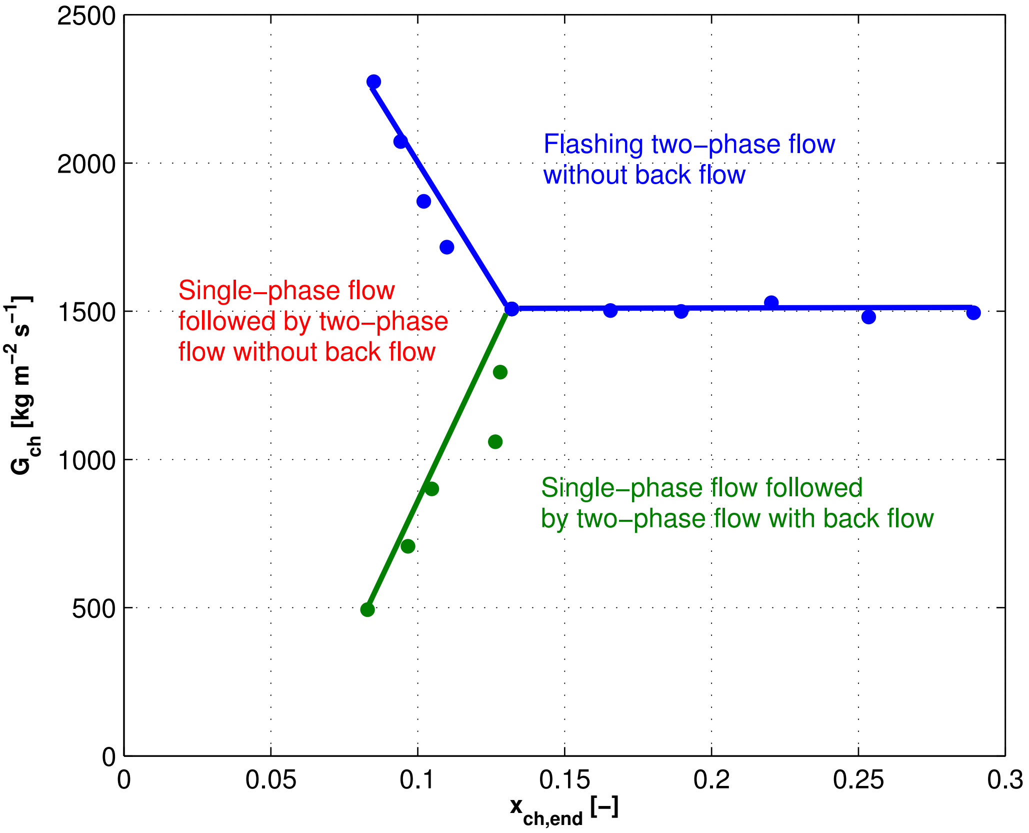

Figure 7.2: Transitions for stable flows of R236fa in the micro-evaporator with the inlet restriction of $e_{in,rest} = 2$.

7.2 Comparison between 1D and 3D heat conduction schemes

Firstly, the 3D heat spreading implementation was validated by imposing a uniform base heat flux of $q_b \approx 43\,\mathrm{W\,cm^{-2}}$ and setting the temperature boundary condition of $T_{IR} = 48\,°\mathrm{C}$ at the silicon base. Since the side walls are assumed to be adiabatic, the actual heat flux at the root of the fins, q_{ft}, should be uniform and equal the base heat flux, as shown in Fig. 7.3.

The comparison between 1D and 3D heat conductions schemes was performed for the two-phase flow of R1234ze(E) in the test section with the inlet restrictions of $e_{in,rest} = 2$ showing the flashing two-phase flow without back flow operating regime. Figure 7.4(a) demonstrates the temperature map at the base of the silicon substrate with a nearly uniform temperature

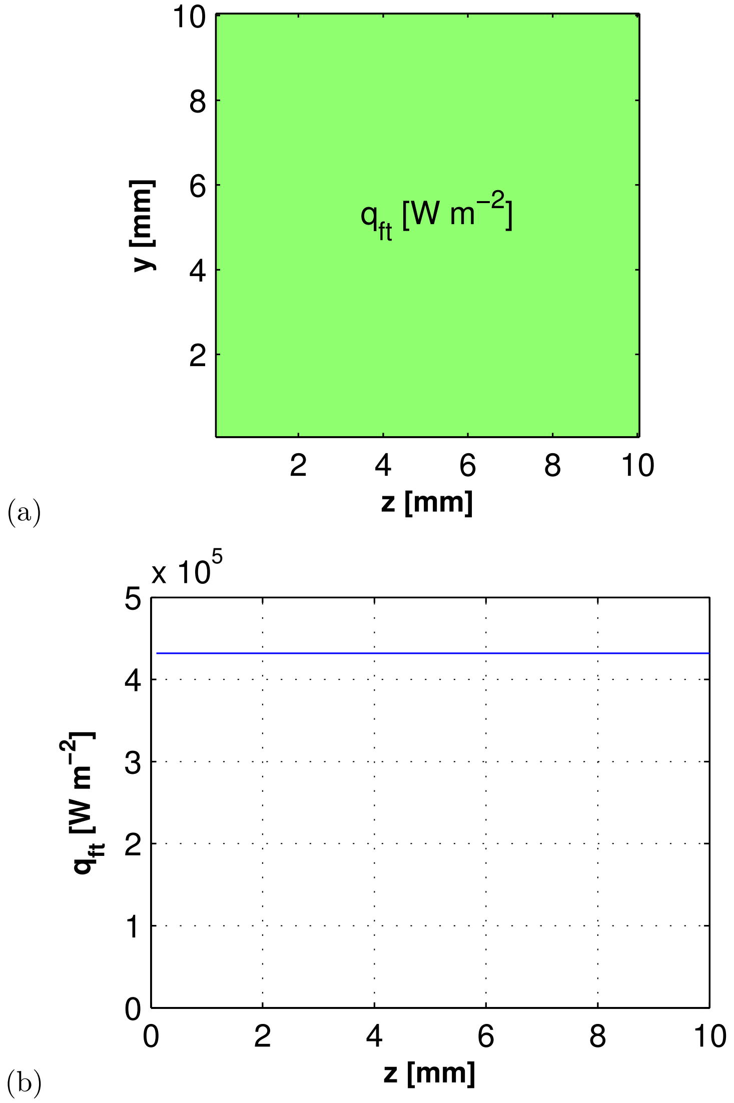

Figure 7.3: Validation of the 3D heat spreading implementation (flow is from left to right): (a) heat flux map at the root of the fins, q_{ft}, and (b) lateral average heat flux distribution along the channel length.

distribution in the lateral direction. The footprint temperatures, where footprint refers to the root of the fins, were calculated using 1D and 3D conduction schemes. The lateral averages of base and footprint temperatures obtained through 1D and 3D calculations, are shown in Fig. 7.4(b). The biggest discrepancy is noticeable at the corners, where the edge effects are significant and they were captured by the 3D conduction model. As pointed out in Chapter 4, the results for the edges will not be used for the heat transfer analysis due to the measurement errirs associated with the edges.

Figure 7.5(a) presents the actual 3D heat flux distribution compared to the uniform 1D heat flux distribution that is commonly assumed in the multi-microchannel studies, both averaged laterally and presented as a function of channel location, z. For the first and the last 5

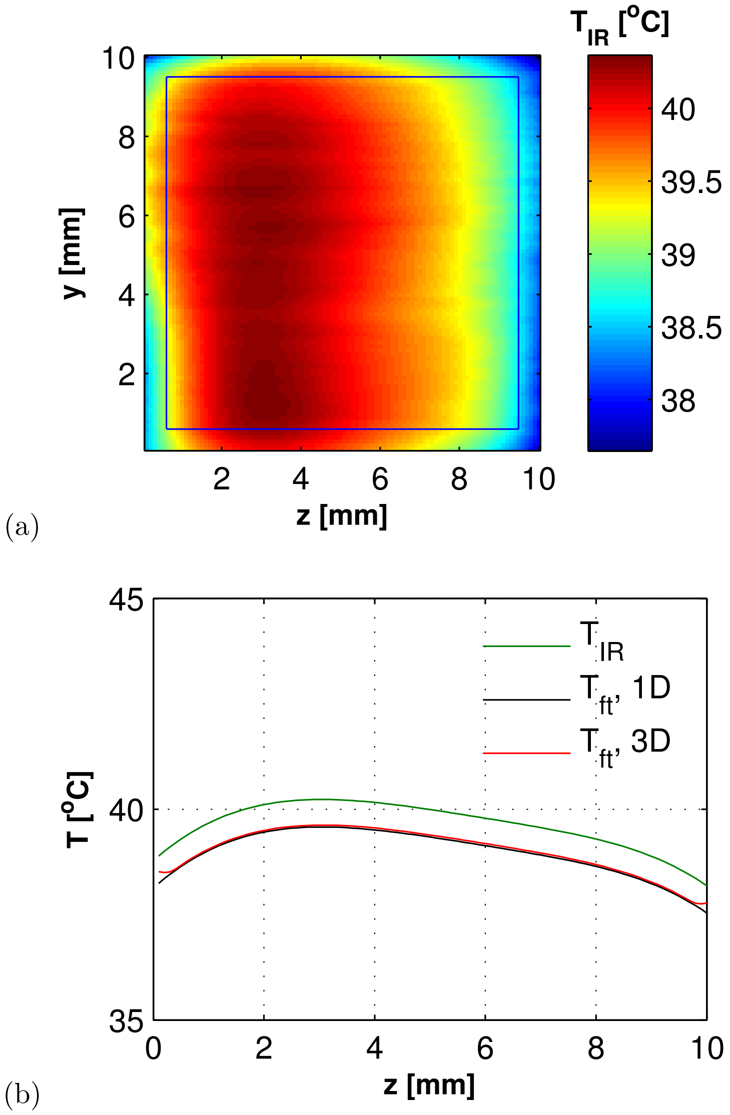
(a)

(b)

Figure 7.4: Two-phase flow of R1234ze(E) in the test section with the inlet restrictions of $e_{in,rest} = 2$ for $G_{ch} = 1\text{'}705\,\mathrm{kg\,m^{-2}\,s^{-1}}$ and $q_b = 32\,\mathrm{W\,cm^{-2}}$: (a) temperature map at the base of the silicon substrate, T_{IR}, and (b) lateral averages of base and footprint temperatures obtained assuming 1D and 3D heat conduction. The area inside the blue square indicates the array of IR temperatures considered in heat transfer analysis.

pixels the calculated values includes edge effects and they will not be analyzed here. As can be seen, the heat spreads towards the colder surrounding regions, here the inlet and the outlet, and the actual heat flux in those zones is first higher and then lower than that assumed in 1D calculations. Therefore, the heat transfer coefficients determined assuming 1D conduction from the base of the silicon micro-evaporator to the root of the fins are underpredicted at the inlet and the outlet of the channel (eliminating the first and the last 5 pixels), as demonstrated in Fig. 7.5(b), where the local vapor quality is calculated with corresponding heat flux. The vapor quality increases linearly with slightly different incremental steps for both of the calculations (Fig. 7.5(c)), as expected for uniform heat flux imposed by the two heaters. If the heat spread-

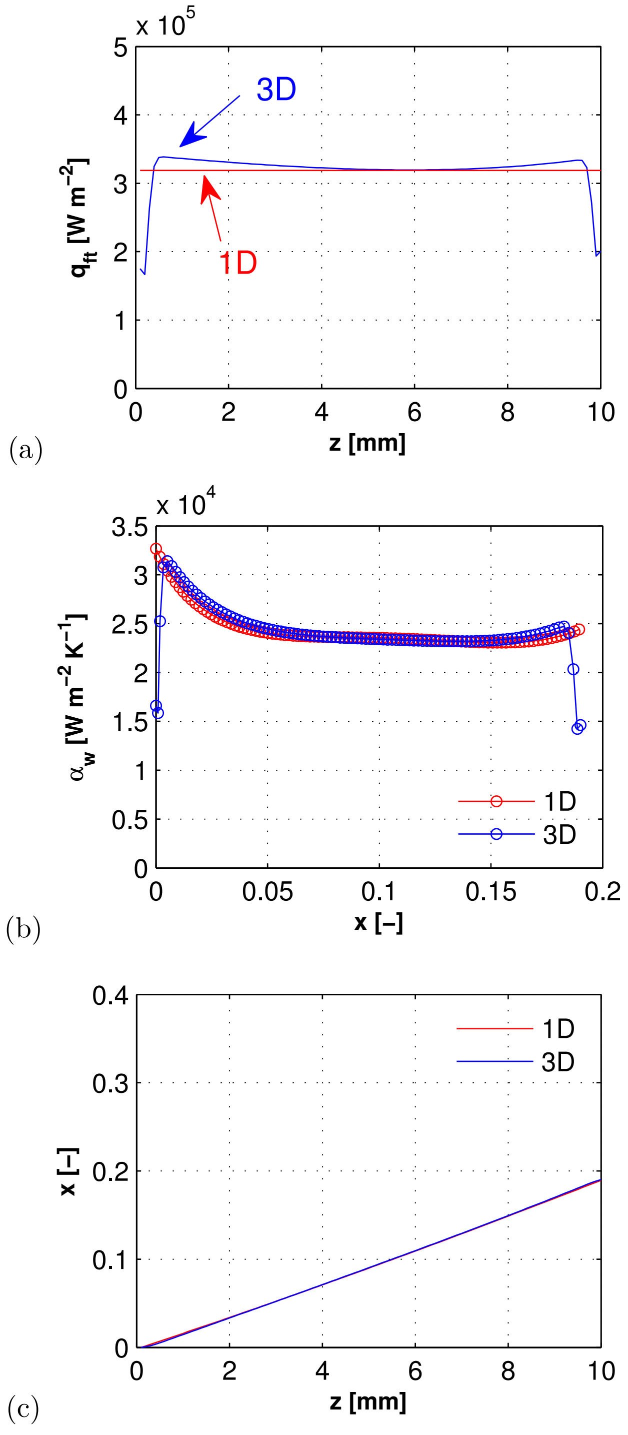

Figure 7.5: Two-phase flow of R1234ze(E) in the test section with the inlet restrictions of $e_{in,rest} = 2$ for $G_{ch} = 1'705\,\mathrm{kg\,m^{-2}\,s^{-1}}$ and $q_b = 32\,\mathrm{W\,cm^{-2}}$: (a) actual heat flux at the root of the fins along the channel length, (b) local wall heat transfer coefficients, α_w, obtained using the 1D and 3D conduction schemes in function of local vapor quality, x, and (c) vapor quality along the length of the channel.

ing is not considered, the heat transfer coefficient is overpredicted at the local minimum, which corresponds to a flow transition. Thus, the 3D heat spreading needs to be accounted for to obtained the most accurate results and data trends.

7.3 Heat transfer coefficient trend with 3D heat spreading

Simultaneous flow and temperature visualizations confirmed that the two-phase flow patterns appearing in the channel and the transitions in between them have a significant influence on the heat transfer. Figure 7.6(a) illustrates the wall heat transfer coefficient, α_w, obtained using 3D heat spreading in the silicon base, plotted versus the longitudinal channel location, z, and compared to the corresponding flow pattern map transition (vertical blue line). The descending trend of α_w at the beginning of the channel (low vapor quality range) corresponds to the coalescing bubble region, where the elongated bubbles coalesce and the local intermittent dry-out patches are formed (Thome et al., 2004). The coalescing bubble – annular flow (CB – AF) transition of Costa-Patry and Thome (2012) represents the local minimum of the heat transfer coefficient well and is given as:

$$x_{CB-AF} = 425 \left(\frac{\rho_v}{\rho_l}\right)^{0.1} \frac{Bo^{1.1}}{Co^{0.5}} \tag{7.1}$$

where Bo is the boiling number and Co is the confinement number. According to the above equation, the transition is a function of the liquid-to-vapor density ratio, as well as the mass flux and heat flux. As pointed out by the authors, this criterion gives similar results to those of Ong (2010), which is used in the present study to find the starting point of annular flow and to determine the local saturation pressure in the microchannel, as explained in Chapter 6.

Figure 7.6(b) shows a video image of the flow aligned with the graph at the top. The color changes along the channel from almost black at the entrance (subcooled flow/bubbly flow) to nearly white (transition region) and becomes gray at the exit. The blue line indicating the CB – AF transition of Costa-Patry and Thome (2012) falls between the second and third zone. This means that more than half of the channel is in the annular flow regime. Due to the thin-film evaporation, a core of vapor surrounded by a ring of liquid flows with high velocity towards the outlet manifold's plenum, providing a good heat transfer rate. As presented in Fig. 7.6(a), after reaching the local minimum, the heat transfer coefficient increases downstream along the channel, which is associated with thinning the liquid film with increasing vapor quality.

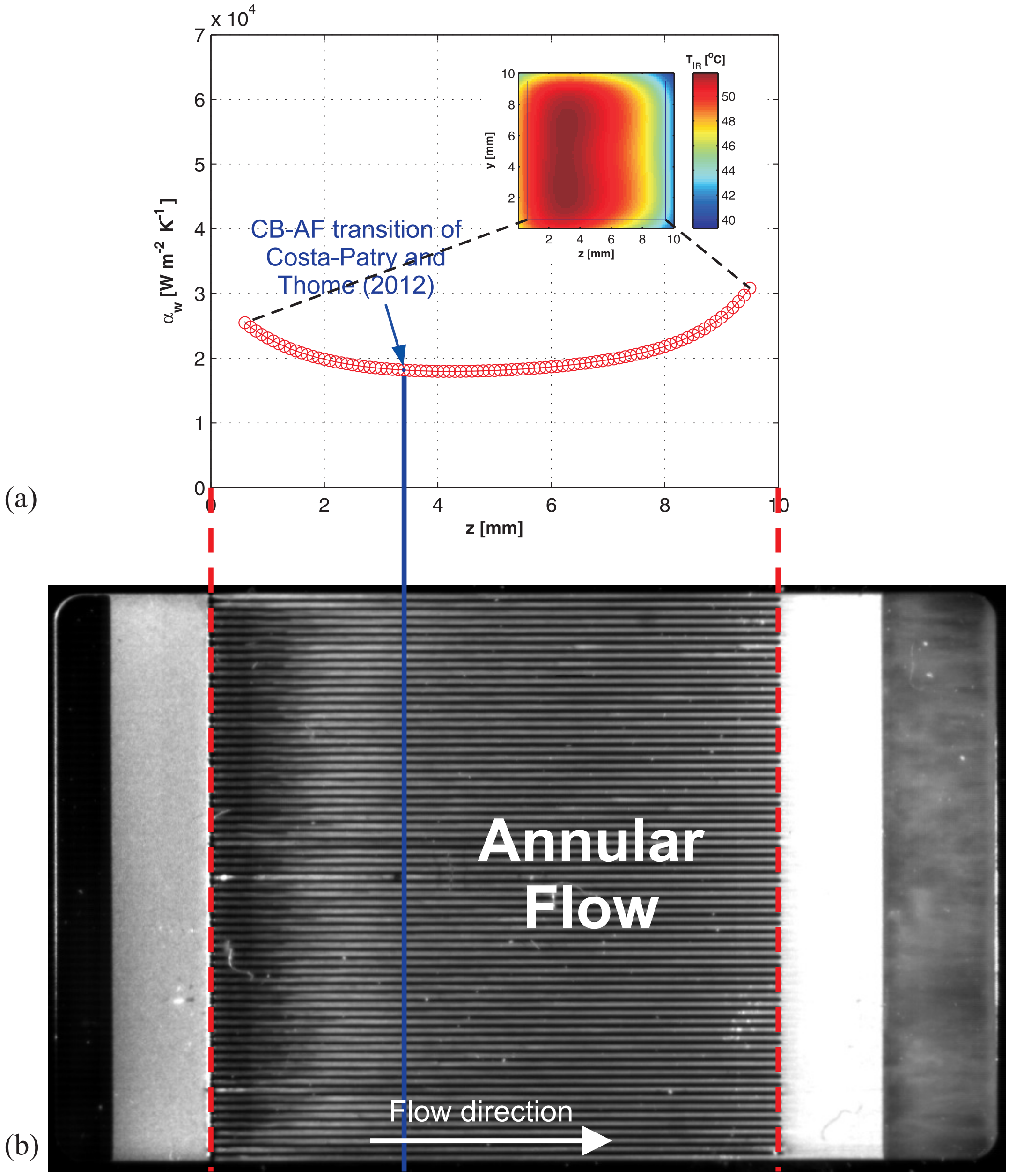

Figure 7.6: The flashing two-phase flow without back flow operating regime of R236fa in the micro-evaporator with the inlet restrictions of $e_{in,rest} = 4$ for $G_{ch} = 2\text{'}096\,\mathrm{kg\,m^{-2}\,s^{-1}}$ and $q_b = 47\,\mathrm{W\,cm^{-2}}$: (a) wall heat transfer coefficient, α_w, and (b) video image of flow.

7.4 Wall heat transfer coefficients

The lateral-averaged wall heat transfer coefficients, α_w, were obtained with a fine resolution and are presented as a function of local vapor quality, x. The effects of channel mass flux, G_{ch}, wall heat flux, q_w, orifice expansion ratio, $e_{in,rest}$, and fluid properties will be shown below for a selected number of data sets. To lighten the text, some more experimental results are shown in Appendix B.

7.4.1 Effect of channel mass flux

Figures 7.7 and 7.8 demonstrate the trends of the wall heat transfer coefficient, α_w, as a function of the local vapor quality for increasing mass flux including the predicted CB - AF transitions of Costa-Patry et al. (2012). They move to lower vapor quality with increasing the mass flux, as shown in Figs. 7.7 and 7.8.

At vapor qualities prior to the line the heat transfer coefficients are only marginally influenced by the mass flux. In the annular flow beyond the transition line, the wall heat transfer coefficient increases with increasing mass flux for a constant vapor quality. As explained previously, the heat transfer coefficient first decreases at low vapor qualities and the local minimum of the heat transfer coefficient corresponds to the CB - AF flow pattern transition, after which the heat transfer coefficient grows considerably when the flow transitions into annular flow. The heat transfer coefficient does not change sharply at the transition zone, but rather has a smooth change in trend. The characteristic U-shape of the heat transfer coefficient trend, illustrated in Fig. 7.8, was observed throughout the current data bank. The descending branch of the curve corresponds to the coalescing elongated bubble flow regime, while the ascending one represents the increasing heat transfer coefficient in the annular flow regime, which is associated with the thinning of the liquid film around the channel perimeter (Thome et al., 2004).

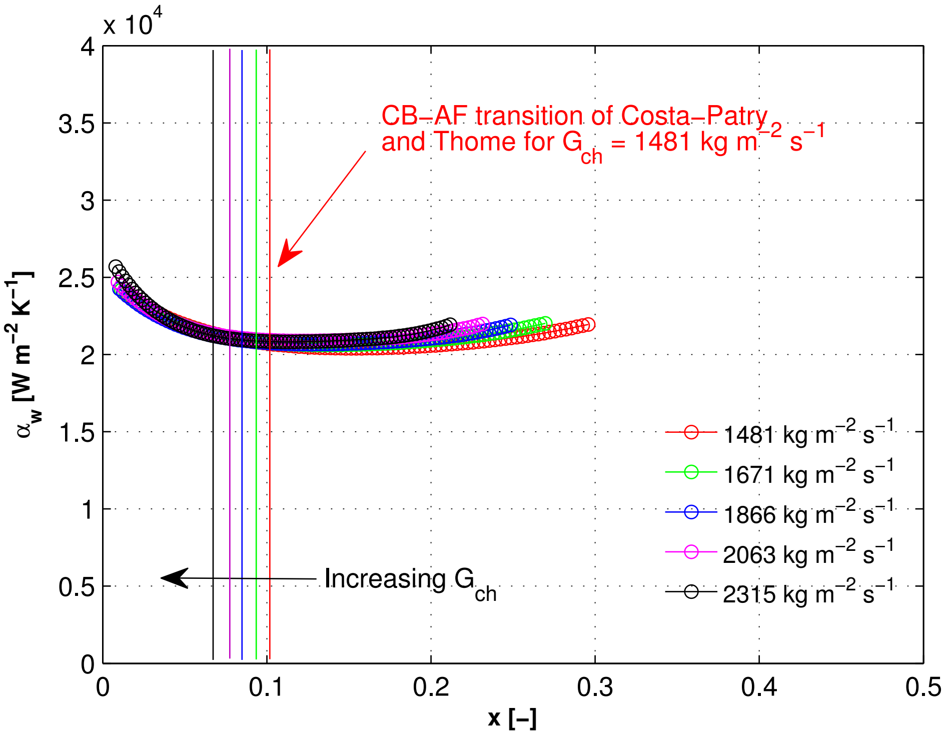

Figure 7.7: Two-phase wall heat transfer coefficient as a function of local vapor quality for R236fa flowing in the test section with the inlet restrictions of $e_{in,rest} = 2$ for $q_w = 175\,\mathrm{kW\,m^{-2}}$.

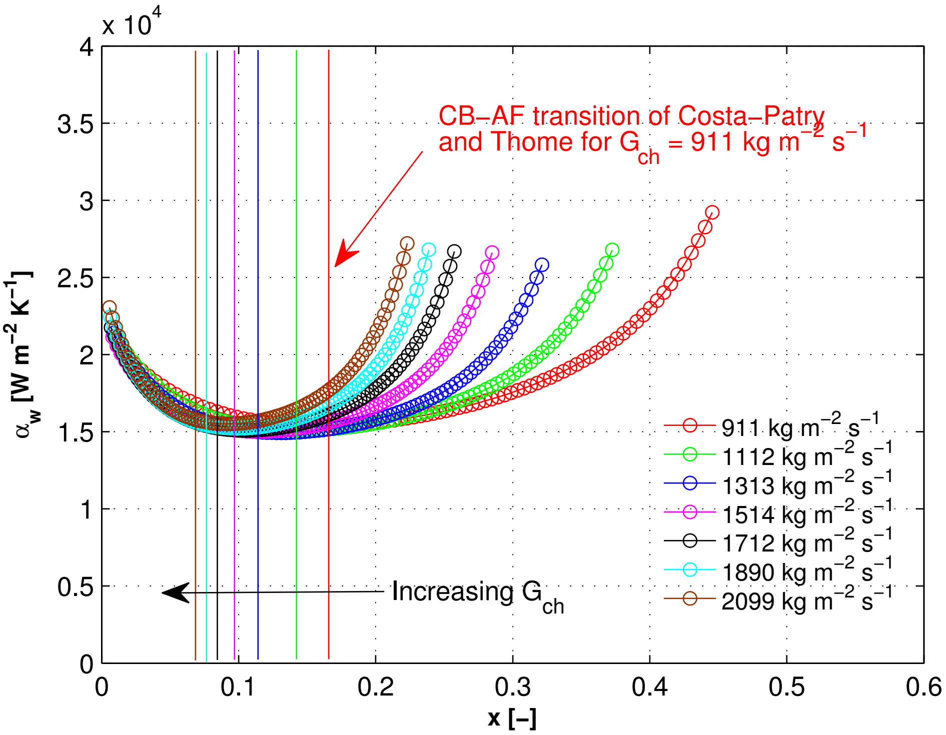

Figure 7.8: Two-phase wall heat transfer coefficient as a function of local vapor quality for R236fa flowing in the test section with the inlet restrictions of $e_{in,rest} = 4$ for $q_w = 171\,\mathrm{kW\,m^{-2}}$.

7.4.2 Effect of wall heat flux

The effect of the wall heat flux, q_w, on the wall heat transfer coefficients, α_w, is discussed based on the selected example. Figure B.14 shows the two-phase wall heat transfer coefficients for R236fa flowing in the micro-evaporator with the inlet restrictions of $e_{in,rest} = 2$ for $G_{ch} \approx 1'500\,\mathrm{kg\,m^{-2}\,s^{-1}}$. It is noticeable that the average level of the wall heat transfer coefficient increases with increasing the wall heat flux. The influence of the wall heat flux diminishes with increasing vapor quality and the q_w versus x curves tend to a common line in annular flow, as mentioned previously by Ong and Thome (2011b) based on their experimental results for a single channel micro-evaporator. For the higher wall heat fluxes, the heat transfer coefficients in annular flow seem to be independent on the x. This might be explained by the formation of cyclical dry-out of the channel as the vapor quality increases. This is similar to the elongated bubble regime as explained by the three-zone model of Thome et al. (2004).

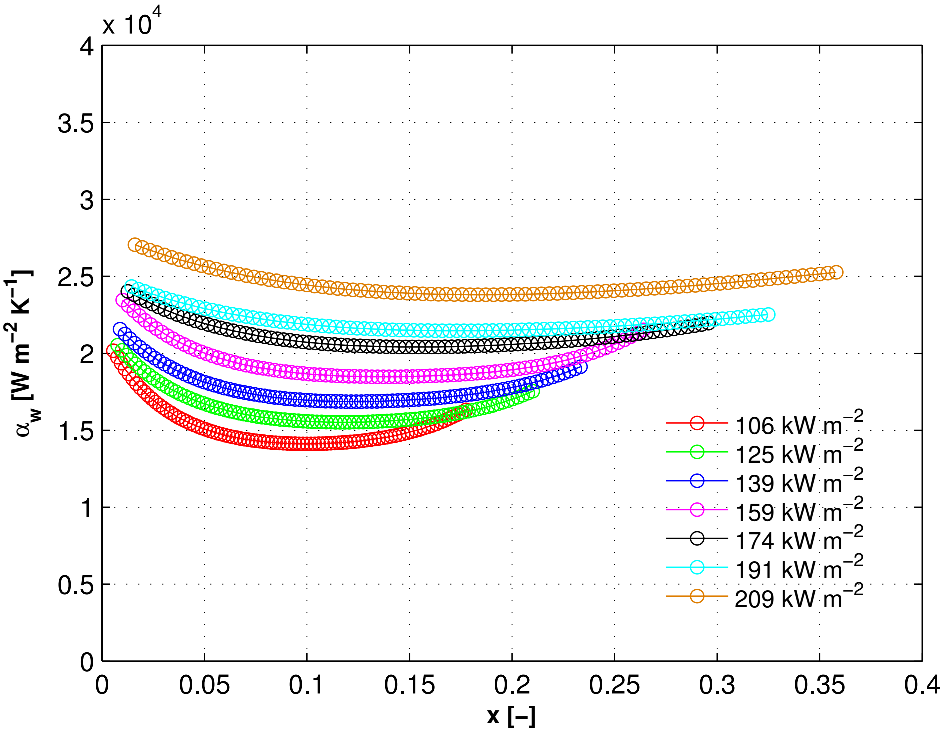

Figure 7.9: Two-phase wall heat transfer coefficient as a function of local vapor quality for R236fa flowing in the test section with the inlet restrictions of $e_{in,rest} = 2$ for $G_{ch} \approx 1'500\,\mathrm{kg\,m^{-2}\,s^{-1}}$.

7.4.3 Effect of fluid properties

Figure 7.10 shows the effect of fluid properties on the wall heat transfer coefficient, α_w, for the mass flux of 1'483±1.5% $\mathrm{kg\,m^{-2}\,s^{-1}}$, while dissipating the wall heat flux of 205.8±3% $\mathrm{kW\,m^{-2}}$. The data sets were obtained in the test section with the same expansion ratio of $e_{in,rest} = 2$. The vapor quality is a function of local saturation conditions (enthalpy) obtained based on the local fluid temperature and therefore its range in the graph depends on the fluid. R1234ze(E) has the highest heat transfer coefficient, which is probably due to its higher vapor-to-liquid density ratio ($\rho_v\,/\,\rho_l \approx 0.028$), as listed in Table 4.1 in Chapter 4. The film thickness is thus thinner and the heat transfer increases, as predicted by the three-zone model of Thome et al. (2004). As can be seen, the trends of the wall heat transfer coefficients are basically the same for all the test fluids.

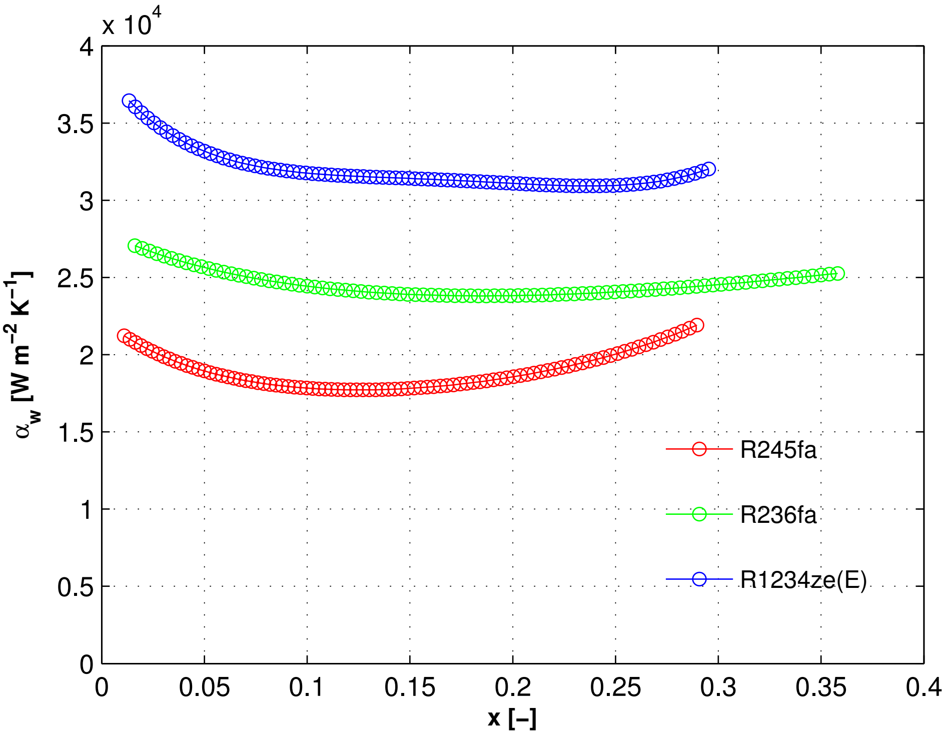

Figure 7.10: Two-phase wall heat transfer coefficient of R245fa, R236fa, and R1234ze(E) flowing in $e_{in,rest} = 2$, $q_w = 205.8\pm3\%\ \mathrm{kW\,m^{-2}}$, $G_{ch} = 1'483\pm1.5\%\ \mathrm{kg\,m^{-2}\,s^{-1}}$.

7.4.4 Effects of orifice expansion ratio

In order to determine the effect of the expansion ratio, $e_{in,rest}$, a comparison was performed for R236fa flowing in the micro-evaporators with different inlet restrictions, namely $e_{in,rest} = 2$ and 4, as shown in Fig. 7.11. The red vertical line corresponds to the predicted CB - AF transition of Costa-Patry et al. (2012). The represented points are from the flashing two-phase flow without back flow operating regime. This regime was found to provide the best flow and temperature stability. Based on the high-speed flow visualization videos, it was determined that the bubbly flow was initiated at the beginning of each channel and almost immediately developed into slug and consequently annular flow.

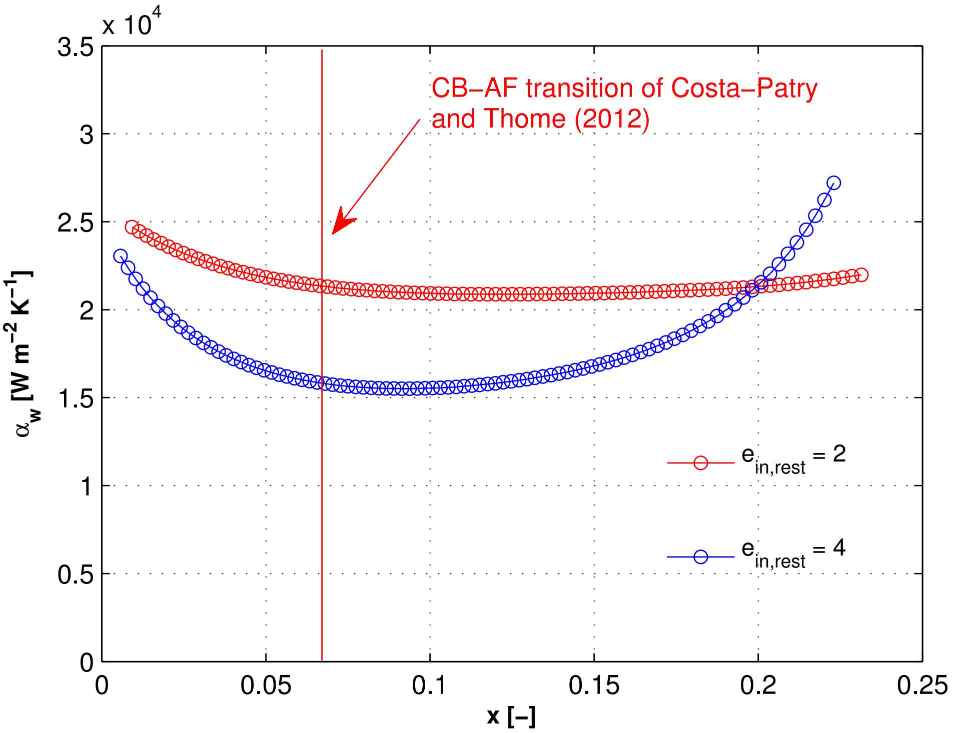

Figure 7.11: Two-phase wall heat transfer coefficient as a function of local vapor quality for R236fa in the test section with the inlet restrictions of $e_{in,rest} = 2$ and 4 for $G_{ch} = 2\text{'}081\,\mathrm{kg\,m^{-2}\,s^{-1}}$ and $q_w = 173\,\mathrm{kW\,m^{-2}}$.

At low vapor qualities, the descending trend of α_w corresponds to the coalescing elongated bubble region, as predicted by the three-zone model of Thome et al. (2004). Nonetheless, the flow patterns within the microchannels might be locally different, which to a certain extend was shown in Chapter 6 to have an effect on the experimental channel pressure drop. After reaching the local minimum, which corresponds relatively well to the transition of Costa-Patry et al. (2012), the heat transfer increases with increasing vapor quality. The test section of $e_{in,rest} = 2$ show a heat transfer coefficient plateau in the mid range of vapor quality (Fig. 7.11). At higher vapor qualities, it slightly increases again. Whereas, for the test section of $e_{in,rest} = 4$, the heat transfer coefficient in annular flow increases more and from a lower value. In this case, the liquid film is perhaps more perturbed by the vapor jet at the channel inlet. That might cause more liquid to be entrained in the vapor core and eventually thin the liquid film at the channel perimeter, thus enhance heat transfer in the annular flow.

7.5 Comparison with prediction methods

The analysis of heat transfer data showed that the heat transfer coefficient, α_w, strongly depends on the flow patterns within a microchannel and the transitions between flow patterns. Therefore, the flow pattern-based model of Costa-Patry and Thome (2012) and a composite heat transfer model of Bertsch et al. (2009), which are widely considered to be the most accurate ones, are compared with the current experimental data for stable flows (the flashing two-phase flow without back flow operating regime). Figure 7.12(a) presents the heat transfer coefficient trends predicted by those models including the experimental results for R236fa flowing in the test section with the inlet restrictions of $e_{in,rest} = 4$ for $G_{ch} = 1\text{'}525\,\mathrm{kg\,m^{-2}\,s^{-1}}$ and $q_w = 155.3\,\mathrm{kW\,m^{-2}}$. The heat transfer coefficient predicted by Bertsch et al. (2009) keeps decreasing with increasing vapor quality. Thus, their correlation does not capture the increasing heat transfer rate in the annular flow. The prediction method of Costa-Patry and Thome (2012) predicts the trend and the value of the heat transfer coefficient well. This is especially true at low and high values of vapor quality and for the location of the local minimum of the heat transfer coefficient. The minimum corresponds to the CB - AF transition and it is given by Eq. (7.1). The largest discrepancies between the predicted and the experimental values are noticeable at this transition, which remains a region of uncertainty in the multi-microchannel heat transfer studies and needs to be further investigated.

The V-shape of the heat transfer coefficient is nowadays a commonly accepted trend, where the descending branch of the curve corresponds to the coalescing bubble flow regime, while the ascending one represents the increasing heat transfer coefficient in the annular flow regime. In the present experimental investigation, in comparison to the previous studies, such as Costa-Patry and Thome (2012), the heat transfer coefficient was measured with a very fine resolution corresponding to a vapor quality increment of a fraction of a percent. It was showed in this study that the heat transfer coefficient has a smooth transition from coalescing bubble to annular flow. The U-shape of the heat transfer coefficient trend in the Costa-Patry et al. (2012) prediction method in Fig. 7.12(b) was obtained by modifying the vapor quality buffer for coalescing bubble to annular flow transition.

In the data sets compared here, the isolated bubble (IB) flow pattern is suppressed by the coalescing bubble regime (CB), although the development length of annular flow (AF) does not change as significantly and the CB - AF transition usually occurs for a length between $2-4\,\mathrm{mm}$ along the channel length, as shown in Fig. 7.6. Moreover, it was observed that the IB and CB regimes are approximately equal in length. Therefore, the new vapor quality buffer is defined as:

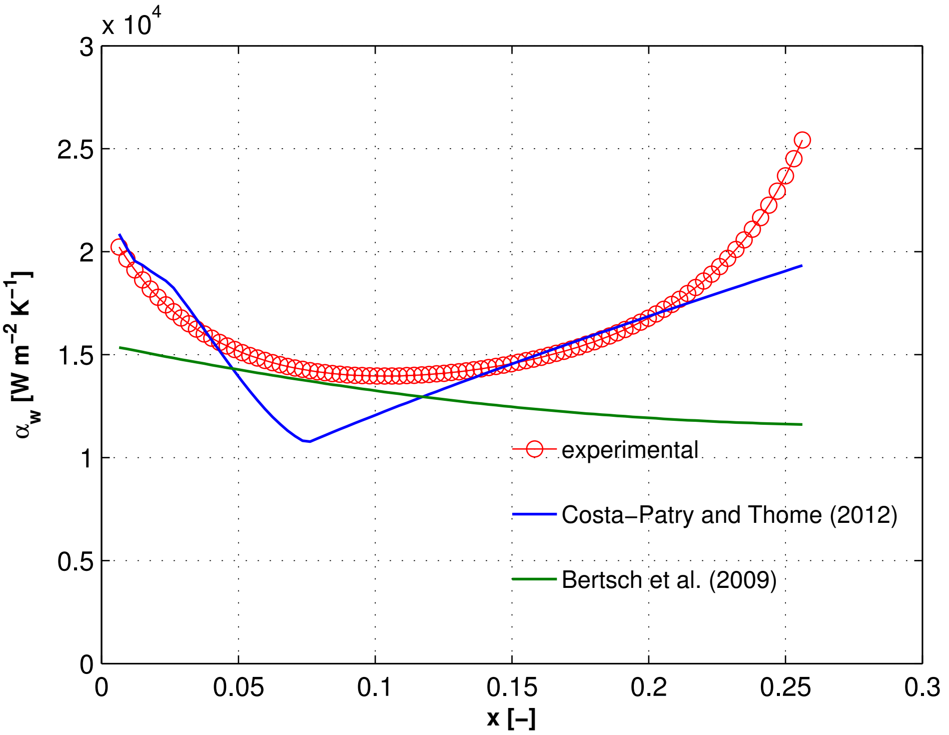

(a)

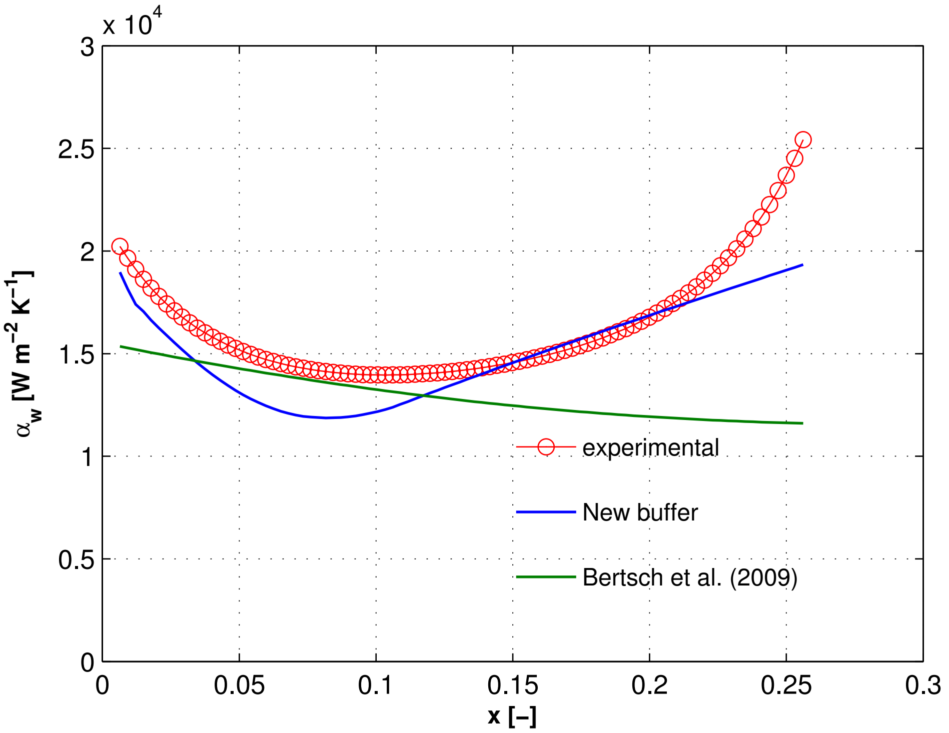

(b)

Figure 7.12: Predicted α_w versus the current experimental results for R236fa in the test section with the inlet restrictions of $e_{in,rest} = 4$ for $G_{ch} = 1'525\,\mathrm{kg\,m^{-2}\,s^{-1}}$ and $q_w = 155.3\,\mathrm{kW\,m^{-2}}$: (a) Costa-Patry and Thome (2012) with $x_{buffer} = \pm x_{exit}/5$, and (b) new buffer $x_{buffer} = \pm 2x_{CB-AF}$.

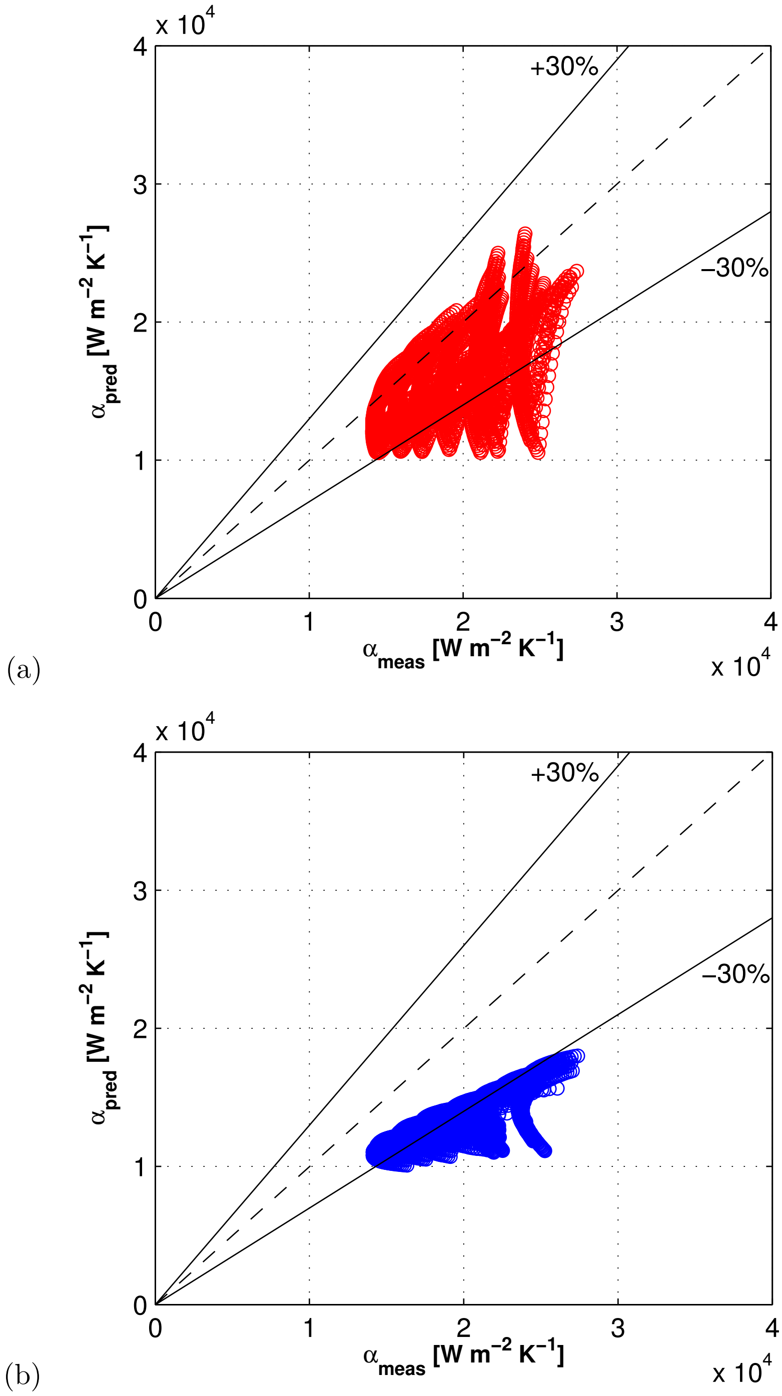

Figure 7.13: Comparison of the experimental local heat transfer coefficients, α_w, of R236fa flowing in $e_{in,rest} = 2$ with the: (a) Costa-Patry and Thome (2012), and (b) Bertsch et al. (2009) prediction methods.

$$x_{buffer} = \pm 2x_{CB-AF} \tag{7.2}$$

where x_{CB-AF} is the coalescing bubble to annular flow transition of Costa-Patry and Thome (2012) given by Eq. (7.1).

As can be seen in Fig. 7.12(b), the V-shape of the Costa-Patry et al. (2012) prediction method transformed to a U-shape. Moreover, the predicted and the experimental heat transfer coefficients at the transition became closer. The sharp IB - CB flow transition in Fig. 7.12(a) at low vapor qualities was smoothed out.

Table 7.2: MAEs [%] for local two-phase heat transfer coefficients of R245fa, R236fa, and R1234ze(E) in $e_{in,rest} = 2$ and 4.

Method	R236fa $e_{in,rest} = 2$	R236fa $e_{in,rest} = 4$	R245fa $e_{in,rest} = 2$	R1234ze(E) $e_{in,rest} = 2$	Total
Bertsch et al. (2009)	31.96	20.69	22.65	40.27	28.89
Costa-Patry and Thome (2012)	18.07	12.32	11.52	44.27	21.55
New buffer	20.33	12.43	14.90	44.74	23.1

In Table 7.2, the flow pattern-based prediction method with a modified buffer is compared with the experimental data along with the other two prediction methods. Figures 7.13 – 7.16 illustrate the comparisons of the predicted and the experimental values of the wall heat transfer coefficients, where the apparent lines corresponds to a single experiment as the vapor quality changes from inlet to outlet (the comparison is performed with local data versus local prediction). The performance of the respective correlations is evaluated by means of the mean absolute error (MAE [%]) given by equation (6.12). Table 7.2 lists the MAEs for 4 different test cases excluding R236fa flowing in $e_{in,rest} = 1.33$, for which the stability of the flow was not achieved. As presented, the experimental data are in good agreement with the existing prediction methods, especially for R245fa and R236fa, which is based on similar conditions to those tested by Costa-Patry and Thome (2012) in their silicon micro-evaporator with similar channel width. Nonetheless, they did not test any fluids with higher saturation pressure, such as R1234ze(E), for which the MAE is the highest. This is probably due to the reduced pressure of physical properties of this fluid. To the knowledge of the author, refrigerant R1234ze(E) has not been tested in silicon microchannels of similar size to this study before. The underpredicted heat transfer coefficients might be an effect of different interactions of R1234ze(E) with Si compared to R245fa or R236fa. The modification of the Costa-Patry and Thome (2012) prediction

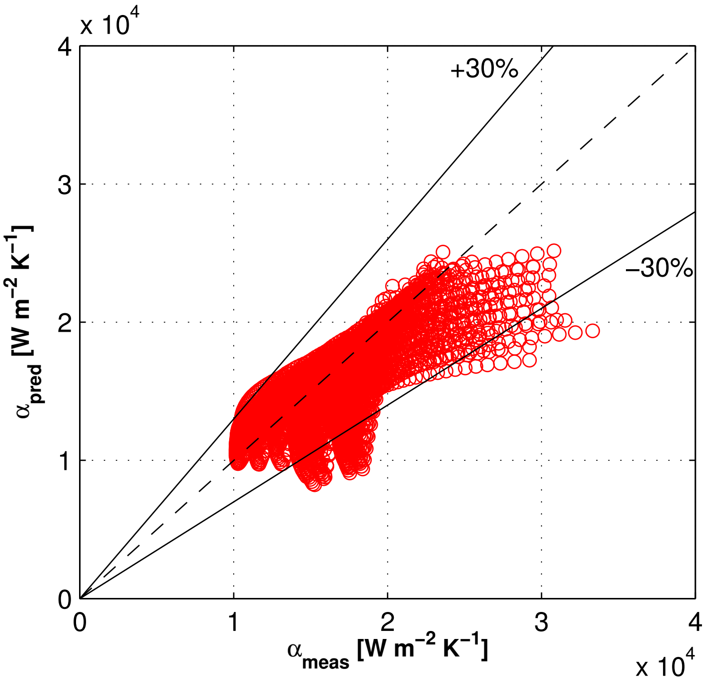

(a)

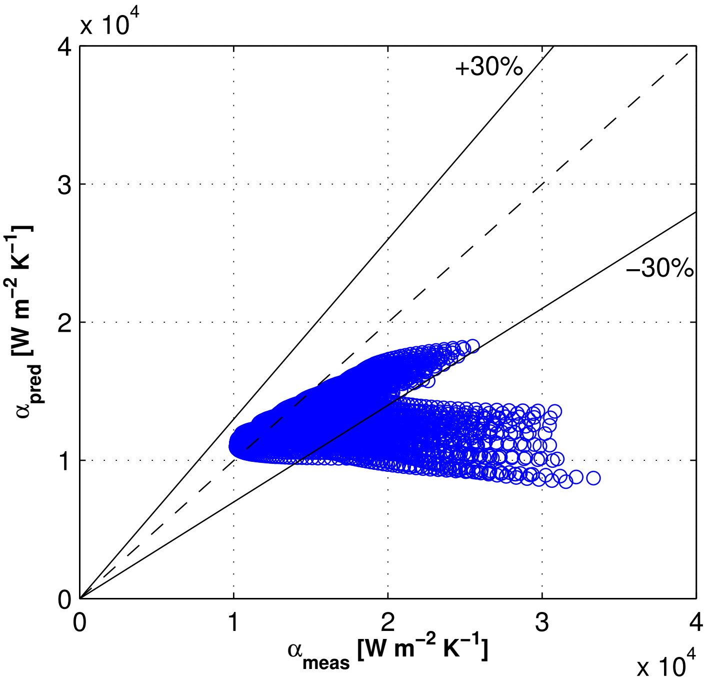

(b)

Figure 7.14: Comparison of the experimental local heat transfer coefficients, α_w, of R236fa flowing in $e_{in,rest} = 4$ with the: (a) Costa-Patry and Thome (2012), and (b) Bertsch et al. (2009) prediction methods.

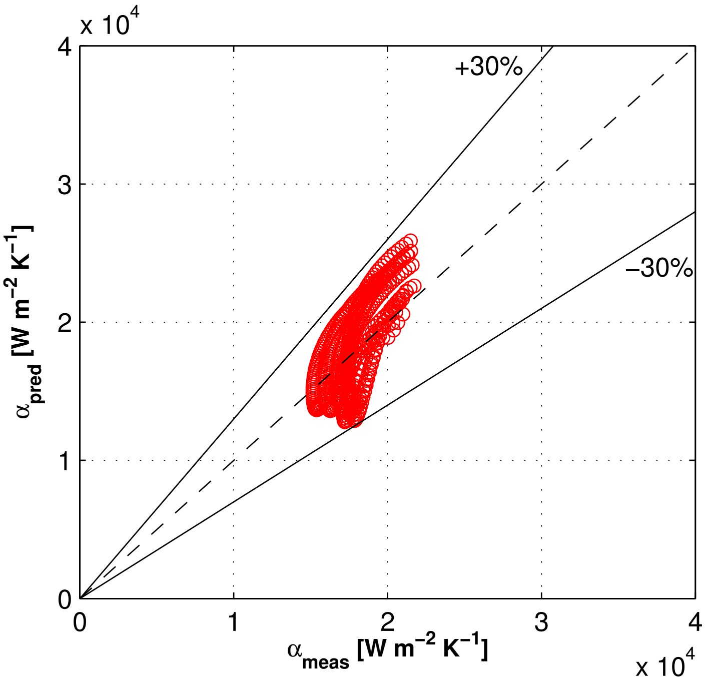

(a)

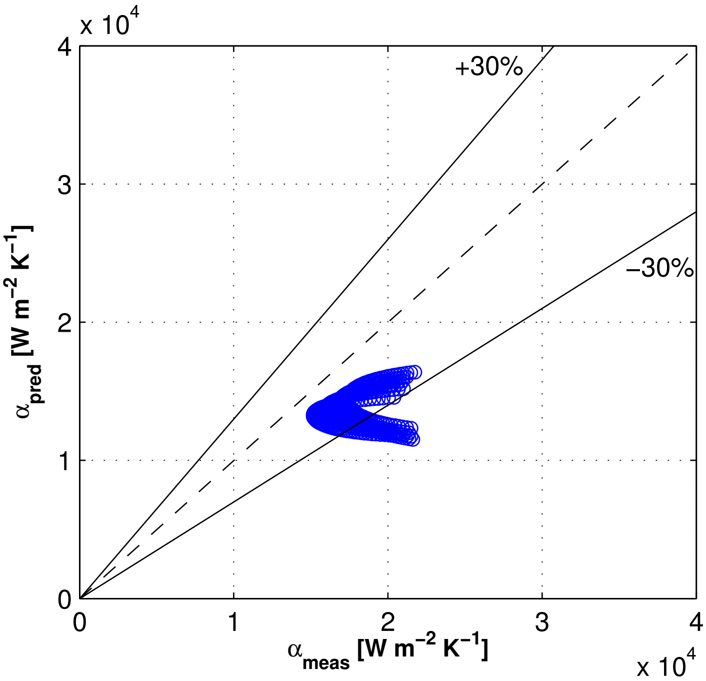

(b)

Figure 7.15: Comparison of the experimental local heat transfer coefficients, α_w, of R245fa flowing in $e_{in,rest} = 2$ with the: (a) Costa-Patry and Thome (2012), and (b) Bertsch et al. (2009) prediction methods.

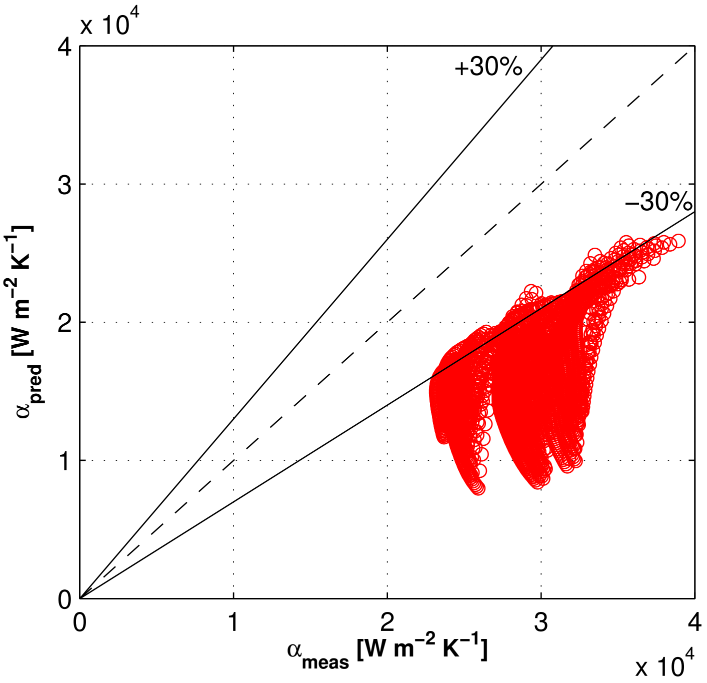

(a)

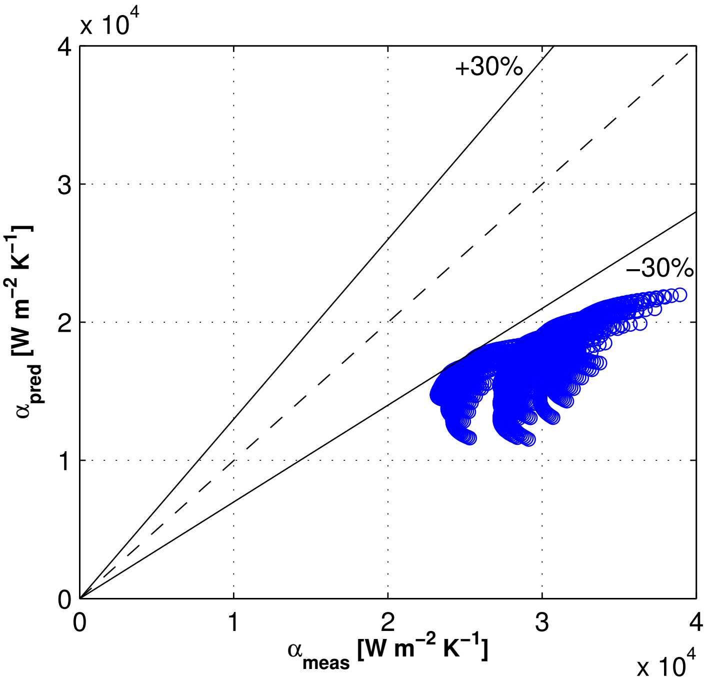

(b)

Figure 7.16: Comparison of the experimental local heat transfer coefficients, α_w, of R1234ze(E) flowing in $e_{in,rest} = 2$ with the: (a) Costa-Patry and Thome (2012), and (b) Bertsch et al. (2009) prediction methods.

method slightly increased the MAE, although the trend is better predicted, as demonstrated in Fig. 7.12. Generally, the models underpredict the experimental data. This might be due to the size of the channels, micro-orifice's entrance effects or due to the fact that the heat loss to the surrounding environment was neglected.

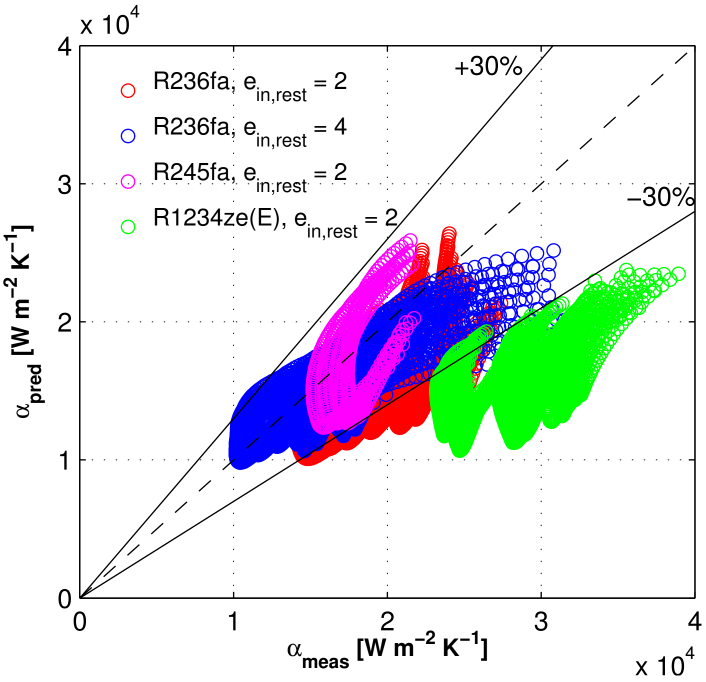

Figure 7.17: Comparison of the experimental and predicted local heat transfer coefficients applying a new vapor quality buffer of $x_{buffer} = \pm 2 x_{CB-AF}$ to the flow pattern-based model of Costa-Patry and Thome (2012). The lines in the graph correspond to the local change in vapor quality for a single experiment.

7.6 Conclusions

The following conclusions can be drawn from the present heat transfer tests and trends analysis:

- The two-phase flow patterns appearing in the channel and the transition in between them were found to have a significant influence on the heat transfer coefficient. The coalescing bubble regime was found to have a decreasing trend in heat transfer coefficient versus vapor quality, while annular flow has an increasing trend in heat transfer coefficient versus vapor quality. The coalescing bubble to annular flow (CB - AF) transition of Costa-Patry and Thome (2012) was found to relatively well predict the location of the minimum in this transition in the current experimental database.
- The heat transfer coefficients were determined with a very fine resolution corresponding to the vapor quality increment of a fraction of a percent that enabled a very detailed view

of the heat transfer coefficients along the channel length in the neighborhood of the flow transition from coalescing bubble to annular flow. It was shown that the heat transfer coefficient does not change sharply at the transition zone, but rather has a smooth change in trend. A characteristic U-shape of the heat transfer coefficient trend was observed, where the descending branch of the curve corresponds to the coalescing bubble flow regime, while the ascending one represents the increasing heat transfer coefficient in the annular flow regime. The shallow, broad minimum is probably due to *churn* flow in between these dominant flow patterns.

- The wall heat transfer coefficient increases with increasing mass flux for a constant vapor quality and its average level increases with increasing wall heat flux for a constant mass flux.
- Refrigerant R1234ze(E) has the highest heat transfer coefficients, which brought the junction temperature to values below 43.1 °C, as listed in Table 5.4. That is only about 10 – 12 °C above the coolant temperature. According to the knowledge of the author, it is the first experimental study in silicon multi-microchannels that investigated the heat transfer performance of this fluid along with two other low-pressure refrigerants. The tests for a medium-pressure refrigerant were possible due to a robust design of the modular test sections with the customized aluminium micro-heater sputtered onto the silicon base to simulate the power dissipated by the active components in a 3D CMOS chip.
- The expansion ratio of the inlet restriction seems to have a noticeable effect on the heat transfer coefficient trend, so that the reduction in the flow area causes more perturbation to the liquid film. The entrained liquid fraction in the vapor core potentially increases and the liquid film at the channel perimeter becomes thinner. Therefore, the annular flow heat transfer coefficient increases.
- The best prediction method was found to be the flow pattern-based model of Costa-Patry and Thome (2012). It predicts the trends and minimum in the data for low aspect ratio channels, where the liquid film is redistributed over an equivalent diameter being two times smaller than that tested by Costa-Patry and Thome (2012). Moreover, a new vapor quality buffer for the transition from coalescing bubble to annular flow of Costa-Patry and Thome (2012) is proposed in order to better reflect the U-shape of the heat transfer coefficient trend. The comparison of the modified method with the experimental results showed good agreement.

Chapter 8

Concluding remarks and recommendations for further investigations

8.1 Final remarks

The present experimental investigation of the two-phase refrigerant flows, namely R245fa, R236fa, and R1234ze(E), opens a new avenue towards two-phase electronics cooling of a future 3D stacked computer chip in order to extent the CMOS performance trend over the next decades. The major achievements and conclusions are stated below:

- New modular test sections, comprised of 67 parallel microchannels, each having a cross-sectional area of $100\,\mathrm{x}\,100\,\mu\mathrm{m}^2$ and 2 customized back-side microheaters, which eliminated the necessity of using thermal interface materials (TIMs), were designed and tested in meticulous manner, utilizing an existing test facility.
- Significant flow instabilities in both time and space, back flow, and flow maldistribution were observed in the micro-evaporator without any inlet restrictions leading to high amplitude, high-frequency temperature and pressure oscillations. Such undesired phenomena were successfully eliminated by placing micro-orifices at the inlet of each channel, thus ensuring a wide range of stable two-phase flow operating conditions and considerably improving flow uniformity.
- Simultaneous high-speed video and infra-red camera visualizations of the two-phase flow and heat transfer dynamics across the micro-evaporator area allowed the various different operating regimes to be identified and then represented by the two-phase flow operational maps.
- In the present research study, the IR camera was successfully applied to visualize the tem-

perature distribution at the base of the silicon micro-evaporator providing two-dimensional temperature fields of 10’000 pixels over a 1 cm^2 heated area. Thus, 600’000 IR temperature measurements per second were recorded at 60 Hz with an accuracy of ±0.2 °C in the temperature range of the two-phase flow experiments.

- The use of micro-orifices is essential for two-phase cooling in order to ensure the stable operation of future 3D interlayer cooling systems. A downstream effect of the micro-orifices’ impinging jet’s of vapor into the channel seems to have a noticeable effect on the channel pressure drops and the heat transfer coefficients, so that the reduction in the flow area causes more perturbation to the liquid film. Therefore, the annular flow heat transfer coefficient increases, due to thinning of the liquid film at the channel perimeter.

- The flashing two-phase flow without back flow operating regime with the best flow stability and heat transfer performance was identified as the optimal operating regime. Due to the flashing effect, the onset of boiling starts at lower heat fluxes, so that the wall-temperature distribution becomes more uniform and the wall-temperature overshoot for the onset of boiling is significantly reduced or eliminated entirely.

- The maximum junction temperature of 57.1 °C at the test section base was measured while dissipating the maximum base heat flux of 48.6 $\mathrm{W\,cm^{-2}}$ for an exit saturation temperature of 31.5 °C.

- The inlet and the outlet restriction pressure losses, respectively $\Delta p_{in,rest}$ and $\Delta p_{out,rest}$, were quantified in order to accurately simulate the hydraulic performance of microchannel evaporators and provide more reliable heat transfer data. The single-phase flow inlet pressure losses were calculated and compared to the adiabatic experimentally measured pressure drops, revealing good agreement. The pressure losses through the outlet restriction were determined experimentally using the method of Costa-Patry et al. (2011b) and correlated based on the outlet conditions separately for each micro-evaporator and each test fluid.

- The 3D heat spreading towards the colder surrounding regions, due to the non-uniformity of the flow boiling heat transfer coefficients versus vapor quality was simulated, to obtain the actual local heat fluxes, which were then used to determine the local heat transfer coefficients.

- The heat transfer coefficients were determined with a very fine resolution (90 pixels) corresponding to a vapor quality increment of a fraction of a percent, which enabled a very detailed view of the trends in the heat transfer coefficients along the channel length in the neighborhood of the flow transition from coalescing bubble to annular flow (CB – AF). It was shown the heat transfer coefficient does not change sharply at the transition zone, but rather has a smooth change in trend. The characteristic U-shape of the heat transfer coefficient trend was observed, where the descending branch of the curve corresponds to the coalescing bubble flow regime, while ascending one represents the increasing heat transfer coefficient in the annular flow regime. The shallow, broad minimum is probably due to *churn* flow occurring in the transition in between these dominant flow patterns.

- The CB - AF transition of Costa-Patry and Thome (2012) was found to predict relatively well the location of the minimum in this transition, when extrapolating their method to the current experimental database of much smaller channels.
- The best heat transfer prediction method was found to be the flow pattern-based model of Costa-Patry and Thome (2012), which was updated here by introducing a new vapor quality buffer for the transition from coalescing bubble to annular flow in order to better reflect the U-shape of the heat transfer coefficient trend. The comparison of the modified method with the experimental results showed good agreement and respected the experimental trends.

8.2 Future recommendations

In future multi-microchannel investigations, attention should be brought to the following aspects:

- two-phase flow stability of multi-microchannel evaporators and their prediction
- higher heat flux and CHF tests, which will require using RTDs to control a down power
- prediction of heat transfer performance for medium- and high-pressure refrigerants in multi-microchannels
- modification of microchannel surface or / and channel microstructure to enhance heat transfer
- study flashing phenomena in the micro-orifices with a high resolution optical system
- development of more precise measurements of the microchannel film flow without disturbing the flow such as use of μPIV
- pressure and mass flow rate measurements in individual channels of a multi-channel test elements.

Appendix A

Error propagation

A.1 Fluid properties

The properties of the test fluids were obtained using the REFPROP 8.0 software (NIST Standard Reference Database 23) with uncertainties between 0.1 and 5% depending on its state and temperature. In general, the estimated uncertainties fall within 0.1 − 0.2%.

A.1.1 Single-phase flow

$$\delta T_{fl} = T_{fl}\left(h_l + \delta h_l, p + \delta p\right) - \delta T_{fl}\left(h, p\right) \tag{A.1}$$

$$\delta h_l = h_l\left(T_{fl} + \delta T_{fl}, p + \delta p\right) - \delta h_l\left(T_{fl}, p\right) \tag{A.2}$$

$$\delta \rho_l = \rho_l\left(T_{fl} + \delta T_{fl}, p + \delta p\right) - \delta \rho_l\left(T_{fl}, p\right) \tag{A.3}$$

$$\delta \mu_l = \mu_l\left(T_{fl} + \delta T_{fl}, p + \delta p\right) - \delta \mu_l\left(T_{fl}, p\right) \tag{A.4}$$

$$\delta c_{pl} = \mu_l\left(T_{fl} + \delta T_{fl}, p + \delta p\right) - \delta \mu_l\left(T_{fl}, p\right) \tag{A.5}$$

A.1.2 Two-phase flow

$$\delta T_{fl,sat} = T_{fl,sat}\left(p_{sat} + \delta p_{sat}\right) - \delta T_{fl,sat}\left(p_{sat}\right) \tag{A.6}$$

$$\delta p_{sat} = p_{sat}\left(T_{fl,sat} + \delta T_{fl,sat}\right) - \delta p_{sat}\left(T_{fl,sat}\right) \tag{A.7}$$

$$\delta h_l = h_l\left(p_{sat} + \delta p_{sat}\right) - \delta h_l\left(p_{sat}\right) \tag{A.8}$$

$$\delta h_v = h_v\left(p_{sat} + \delta p_{sat}\right) - \delta h_v\left(p_{sat}\right) \tag{A.9}$$

$$\delta \rho_l = \rho_l\left(p_{sat} + \delta p_{sat}\right) - \delta \rho_l\left(p_{sat}\right) \tag{A.10}$$

$$\delta\mu_l = \mu_l\left(p_{sat} + \delta p_{sat}\right) - \delta\mu_l\left(p_{sat}\right) \tag{A.11}$$

A.2 Derived parameters

The errors of the derived parameters were computed using the method of Kline and McClintock (1953). The following equations were applied.

A.2.1 Expansion ratio

$$\delta e_{in,rest}^2 = \left(\frac{1}{W_{in,rest}}\delta W_{ch}\right)^2 + \left(\frac{W_{ch}}{W_{in,rest}^2}\delta W_{in,rest}\right)^2 \tag{A.12}$$

A.2.2 Aspect ratio

$$\delta a^2 = \left(\frac{1}{W_{ch}}\delta H_{ch}\right)^2 + \left(\frac{H_{ch}}{W_{ch}^2}\delta W_{ch}\right)^2 \tag{A.13}$$

A.2.3 Channel mass flux

$$\delta G_{ch}^2 = \left(\frac{1}{NW_{ch}H_{ch}}\delta M\right)^2 + \left(\frac{M}{NW_{ch}H_{ch}^2}\delta H_{ch}\right)^2 + \left(\frac{M}{NW_{ch}^2H_{ch}}\delta W_{ch}\right)^2 \tag{A.14}$$

For the flow rate, M, lower than $ZS/0.001$:

$$\delta M = \pm\frac{ZS}{M}\cdot 100\% \tag{A.15}$$

where ZS is the zero stability and it is equal $5.56\cdot 10^{-7}\,\mathrm{kg\,s^{-1}}$.

A.2.4 Base heat flux

$$\delta q_b^2 = \left(\frac{\varphi I}{L_hB}\delta V\right)^2 + \left(\frac{\varphi V}{L_hB}\delta I\right)^2 + \left(\frac{\varphi IV}{L_hB^2}\delta B\right)^2 + \left(\frac{\varphi IV}{L_h^2B}\delta L_h\right)^2 + \left(\frac{IV}{L_hB}\delta\varphi\right)^2 \tag{A.16}$$

A.2.5 Pressures

Inlet restriction pressure loss

$$\delta\Delta p^2_{in,rest} = \delta\Delta p^2_{cont,1} + \delta\Delta p^2_{cont,2} + \delta\Delta p^2_{cont,3} + \delta\Delta p^2_{\exp,1} \tag{A.17}$$

where

$$\delta\Delta p^2_{cont,1} = \left(\frac{S_{cont,1}G_{in,slit}}{\rho_l}\delta G_{in,slit}\right)^2 + \left(\frac{S_{cont,1}G^2_{in,slit}}{2\rho_l^2}\delta\rho_l\right)^2 \tag{A.18}$$

$$\delta\Delta p^2_{cont,2} = \left(\frac{S_{cont,2}G_{ts,pl}}{\rho_l}\delta G_{ts,pl}\right)^2 + \left(\frac{S_{cont,2}G^2_{ts,pl}}{2\rho_l^2}\delta\rho_l\right)^2 \tag{A.19}$$

$$\delta\Delta p^2_{cont,3} = \left(\frac{S_{cont,3}G_{in,rest}}{\rho_l}\delta G_{in,rest}\right)^2 + \left(\frac{S_{cont,3}G^2_{in,rest}}{2\rho_l^2}\delta\rho_l\right)^2 \tag{A.20}$$

and

$$S_{cont,1} = 1 - \left(\frac{A_{in,slit}}{A_{mf}}\right)^2 + K_{cont,1} \tag{A.21}$$

$$S_{cont,2} = 1 - \left(\frac{A_{ts,pl}}{A_{in,slit}}\right)^2 + K_{cont,2} \tag{A.22}$$

$$S_{cont,3} = 1 - \left(\frac{NA_{in,rest}}{A_{ts,pl}}\right)^2 + K_{cont,3} \tag{A.23}$$

with

$$K_{cont,1} = 0.0088\left(\frac{H_{in,slit}}{W_{in,slit}}\right)^2 - 0.1785\frac{H_{in,slit}}{W_{in,slit}} + 1.6027 \tag{A.24}$$

$$K_{cont,2} = 0.0088\left(\frac{H_{ts,pl}}{W_{ts,pl}}\right)^2 - 0.1785\frac{H_{ts,pl}}{W_{ts,pl}} + 1.6027 \tag{A.25}$$

$$K_{cont,3} = 0.0088\left(\frac{H_{in,rest}}{W_{in,rest}}\right)^2 - 0.1785\frac{H_{in,rest}}{W_{in,rest}} + 1.6027 \tag{A.26}$$

Moreover

$$\delta\Delta p^2_{\exp,1} = \left(\frac{S_{\exp,1}G_{in,rest}}{\rho_l}\delta G_{in,rest}\right)^2 + \left(\frac{S_{\exp,1}G^2_{in,rest}}{2\rho_l^2}\delta\rho_l\right)^2 \tag{A.27}$$

where $S_{\exp,1}$ might refer to single-phase flow (sp) or two-phase flow (tp):

$$S_{\exp,1-sp} = -2\times 1.33\left(\frac{A_{in,rest}}{A_{ch}}\right)\left[1-\left(\frac{A_{in,rest}}{A_{ch}}\right)\right] \tag{A.28}$$

$$S_{\exp,1-tp} = \left[\frac{A_{in,rest}}{A_{ch}}\left(\frac{A_{in,rest}}{A_{ch}}-1\right)\right]\left(1-x\left(L_{in,rest}\right)\right)^2\left[1+\frac{C}{X_{tt}}+\frac{1}{X^2_{tt}}\right] \tag{A.29}$$

A.2.6 Frictional channel pressure drop

$$\begin{aligned}\delta\Delta p_{ch}^{2} = &\left(4\frac{G_{ch}^{2}}{2\rho_{l}}\frac{L_{ch}}{D_{h}}\delta f\right)^{2} + \left(8f\frac{G_{ch}}{2\rho_{l}}\frac{L_{ch}}{D_{h}}\delta G_{ch}\right)^{2} + \left(4f\frac{G_{ch}^{2}}{2\rho_{l}^{2}}\frac{L_{ch}}{D_{h}}\delta\rho_{l}\right)^{2} \\ &+ \left(4f\frac{G_{ch}^{2}}{2\rho_{l}}\frac{1}{D_{h}}\delta L_{ch}\right)^{2} + \left(4f\frac{G_{ch}^{2}}{2\rho_{l}}\frac{L_{ch}}{D_{h}^{2}}\delta D_{h}\right)^{2}\end{aligned} \tag{A.30}$$

Outlet restriction pressure loss

$$\delta\Delta p_{out,rest}^{2} = \delta p_{ch,end}^{2} + \delta p_{out}^{2} \tag{A.31}$$

where

$$\delta p_{ch,end} = p_{sat}\left(T_{IR,z=10\mathrm{mm}} + \delta T_{IR,z=10\mathrm{mm}}\right) - p_{sat}\left(T_{IR,z=10\mathrm{mm}}\right) \tag{A.32}$$

Channel pressure drop

$$\delta\Delta p_{ch}^{2} = \delta\Delta p_{total}^{2} + \delta\Delta p_{in,rest}^{2} + \delta\Delta p_{out,rest}^{2} \tag{A.33}$$

A.2.7 Vapor quality

$$\delta x^{2} = \left(\frac{\delta h\left(z\right)}{h_{lv}(p_{sat})}\right)^{2} + \left(\frac{\delta h_{l}(p_{sat})}{h_{lv}(p_{sat})}\right)^{2} + \left(\frac{h(z) - h_{l}(p_{sat})}{h_{lv(p_{sat})}^{2}}\delta h_{LV}(p_{sat})\right)^{2} \tag{A.34}$$

A.2.8 Silicon thermal conductivity

$$\delta k_{Si} = 0.0014T\delta T - 0.5416\delta T \tag{A.35}$$

A.2.9 Footprint temperature

$$\delta T_{ft}^{2} = \delta T_{IR}^{2} + \left(\frac{d_{Si}}{k_{Si}}\delta q_{Si}\right)^{2} + \left(\frac{q_{Si}}{k_{Si}}\delta d_{Si}\right)^{2} + \left(\frac{q_{Si}d_{Si}}{k_{Si}^{2}}\delta k_{Si}\right)^{2} \tag{A.36}$$

A.2.10 Heat transfer coefficient

For the ΔT between the wall and the temperature of the fluid, the error is:

$$\delta \Delta T^2 = \delta T_{ft}^2 + \delta T_{fl}^2 \tag{A.37}$$

$$\delta \alpha_w^2 = \left(\frac{1}{\Delta T} \delta q_w \right)^2 + \left(\frac{q_w}{\Delta T^2} \delta \Delta T \right)^2 \tag{A.38}$$

where

$$\delta q_w = \frac{q_w}{q_{Si}} \delta q_{Si} \tag{A.39}$$

A.2.11 Multi-dimensional heat conduction

$$\delta T_w = \delta T_{U,d_{Si}} \tag{A.40}$$

$$\delta q_w = \frac{1}{dydz} \delta Q_{U,d_{Si}} \tag{A.41}$$

$$\delta Q_U^2 = \delta Q_D^2 + \delta Q_L^2 + \delta Q_F^2 + \delta Q_R^2 + \delta Q_B^2 \tag{A.42}$$

$$\delta Q_L^2 = \left(dxdy \frac{\Delta T}{dz} \delta k_{Si} \right)^2 + \left(dxdy \frac{k_{Si}}{dz} \delta \Delta T \right)^2 = \delta Q_R^2 \tag{A.43}$$

$$\delta Q_F^2 = \left(dxdz \frac{\Delta T}{dy} \delta k_{Si} \right)^2 + \left(dxdz \frac{k_{Si}}{dy} \delta \Delta T \right)^2 = \delta Q_B^2 \tag{A.44}$$

$$\delta \Delta T^2 = \delta T_{CV}^2 + \delta T_{notation}^2 \tag{A.45}$$

where the subscript *notation* indicates: D – down, U – up, F – front, B – back, L – left, and R – right.

Appendix B

Further results

B.1 Total adiabatic pressure drops

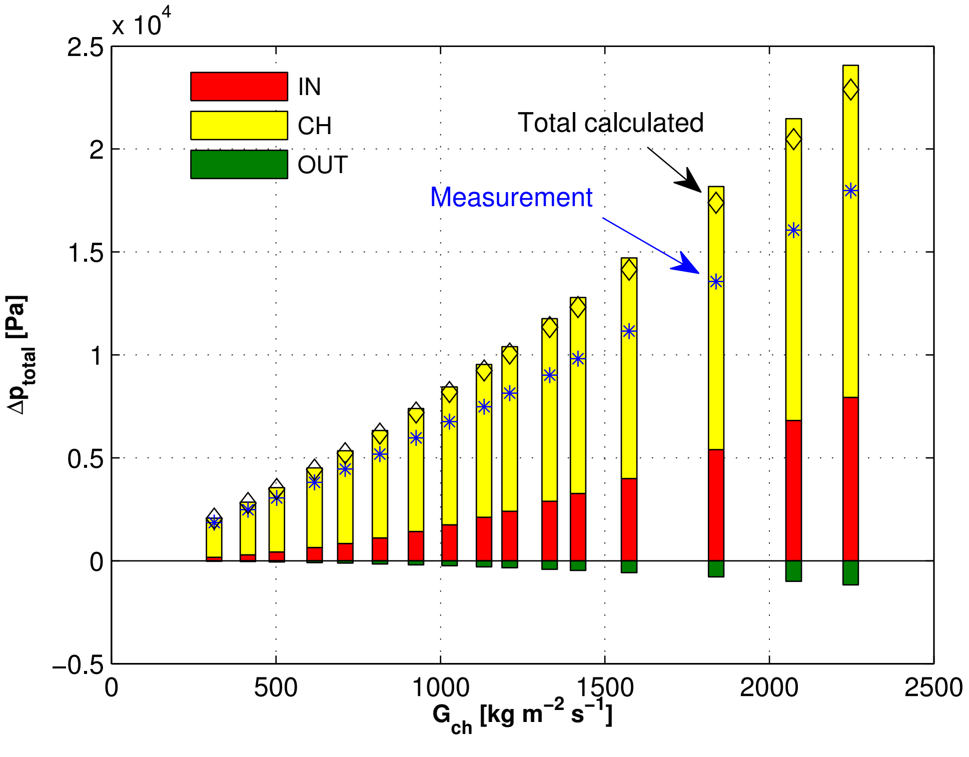

Figure B.1: Adiabatic pressure gradients for R236fa in the test section with the inlet restrictions of $e_{in,rest} = 1.33$.

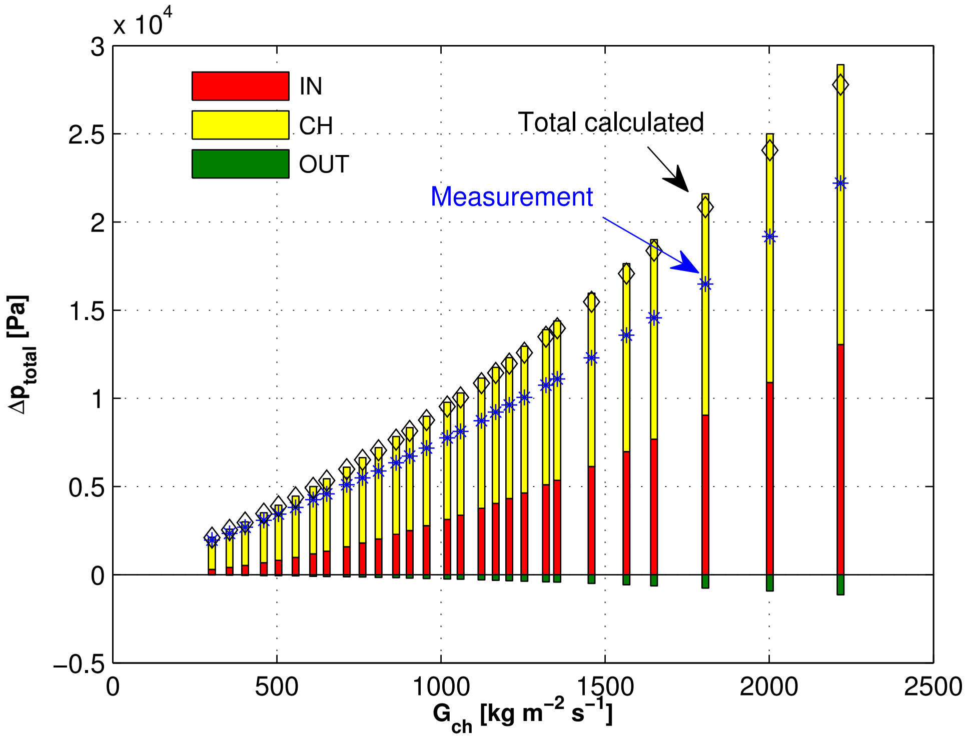

Figure B.2: Adiabatic pressure gradients for R236fa in the test section with the inlet restrictions of $e_{in,rest} = 2$.

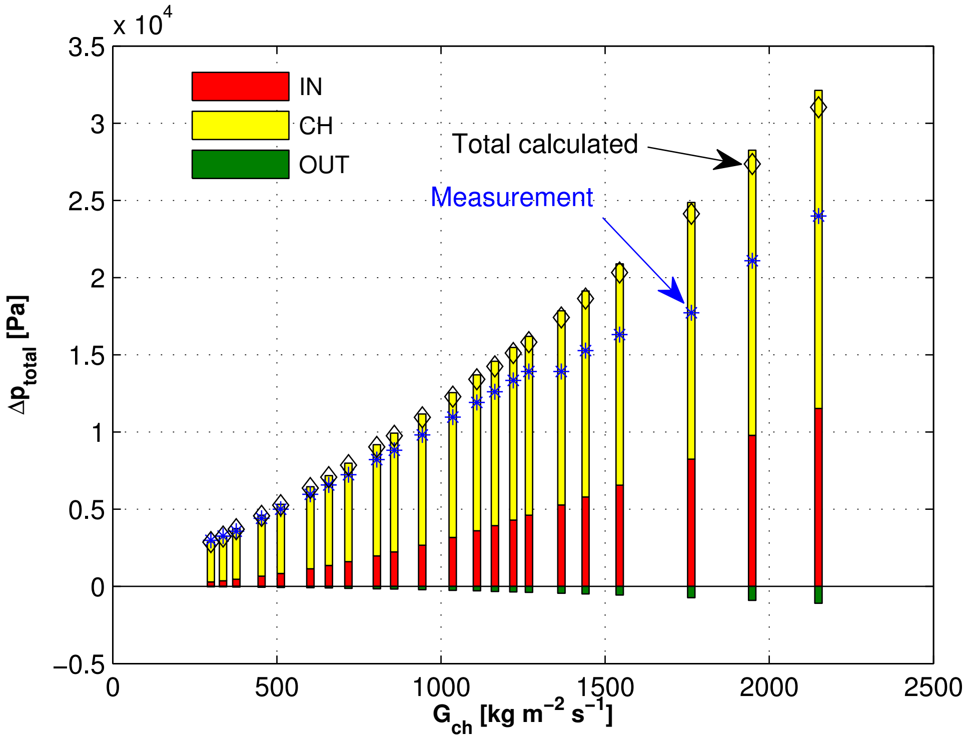

Figure B.3: Adiabatic pressure gradients for R245fa in the test section with the inlet restrictions of $e_{in,rest} = 2$.

B.2 Total two-phase flow pressure drops under uniform heating

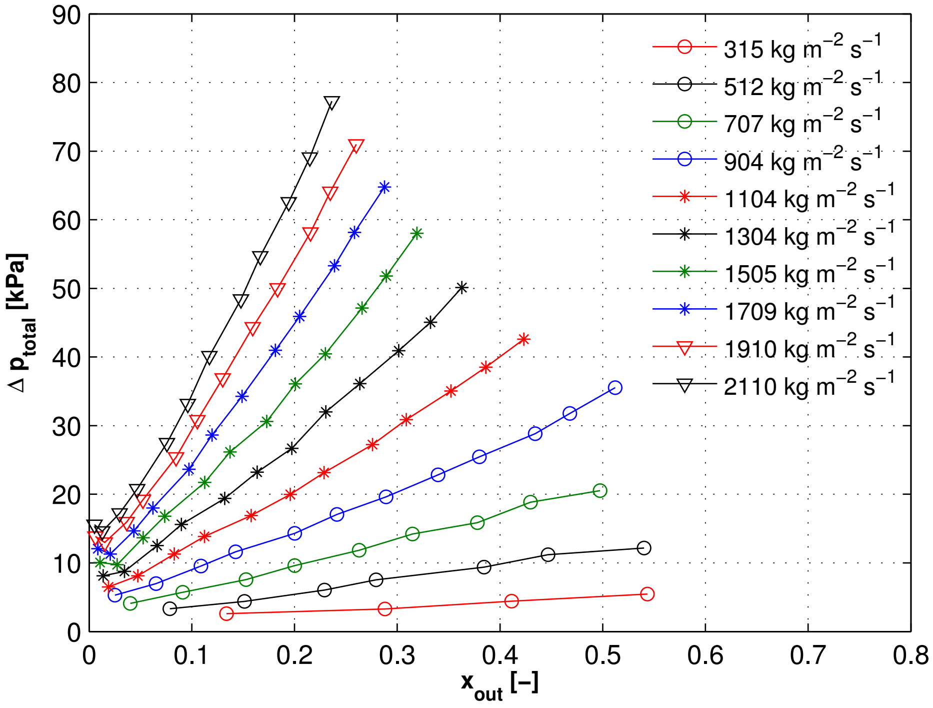

Figure B.4: Δp_{total} versus x_{out} for R236fa in the test section of $e_{in,rest} = 1.33$, where G_{ch} for an individual data point might vary ±10% of the reported nominal value of the curve.

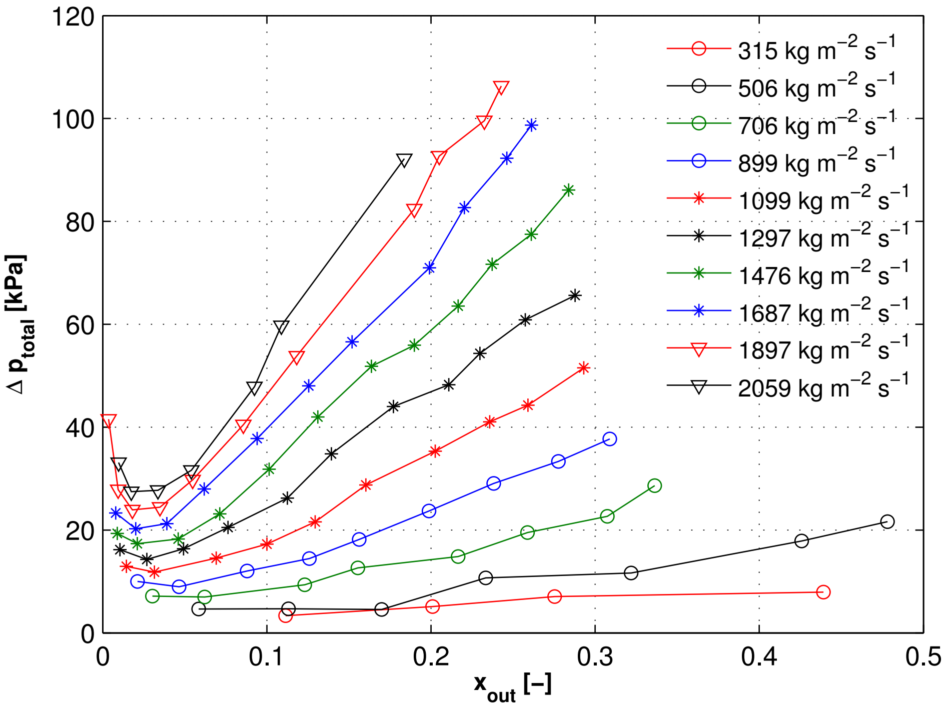

Figure B.5: Δp_{total} versus x_{out} for R245fa in the test section of $e_{in,rest} = 2$, where G_{ch} for an individual data point might vary ±10% of the reported nominal value of the curve.

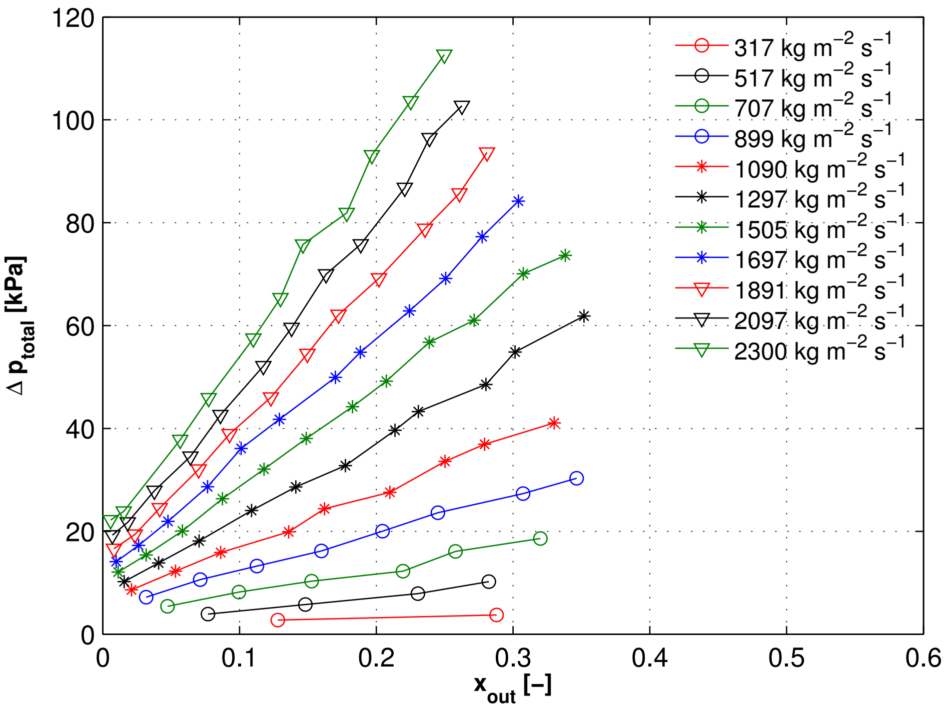

Figure B.6: Δp_{total} versus x_{out} for R236fa in the test section of $e_{in,rest} = 2$, where G_{ch} for an individual data point might vary ±5.36% of the reported nominal value of the curve.

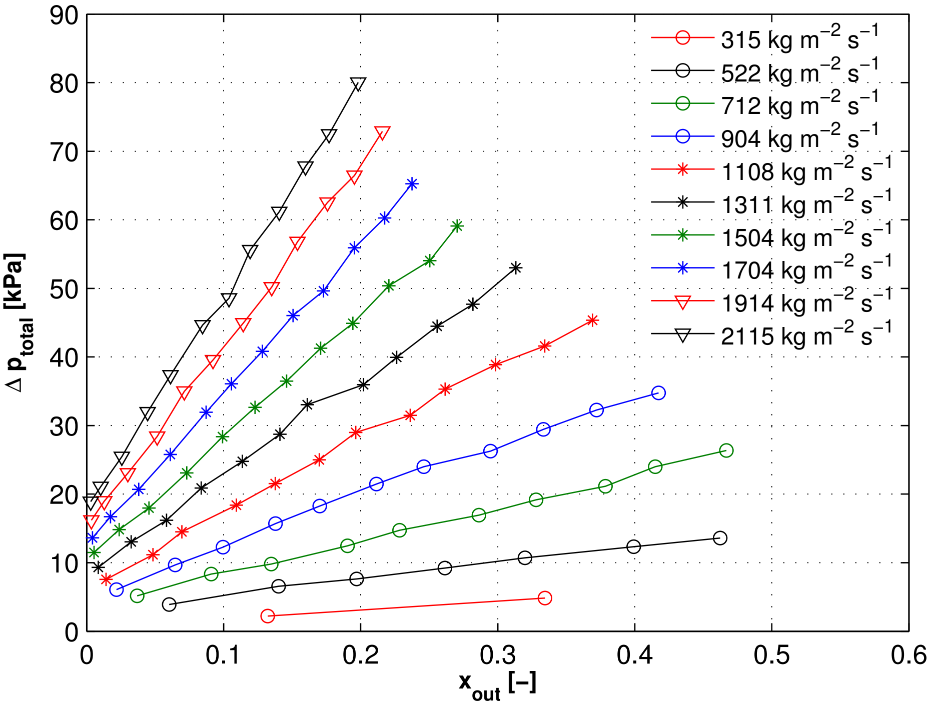

Figure B.7: Δp_{total} versus x_{out} for R1234ze(E) in the test section of $e_{in,rest} = 2$, where G_{ch} for an individual data point might vary ±3.33% of the reported nominal value of the curve.

B.3 Two-phase flow channel pressure drops

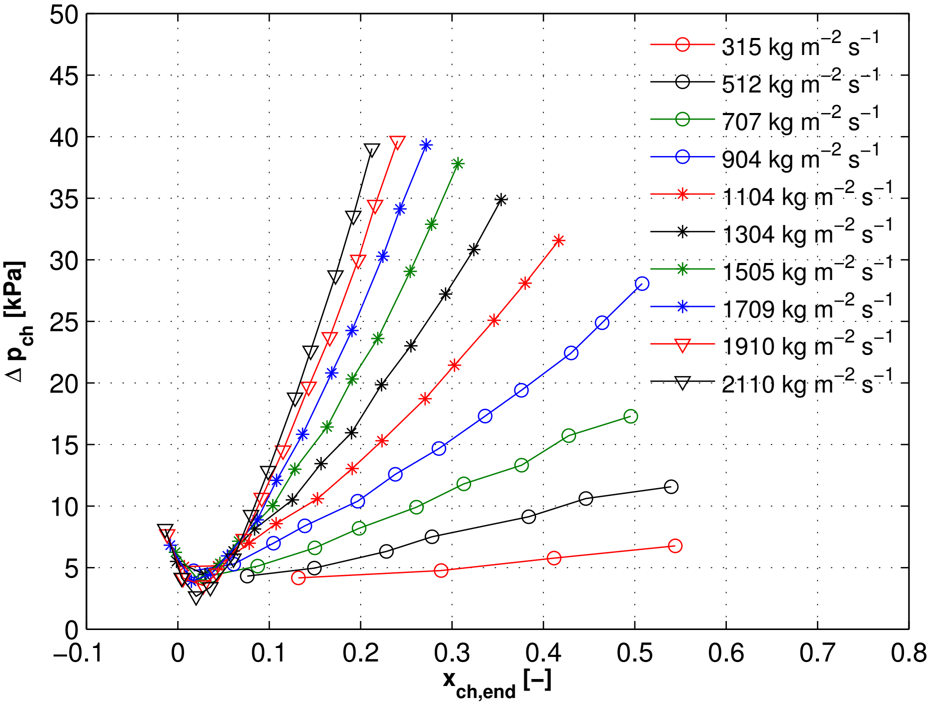

Figure B.8: Δp_{ch} for R236fa flowing within the micro-evaporator with the inlet restrictions of $e_{in,rest} = 1.33$.

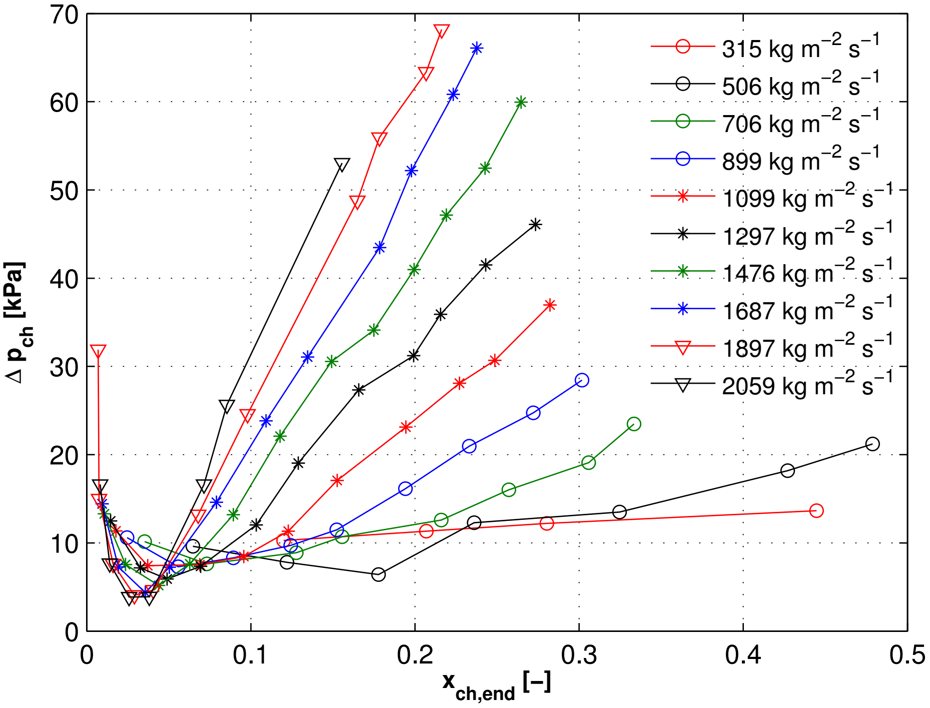

Figure B.9: Δp_{ch} for R245fa flowing within the micro-evaporator with the inlet restrictions of $e_{in,rest} = 2$.

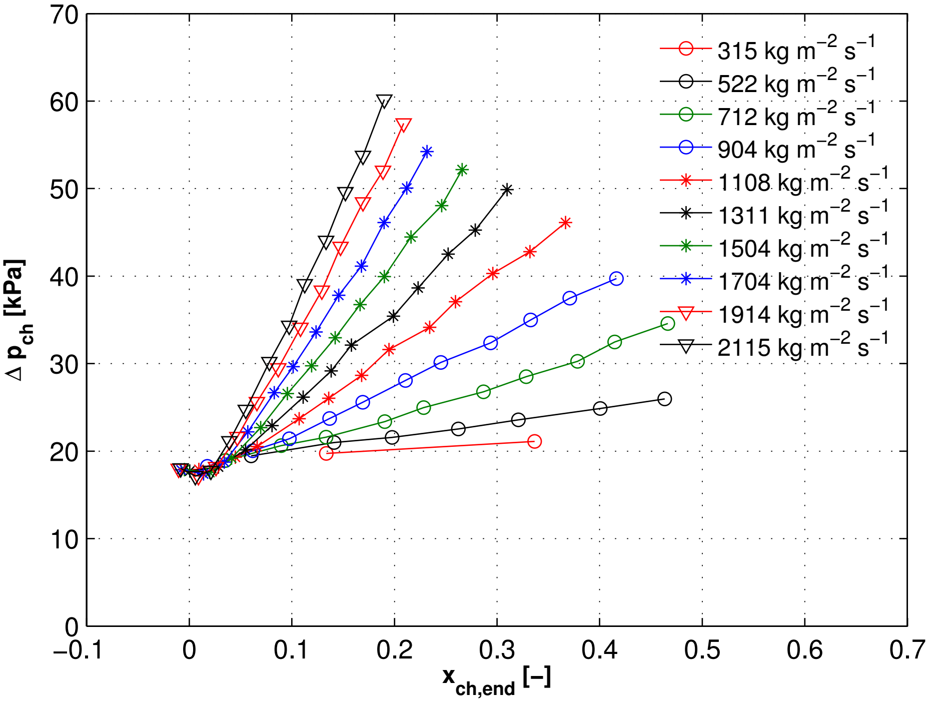

Figure B.10: Δp_{ch} for R1234ze(E) flowing within the micro-evaporator with the inlet restrictions of $e_{in,rest} = 2$.

B.4 Two-phase heat transfer coefficient with 3D heat spreading

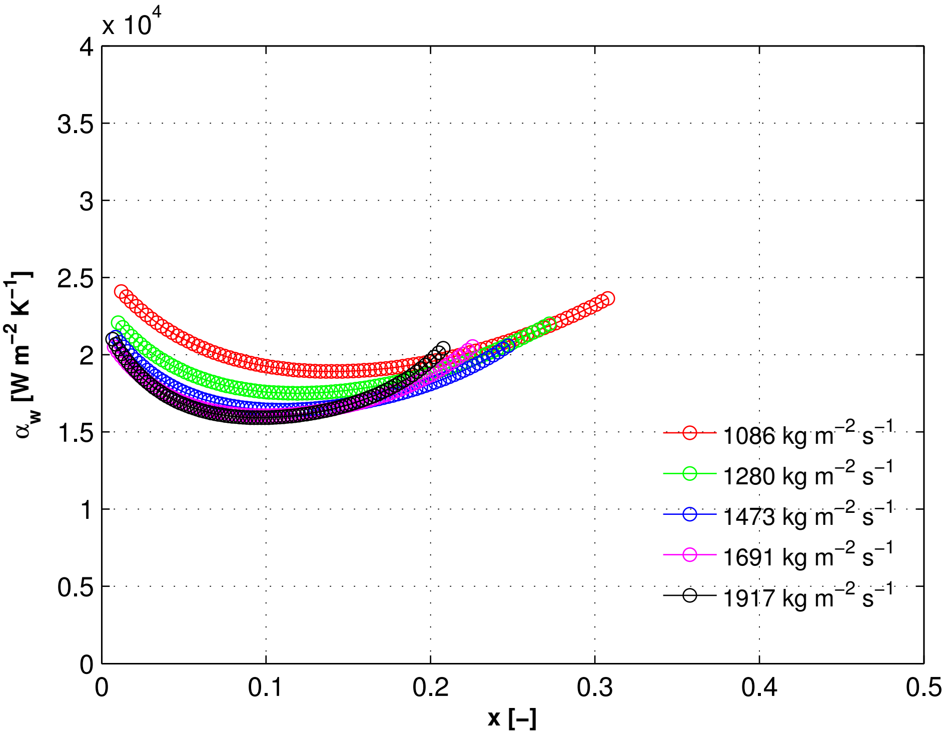

Figure B.11: α_w versus x for R245fa flowing in the test section with the inlet restrictions of $e_{in,rest} = 2$ for $q_w = 172\,\mathrm{kW\,m^{-2}}$.

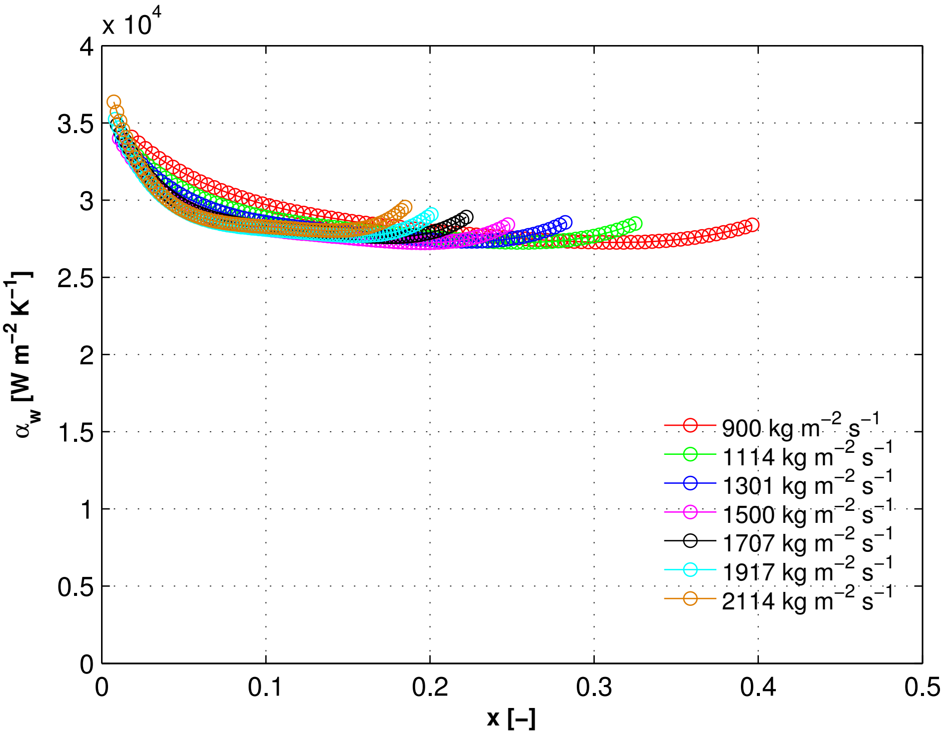

Figure B.12: α_w versus x for R1234ze(E) flowing in the test section with the inlet restrictions of $e_{in,rest} = 2$ for $q_w = 175\,\mathrm{kW\,m^{-2}}$.

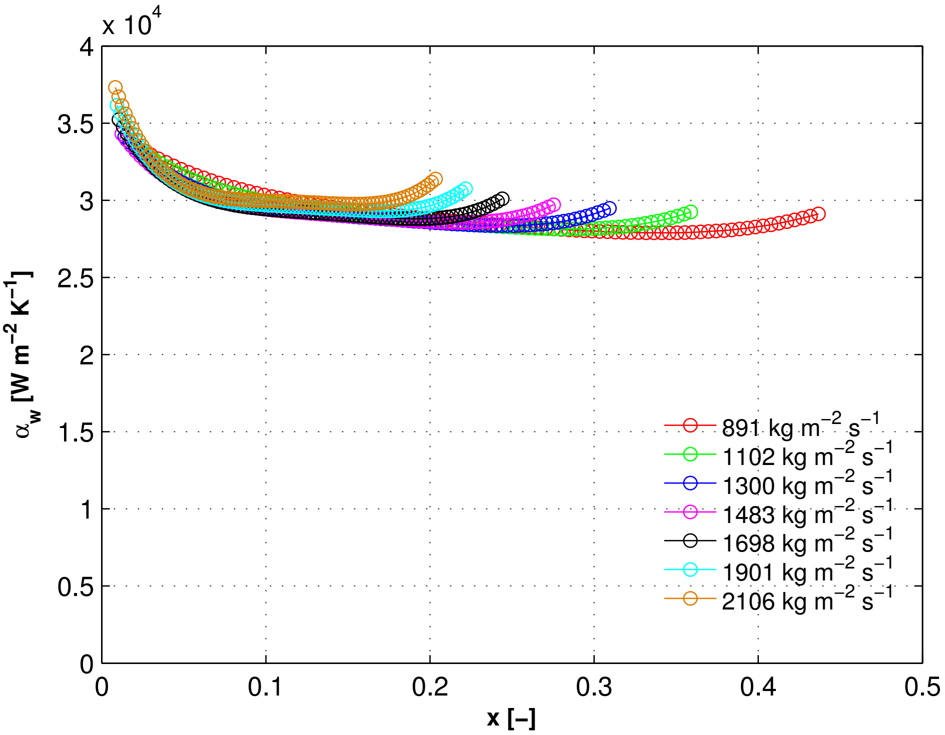

Figure B.13: α_w versus x for R1234ze(E) flowing in the test section with the inlet restrictions of $e_{in,rest} = 2$ for $q_w = 192\,\mathrm{kW\,m^{-2}}$.

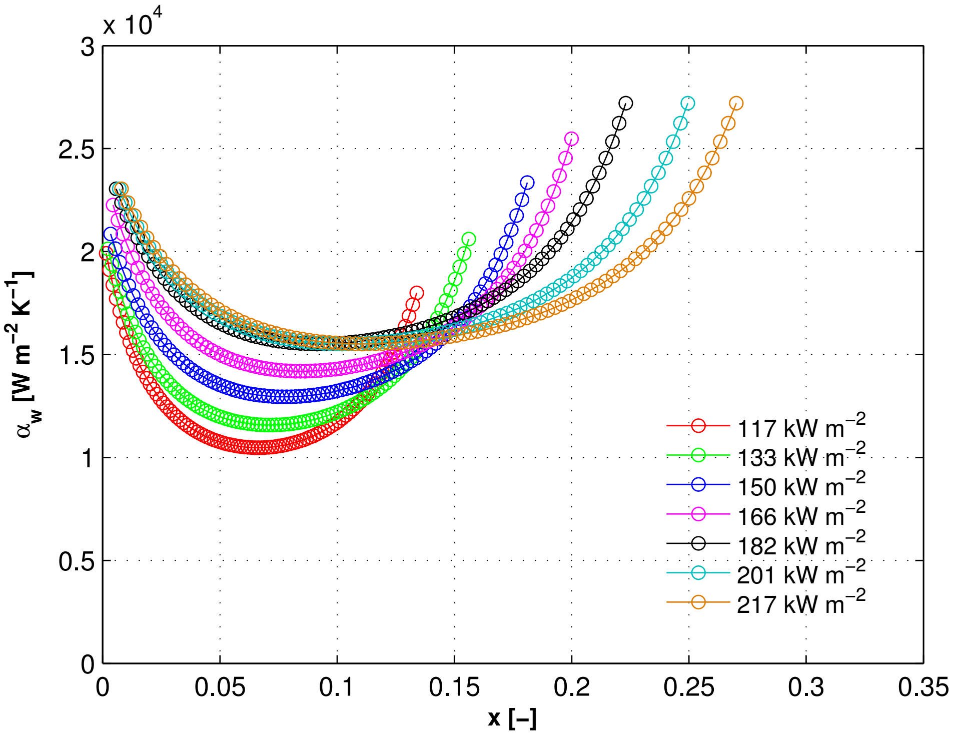

Figure B.14: α_w versus x for R236fa flowing in the test section with the inlet restrictions of $e_{in,rest} = 4$ for $G_{ch} \approx 2'100\,\mathrm{kg\,m^{-2}\,s^{-1}}$.

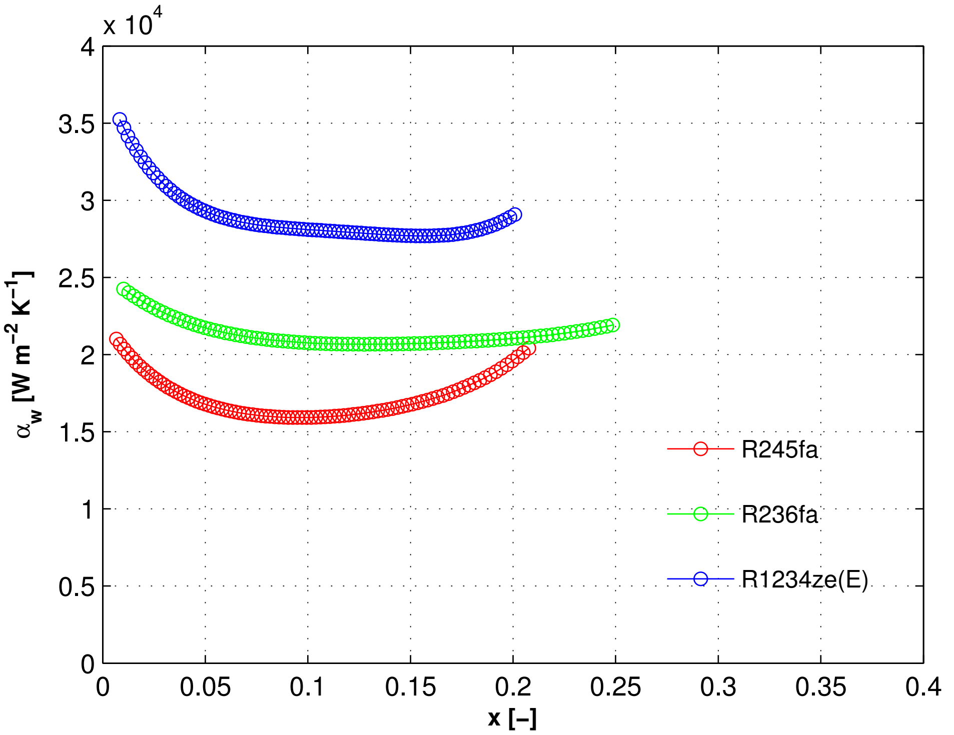

Figure B.15: Two-phase wall heat transfer coefficient of R245fa, R236fa, and R1234ze(E) flowing in $e_{in,rest} = 2$, $q_w \approx 175\,\mathrm{kW\,m^{-2}}$, $G_{ch} \approx 1'900\,\mathrm{kg\,m^{-2}\,s^{-1}}$.

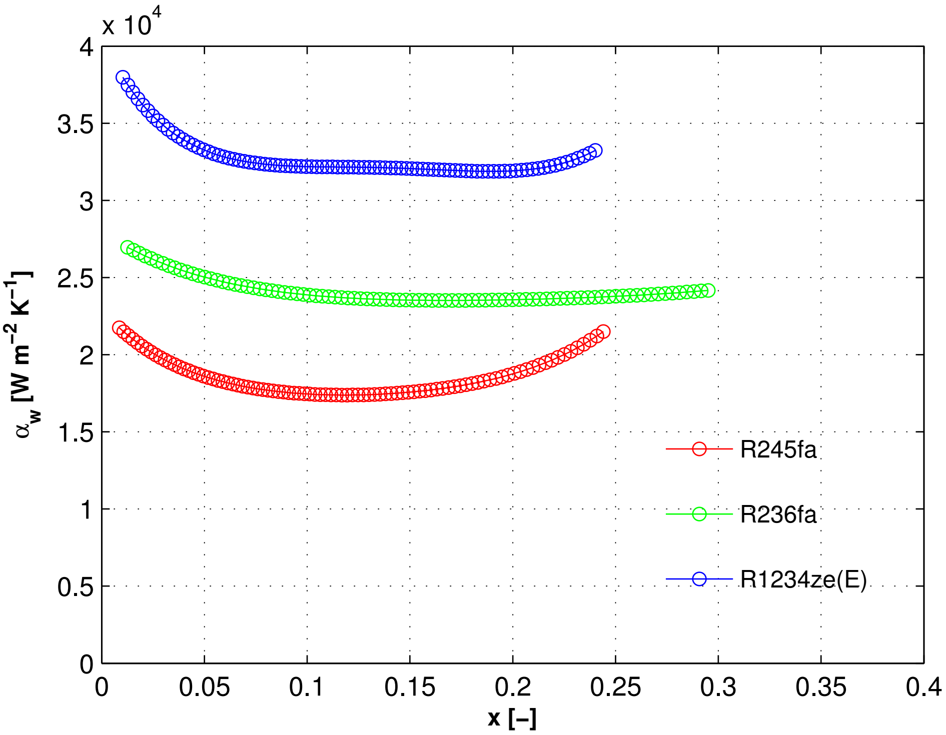

Figure B.16: Two-phase wall heat transfer coefficient of R245fa, R236fa, and R1234ze(E) flowing in $e_{in,rest} = 2$, $q_w \approx 210\,\mathrm{kW\,m^{-2}}$, $G_{ch} \approx 1'900\,\mathrm{kg\,m^{-2}\,s^{-1}}$.

Appendix C

Existing heat transfer prediction methods compared with the current results

This appendix describes in more detail the two heat transfer prediction methods, namely the correlation of Bertsch et al. (2009) and the model of Costa-Patry et al. (2012), used for comparison with the experimental results. Recently, these two methods have been shown to be the most accurate ones (Costa-Patry et al., 2012).

C.1 A composite heat transfer correlation of Bertsch et al. (2009)

The heat transfer prediction method of Bertsch et al. (2009) is based on the Chen (1966) correlation and assumes that the flow boiling heat transfer coefficient is a sum of weighted nucleate and convective heat transfer terms:

$$\alpha_{FB} = \alpha_{NB} S + \alpha_{conv,tp} F \tag{C.1}$$

where S is a suppression factor applied to the nucleate boiling term that in small channels takes into account a dryout condition as the vapor quality increases. Their model stands for a linear decrease of the nucleate boiling heat transfer coefficient, α_{NB}, with increasing vapor quality:

$$S = 1 - x \tag{C.2}$$

and F is an enhancement factor applied to the convective heat transfer term taking into account the enhanced convection due to higher flow velocities at higher vapor qualities:

$$F = 1 + a \cdot e^{-b \cdot Co} \cdot \left(x^2 - x^6\right) \tag{C.3}$$

where a and b are constants determined based on the experimental results from 14 studies available in the literature for 12 different fluids, vertical and horizontal channels (both single and multiple) with diameters ranging from 0.16 to 2.92 mm and confinement numbers, Co, from 0.3 to 4.0. The parameters a and b are here equal to 80 and 0.6, respectively. The model considers the effect of bubble confinement in small channels by means of the factor F, while the nucleate boiling suppression factor, S, appears to be independent of the channel diameter (Bertsch et al., 2008).

Furthermore, the nucleate boiling contribution is expressed by the Cooper (1984) nucleate pool boiling correlation:

$$\alpha_{NB} = 55 \cdot p_r^{0.12-0.2 \cdot \log_{10} R_p} \cdot \left(-\log_{10} p_r\right)^{-0.55} \cdot M_{mol}^{-0.5} \cdot q^{0.67} \tag{C.4}$$

where R_p is the surface roughness according to DIN 4762, which should be set equal to 1 μm if this parameter is unknown. Notably, the authors did not actually observed nucleate boiling in microchannels, but only hypothesized its existence.

Afterwards, the convective heat transfer coefficient is calculated as follows:

$$\alpha_{conv,tp} = \alpha_{conv,l}\left(1 - x\right) + \alpha_{conv,v} x \tag{C.5}$$

where the convective heat transfer in the liquid and the vapor phase is described by the Hausen (1943) correlation for developing laminar flow, respectively:

$$\alpha_{conv,l} = \left(3.66 + \frac{0.0668 \cdot \frac{D_h}{L} \cdot \mathrm{Re}_l \cdot \mathrm{Pr}_l}{1 + 0.04 \cdot \left[\frac{D_h}{L} \cdot \mathrm{Re}_l \cdot \mathrm{Pr}_l\right]^{\frac{2}{3}}}\right) \cdot \frac{k_l}{D_h} \tag{C.6}$$

$$\alpha_{conv,v} = \left(3.66 + \frac{0.0668 \cdot \frac{D_h}{L} \cdot \mathrm{Re}_v \cdot \mathrm{Pr}_v}{1 + 0.04 \cdot \left[\frac{D_h}{L} \cdot \mathrm{Re}_v \cdot \mathrm{Pr}_v\right]^{\frac{2}{3}}}\right) \cdot \frac{k_v}{D_h} \tag{C.7}$$

with the tubular Reynolds numbers of saturated liquid and saturated vapor defined as:

$$\mathrm{Re}_l = \frac{G \cdot D_h}{\mu_l} \tag{C.8}$$

$$\mathrm{Re}_v = \frac{G \cdot D_h}{\mu_v} \tag{C.9}$$

C.2 Flow pattern-based model of Costa-Patry et al. (2012)

It is commonly accepted that the heat transfer coefficient trend strongly depends on the two-phase flow patterns within a channel and the transitions between them (Szczukiewicz et al., 2012b). Figure C.1 illustrates the experimental results of Costa-Patry and Thome (2011) obtained for a multi-microchannel test element with 35 local heaters. As seen, good agreement between those and the heat transfer prediction methods, namely the three-zone model of Thome et al. (2004) and the annular model of Cioncolini and Thome (2011), was shown within their range of applicability defined by the coalescing bubble to the annular flow transition (CBA transition in Fig. C.1).

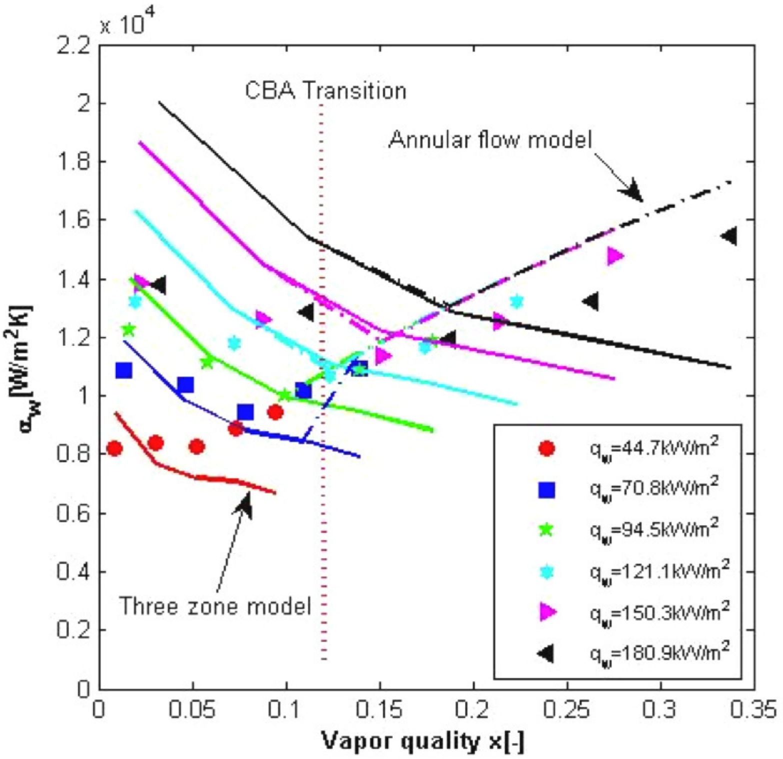

Figure C.1: Multi-microchannel two-phase flow heat transfer coefficient versus vapor quality for R236fa and $G_{ch} = 823\,\mathrm{kg\,m^{-2}\,s^{-1}}$. Figure extracted from Costa-Patry and Thome (2011).

A new flow pattern-based model was then proposed that combines the above-mentioned heat transfer prediction methods assuming the prorated heat transfer coefficient values around the flow transition since, as stated by the authors, it always changes smoothly between the flow regimes. The prorated heat transfer coefficient is expressed as follows:

$$\alpha_{CB-AF} = (1-r)\,\alpha_{3Z} + \frac{r\alpha_{AF}}{(1-r)\,\alpha_{3Z} + r\alpha_{AF}} \times \left(r\alpha_{AF} - (1-r)\,\alpha_{3Z}\right) \tag{C.10}$$

where the subscripts $3Z$ denotes the three-zone model of Thome et al. (2004) and AF refers to the annular model of Cioncolini and Thome (2011). The parameter r in Eq. (C.10) is a proration factor:

$$r = \frac{x - x_{CB-AF}}{0.2x_{exit}} + 0.5 \tag{C.11}$$

The range of proration is given by the vapor quality buffer:

$$x_{buffer} = x_{CB-AF} \pm \frac{x_{exit}}{5} \tag{C.12}$$

where: x_{exit} is the outlet vapor quality evaluated based on the energy balance neglecting the effect of flashing due to the pressure losses and x_{CB-AF} is the transition from coalescing to annular flow defined by Eq. (7.1).

The descriptions of the original models of Thome et al. (2004) and Cioncolini and Thome (2011) are provided below, respectively, in Sections C.2.1 and C.2.2, while Section C.2.3 presents the modifications that have been made in each of them.

C.2.1 Three-zone model of Thome et al. (2004)

The three-zone model describes the evaporation of elongated bubbles in microchannels as a sequential and cyclical passage of a liquid slug (without any entrained vapor bubbles), an evaporating elongated bubble (the film surrounding the bubble is formed from liquid removed from the liquid slug), and a vapor slug if the liquid film dries out. Figure C.2 presents such a triplet, which repeats over time.

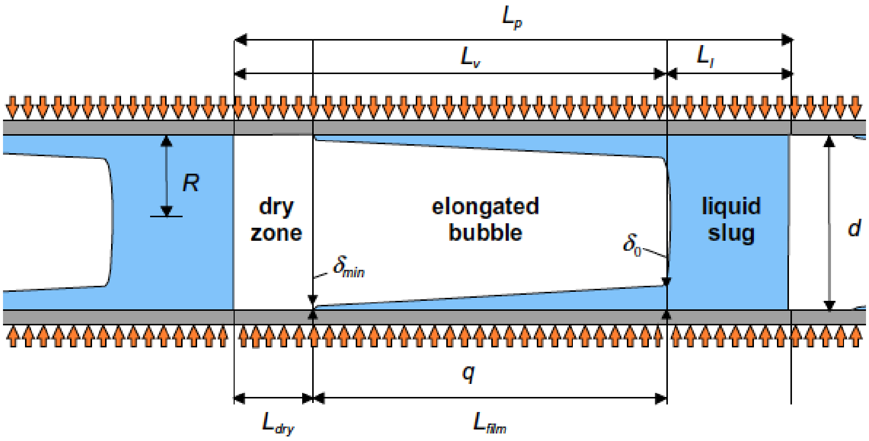

Figure C.2: A triplet of liquid slug, an elongated bubble and a vapor slug. Figure extracted from Thome et al. (2004)

Then, the local time-averaged heat transfer coefficient at a fixed location z along a microchannel during flow and evaporation of an elongated bubble at a constant, uniform heat flux boundary condition is:

$$\alpha(z) = \frac{t_l}{\tau}\alpha_l(z) + \frac{t_{film}}{\tau}\alpha_{film}(z) + \frac{t_v}{\tau}\alpha_v(z) \tag{C.13}$$

where τ is a period of pair generation:

$$f = \frac{1}{\tau} = \left[\frac{\rho_l c_{p,l}\Delta T_{sat}}{\rho_v \Delta h_{lv} R}\right]^2 \frac{12 D_{t,l}}{\pi} \tag{C.14}$$

where D_t is the thermal diffusivity in $\mathrm{m^2\,s^{-1}}$.

The following assumptions have been made to develop the three-zone model:

1. The flow is homogeneous, which states that the liquid and vapor velocities are equal.
2. A time-constant heat flux is uniformly distributed over the inner wall of the microchannel.
3. The temperatures of the liquid and vapor remain at T_{sat}, which means that all the energy delivered to the fluid is used for vaporization.
4. The local saturation temperature is determined based on the vapor pressure curve.
5. At $x = 0$ until it grows to the size of the channel diameter, the liquid slug initially contains all liquid that flows past the nucleating bubble.
6. No vapor shear stress on the liquid film, which remains attached to the channel wall.
7. The film thickness, δ_0, is much smaller than the tube radius of R.
8. The channel wall has no thermal inertia.

The model is initialized with the total mass flow rate given as:

$$M_{total} = M_{l,0} + \frac{4}{3}\pi R^3 \frac{\rho_v}{\tau} \tag{C.15}$$

thus

$$G_{total} = G + \frac{4}{3}\pi R \frac{\rho_v}{\tau} \approx G \tag{C.16}$$

The assumption that G_{total} is equal G is fairly good except for CO_2.

Furthermore, the initial lengths are for:

- a liquid slug

$$L_{l,0} = \frac{G}{\rho_l}\tau \tag{C.17}$$

- vapor

$$L_{v,0} = \frac{4}{3}R \tag{C.18}$$

- a pair

$$L_{p,0} = L_{l,0} + L_{v,0} = \frac{G}{\rho_l}\tau + \frac{4}{3}R \tag{C.19}$$

Whereas, the length of the tube $L_{x=1}$, at which the fluid is totally evaporated is calculated based on the energy balance on the internal surface of the tube with a constant and uniform heat flux boundary condition:

$$M_{total}\left[1 - x_0\right]\Delta h_{lv} = \pi R^2 G_{total}\left[1 - x_0\right]\Delta h_{lv} = 2\pi q R L_{x=1} \tag{C.20}$$

where x_0 is a mean initial vapor quality calculated from the mass flow rate of liquid and vapor during the time period of τ:

$$x_0 = \frac{M_{v,0}}{M_{l,0} + M_{v,0}} = \frac{1}{1 + \frac{3G\tau}{4\rho_v R}} \tag{C.21}$$

Then, substituting Eq. (C.21) into Eq. (C.20):

$$L_{x=1} = \frac{R\Delta h_{lv}}{2q}G \tag{C.22}$$

Based on 2$^{\text{nd}}$ assumption of the three-zone model, the vapor quality profile along the tube is linear:

$$x\left(z\right) = \left(\frac{1 - x_0}{L_{x=1}}\right)z + x_0 \tag{C.23}$$

where z is the axial distance from the point of bubble nucleation at x_0.

Assuming that the flow is homogeneous, the liquid and vapor velocities are, respectively:

$$U_l = \frac{G_{total}}{\rho_l}\left(\frac{1 - x}{1 - \varepsilon_{tp}}\right) \tag{C.24}$$

$$U_v = \frac{G_{total}}{\rho_v}\left(\frac{x}{\varepsilon_{tp}}\right) \tag{C.25}$$

where ε_{tp} is the homogeneous cross-sectional void fraction expressed as a function of vapor quality:

$$\varepsilon_{tp} = \frac{1}{1 + \left(\frac{1-x}{x}\right)\frac{\rho_v}{\rho_l}} \tag{C.26}$$

since the volumetric void fraction for this special case is identical to the cross-sectional void fraction.

Finally, the velocity of the pair is:

$$U_p = G_{total}\left[\frac{x}{\rho_v} + \frac{1-x}{\rho_l}\right] \tag{C.27}$$

It is worthwhile noting that normally the p_l is much greater that p_v, therefore:

$$U_p \approx G_{total}\left(\frac{x}{\rho_v}\right) \tag{C.28}$$

and the pair/triplet velocity varies nearly linearly along the tube.

Following Eq. (C.27), the mean equivalent length of the pair at each location during τ is:

$$L_p = \tau U_p = \tau G_{total}\left[\frac{x}{\rho_v} + \frac{1-x}{\rho_l}\right] \tag{C.29}$$

and

$$L_l = (1-\varepsilon)\, L_p = \tau\frac{G_{total}}{\rho_l}\,(1-x) \tag{C.30}$$

$$L_v = \varepsilon L_p = \tau\frac{G_{total}}{\rho_l}x \tag{C.31}$$

Then, the time periods that correspond to the presence of a liquid and vapor slugs passing through the cross-section at location z are, respectively:

$$t_l = \frac{L_l}{U_p} = \frac{\tau}{1 + \frac{\rho_l}{\rho_v}\frac{x}{1-x}} \tag{C.32}$$

$$t_v = \frac{L_v}{U_p} = \frac{\tau}{1 + \frac{\rho_v}{\rho_l}\frac{1-x}{x}} \tag{C.33}$$

The model involves the prediction of the initial film thickness, which is difficult to measure experimentally. Starting from the Moriyama and Inoue (1996) correlation, it is described in terms of the Bond number as follows:

$$\begin{cases} \frac{\delta_0/D_{tube}}{\delta^{*0.84}} = 0.1 \quad \text{for} \quad \text{Bond} > 2 \\ \frac{\delta_0/D_{tube}}{\delta^{*0.84}} = 0.07\text{Bond}^{0.41} \quad \text{for} \quad \text{Bond} \leq 2 \end{cases} \tag{C.34}$$

where: D_{tube} is the tube diameter and Bond is the Bond number in function of the acceleration of the front of the bubble:

$$\text{Bond} = \frac{\rho_l D_{tube}^2}{\sigma} \frac{\mathrm{d}}{\mathrm{dt}} \left(U_{interface}\right) \simeq \frac{\rho_l D_{tube}^2}{\sigma} \frac{U_{interface}}{t_G} \tag{C.35}$$

In Eq. (C.34), δ^* is the dimensionless boundary layer thickness in front of the bubble:

$$\delta^* = \frac{\sqrt{\nu_l t_G}}{D_{tube}} \tag{C.36}$$

where t_G is the time need for the bubble to reach a particular radius, here $t_G = D_{tube} \,/\, U_p$.

In order to ensure the continuity in estimating the initial liquid film over the whole range of conditions, the method of Churchill and Usagi (1972) is employed:

$$\frac{\delta_0}{D_{tube}} = \delta^{*0.84} \left[\left(0.07\text{Bond}^{0.41}\right)^{-8} + 0.1^{-8}\right]^{-\frac{1}{8}} \tag{C.37}$$

Further improvement of the liquid film thickness measurement was provided by Addlesee and Kew (2002) leading to the following formula:

$$\frac{\delta_0}{D_{tube}} = C_{\delta 0} \left(3\sqrt{\frac{\nu_l}{U_p D_{tube}}}\right)^{0.84} \left[\left(0.07\text{Bond}^{0.41}\right)^{-8} + 0.1^{-8}\right]^{-\frac{1}{8}} \tag{C.38}$$

where

$$\text{Bond} = \frac{\rho_l D_{tube}}{\sigma} U_p^2 \tag{C.39}$$

The initial thickness of the liquid film will change due to vaporization by the heat flux, q, at the inner wall of the tube. Therefore, based on the 3rd assumption of the three-zone model:

$$q \left(2\pi R \Delta z\right) = -\rho_l 2\pi \left(R - \delta\right) \frac{\mathrm{d}\delta}{\mathrm{d}t} \Delta z \Delta h_{lv} \tag{C.40}$$

which leads to:

$$\mathrm{d}\delta = -\frac{q}{\rho_l \Delta h_{lv}} \frac{R}{R - \delta} \mathrm{d}t \tag{C.41}$$

Integrating Eq. (C.41) with the initial condition $\delta(z,0) = \delta_0(z)$ and assuming $R - \delta \approx R$ gives:

$$\delta\left(z,t\right)=\delta_0\left(z\right)-\frac{q}{\rho_l\Delta h_{lv}}t \tag{C.42}$$

Prior to the heat transfer coefficient calculations, the time periods of film, t_{film}, and the dry-out zone, t_{dry}, as well as the final thickness of δ_{end} need to be estimated, so that if:

- $t_{dry,film} > t_v$

$$\delta_{end}\left(z\right)=\delta\left(z,t_v\right) \tag{C.43}$$

$$t_{film}=t_v \tag{C.44}$$

$$t_{dry}=t_v-t_{film} \tag{C.45}$$

$$L_{dry}=U_p t_{dry} \tag{C.46}$$

- $t_{dry,film} < t_v$

$$\delta_{end}\left(z\right)=\delta_{min} \tag{C.47}$$

$$t_{film}=t_{dry,film} \tag{C.48}$$

$$t_{dry}=t_v-t_{film} \tag{C.49}$$

$$L_{dry}=U_p t_{dry} \tag{C.50}$$

where the maximum duration of the existence of the film, $t_{dry,film}$, at position z is:

$$t_{dry,film}\left(z\right)=\frac{\rho_l\Delta h_{lv}}{q}\left[\delta_0\left(z\right)-\delta_{\min}\right] \tag{C.51}$$

Now, in Eq. (C.13), the heat transfer coefficients are:

- for liquid film

$$\alpha_{film}\left(z\right)\frac{1}{t_{film}}\int_0^{t_{film}}\frac{k_l}{\delta\left(z,t\right)}\mathrm{d}t=\frac{k_l}{\delta_0-\delta_{end}}\ln\left(\frac{\delta_0}{\delta_{end}}\right) \tag{C.52}$$

- for liquid and vapor slugs

$$\alpha=\left(\alpha_{lam}^4+\alpha_{turb}^4\right)^{\frac{1}{4}}=\frac{k}{D_{tube}}\left(Nu_{lam}^4+Nu_{turb}^4\right)^{\frac{1}{4}} \tag{C.53}$$

where the average laminar and turbulent Nusselt numbers at z are

$$Nu_{lam,z}=2\times 0.455\sqrt[3]{\mathrm{Pr}}\sqrt{\frac{D_{tube}\mathrm{Re}}{L\left(z\right)}} \tag{C.54}$$

$$Nu_{turb,z} = \frac{\frac{\xi}{8}\left[\mathrm{Re} - 1000\right]\mathrm{Pr}}{1 + 12.7\sqrt{\frac{\xi}{8}}\left(\mathrm{Pr}^{\frac{2}{3}} - 1\right)}\left[1 + \left(\frac{D_{tube}}{L\left(z\right)}\right)^{\frac{2}{3}}\right] \tag{C.55}$$

and

$$\xi = \left(1.82\log_{10}\mathrm{Re} - 1.64\right)^{-2} \tag{C.56}$$

The model requires few constant to be determined based on the experimental results. There are as follows:

1. $\delta_{min} = 0.3$, which is the minimum liquid film thickness related to the unknown roughness of the surface and the thermo-physical properties of the fluid,
2. $C_{\delta 0} = 0.29$, which is the correction factor on the prediction of δ_0 taking into account the difference between the fluids and the geometries under investigation,
3. f being the pair frequency; its optimum values is estimated as:

$$f_{opt} = \left(\frac{q}{q_{ref}}\right)^{1.74} \tag{C.57}$$

and

$$q_{ref} = 3328\left(\frac{p_{sat}}{p_{crit}}\right)^{-0.5} \tag{C.58}$$

The values of δ_{min} and $C_{\delta 0}$, as well as the constants in Eqs. (C.57) and (C.58) provided above are applicable in the general three-zone model (Dupont et al., 2004).

C.2.2 Unified heat and flow model for annular flows of Cioncolini and Thome (2011) including entrainment prediction method of Cioncolini et al. (2009)

In annular flow, which is shown schematically in Fig. C.3, the unified heat transfer model of Cioncolini and Thome (2011) is considered that assumes the annular liquid film to incompressible and the liquid to be Newtonian with constant physical properties for a fluid in steady state condition.

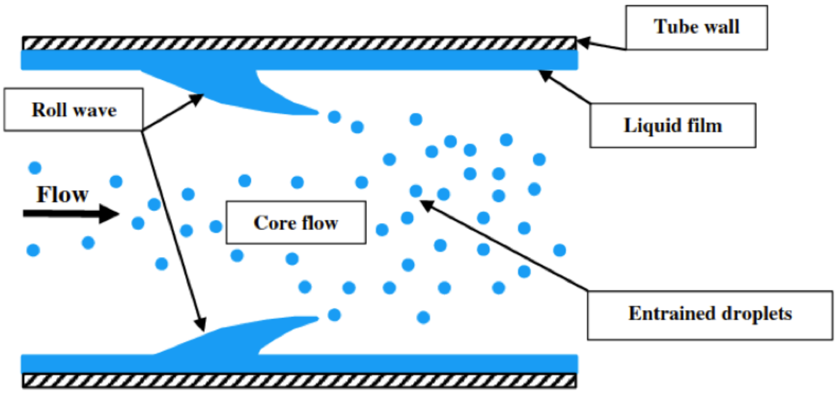

Figure C.3: Schematic representation of annular two-phase flow. Figure extracted from Cioncolini and Thome (2011)

As stated, the heat transfer coefficient, α, is determined using following equation:

$$Nu = \frac{\alpha\delta_{film}}{k_l} = 77.6 \times 10^{-3}\delta_{film}^{+0.90}\mathrm{Pr}_l^{0.52} \tag{C.59}$$

where: δ^+_{film} is dimensionless average liquid film thickness:

$$\delta^+_{film} = \max\left(\sqrt{\frac{2\Gamma^+_{lf}}{R^+}}; 0.066\frac{\Gamma^+_{lf}}{R^+}\right) = \frac{\delta_{film}}{y^*} \tag{C.60}$$

where: R^+ is the dimensionless tube radius and the Γ^+_{lf} is the dimensionless liquid mass flow rate calculated using:

$$\frac{\Gamma^+_{lf}}{R^+} = \frac{(1-e_{LF})\,(1-x)\,\Gamma}{2\pi\mu_l R} = (1-e_{LF})\,(1-x)\,\frac{GD_{tube}}{4\mu_l} \tag{C.61}$$

and

$$y^* = \frac{\mu_l}{\rho_l\sqrt{\frac{\tau_w}{\rho_l}}} \tag{C.62}$$

$$\tau_w = \frac{1}{2}f_{tp}\rho_c U_c \tag{C.63}$$

where c denotes vapor core.

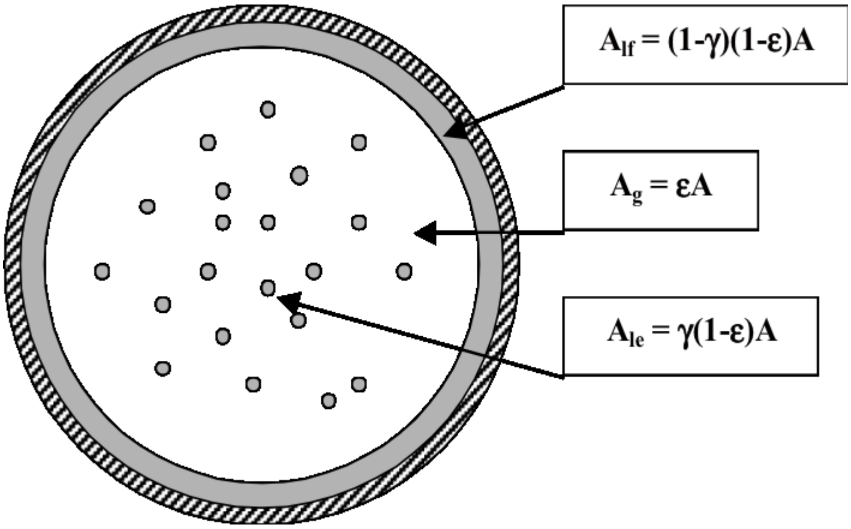
$A_{lf} = (1-\gamma)(1-\varepsilon)A$
$A_g = \varepsilon A$
$A_{le} = \gamma(1-\varepsilon)A$

Figure C.4: Schematic representation of the cross-sectional area A split among the phases. Figure extracted from Cioncolini et al. (2009).

The entrained liquid fraction, e_{LF}, shown schematically in Fig. C.4, as well as the two-phase flow friction factor, f_{tp}, are obtained applying the prediction method of Cioncolini et al. (2009). More details about this model can be found in Chapter 2. The e_{LF} might be also estimated using the more recent prediction method of Cioncolini and Thome (2012). Both of these models show the strong dependence of the vapor core Weber number, We_c on the annular flow. It needs to be clarified that Eq. (C.59) is used when:

$$\begin{cases} 10 \leq \delta^{+}_{film} \leq 800 \\ 0.86 \leq \mathrm{Pr} \leq 6.1 \end{cases} \tag{C.64}$$

C.2.3 Modification to the original heat transfer prediction methods

It has been shown in Costa-Patry et al. (2012) that several modifications to the original heat transfer models of Thome et al. (2004) for elongated bubble flow regime and Cioncolini and Thome (2011) for annular flow are required in order to improve their performance in predicting heat transfer coefficient.

Three-zone model of Thome et al. (2004)

Firstly, the model was modified by setting the minimum film thickness to the measured wall roughness since the roughness breaks the liquid film, as shown in Fig. C.5. It is worthwhile to mention that this has been already proposed in the previous studies of Agostini et al. (2008c) in silicon test section, Ong and Thome (2011b) in stainless steel microtubes, Vakili-Farahani et al. (2012) in aluminium multiport tubes, while the study of Costa-Patry et al. (2012) included silicon and copper test sections.

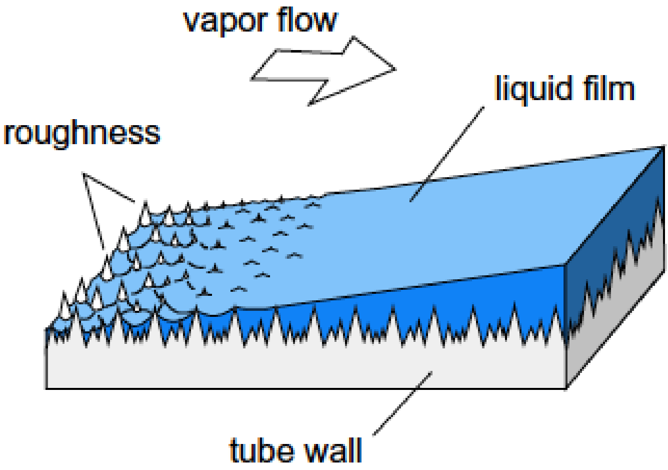

Figure C.5: Schematic of the transition from film evaporation to vapor convection in the dry zone. Figure extracted from Thome et al. (2004)

Secondly, the developing flow Nusselt number correlations were replaced by fully-developed ones for laminar and turbulent flow, respectively:

$$Nu_{lam} = 4.36 \tag{C.65}$$

$$Nu_{turb} = \frac{\mathrm{Pr}\,\frac{\xi}{8}\,(\mathrm{Re}-1000)}{1+12.7\left(\frac{\xi}{8}\right)^{0.5}\left(\mathrm{Pr}^{\frac{2}{3}}-1\right)} \tag{C.66}$$

where ξ is a frictional pressure drop coefficient.

Finally, the liquid film heat transfer from Eq. (C.52) is now given by:

$$\alpha_{film} = \frac{k_l}{\delta_0-\delta_{end}+1\times10^{-9}}\ln\left(\frac{\delta_0}{\delta_{end}}\right) \tag{C.67}$$

Annular flow model of Cioncolini and Thome (2011)

The annular flow model of Cioncolini and Thome (2011) was developed for circular channels. Therefore, in order to conserve the liquid cross-sectional area proportions in rectangular channels, the equivalent diameter is used:

$$D_e = \sqrt{\frac{4W_{ch}H_{ch}}{\pi}} \tag{C.68}$$

Moreover, the true value of the perimeter of $P = 2H_{ch} + W_{ch}$ is applied, whereas the cross-sectional area taken for a circular channel is as follows:

$$A = \frac{\pi}{4}\left(D_e^2 - (D_e - 2\delta)^2\right) \tag{C.69}$$

In the end, the equivalent liquid film thickness for the rectangular channel is calculated as:

$$\delta_{film,e} = \frac{A}{P} \tag{C.70}$$

with A and P specified as above.

C.3 Validation of Matlab implementations

The Matlab implementations were validated versus the results available in the literature with a good match. Figure C.6 shows an example of such a validation for the three-zone model of Thome et al. (2004) considering the global parameter.

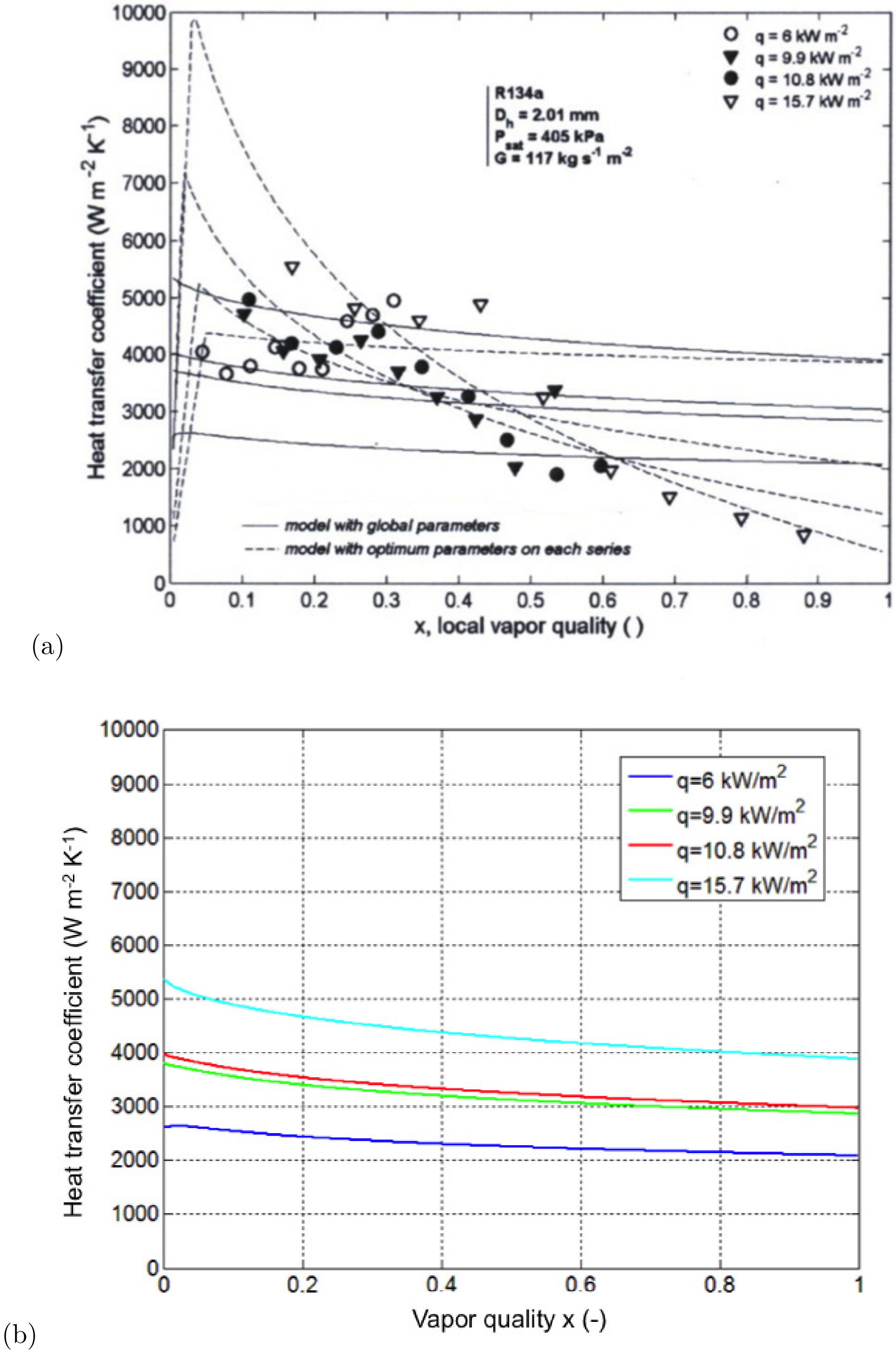

Figure C.6: Validation of the Matlab implementation of the three-zone model of Thome et al. (2004) using the global parameters: (a) the results available in the literature, and (b) the simulated heat transfer coefficients.

Bibliography

A. J. Addlesee and P. A. Kew. Development of the liquid film thickness above a sliding bubble. *Transactions of Institute of Chemical Engineering*, 80:272–277, 2002.

B. Agostini and A. Bontemps. Vertical flow boiling of refrigerant R134a in small channels. *International Journal of Heat and Fluid Flow*, 26:296–306, 2005.

B. Agostini, A. Bontemps, B. Watel, and B. Thonon. Boiling heat transfer in minichannels: Influence of the hydraulic diameter. In *International Congress of Refrigeration*, 2003.

B. Agostini, A. Bontemps, and B. Thonon. Effects of geometrical and thermophysical parameters on heat transfer measurements in small-diameter channels. *Heat Transfer Engineering*, 27(1):14–24, 2006.

B. Agostini, M. Fabbri, J. E. Park, L. Wojtan, J. R. Thome, and B. Michel. State of the art of high heat flux cooling technogies. *Heat Transfer Engineering*, 28(4):258–281, 2007.

B. Agostini, R. Revellin, J. R. Thome, M. Fabbri, B. Michel, D. Calmi, and U. Kloter. High heat flux flow boiling in silicon multi-microchannels – Part III: Saturated critical heat flux of R236fa and two-phase pressure drops. *International Journal of Heat and Mass Transfer*, 51:5426–5442, 2008a.

B. Agostini, J. R. Thome, M. Fabbri, and B. Michel. High heat flux two-phase cooling in silicon multimicrochannels. *IEEE Transactions on Components and Packaging Technologies*, 31:691–701, 2008b.

B. Agostini, J. R. Thome, M. Fabbri, B. Michel, D. Calmi, and U. Kloter. High heat flux flow boiling in silicon multi-microchannels – Part I: Heat transfer characteristics of refrigerant R236fa. *International Journal of Heat and Mass Transfer*, 51:5400–5414, 2008c.

B. Agostini, J. R. Thome, M. Fabbri, B. Michel, D. Calmi, and U. Kloter. High heat flux flow boiling in silicon multi-microchannels – Part II: Heat transfer characteristics of refrigerant R245fa. *International Journal of Heat and Mass Transfer*, 51:5415–5425, 2008d.

A. A. Arcanjo, C. B. Tibirica, and G. Ribatski. Evaluation of flow patterns and elongate bubble characteristics during the flow boiling of halocarbon refrigerants in a micro-scale channel. *Experimental Thermal and Fluid Science*, 34:766–775, 2010.

J. Barber, K. Sefiane, D. Brutin, and L. Tadrist. Hydrodynamics and heat transfer during flow boiling instabilities in a single microchannel. *Applied Thermal Engineeging*, 29:1299–1308, 2009.

J. Barber, D. Brutin, K. Sefiane, J. L. Gardarein, and L. Tadrist. Unsteady-state fluctuation analysis during bubble growth in a rectangular microchannel. *International Journal of Heat and Mass Transfer*, 54:4784–4795, 2011.

S. S. Bertsch, E. A. Groll, and S. V. Garimella. Review and comparative analysis of studies on saturated flow boiling in small channels. *Nanoscale and Microscale Thermophysical Engineering*, 12 (3):187–227, 2008.

S. S. Bertsch, E. A. Groll, and S. V. Garimella. A composite heat transfer correlation for saturated flow boiling in small channels. *International Journal of Heat and Mass Transfer*, 52:2110–2118, 2009.

R. R. Bhide, S. G. Singh, A. Sridharan, S. P. Duttagupta, and A. Agrawal. Pressure drop and heat transfer characteristics of boiling water in sub-hundred micron channel. *Experimental Thermal and Fluid Science*, 33:963–975, 2009.

S. Bilir. Laminar flow heat transfer in pipes including two-dimensional wall and fluid axial conduction. *International Journal of Heat and Mass Transfer*, 38(9):1619–1625, 1995.

D. Bogojevic, K. Sefiane, A. J. Walton, H. Lin, and G. Cummins. Two-phase flow instabilities in a silicon microchannels heat sink. *International Journal of Heat and Fluid Flow*, 30:854–867, 2009.

D. Bogojevic, K. Sefiane, A. J. Walton, H. Lin, G. Cummins, D. B. R. Kenning, and T. G. Karayiannis. Experimental investigation of non-uniform heating effect on flow boiling instabilities in a microchannel-based heat sink. *International Journal of Thermal Sciences*, 50:309–324, 2011.

N. Borhani, B. Agostini, and J. R. Thome. A novel time strip flow visualisation technique for investigation of intermittent dewetting and dryout in eleongated bubble flow in a microchannel evaporator. *International Journal of Heat and Mass Transfer*, 53:4809–4818, 2010.

H. Boye, Y. Staate, and J. Schmidt. Experimental investigation and modelling of heat transfer during convective boiling in a minichannel. *International Journal of Heat and Mass Transfer*, 50(1-2): 208–215, 2007.

G. M. Carlomagno and G. Cardone. Infrared thermography for convective heat transfer measurements. *Experiments in Fluids*, 49(6):1187–1218, 2010.

G. P. Celata, M Cumo, V. Marconi, S. J. McPhail, and G. Zummo. Microtube liquid single-phase heat transfer in laminar flow. *International Journal of Heat and Mass Transfer*, 49:3538–3546, 2006.

G. P. Celata, S. K. Saha, G. Zummo, and D. Dossevi. Heat transfer characteristics of flow boiling in a single horizontal microchannel. *International Journal of Thermal Sciences*, 49:1086–1094, 2010.

F. Chauvet, S. Cazin, P. Duru, and M. Prat. Use of infrared thermography for the study of evaporation in a square capillary tube. *International Journal of Heat and Mass Transfer*, 53(9-10): 1808–1818, 2010.

J. C. Chen. Correlation for boiling heat transfer to saturated fluids in convective flow. *Industrial and Engineering Chemistry Process Design and Development*, 5(3):322–329, 1966.

T. Chen and S. V. Garimella. Measurement and high-speed visualization of flow boiling of a dielectric fluid in a silicon microchannel heat sink. *International Journal of Heat and Mass Transfer*, 32:957–971, 2006.

L. Cheng, G. Ribatski, and J. R. Thome. Two-phase flow patterns and flow-pattern maps: Fundamentals and applications. *Applied Mechanics Reviews*, 61:1–28, 2008.

D. Chisholm. A theoretical basis for the Lockhart-Martinelli correlation for two-phase flow. *International Journal of Heat and Mass Transfer*, 10:1767–1778, 1967.

D. Chisholm and A. D. K. Laird. Two-phase flow in rough tubes. *Journal of Heat Transfer (Transactions of the ASME)*, 80:276–286, 1958.

P. M.-Y. Chung and M. Kawaji. The effect of channel diameter on a adiabatic two-phase flow characteristics in microchannels. *International Journal of Multiphase Flow*, 30:735–761, 2004.

S. W. Churchill and R. Usagi. A general expression for the correlation of rates of transfer and the other phenomena. *American Institute of Engineering of Chemical Engineering Journal*, 18:1121–1128, 1972.

A. Cicchitti, C. Lombardi, M. Silvestri, G. Soldaini, and R. Zavattarelli. Two-phase cooling experiments – pressure drop, heat transfer and burnout measurements. *Energia Nucleare*, 7: 407–425, 1960.

A. Cioncolini and J. R. Thome. Algebraic turbulence modeling in adiabatic and evaporating annular two-phase fow. *International Journal of Heat and Fluid Flow*, 32:805–817, 2011.

A. Cioncolini, J. R. Thome, and C. Lombardi. Unified macro-to-microscale method to predict two-phase frictional pressure drops of annular flows. *International Journal of Multiphase Flow*, 35: 1138–1148, 2009.

Andrea Cioncolini and John Richard Thome. Entrained liquid fraction prediction in adiabatic and evaporating annular two-phase flow. *Nuclear Engineering and Design*, 243:200–213, 2012.

K. D. Cole and B. Cetin. The effect of axial conduction on heat transfer in a liquid microchannel flow. *International Journal of Heat and Mass Transfer*, 54(11-12):2542–2549, 2011.

J. G. Collier and J. R. Thome. *Convective boiling and condensation.* Oxford Univesity Press, 1994.

L. Consolini and J. R. Thome. A heat transfer model for evaporation of coalescing bubbles in micro-channel flow. *International Journal of Heat and Fluid Flow*, 31:115–125, 2010.

M. G. Cooper. Heat flow rates in saturated nucleate pool boiling - a wide-ranging experimentation using reduced properties. *Advances in Heat Transfer*, 16:157–239, 1984.

A. K. Coskun, T. Rosing, K. Whisnant, and K. Gross. Static and dynamic temperature-aware scheduling for multiprocessor SoCs. *IEEE Transactions on Very Large Scale Integration (VLSI) Systems*, 16(9):1127–1140, 2008a.

A. K. Coskun, T. Rosing, K. Whisnant, and K. Gross. Temperature-aware MPSoCs scheduling for reducing hot spots and gradients. In *Proceedings of the 2008 Asia and South Pacific Design Automation Conference (ASP-DAC '08)*, 2008b.

A. K. Coskun, J. L. Ayala, D. Atienza, and T. Rosing. Modeling and dynamic management of 3D multicore systems with liquid cooling. In *Proceedings of the 17th Annual IFIP/IEEE International Conference on Very Large Scale Integration (VLSI-SoC)*, 2009.

E. Costa-Patry. *Cooling high heat flux micro-electronic systems using refrigerants in high aspect ratio multi-microchannel evaporators.* PhD thesis, Ecole Polytechnique Federale de Lausanne, 2011.

E. Costa-Patry and J. R. Thome. Two-phase flow boiling in microchannels for cooling of micro-electronics. In *8th International Conference on Heat Transfer, Fluid Mechanics and Thermodynamics*, 2011.

E. Costa-Patry and J. R. Thome. Flow pattern based flow boiling heat transfer model for microchannels. In *ECI 8th International Conference on Boiling and Condensation Heat Transfer*, 2012.

E. Costa-Patry, J. Olivier, S. Paredes, and J. R. Thome. Hot-spot self-cooling effects on two-phase flow of R245fa in 85 μm-wide multi-microchannels. In *16th International Workshop on Thermal Investigation of ICs and Systems (THERMINIC)*, 2010.

E. Costa-Patry, J. Olivier, B. Michel, and J. R. Thome. Two-phase flow of refrigerant in 85 μm-wide multi-microchannels: Part II – Heat transfer with 35 local heaters. *International Journal of Heat and Fluid Flow*, 32:464–476, 2011a.

E. Costa-Patry, J. Olivier, B. A. Nichita, B. Michel, and J. R. Thome. Two-phase flow of refrigerant in 85 μm-wide multi-microchannels: Part I – Pressure drop. *International Journal of Heat and Fluid Flow*, 32:451–463, 2011b.

E. Costa-Patry, S. Nebuloni, J. Olivier, and J. R. Thome. On-chip two-phase cooling with refrigerant 85 μm-wide multi-microchannel evaporator under hot-spot conditions. *IEEE Transactions on Components, Packaging and Manufacturing Technology*, 2(2):311–320, 2012.

E. J. Davis and T. J. Cooper. Thermal entrance effects in stratified gas-liquid flow: experimental investigation. *Chemical Engineering Science*, 24:509–520, 1969.

M. Cortina Diaz and J. Schmidt. Flow boiling of n-hexane in small channels heat transfer measurements and flow pattern observations. *Chemical Engineering Technology*, 3:389–394, 2007a.

M. Cortina Diaz and J. Schmidt. Experimental investigation of transient boiling heat transfer in microchannels. *International Journal of Heat and Fluid Flow*, 28(1):95–102, 2007b.

M. Cortina Diaz, H. Boye, I. Hapke, J. Schmidt, Y. Staate, and Z. Zhekov. Investigation of flow boiling in narrow channels by thermographic measurements of local wall temperatures. *Microfluidics and Nanofluidics*, 2(1):1–11, 2006.

V. Dupont and J. R. Thome. Evaporation in microchannels: influence of the channel diameter on heat transfer. *Microfluidics and Nanofluidics*, 1:119–127, 2005.

V. Dupont, J. R. Thome, and A. M. Jacobi. Heat transfer model for evaporation in microchannels. Part II: comparison with the database. *International Journal of Heat and Mass Transfer*, 47:3387–3401, 2004.

D. J. Farina. Making surface temperature measurements using liquid crystal thermograhy. *Electronics Cooling*, 1(2):10–15, 1995.

A. G. Fedorov and R. Viskanta. Three-dimensional conjugate heat transfer in the microchannel heat sink for electronic packaging. *International Journal of Heat and Mass Transfer*, 43:399–415, 2000.

X. Fu, S. L. Qi, P. Zhang, and R. Z. Wang. Visualization of flow boiling of liquid nitrogen in a vertical mini-tube. *International Journal of Multiphase Flow*, 34:333–351, 2008.

E. Galvis and R. Culham. Measurements and flow pattern visualizations of two-phase flow boiling in single channel evaporators. *International Journal of Multiphase Flow*, 42:52–61, 2012.

G. Gamrat, M. Favre-Marinet, and D. Asendrych. Conduction and entrance effects on laminar liquid flow and heat transfer in rectabgulat microchannels. *International Journal of Heat and Mass Transfer*, 48:2943–2954, 2005.

I. Hapke, H. Boye, and J. Schmidt. Onset of nucleate boiling in minichannels. *International Journal of Thermal Sciences*, 39(4):505–513, 2000.

I. Hapke, H. Boye, and J. Schmidt. Flow boiling of water and n-heptane in micro channels. *Microscale Thermophysical Engineering*, 6(2):99–115, 2002.

S. Hardt, B. Schilder, D. Tiemann, G. Kolb, V. Hessel, and P. Stephan. Analysis of flow patterns emerging during evaporation in parallel microchannels. *International Journal of Heat and Mass Transfer*, 50(1-2):226–239, 2007.

T. Harirchian and S. V. Garimella. Microchannel size effects on local flow boiling heat transfer to a dielectric fluid. *International Journal of Heat and Mass Transfer*, 51:3724–3735, 2008.

T. Harirchian and S. V. Garimella. Effects of channel dimension, heat flux, and mass flux on flow boiling regimes in microchannels. *International Journal of Multiphase Flow*, 35:349–362, 2009a.

T. Harirchian and S. V. Garimella. The critical role of channel cross-sectional area in microchannel. *International Journal of Multiphase Flow*, 35:904–913, 2009b.

T. Harirchian and S. V. Garimella. A comprehensive flow regime map for microchannel flow boiling with quantitative transition criteria. *International Journal of Heat and Mass Transfer*, 53: 2694–2702, 2010.

T. Harirchian and S. V. Garimella. Flow regime-based modeling of heat transfer and pressure drop in microchannel flow boiling. *International Journal of Heat and Mass Transfer*, 55:1246–1260, 2012.

H. Hausen. Darstellung des warmeuberganges in rohren durch verallgemeinerte potenzbeziehungen. *Z. VDI Beiheft Verfahrenstechnik*, 4:91–102, 1943.

G. Hetsroni, A. Mosyak, and Z. Segal. Nonuniform temperature distribution in electronic devices cooled by flow in parallel microchannels. *IEEE Transactions on Components and Packaging Technologies*, 24:16–23, 2001.

G. Hetsroni, A. Mosyak, Z. Segal, and G. Ziskind. A uniform temperature heat sink for cooling of electronic devices. *International Journal of Heat and Mass Transfer*, 45:3275–3286, 2002.

G. Hetsroni, A. Mosyak, Z. Segal, and E. Pogrebnyak. Two-phase flow patterns in parallel micro-channels. *International Journal of Multiphase Flow*, 29(3):341–360, 2003.

G. Hetsroni, A. Mosyak, E. Pogrebnyak, and Z. Segal. Explosive boiling of water in parallel micro-channels. *International Journal of Multiphase Flow*, 31(4):371–392, 2005.

G. Hetsroni, A. Mosyak, E. Pogrebnyak, and Z. Segal. Periodic boiling in parallel microchannels at low vapor quality. *International Journal of Multiphase Flow*, 32:1141–1159, 2006.

G. Hetsroni, A. Mosyak, E. Pogrebnyak, and Z. Segal. Heat transfer of gas-liquid mixture in micro-channel heat sink. *International Journal of Heat and Mass Transfer*, 52:3963–3971, 2009.

G. Hetsroni, A. Mosyak, E. Pogrebnyak, and R. Rozenblit. Infrared temperature measurements in micro-channels and micro-fluid systems. *International Journal of Thermal Sciences*, 50:853–868, 2011.

X. Huo, L. Chen, Y. S. Tian, and T. G. Karayiannis. Flow boiling and flow regimes in small diameter tubes. *Applied Thermal Engineering*, 24:1225–1239, 2004.

I. E. Idelcik. *Memento des pertes de charge.* Eyrolles, Paris, 1999.

F. P. Incropera, D. P. Dewitt, T. L. Bergman, and A. S. Lavine. *Fundamentals of Heat and Mass Transfer.* John Wiley & Sons, 6*th* edition, 2007.

A. M. Jacobi and J. R. Thome. Heat transfer model for evaporation of eleongated bubble flows in microchannels. *Journal of Heat Transfer*, 124:1131–1136, 2002.

I. Jiang, M. Wong, and Y. Zohar. Forced convection boiling in a microchannel heat sink. *Journal of Microelectromechanical Systems*, 10(1):80–87, 2001.

L. Jiang, J. M. Koo, L. Zhang, E. Wang, S. Im, S. Yao, S. Zeng, A. Bari, J. G. Santiago, T. W. Kenny, and K. E. Goodson. Progress on two-phase convection in microchannel heat sinks. In *Proceedings of 4th Pacific Rim Thermal Science and Energy Engineering Workshop (PaRTSEE-4)*, 2002.

N. Kakuta, K. Kondo, A. Ozaki, H. Arimoto, and Y. Yamada. Temperature imaging of submillimeter-thick water using a near-infrared camera. *International Journal of Heat and Mass Transfer*, 52:4221–4228, 2009.

N. Kakuta, Y. Fukuhara, K. Kondo, H. Arimoto, and Y. Yamada. Temperature imaging of water in a microchannel using thermal sensitivity of near-infrared absorption. *Lab on a Chip*, 11: 3479–3486, 2011.

S. G. Kandlikar. Scale effectd on flow boiling heat transfer in microchannels: A fundamental perspective. *International Journal of Thermal Sciences*, 49:1073–1085, 2010.

T. G. Karayiannis, D. Shiferaw, D. B. R. Kenning, and V. V. Wadekar. Flow patterns and heat transfer for flow boiling in small to micro diameter tubes. *Heat Transfer Engineering*, 31(4): 257–275, 2010.

Y. Katto and H. Ohno. An improved version of generalized correlation of critical heat flux for the forced convective boiling in uniformly heated vertical tubes. *International Journal of Heat and Mass Transfer*, 27(9):1641–1648, 1984.

A. Kawahara, M. Sadatomi, K. Okayama, M. Kawaji, and P. M.-Y. Chung. Effects of channel diameter and liquid properties on void fraction in adiabatic two-phase flow through microchannels. *Heat Transfer Engineering*, 26(3):13–19, 2005.

T. H. Kim, E. Kommer, S. Dessiatoun, and J. Kim. Measurement of two-phase flow and heat transfer parameters using infrared thermography. *International Journal of Multiphase Flow*, 40:56–67, 2012.

S. J. Kline and F. A. McClintock. Describing uncertainties in single-sample experiments. *Mechanical Engineering*, 75:3–8, 1953.

M. J. Kohl, S. I. Abdel-Khalik, S. M. Jeter, and D. L. Sadowski. An experimental investigation of microchannel flow with internal pressure measurements. *International Journal of Heat and Mass Transfer*, 48:1518–1533, 2005.

E. Kommer, A. Scammell, V. Solotych, S. Dessiatoun, and J. Kim. Multiphase convective heat transfer in microgravity via infrared thermography. In *ECI 8th International Conference on Boiling and Condensation Heat Transfer*, 2012.

D. Krebs, V. Narayanan, J. Liburdy, and D. Pence. Spatially resolved wall temperature mesurements during flow boiling in microchannels. *Experimental Thermal and Fluid Science*, 34:434–445, 2010.

P. S. Lee and S. V. Garimella. Saturated flow boiling heat transfer and pressure drop in silicon microchannel array. *International Journal of Heat and Mass Transfer*, 51:789–806, 2008.

D. Lelea. The conjugate heat transfer of the partially heated microchannels. *Heat and Mass Transfer*, 44:33–41, 2007.

T.-Y. Lin and S. G. Kandlikar. A theoretical model for axial heat conduction effects during single-phase flow in microchannels. *Journal of Heat Transfer*, 134:1–6, 2012.

Z. Liu, Y. Zhao, and M. Takei. Experimental study on axial wall heat conduction for convective heat transfer in stainless steel tube. *Heat and Mass Transfer*, 43:587–594, 2007.

R. W. Lockhart and R. C. Martinelli. Proposed correlation of data for isothermal two-phase, two-component flow in pipes. *Chemical Engineering Progress*, 45:39–48, 1949.

Y. Madhour, J. Olivier, E. Costa-Patry, S. Paredes, B. Michel, and J. R. Thome. Flow boiling of R134a in a multi-microchannel heat sink with hotspot heaters for energy-efficient microelectronic CPU cooling applications. *IEEE Transactions on Components, Packaging and Manufacturing Technology*, 1(6):873–883, 2011.

G. Maranzana, I. Perry, and D. Maillet. Mini- and micro-channels: influence of axial conduction in the wall. *International Journal of Heat and Mass Transfer*, 47:3993–4004, 2004.

J. B. Marcinichen, J. R. Thome, and B. Michel. Cooling of microprocessors with micro-evaporation: A novel two-phase cooling cycle. *International Journal of Refrigeration*, 33:1264–1276, 2010.

J. B. Marcinichen, J. A. Olivier, and J. R. Thome. Reasons to use two-phase refrigerant cooling. *Electronics Cooling*, 17(1):22–27, March 2011.

C. Martin-Callizo, B. Palm, W. Owhaib, and R. Ali. Flow boiling visualization of R-134a in a vertical channel of small diameter. *Journal of Heat Transfer*, 132(3):1–8, 2010.

A. W. Mauro, J. R. Thome, D. Toto, and G. P. Vanoli. Saturated critical heat flux in a multi-microchannel heat sink fed by a split flow system. *Experimental Thermal and Fluid Science*, 34:81–92, 2010.

K. Mishima and T. Hibiki. Some characteristics ofair-water two-phase flow in small diameter vertical tubes. *International Journal of Multiphase Flow*, 22(4):703–712, 1996.

M. K. Moharana, P. K. Singh, and S. Khandekar. Axial heat conduction in the context of developing flows in microchannels. In *9th International Conference on Nanochannels, Microchannels, and Minichannels*, 2011.

M. K. Moharana, P. K. Singh, and S. Khandekar. Optimum Nusselt number for simulataneously developing internal flow under conjugate conditions in a square microchannel. *Journal of Heat Transfer*, 134:1–10, 2012.

G. E. Moore. Cramming more components onto integrated circuits. *Electronics*, 38:114–117, 1965.

G. L. Morini. Scaling effects for liquid flows in microchannels. *Heat Transfer Engineering*, 27(4): 64–73, 2006.

K. Moriyama and A. Inoue. Thickness of the liquid film formed by a growing bubble in a narrow gap between two horizontal plates. *Journal of Heat Transfer*, 118:132–139, 1996.

H. Muller-Steinhagen and K. Heck. A sinple friction pressure drop correlation for two-phase flow in pipes. *Chemical Engineering Progress*, 20:297–308, 1986.

Y. S. Muzychka and M. M. Yovanovich. Laminar forced convection heat transfer in the combined entry region of non-cicular ducts. *Transactions of the ASME*, 54126:54–61, 2004.

M. Ochs, T. Horbach, A. Schulz, R. Koch, and H.-J. Bauer. A novel calibration method for an infrared thermography system applied to heat transfer experiments. *Measurement Science and Technology*, 20(7):1–9, 2009.

C. L. Ong. *Macro-to-microchannel transition in two-phase flow and evaporation.* PhD thesis, Ecole Polytechnique Federale de Lausanne, 2010.

C. L. Ong and J. R. Thome. Flow boiling heat trasnfer of R134a, R236fa and R245fa in a horizontal 1.030 mm circular channel. *Experimental Thermal and Fluid Science*, 33:651–663, 2009.

C. L. Ong and J. R. Thome. Macro-to-microchannel transition in two-phase flow: Part I - Two-phase flow patterns and film thickness measurements. *Experimental Thermal and Fluid Science*, 35: 37–47, 2011a.

C. L. Ong and J. R. Thome. Macro-to-microchannel transition in two-phase flow: Part II - Flow boiling heat transfer and critical heat flux. *Experimental Thermal and Fluid Science*, 35:873–886, 2011b.

J. E. Park. *Critical heat flux in multi-microchannel copper elements with low pressure refrigerants.* PhD thesis, Ecole Polytechnique Federale de Lausanne, 2008.

J. E. Park and J. R. Thome. Critical heat flux in multi-microchannel copper elements with low pressure refrigerants. *International Journal of Heat and Mass Transfer*, 53:110–122, 2010.

J. E. Park, J. R. Thome, and B. Michel. Effect of inlet orifices on saturated CHF and flow visualisation in multi-microchannel heat sinks. In *25th IEEE Semiconductor Thermal Measurement and Management (SEMI-THERM) Symposium*, 2009.

V. A. Patil and V. Narayanan. Measurement of near wall liquid temperatures in single-phase flow through silicon microchannels. In *Proceedings of the 3rd International Conference on Microchannels ans Minichannels*, 2005.

V. A. Patil and V. Narayanan. Spatially resolved temperature measurement in microchannels. *Microfluidics and Nanofluidics*, 2:291–300, 2006.

R. B. Peterson. Numerical modeling of conduction effects in microscale counterflow heat exchangers. *Microscale Thermophysical Engineering*, 3(1):17–30, 1999.

S. Piva. Axial wall conduction preheating effects in high Peclet number laminar forced convection. *International Journal of Heat and Mass Transfer*, 39(16):3511–3517, 1996.

S. Rainieri and G. Pagliarini. Data processing technique applied to the calibration of a high performance FPA infrared camera. *Infrared Physics & Technology*, 43(6):345–351, 2002.

R. Revellin. *Experimental two-phase fluid flow in microchannels.* PhD thesis, Ecole Polytechnique Federale de Lausanne, 2005.

R. Revellin and J. R. Thome. A theoretical model for the prediction of the critical heat flux in heated microchannels. *International Journal of Heat and Mass Transfer*, 51:1216–1225, 2008.

R. Revellin, V. Dupont, T. Ursenbacher, J. R. Thome, and I. Zun. Characterization of two-phase flows in microchannels: Optical measurement technique and flow parameter results for R-134a in a 0.5 mm channel. *International Journal of Multiphase Flow*, 32(7):755–774, 2006.

A. Rogalski. Infrared detectors: an overview. *Infrared Physics & Technology*, 43(3-5):187–210, 2002.

M. M. Sabry, A. Sridhar, D. Atienza, Y. Temiz, Y. Leblebici, S. Szczukiewicz, N. Borhani, J. R. Thome, T. Brunschwiler, and B. Michel. Towards thermally-aware design of 3D MPSoCs with inter-tier cooling. In *Design, Automation and Test in Europe*, 2011.

S. Saisorn, J. Kaew-On, and S. Wongwises. Flow pattern and heat transfer characteristics of R-134a refrigerant during flow boiling in a horizontal circular mini-channel. *International Journal of Heat and Mass Transfer*, 53:4023–4038, 2010.

S. Saitoh, H. Daiguji, and E. Hihara. Effect of tube diameter on boiling heat transfer of R-134a in horizontal small-diameter tubes. *International Journal of Heat and Mass Transfer*, 48:4973–4984, 2005.

S. Saitoh, H. Daiguji, and E. Hihara. Correlation for boiling heat trnasfer of R-134a in horizontal tubes including effect of tube diameter. *International Journal of Heat and Mass Transfer*, 50:5215–5225, 2007.

B. Schneider, A. Kosar, and Y. Peles. Hydrodynamic cavitation and boiling in refrigerant (R-123) flow inside microchannels. *International Journal of Heat and Mass Transfer*, 50:2838–2854, 2007.

A. Serizawa, Z. Feng, and Z. Kawara. Two-phase flow in microchannels. *Experimental Thermal and Fluid Science*, 26:703–714, 2002.

R. K. Shah and A. L. London. *Laminar flow forced convection in ducts.* Academic Press, 1978.

H. R. Shanks, P. H. Sidles P. D. Maycock, and G. C. Danielson. Thermal conductivity of silicon from 300 to 1400 K. *Physical Review*, 130(5):1743–1748, 1963.

D. Shiferaw, X. Huo, T. G. Karayiannis, and D. B. R. Kenning. Examination of heat transfer correlations and a model for flow boiling of R134a in small diameter tubes. *International Journal of Heat and Mass Transfer*, 50:5177–5193, 2007.

D. Shiferaw, T. G. Karayiannis, and D. B. R. Kenning. Flow boiling in a 1.1 mm tube with R134a: Experimental results and comparison with model. *International Journal of Thermal Sciences*, 48(2):331–341, 2009.

D. Steiner. *VDI-Warmeatlas (VDI Heat Atlas).* Verein Deutscher Ingenieure, Dusseldorf, Chapter Hbb, 1993.

S. Su, S. Huang, and X. Wang. Study of boiling ncipience and heat transfer enhancement in forced flow through narrow channels. *International Journal of Multiphase Flow*, 31:253–260, 2005.

S. Szczukiewicz, N. Borhani, and J. R. Thome. Two-phase flow boiling in a single layer of future high-performance 3D stacked computer chips. In *13th IEEE Intersociety Conference on Thermal and Thermomechanical Phenomena in Electronic Systems*, 2012a.

S. Szczukiewicz, N. Borhani, and J. R. Thome. Two-phase heat transfer and high-speed visualization of refrigerant flows in $100 \times 100\,\mu\text{m}^2$ silicon multi-microchannels. In *ECI 8th International Conference on Boiling and Condensation Heat Transfer*, 2012b.

J. R. Thome. Boiling in microchannels: a review of experiment and theory. *International Journal of Heat and Fluid Flow*, 25:128–139, 2004.

J. R. Thome. State-of-the-art overview of boiling and two-phase flows in microchannels. *Heat Transfer Engineering*, 27(9):4–19, 2006.

J. R. Thome. Wolverine Engineering Data Book III. http://www.wlv.com, 2010.

J. R. Thome and L. Consolini. Mechanisms of boiling in micro-channels: Critical assessement. *Heat Transfer Engineering*, 31(4):288–297, 2010.

J. R. Thome, V. Dupont, and A. M. Jacobi. Heat transfer model for evaporation in microchannels. Part I: presentation of the model. *International Journal of Heat and Mass Transfer*, 47:3387–3401, 2004.

C. B. Tibirica, G. Ribatski, and J. R. Thome. Flow boiling characteristics for R1234ze(E) in 1.0 and 2.2 mm circular channels. *Journal of Heat Transfer*, 134:1–8, 2012.

I. Tiselj, G. Hetsroni, B. Mavko, A. Mosyak, E. Pogrebnyak, and Z. Segal. Effect of axial conduction on the heat transfer in micro-channels. *International Journal of Heat and Mass Transfer*, 47:2551–2565, 2004.

UNFCCC. Kyoto Protocol to the United Nations Framework Convention on Climate Change. http://unfccc.int/kyoto_protocol/items/2830.php/, 1997.

Farzad Vakili-Farahani, B. Agostini, and J. R. Thome. Experimental study on flow boiling heat trnasfer of multiport tubes with R245fa and R1234ze(E). In *ECI 8th International Conference on Boiling and Condensation Heat Transfer*, 2012.

B. Vick and M. N. Ozisik. An exact analysis of low Peclet number heat transfer in laminar flow with axial conduction. *Letter in Heat and Mass Transfer*, 8:1–10, 1981.

P. A. Walsh, E. J. Walsh, and Y. S. Muzychka. Heat transfer model for gas-liquid slug flows under constant flux. *International Journal of Heat and Mass Transfer*, 53(15-16):3193–3201, 2010.

G. Wang, P. Cheng, and H. Wu. Unstable and stable flow boiling in parallel microchannels and in a single microchannel. *International Journal of Heat and Mass Transfer*, 50:4297–4310, 2007.

G. Wang, P. Cheng, and A. E. Bergles. Effects of inlet and outlet configurations on flow boiling instabilities in parallel microchannels. *International Journal of Heat and Mass Transfer*, 51:2261–2281, 2008.

F. M. White. *Fluid mechanics.* McGraw-Hill, 4*th* edition, 1999.

L. Wojtan, R. Revellin, and J. R. Thome. Investigation of saturated critical heat flux in a single uniformly heated microchannel. *Experimental Thermal and Fluid Science*, 30:765–774, 2006.

M. A. Woldesemayat and A. J. Ghajar. Comparison of void fraction correlations for different flow patterns in horizontal and upward inclined pipes. *International Journal of Multiphase Flow*, 33: 347–370, 2007.

H. Y. Wu and P. Cheng. Visualization and measurement of periodic boiling in silicon microchannels. *International Journal of Heat and Mass Transfer*, 46:2603–2614, 2003a.

H. Y. Wu and P. Cheng. An experimental study of convective heat transfer in silicon microchannels with different surface conditions. *International Journal of Heat and Mass Transfer*, 46:2547–2556, 2003b.

H. Y. Wu and P. Cheng. Boiling instability in parallel silicon microchannels at different heat flux. *International Journal of Heat and Mass Transfer*, 47:3631–3641, 2004.

H. Y. Wu, P. Cheng, and H. Wang. Pressure drop and flow boiling instabilities in silicon microchannel heat sinks. *Journal of Micromechanics and Microengineering*, 16:2138–2146, 2006.

J. Xu, S. Shen, Y. Gan, Y. Li, W. Zhang, and Q. Su. Transient flow pattern based microscale boiling heat transfer mechanisms. *Journal of Micromechanics and Microengineering*, 15(6):1344–1361, 2005.

J. L. Xu, W. Zhang, Q. W. Wang, and Q.C. Su. Flow instability and transient flow patterns inside intercrossed silicon microchannel array in a micro-timescale. *International Journal of Multiphase Flow*, 32(5):568–592, 2006.

C.-Y. Yang and C.-C. Shieh. Flow pattern of air-water and two-phase R-134a in small circular tubes. *International Journal of Multiphase Flow*, 27:1163–1177, 2001.

L. Zhang, J.-M. Koo, L. Jiang, M. Asheghi, K. E. Goodson an J. G. Santiago, and T. W. Kenny. Measurements and modeling of two-phase flow in microchannels with nearly constant heat flux boundary conditions. *Journal of Microelectromechanical Systems*, 11(1):12–19, 2002.

P. Zhang and X. Fu. Two-phase flow characteristics of liquid nitrogen in vertically upward 0.5 and 1.0 mm micro-tubes: Visualization studies. *Cryogenics*, 49:565–575, 2009.

T. Zhang, Y. Peles, J. T. Wen, and M. K. Jensen. Two-phase flow instability analysis for transient electronics cooling. In *12th IEEE Intersociety Conference on Thermal and Thermomechanical Phenomena in Electronic Systems*, 2010.

T. Zhang, J. T. Wen, Y. Peles, J. Catano, R. Zhou, and M. K. Jensen. Two-phase refrigerant flow instability analysis and active control in transient electronics cooling systems. *International Journal of Multiphase Flow*, 37:84–97, 2011.

Curriculum Vitae

Personal information

Name	Sylwia Szczukiewicz
Date of birth	9th October, 1985
Birthplace	Busko-Zdrój, Poland
Nationality	Polish
E-mail	sylwia.szczukiewicz@epfl.ch

Education

2009 – 2012	**Doctoral Student and Assistant**, Laboratory of Heat and Mass Transfer, Swiss Federal Institute of Technology Lausanne (EPFL), Switzerland
2009	**Master of Science in Mechanical Engineering**, Department of Mechatronics and Machine Building, Kielce University of Technology (PŚk), Poland

Awards and recognitions

2009	Kielce Stanislaw Staszic's Foundation Award
2009	A master thesis of distinction upon the recommendation of the External Examiner and the examination committee

Professional experience

2009 – 2012	Swiss Federal Institute of Technology (EPFL), Laboratory of Heat and Mass Transfer, Lausanne, laboratory activities, student supervision and training.

Journal publications

1. S. Szczukiewicz, N. Borhani, J. R. Thome, Two-Phase Flow Operational Maps for Multi-Microchannel Evaporators, *International Journal of Heat and Fluid Flow*, 2012 (submitted).

2. S. Szczukiewicz, N. Borhani, J. R. Thome, Two-Phase Heat Transfer and High-Speed Visualization of Refrigerant Flows in 100 x 100 μm^2 Silicon Multi-Microchannels. *International Journal of Refrigeration*, doi: 10.1016/j.ijrefrig.2012.11.014.

3. C. Tibiriçá Bigonha, S. Szczukiewicz, G. Ribatski, J. R. Thome, Critical Heat Flux of R134a and R245fa inside small diameter tubes, *Heat Transfer Engineering*, doi:10.1080/01457632.2012.722457.

Conference articles

1. S. Szczukiewicz, N. Borhani, J. R. Thome, Two-Phase Heat Transfer and High-Speed Visualization of Refrigerant Flows in 100 x 100 μm^2 Silicon Multi-Microchannels. *ECI 8th International Conference on Boiling and Condensation Heat Transfer*, Switzerland, 2012.

2. S. Szczukiewicz, N. Borhani, J. R. Thome, Two-Phase Flow Boiling in a Single Layer of Future High-Performance 3D Stacked Computer Chips, *ITherm2012: 13th Intersociety Conference on Thermal and Thermomechanical Phenomena in Electronic Systems*, USA, 2012.

3. M. M. Sabry, A. Sridhar, D. Atienza, Y. Temiz, Y. Leblebici, S. Szczukiewicz, N. Borhani, J. R. Thome, T. Brunschwiler, B. Michel, Towards Thermally-Aware Design of 3D MPSoCs with Inter-Tier Cooling, *DATE2011: Design, Automation and Test in Europe Conference*, France, 2011.

4. C. Tibiriçá Bigonha, S. Szczukiewicz, G. Ribatski, J. R. Thome, Critical Heat Flux of R134a and R245fa in 2.2 mm Circular Tube, *ENCIT2010: 13th Brazilian Congress of Thermal Sciences and Engineering*, Brazil, 2010.

5. S. Szczukiewicz, N. Borhani, J. R. Thome, Experimental Investigation of Diabatic Flow in Microchannels using Infra-Red Thermography. *XIV Heat and Mass Transfer Symposium*, Poland, 2010 (in polish).